

On-chip THz studies of low-dimensional semiconductor systems

DIVYANG KISHORE MISTRY (BENG)

Submitted in accordance with the requirements for the degree of

Doctor of Philosophy

The University of Leeds

School of Electronic and Electrical Engineering

November 2013

The candidate confirms that the work submitted is his own, except where work which has formed part of jointly authored publications has been included.

The candidate confirms that the appropriate credit has been given within the thesis where reference has been made to the work of others.

This copy has been supplied on the understanding that it is copyright material and that no quotation from the thesis may be published without proper acknowledgement.

© 2013 The University of Leeds and Divyang Kishore Mistry

This thesis is dedicated to my loving parents

Acknowledgements

I would like to thank my supervisors Professor John Cunningham, Professor Edmund Linfield and Professor Giles Davies for their support and guidance throughout the course of this project.

Special thanks go to Dr Chris Wood for his untiring assistance in all the experimental aspects of the project, without which, this project would not be as successful. I would also like to thank Dr Lianhe Li for providing all semiconductor wafer structures used throughout the course of this project. My great appreciation goes to Dr Matthew Byrne for his invaluable assistance and support throughout my work and Dr Andrew Burnett for proof reading my thesis.

I would like to show my appreciation to fellow PhD students, Chris Russell, Nii-Dodoo Amoo-Dodoo, Nicholas Hunter, Wilson Muchenje, Siddhant Chowdhury and Raed Al hathloul for having useful and never ending discussions and making my time enjoyable during my PhD.

On personal level, I would like to thank my parents for supporting me in my endeavours all these years and my extended family and friends for their continual support and encouragement. Last, but certainly not the least, my fiancée, and little pink rock in my life, Priyanka, who has supported me throughout the final stages of my PhD.

Abstract

A wide range of novel on-chip integration techniques were developed to explore the low-temperature perturbation of GaAs/AlGaAs based confined electron systems at terahertz frequencies. A new methodology for pump-probe transmission measurements of THz pulses along on-chip coplanar waveguides is demonstrated, allowing generation of guided THz signals and subsequent detection after propagation through in-plane integrated nanoscale devices at sub-Kelvin temperatures and under magnetic fields.

Initially, several methods that demonstrate introducing a guided-wave THz signal into an embedded two-dimensional electron system (2DES), involve the assembly of discrete substrate chips containing either the THz photoconductive material or a 2DES. The introduction of novel, monolithic integration of the 2DES layer and the THz photoconductive layer into a fully integrated epitaxially grown heterostructure, allowed successful incorporation of both the 2DES and the on-chip THz waveguides onto a single chip. The independent characterisation measurements of both the incorporated systems allowed optimisation of the monolithic structure, resulting in achievement of undiminished performance for both the 2DES and the on-chip THz waveguides.

A full characterisation of THz pulses interacting with an embedded 2DES, using both injected and capacitive, evanescent field coupling of the THz signal, are first performed at variable temperatures from (4 K to 300 K). It is found from the experimental observations that the temperature dependent 2DES resistivity can be directly probed from the time-domain transmitted THz pulses. Independently, a new method for sub-Kelvin excitation and detection of on-chip THz frequency radiation at temperatures as low as 200 mK and magnetic fields up to 12 T is also demonstrated,

which was employed to probe the magneto conductivity of the 2DES through THz pulse injection using on-chip waveguides.

The successful demonstration of THz pulse injection in low-dimensional electron systems using on-chip waveguides at sub-Kelvin temperatures and under magnetic fields paves the way for enhancing the studies of single electron transport, by investigating the properties of 1D or 0D quantum systems in the terahertz-frequency range.

Table of Contents

Acknowledgements	iii
Abstract.....	iv
Table of Contents	vi
Table of Figures.....	xi
Abbreviations	xxviii
Chapter 1: Introduction	1
1.1. Motivation	1
1.2. Thesis outline	2
1.3. Mesoscopic electron transport.....	4
1.4. Two-dimensional electron systems (2DES)	7
1.4.1. 2DES in GaAs/Al _x Ga _{1-x} As heterostructure.....	9
1.4.2. Electron transport properties in a 2DES	12
1.4.3. The quantum Hall Effect	15
1.5. THz time-domain spectroscopy.....	19
1.5.1. THz generation and detection.....	19
1.5.2. Free space THz spectroscopy systems.....	23
1.5.3. THz waveguide spectroscopy systems	25

1.6.	On-chip THz-TDS systems	27
1.6.1.	On-chip THz generation and detection.....	28
1.6.2.	Waveguide geometries	30
1.6.3.	Transmission line theory for coplanar waveguides	34
1.6.4.	Pump Probe measurement	37
1.7.	THz-TDS studies of 2DES	39
Chapter 2: On-chip THz waveguide and its integration with 2DES		42
2.1.	Introduction	42
2.2.	Characterisation of on-chip THz waveguides	43
2.3.	Integration of on-chip THz waveguides and 2DES.....	49
2.3.1.	Flip-chip technique	50
2.3.1.1.	Evanescent field coupling.....	51
2.3.1.2.	Direct electrical coupling.....	55
2.3.2.	Three-chip substrate assembly technique	56
2.3.3.	Epitaxial transfer method.....	61
2.3.4.	Monolithic integration technique.....	65
2.4.	First generation of monolithic integrated structures.....	67
2.4.1.	Characterisation of photoconductive layer	69
2.4.2.	Characterisation of 2DES	72
2.5.	Second generation of monolithic integrated structures	75
2.5.1.	Characterisation of 2DES	77

2.5.2. Characterisation of photoconductive layer	79
2.6. Summary	82

Chapter 3: THz generation and detection at Milli-Kelvin temperatures and

under magnetic fields	84
3.1. Introduction	84
3.2. Experimental setup	85
3.2.1. $^3\text{He}/^4\text{He}$ dilution refrigerator	85
3.2.2. Photonic crystal fibers	89
3.2.3. On-chip THz-TDS system	95
3.2.4. On-chip THz waveguide devices	98
3.3. On-chip THz transmission studies at room temperature	102
3.3.1. DC characterisation of photoconductive switches	102
3.3.2. Input pulses	104
3.3.3. Output pulses	108
3.4. On-chip THz transmission studies at cryogenic temperatures and under magnetic fields	111
3.4.1. DC characterisation and dynamic imaging of photoconductive switches	112
3.4.2. Transmitted THz pulses	114
3.5. Summary	118

Chapter 4: THz interaction with a 2DES between 300 K and 4 K	119
4.1. Introduction	119
4.2. 2DES integrated THz waveguides and experimental techniques	119
4.2.1. Pulse injection waveguide devices	120
4.2.1.1. Device fabrication.....	121
4.2.1.2. Lumped element model	123
4.2.2. Capacitive coupling waveguide devices	125
4.2.2.1. Device fabrication.....	126
4.2.2.2. Lumped element model	127
4.2.3. Experimental setup	129
4.3. Picosecond pulse injection in 2DES.....	131
4.3.1. Input pulses.....	132
4.3.2. Transmitted pulses	139
4.4. Waveguide spectroscopy of 2DES	145
4.4.1. Room temperature device characterisation.....	146
4.4.2. 2DES spectroscopy at cryogenic temperatures.....	149
4.5. Summary	153
Chapter 5: THz interaction with 2DESs at milli-Kelvin temperatures and under magnetic fields	155
5.1. Introduction	155
5.2. Analytical modelling of THz pulse interactions with confined 2DES	156

5.3. Picosecond pulse injection into a 2DES under magnetic field.....	161
5.3.1. DC characteristics of 2DES	161
5.3.2. Sample temperature	165
5.3.3. Input pulses.....	167
5.3.4. Transmitted pulses	171
5.4. Summary	178
Chapter 6: Conclusions and Future work	181
6.1. Project overview.....	181
6.2. Future Work	184
6.2.1. Improvements and modifications in pulse injection geometry	184
6.2.2. Measurement of ps pulse interaction using capacitive coupling geometry under magnetic fields.....	186
Publications and Conference Proceedings.....	187
Appendix 1: Hall bar fabrication	188
Appendix 2: Selective etch for first generation integrated structure	189
Appendix 3: Selective etch for second generation integrated structure.....	190
References	191

Table of Figures

Figure 1.1 Illustration of the diffusive motion of a charge particle in an impure metal at temperature close to absolute zero. The electron motion shows the influence of impurity scattering (shown by the mean free path l_e), and rare inelastic scattering events (blue circles, shown by the phase coherence length l_ϕ).	5
Figure 1.2 Demonstration of ‘size quantization’, as the dimensions of the electron system become comparable to the Fermi wavelength λ_F , resulting in (a) two-dimensional and (b) one-dimensional electron systems.	7
Figure 1.3 Schematic of a two-dimensional electron system formed in a Si MOS-FET. The two ohmic contacts (OC) formed on the bulk Si act as source and drain, while the metal electrode formed on SiO_2 layer acts as gate.	8
Figure 1.4 Energy band across the GaAs/AlGaAs heterostructure. (a) for the undoped scenario, (b) after n-type doping of AlGaAs with Si dopants, and (c) resulting band structure after 2DES formation at the heterojunction, with the Fermi energy at equilibrium across the GaAs/AlGaAs structure.	10
Figure 1.5 Schematic of a MBE grown GaAs/AlGaAs heterostructure having 2DES confined at the heterojunction. The addition of the undoped AlGaAs ‘spacer’ layer between the Si-doped AlGaAs and GaAs layer reduces the impact of ionized scattering on the confined charge carriers.	11
Figure 1.6 Progress in improving carrier mobility in 2DESs, up to the present record of $36,000,000 \text{ cm}^2/\text{Vs}$, together with the information on the technical modifications and innovation required for GaAs/AlGaAs heterostructures, displayed for the last three decades [53].	12
Figure 1.7 (a) Density of states for a 2DES. (b) Heterojunction interface showing quantized sub-band energies (E_1, E_2, E_3) and Fermi energy E_F , where $V(z)$ is the potential barrier controlling the boundary conditions of the 2DES.	13

Figure 1.8 A four-terminal Hall bar geometry formed on GaAs/AlGaAs heterostructure containing the 2DES with source and drain ohmic contacts shown by S and D. The electron transport coefficients are measured using ohmic contacts A-D, under influence of electric E and magnetic fields B, with x, y and z axes showing their respective direction.....	14
Figure 1.9 The Quantum Hall effect measurement using the Hall bar geometry at $T < 24$ mK, showing the Hall resistivity ρ_{xy} getting quantized at values of h/ie^2 and the Shubnikov-de Haas oscillations occurring in the diagonal resistivity ρ_{xx}	16
Figure 1.10 Energy spectrum of the 2DES under magnetic fields, demonstrating the occurrence of LLs and spin splitting, taken from reference [54]. The spectrum shown here is considered for an ideal case (i.e. disorder free system).....	17
Figure 1.11 Illustration of the density of states in a 2D electron system for increasing magnetic fields. At $B = 0$, there is a uniform density of states. At finite magnetic field, discrete LLs are formed and separated by $\hbar\omega_c$. The LLs are delta functions in the ideal case, but are broadened due to disorder in the system. As the magnetic field further increases the Fermi level passes through successive LLs.....	18
Figure 1.12 Schematic of the dipole-like photoconductive switch used for emission of free space pulsed THz radiation.	21
Figure 1.13 Electro optic detection of the THz pulses using the Pockels effect [12]. The quarter wave plate is labelled $\lambda/4$	23
Figure 1.14 Example of a free-space THz time-domain spectroscopy, showing the THz generation using a photoconductive antenna and the THz detection using an electro-optic crystal, taken from reference [71]. The internal reflection of the electro-optic crystal shows the probe beam propagating at an angle β to the THz beam in the crystal. The quarter wave plate is labelled $\lambda/4$, and the Wollaston prism is labelled W.	24

- Figure 1.15 Example of a free-space THz-TDS system employing pairs of parabolic mirrors to guide the propagating THz radiation through various ‘sample’ under test, taken from reference [55]. The propagating THz waves are enclosed in a nitrogen-purged box to avoid absorption by water content in the surrounding atmosphere. 25
- Figure 1.16 Example of THz-TDS system using free-space coupled metallic wire waveguide, taken from reference [79]. (a) Side view of the photoconductive emitter with the metallic wire tip connecting the positive electrode. (b) The schematic of the experimental setup used (BS represents beam splitter, PC represents photoconductive switch emitter, WP represents Wollaston prism, and BPD represents balanced photodiodes). 27
- Figure 1.17 Illustration of ps time scale electrical transient generated using a photoconductive switch for on-chip THz systems. (a) 2D cross section of a typical photoconductive switch, with NIR laser beam illuminating the switch gap and (b) photogenerated charge separation in the applied DC electric field. 29
- Figure 1.18 Schematic representation of a pair of photoconductive switch region defined between the metal electrodes and the integrated signal conductor of the CPW. The experimental configuration is also shown for measuring the characteristics of a switch region in terms of photocurrent generated across applied bias. 30
- Figure 1.19 2D cross section of (a) the microstrip line, and (b) the planar Goubau line. Also shown are the electric and magnetic fields surrounding an electrical pulse as it propagates along the signal conductor..... 30
- Figure 1.20 2D cross section of (a) the coplanar slot line, and (b) the coplanar strip line. Also shown the electric and magnetic fields surrounding an electrical pulse as it propagates along the signal conductor..... 32
- Figure 1.21 2D cross section of the CPW structure including the signal conductor and the ground planes. It also illustrates (a) the symmetric mode and (b) the anti-symmetric mode for the transverse propagating electric and magnetic fields..... 33

Figure 1.22 (a) Arial view of a short length (Δx) coplanar waveguide, showing the physical geometry dimensions, and (b) an equivalent two wire line lumped element circuit model representing the three terminal coplanar waveguide. The single ground conductor in the lumped element model represents both the ground planes of the CPW.	34
Figure 1.23 Example of a lossless transmission line terminated with a load impedance Z_L	36
Figure 1.24 Pump-probe arrangement used for on-chip THz-TDS systems.	37
Figure 1.25 Example of a pump-probe arrangement for on-chip generation and detection of THz pulses. A DC voltage bias is applied across the pump switch gap. The electrical transient generated with the pump beam, is launched on to the on-chip waveguide and can be sampled before and after propagation along the waveguide using probe beam at position 1 and 2 respectively.	38
Figure 1.26 Diagram of the procedure used for extracting propagating pulse speed by measuring the pulses before and after propagation (position 1 and 2 respectively), along the active length of (L) of the on-chip waveguide. The diagram illustrates the change in the probe-beam path length by a distance $\sim L \cos\theta$ when it is transferred from position 1 to position 2, or vice-versa.	39
Figure 1.27 Similar pump-probe arrangement as shown in Figure 1.25, for generation and sampling of THz pulses along an on-chip waveguide. In this case, the evanescent field of the propagating pulses along the waveguide is used for spectroscopy of the nanoscale device under test (NDUT).	41
Figure 2.1 (a) Schematic of the SI-GaAs based heterostructure, containing the LT-GaAs photoconductive layer grown on top of the optical barrier (AlAs), using MBE. (b) The overlaid CPW device design consisting of the four switch regions coupled with the Ti/Au signal conductor and ground planes.	43

Figure 2.2 Diagram of the on-chip waveguide measurement setup operating at room temperature. The beam from the Ti:sapphire laser was split into pump and probe beams using the beam splitter. The pump beam was passed along paths 4-7, before being focussed onto the sample. The probe beam was optically modulated and passed along an optical delay line via paths 8-11, before being focussed onto the sample.	44
Figure 2.3 DC characteristics measured in terms of current versus applied voltage at varying laser powers, for (a) pump and (b) probe photoconductive switch gap defined on either side of the waveguide.	45
Figure 2.4 The time-domain scan of the generated THz pulse using switch region 1 as the source and switch region 2 as the detector. The main THz peak with time duration of 2.4 ps is followed by the two time delayed reflection peaks, a and b.	46
Figure 2.5 Demonstration of the pulse paths required to generate the two time-domain reflections peaks, a and b (in Figure 2.4), following the generated THz pulse peak.	47
Figure 2.6 Example of the time-domain pulse transmitted along the 1.5 mm coplanar waveguide, measured using switch region 1 as the source and switch region 3 as the detector. The FWHM was measured to be 3.2 ps.	48
Figure 2.7 Fast Fourier Transform performed on the THz peak seen in Figure 2.6, showing the usable frequency bandwidth of the CPW devices up to ~400 GHz with peak signal-to-noise ratio of ~100:1.	48
Figure 2.8 Illustration of the two separate chips used for ‘flip-chip’ integration technique. Where, (a) shows the chip containing the sapphire substrate with the photoconductive material and the overlaid CPW. (b) shows the chip containing the GaAs substrate with the GaAs/AlGaAs heterostructure containing the 2DES grown on top.	50
Figure 2.9 Graphical illustration of the ‘flip-chip’ approach, showing coupling of the propagating pulse along the CPW with the flipped GaAs/AlGaAs heterostructure chip containing the 2DES. The integrated generation and detection photoconductive switch shows the location points for pulse launch and detection.	51

- Figure 2.10 Experimental arrangement showing the demonstration of ‘flip-chip’ evanescent field coupling technique, taken from reference [10]. (a) shows the geometry of the CPW used, with the location points for ps pulse generation and detection along the CPW shown by L and D. (b) The configuration of the integrated structure used, showing the 2DES chip flipped and epoxied to the waveguide chip..... 52
- Figure 2.11 Diagram of the experimental arrangement for evanescent field coupling of on-chip CPW with the 2DES, taken from reference [71]. 53
- Figure 2.12 Experimental data showing the time-domain scans of the transmitted pulse measured after propagation along the 1.5 mm active length of the CPW (as shown in Figure 2.1 (b)), with the flipped 2DES chip in close proximity distances and in full contact with the waveguide surface..... 54
- Figure 2.13 Graphical illustration of the ‘flip-chip’ approach, showing direct electrical coupling of the propagating pulse along a CPW with the flipped GaAs/AlGaAs heterostructure chip containing the 2DES. The electrical connection is made through the direct contact between the signal conductor and the ohmic contacts. The integrated generation and detection photoconductive switch shows the location points for pulse launch and detection..... 55
- Figure 2.14 Experimental configuration previously established for demonstrating the ‘flip-chip’ arrangement to electrically couple the ps pulses travelling along the CPW with the flipped 2DES chip, taken from reference [98]. The four ohmic contacts formed on the flipped 2DES chip surface are directly bonded to the signal conductor and the ground planes of the CPW. The location points for ps pulse generation and detection along the CPW shown by L and D respectively. 56
- Figure 2.15 Graphical illustration of the ‘three-chip substrate assembly’ method, showing the ‘post-fabrication’ assembly of the CPW overlaid on three different chips onto a supporting host substrate. The left and right chips contain the photoconductive switch gaps for THz generation and detection, whereas the chip in the middle contains the active 2DES device coupled with the signal conductor of the CPW. 57

- Figure 2.16 Optical image of an integrated device using three-chip substrate assembly method for coupling on-chip CPW with a 2DES device, taken from reference [103]. The left and right chips containing the photoconductive switches are fabricated from the ErAs:InGaAs photoconductive material, while the central chip containing the 2DES is fabricated from a GaAs/AlGaAs heterostructure. 58
- Figure 2.17 Optical microscopic image of the CPW device geometry implementing ‘multiple-chip assembly’ technique. (a) shows the image of a continuous CPW device with integrated generation and detection photoconductive switch gaps on a single LT-GaAs substrate chip. (b) shows the image of an interface between multiple CPW sections (after cleaving and re-assembling of the continuous CPW device). The CPW sections including the integrated generation and detection photoconductive switch gaps on multiple LT-GaAs substrate chips were electrically connected using a conductive epoxy..... 59
- Figure 2.18 Experimental data showing the comparison between the transmitted pulse measurements along a CPW overlaid on a single LT-GaAs substrate chip and along a electrically connected multiple CPW sections overlaid on two different LT-GaAs substrate chips. 60
- Figure 2.19 Optical microscopic image of the interface between CPW sections cleaved and re-assembled from the separate GaAs substrate chips. The image shows the resulting finite gap between the two chips due to presence of interface dislocations. 61
- Figure 2.20 Layer-by-layer view of the implementation of the epitaxial transfer method, for integrating ultra-thin films of the LT-GaAs photoconductive layer and 2DES on a host substrate (quartz). The electrical coupling of the 2DES with the overlaid on-chip CPW is carried out via ohmic contacts formed on the film containing the 2DES. While the LT-GaAs films are used defining switch regions for generation and detection of propagating ps timescale pulses..... 62

Figure 2.21 Schematic of the MBE grown layer structures used for the epitaxial lift-off and transfer of (a) GaAs/AlGaAs heterostructure containing the 2DES, and (b) LT-GaAs photoconductive layer. The incorporation of the AIAs release layer shown in both structures aids the epitaxial lift-off process.....	63
Figure 2.22 Optical microscopic image demonstrating the micro-cracking of the LT-GaAs film after epitaxially transferred from the MBE structure and covalently bonded onto a quartz substrate.	64
Figure 2.23 Typical dependence of the photo-generated carrier lifetime on the MBE growth temperature for as-grown (un-annealed) LT-GaAs photoconductive layer, taken from reference [65].	66
Figure 2.24 Schematic of the MBE grown layer structure used for the first generation monolithic integration of the LT-GaAs photoconductive layer with the 2DES heterostructure.	67
Figure 2.25 Simulated conduction band profile showing the distribution of carrier concentration across the layer structure for the first generation monolithic integration of LT-GaAs layer on top of the 2DES heterostructure.	68
Figure 2.26 Main figure: the DC characteristics of one of the four switch gaps defined on the surface of the monolithically integrated LT-GaAs layer, measured in terms of current generated with respect to the applied bias in dark and illumination conditions. Inset: the DC characteristics of the switch gap defined on the surface of the reference structure (i.e. containing the LT-GaAs with no 2DES, as shown in Figure 2.1(a)) under similar conditions.	70
Figure 2.27 Experimental data of the THz pulses propagating along the CPW defined on the surface of the monolithically integrated LT-GaAs layer. The measurement show the time-domain ps pulse comparison observed at the input of the device (prior to the propagation down the CPW) and the device output.	71
Figure 2.28 Experimental data for the dark measurement of Hall (ρ_{xy}) and diagonal (ρ_{xx}) resistivity of the first generation monolithically integrated 2DES, taken using a four-terminal Hall bar device configuration at 1.4 K.	73

Figure 2.29 Experimental data for the light (after illumination) measurement of Hall (ρ_{xy}) and diagonal (ρ_{xx}) resistivity of the first generation monolithically integrated 2DES, taken using a four-terminal Hall bar device configuration at 1.4 K.....	74
Figure 2.30 Schematic of the MBE grown layer structure used for the second generation monolithic integration of the LT-GaAs photoconductive layer with the 2DES heterostructure.	75
Figure 2.31 Simulated conduction band profile showing the distribution of carrier concentration across the layer structure for the second generation monolithic integration of LT-GaAs layer below the 2DES heterostructure.	76
Figure 2.32 Experimental data for the dark measurement of Hall (ρ_{xy}) and diagonal (ρ_{xx}) resistivity of the second generation monolithically integrated 2DES, taken using a four-terminal Hall bar device configuration at 1.4 K.	78
Figure 2.33 Experimental data for the light (after illumination) measurement of Hall (ρ_{xy}) and diagonal (ρ_{xx}) resistivity of the second generation monolithically integrated 2DES, taken using a four-terminal Hall bar device configuration at 1.4 K.	78
Figure 2.34 Main figure: the DC characteristics of one of the four switch gaps defined on the exposed surface of the monolithically integrated LT-GaAs layer, measured in terms of current generated with respect to the applied bias in dark and illumination conditions. Inset: the DC characteristics of the switch gap defined on the surface of the reference structure (i.e. containing the LT-GaAs with no 2DES, as shown in Figure 2.1(a)) under similar conditions.....	80
Figure 2.35 Experimental data of the THz pulses propagating along the CPW defined on the exposed surface of the monolithically integrated LT-GaAs layer. The measurement show the time-domain ps pulse comparison observed at the input of the device (prior to the propagation down the CPW) and the device output.	81
Figure 3.1 P-T phase diagram of ^4He	85
Figure 3.2 Phase diagram for ^3He - ^4He mixtures.	86

Figure 3.3 Oxford instruments DR 200 cryo-free dilution refrigerator.	87
Figure 3.4 Diagram of various critical temperature plates inside the dilution unit.....	88
Figure 3.5 Cross-section schematic, showing structure of (a) Solid core and (b) Hollow core optical fibers.....	90
Figure 3.6 Diagram of optical setup used for testing optical fibers.	91
Figure 3.7 Experimental data showing the comparison of pulse duration at $\lambda \sim 810$ nm, between a free space laser pulse and a transmitted laser pulse through a ~ 1 m long hollow core fiber.....	92
Figure 3.8 Experimental data showing the comparison of laser pulse durations for transmission through a ~ 1 m long hollow core fiber at two different wavelengths ($\lambda \sim 780$ and 810 nm).	93
Figure 3.9 Experimental data showing the comparison of pulse duration at $\lambda \sim 810$ nm, between a free space laser pulse and a transmitted laser pulse through a ~ 1 m long silica core fiber.	94
Figure 3.10 System diagram of THz-TDS used for operating on-chip waveguides at cryogenic temperatures. The 100 fs laser pulses from Ti:sapphire laser are beam split and compressed before being channelled down two optical fibers for accessing the dilution fridge.....	96
Figure 3.11 Illustration of the cryogenic sample holder used, together with the two pairs of piezoelectric stages for positioning and alignment of free space laser beams.	97
Figure 3.12 Schematic of LT-GaAs/AlAs/GaAs photoconductive heterostructure grown using MBE.	99
Figure 3.13 Main figure: Diagram of a THz coplanar waveguide device (Sample1) used in this work, containing a transmission line between contact pads (2 and 5) and four converging biasing electrodes defining simple PCS gap regions. Inset: Enhanced view of one of the four switch regions showing dimensions of the switch gap, transmission line and probe arms.	100

Figure 3.14 Main figure: Diagram of a THz coplanar waveguide device (Sample2) used, containing a transmission line between contact pads (2 and 5) and four converging biasing electrodes defining two simple PCS gap regions (pump switch) and two IPCS gap regions(probe switch). Inset: Enhanced view of one of the IPCS pairs showing dimensions of the switch gap, transmission line and probe arms.....	101
Figure 3.15 Main figure: Current versus applied voltage for Sample 2, for (a) the simple PCS gap pump switch and (b) IPCS gap probe switch at varying laser powers. Inset: Current achieved at 30 V for each power.....	103
Figure 3.16 Main figure: Current versus applied voltage for Sample 1, for (a) the pump switch and (b) probe switch at varying laser powers. Inset: Current achieved at 30 V for each power.....	103
Figure 3.17 Comparison of the generated THz pulse scans for both pairs of switch regions on Sample 1 showing the two main reflection peaks.	105
Figure 3.18 Demonstration of the pulse paths required for the origin of the two subsequent reflections a and b, following the main generated THz pulse.	106
Figure 3.19 Comparison of the generated THz pulse scans for both pairs of switch regions (SPCSs and IPCSs) on Sample 2 showing the two main reflection peaks. Also shown added reflections ‘x’ occurring between different geometries of pump and probe switch.	107
Figure 3.20 Normalised generated THz pulse scans for Sample 2 using both pairs of switch regions (SPCSs and IPCSs), showing the variation of FWHM of the THz pulse with respect to the switch pair geometry used.....	108
Figure 3.21 Example of a pulse transmitted along the 1.2 mm coplanar waveguide for Samples 1 and 2, using switch region 1 as the source and switch region 3 as the detector in both cases.....	109
Figure 3.22 Main figure: Transmitted THz pulse scans for Sample 2 at varying pump and probe beam powers. Inset: Variation of transmitted pulse peak amplitude with respect to beam powers.	110
Figure 3.23 Fast Fourier transform of the transmitted time-domain signals shown in Figure 3.21 for Sample 1 and 2.....	111

Figure 3.24 Current versus applied voltage for Sample 2 for (a) the pump switch and (b) the probe switch taken at 100 mK and varying magnetic fields.....	113
Figure 3.25 The photocurrent image map of the pump switch pair (light regions showing higher current) taken at (a) 200 mK, 0 T and, (b) 200 mK, 9.5 T. The comparison between the actual physical switch pair geometry design on the sample and its photocurrent image map is also shown.	114
Figure 3.26 Main figure: Experimental measurement of a transmitted pulse along the CPW (Sample 2) taken at 100 mK and 0 T. Inset: FFT of the portion of the time-domain signal before first reflection.	115
Figure 3.27 The normalised amplitude time-domain spectra of the transmitted pulse taken at 100 mK and varying magnetic fields from 0 – 9.5 T offset by 1 unit per trace.....	116
Figure 3.28 (a) The photocurrent image map of the pump switch pair (light regions showing higher current) and, (b) the corresponding image map based on the transmitted THz pulse amplitude (red regions showing peak transmitted pulse amplitude detected). Data were taken at 200 mK and 0 T.....	117
Figure 3.29 (a) A photocurrent image map of the pump switch pair (light regions showing higher current) and, (b) the corresponding image map based on the transmitted THz pulse amplitude (red regions showing higher peak transmitted pulse amplitude detected). Data were taken at 200 mK and 9.5 T.	117
Figure 4.1 Schematic of ‘picosecond pulse injection’ device with 2DES embedded into coplanar waveguide with probe arms defining regions for photoconductive excitation of exposed LT-GaAs layer.....	120
Figure 4.2 Schematic diagram showing the main stages of fabrication for the picosecond pulse injection devices (a) Monolithic integrated structure grown using MBE. (b) ‘sub-mesa’ etching. (c) 2DES ‘super-mesa’ etching. (d) AuGeNi metallisation for Ohmic contact. (e) CPW metallisation.	122

Figure 4.3 Main figure: Diagram of the THz CPW device fabricated, containing the 2DES strip integrated in the signal conductor and four biasing electrodes defining PCS gap regions. Inset: Detailed view of one of the four switch regions.	123
Figure 4.4 A lumped element circuit model representation of the 2DES integrated with coplanar waveguide for picosecond pulse injection.....	124
Figure 4.5 Schematic of ‘capacitive coupling waveguide’ device with active region of the CPW overlaid on the sub-mesa containing the 2DES system located ~70 nm below.	126
Figure 4.6 Schematic diagram showing the main stages of the capacitive field coupling CPW device fabrication. (a) Monolithic integrated structure grown using MBE. (b) ‘sub-mesa’ etching. (c) CPW metallisation.....	127
Figure 4.7 A lumped element circuit model representation of capacitively coupled waveguide overlaid on top of the 2DES layer.	128
Figure 4.8 System diagram of THz-TDS used for operating 2DES integrated THz waveguides at cryogenic temperatures using continuous He flow cryostat.	129
Figure 4.9 Schematic diagram of the THz waveguide device mounted within the continuous flow cryostat, with optical access provided by transparent quartz windows.	130
Figure 4.10 (a) Microscope image of a pulse injection device with integrated 100- μm -long 2DES strip. (b) Microscope image of a reference device with 100 μm long gap.	131
Figure 4.11 Experimental data of the generated THz pulse scan for the reference device taken at 300 K, showing the secondary reflection ‘a’ arising from the integrated gap.	132
Figure 4.12 Demonstration of the pulse path required for the origin of the reflection ‘a’, following the main generated THz pulse.....	133
Figure 4.13 Experimental data of the generated THz pulse scan for the 2DES Mesa device taken at 300 K, showing the secondary reflection ‘a’ arising from the integrated 2DES-CPW interface.....	134

Figure 4.14 Peak amplitudes of incident and reflected pulses for (a) reference device and (b) 2DES mesa device at different biases and beam powers.	135
Figure 4.15 Normalised pulse peak amplitude comparison between the THz pulse and the reflection for (a) reference device and (b) 2DES mesa device.....	136
Figure 4.16 Comparison of the normalised generated THz pulse scans for the reference device, measured at varying temperatures, using switch region 1 as source and switch region 2 as detector.	137
Figure 4.17 Comparison of the normalised generated THz pulse scans for the 2DES mesa device, measured at varying temperatures, using switch region 1 as source and switch region 2 as detector.	138
Figure 4.18 Comparison of the first reflection amplitude seen in the reference device and the pulse injection device as a function of temperature	138
Figure 4.19 Setup for measuring transmitted pulses, showing the bias arrangement and the alignment of pump and probe beams.....	139
Figure 4.20 2D cross-section of the CPW, showing (a) the odd mode and (b) the even mode for the transverse propagating electric and magnetic fields.....	140
Figure 4.21 Comparison of transmitted pulses along the reference device with integrated gap, measured at different temperatures using switch region 1 as the source and switch region 3 as the detector.....	140
Figure 4.22 Examples of pulses transmitted through the CPW with integrated gap, with odd mode and even mode preferentially excited. The transmitted pulse scans measured at 300 K and 4 K are shown.....	142
Figure 4.23 Example of transmitted pulses along the CPW device with integrated 2DES strip, measured at (a) 300 K and (b) 4 K, using switch region 1 as the source and switch region 3 as the detector.....	143
Figure 4.24 Examples of pulses transmitted through the CPW with integrated 2DES, with odd mode and even mode preferentially excited. The transmitted pulse scans measured at 300 K and 4 K are shown.....	144

Figure 4.25 With odd mode preferentially excited, the transmitted pulse amplitude variation with decreasing temperatures compared for the reference device and the 2DES mesa device. For a direct comparison, the transmitted pulse amplitude data set shown is normalised to the maximum amplitude observed between both the devices.	145
Figure 4.26 Diagram of the capacitive field coupling THz CPW device, containing active region of the signal conductor and ground planes overlaid on top the 1.2 mm long ‘sub-mesa’ containing the 2DES.	146
Figure 4.27 Example of an input pulse measured for a capacitive coupling waveguide device at 300 K, using switch region 1 as source and switch region 2 as detector.	147
Figure 4.28 Schematic of the pulse path creating secondary reflections ‘b’ and ‘c’, following the main generated THz pulse.	147
Figure 4.29 Example of a transmitted pulse measured for capacitive coupling waveguide device at 300 K, using switch region 1 as source and switch region 3 as detector.	148
Figure 4.30 Comparison of time-domain transmitted pulse scan measured at varying temperatures on capacitive field coupling device.	149
Figure 4.31 Variation of transmitted pulse amplitude with decreasing temperatures or increasing 2DES conductivity.	151
Figure 4.32 Example of a time-domain pulse transmitted along the CPW on capacitive coupling device at 4 K, using switch region 1 as source and switch region 3 as detector.	151
Figure 4.33 Frequency spectrum comparison of the transmitted time-domain signals observed at varying temperatures and as shown in Figure 4.30. The (grey) dashed line corresponds to the fundamental frequency of the standing wave, with resonance frequencies of the second and third order harmonics shown by (red and blue) dashed lines.	153
Figure 5.1 Charge fluctuation in a 2DES of length L, created by primary applied electric field E.	157

Figure 5.2 Charge fluctuation in a 2DES of length L , created by an externally applied electric field E and also external magnetic field B perpendicular to the 2DES.	158
Figure 5.3 Analytical simulations showing the first six magneto plasmon modes ($i = 1...6$) in a 2DES with a fixed confinement width of (x μm), for different charge densities measured under (a) dark conditions (Sheet density, $n_s = 3.5 \times 10^{11} \text{ cm}^{-2}$) and (b) under illumination (Sheet density, $n_s = 6 \times 10^{11} \text{ cm}^{-2}$).	159
Figure 5.4 Analytical simulations showing the first six magneto plasmon modes in a 2DES, considering identical charge densities under illumination ($n_s = 6 \times 10^{11} \text{ cm}^{-2}$) with different 2DES confinement width of (x μm) (a) $30 \mu\text{m}$ and (b) 1 cm	160
Figure 5.5 The experimental arrangement for measuring DC transport properties of the coupled 2DES with the centre conductor. The 2DES resistance is extracted by measuring the current under constant DC bias applied using a two-terminal geometry.	162
Figure 5.6 Current measured through a 2DES coupled with the centre conductor of a THz waveguide device, measured as a function of applied magnetic field.	162
Figure 5.7 Two-terminal 2DES conductance measured as a function of magnetic field.	164
Figure 5.8 The Hall resistance measured from the 2DES coupled with the THz waveguide. Hall resistance is quantized at values of h/ve^2	165
Figure 5.9 The Hall resistivity measured from the 2DES coupled with the THz waveguide (a) in the dark and (b) under illumination by an 800nm pump-probe laser beam arrangement. Hall resistance is quantized at values of h/ve^2	166
Figure 5.10 Hall bar configuration for coupling 2DES with THz CPW to perform <i>in situ</i> four-terminal quantum Hall characterisation.	167
Figure 5.11 Experimental data of the generated THz pulse with secondary reflections for pulse injection device taken at 200 mK and 0 T magnetic field, using PCS 1 as the source and PCS 2 as the detector.	168

Figure 5.12 A contour plot of the time-domain generated pulse scan illustrating the behaviour of main THz pulse and secondary reflections with varying magnetic fields at 200 mK.	169
Figure 5.13 (a) A higher resolution contour plot showing the behaviour of the main generated THz pulse and the following time-domain reflection pulse from the CPW-2DES interface with increasing magnetic fields.....	170
Figure 5.14 Main figure: Experimental data of the transmitted THz pulse propagated through the 2DES strip taken at 200 mK and 0 T magnetic field, using PCS 1 as the source and PCS 3 as the detector. Inset: Experimental data of the transmitted THz pulse propagated through the 2DES strip taken at 4 K, using PCS 1 as the source and PCS 3 as the detector.....	172
Figure 5.15 A contour plot of the time-domain transmitted pulse scan illustrating the behaviour of the main THz pulse peak (around 0 ps) and secondary reflections after propagating through the 2DES in varying magnetic fields.....	174
Figure 5.16 Comparison of the transmitted THz signal amplitude as a function of magnetic field (symbols) with the 2-terminal 2DES conductivity (line) measured at 200 mK temperature.	175
Figure 5.17 Main figure: Experimental data of the transmitted THz pulse propagated through the 2DES strip taken at 200 mK and 1 T magnetic field, using PCS 1 as the source and PCS 3 as the detector. Inset: Experimental data of the transmitted THz pulse propagated through the 2DES strip taken at 300 K, using PCS 1 as the source and PCS 3 as the detector.....	176
Figure 5.18 Frequency spectra of the time-domain transmitted pulses shown in Figure 5.15 at selected magnetic fields, normalised between 0 –1. Data offset by 1 for clarity. The dotted lines show the anticipated magneto plasmon resonance frequencies at corresponding magnetic fields, analytically modelled for the pulse injection device used.....	177
Figure 6.1 Schematic diagrams of CPW based devices designed to measure the ps response of (a) a 1DES and (b) a quantum dot system.	185

Abbreviations

2DES	Two-dimensional electron systems
GaAs	Gallium arsenide
AlGaAs	Aluminium gallium arsenide
CPW	Coplanar waveguide
THz	Terahertz
TDS	Time domain spectroscopy
NIR	Near infrared
MBE	Molecular beam epitaxy
QHE	Quantum Hall Effect
LL	Landau level
FWHM	Full width half maximum
NDUT	Nanoscale device under test
FFT	Fast Fourier transform
IDT	Interdigitated transducer
TEM	Transverse electromagnetic
LED	Light emitting diode

Chapter 1: Introduction

1.1. Motivation

The development of future electronic devices based on nanostructures operating at very high frequencies requires the understanding of the underlying fundamental physics. Over the past few decades, the studies of electron transport in low-dimensional quantum confined semiconductor systems have revealed some of the elemental features of the physics of nanostructures. The nature of electron transport in such systems has led to some of the major discoveries in the field, such as the Quantum Hall Effect [1] and the conduction measurement of ballistic channels [2], enabling physicists to define universal quantum standard of resistance. However these studies have mainly been carried out using steady state measurements. The work presented in this thesis is aimed at studying electron transport properties under THz frequency excitation, through time-resolved measurements with picosecond resolution. This will allow monitoring the spatial position of single electrons by changing their quantum state on a picosecond time scale.

The field of terahertz science and technology has seen a significant advancement in wide range of spectroscopy applications [3-6]. With the energy range from 1 meV to 100 meV, the THz radiation is sensitive to the energy response of charge particles in quantum confined systems. Moreover, the THz frequency region is well suited for the study of carrier resonances and intraband transitions in low-dimensional semiconductor systems. The time resolved pulsed terahertz spectroscopy systems has developed into an influential means for studying charge carrier dynamics in semiconductor nanostructures

[7-11]; since, it also allows phase information to be extracted as oppose to frequency domain spectroscopy studies.

Initially, the free-space mode of propagation was employed for pulsed THz spectroscopy of quantum confined systems, but more recently with the development of on-chip pulsed THz guided technology, the latter is becoming a more favourable alternative. The on-chip THz technology offers key advantages for spectroscopy applications [12, 13]. These include a compact THz generation and detection scheme using photoconductive switches and larger interaction length between the probing signal and the nanoscale device under test. Other benefits of on-chip THz technology over free space THz systems include its adaptability in operation at cryogenic environments and under high magnetic fields. These properties make it an ideal choice for making time-resolved measurements of quantum electron transport properties in confined semiconductors and in doing so, a compelling new approach for defining a quantum standard of electronic current.

In addition to integration of on-chip time-resolved THz systems with nanoscale devices, this project had the aim of developing an underpinning generic measurement technology that can allow spectroscopy applications of on-chip THz systems to be realized for the first time at milli-Kelvin temperatures.

1.2. Thesis outline

The rest of this chapter involves an overview of the mesoscopic electron transport properties observed in low-dimensional confined semiconductor nanostructures, particular two-dimensional electron systems (2DES). It is followed by a discussion on several areas of THz technology, including generation, propagation and detection in free

space and on-chip systems. Lastly, pulsed THz time-resolved studies of quantum confined systems are reviewed.

Chapter 2 presents a review of techniques used for integration of the on-chip THz systems with the 2DES for measuring time resolved ballistic transport within the 2DES. An in depth discussion on the optimisation of the monolithic integration approach that is used in the current work for coupling on-chip THz waveguides with the 2DES is presented.

Chapter 3 presents the first measurements of on-chip THz pulse generation and detection using conventional pump-probe techniques at milli-Kelvin temperature range and under magnetic fields. The chapter provides a detailed description of the generic measurement setup developed and used, followed by a discussion on the device designs and fabrication.

Chapter 4 reviews two different methods employed in this work used for variable temperature time-domain spectroscopy of a 2DES using on-chip coplanar waveguide devices.

Chapter 5 is focussed on the investigation of electron transport in a 2DES under the influence of ps time scale pulses electrically injected at temperatures down to the sub-Kelvin range and under magnetic fields. The experimental results, together with analytical modelling are presented and discussed.

The final chapter gives an overview of the project, with a discussion on the possible future directions for continuing the work presented in this thesis.

1.3. Mesoscopic electron transport

The classical charge transport in metals considers 3D Cartesian coordinates of freedom and is described by the Drude theory [14]. For this case, the DC-conductivity of the metal is given by,

$$\sigma = \frac{ne^2\tau}{m} \quad (1.1)$$

where, n is the electron density with charge $(-e)$, m is the effective mass and τ is the mean free time. The mean free time τ in this case, incorporates all of the scattering processes the electrons suffer from static impurities, vacancies, dislocations, and also from elementary processes like electron-phonon and electron-electron scattering. Since these scattering processes are independent and additive, they make the electron transport incoherent and diffusive, thereby affecting the important physical length scales associated with the electron transport. At sufficiently low temperatures, the scattering process that cause the incoherent electron transport, such as electron-phonon scattering, more or less freezes out, leaving electron transport dominated by impurity scattering (which is not incoherent). An illustration of diffusive transport dominated by impurity scattering with rare phase randomizing processes at low temperatures is shown in Figure 1.1. The conductivity will therefore deviate from the classical form (given by Equation 1.1) according to the quantum nature of the electrons, which forms the backbone of the physics of mesoscopic electron transport phenomena.

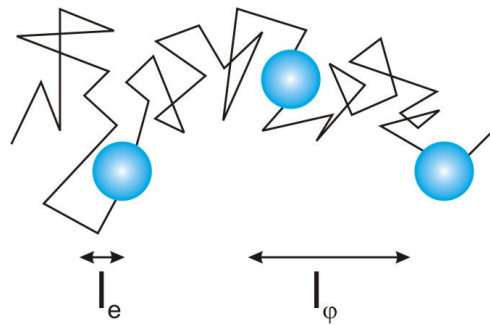


Figure 1.1 Illustration of the diffusive motion of a charge particle in an impure metal at temperature close to absolute zero. The electron motion shows the influence of impurity scattering (shown by the mean free path l_e), and rare inelastic scattering events (blue circles, shown by the phase coherence length l_ϕ).

The quantum nature of electron transport such as ‘Quasi – ballistic’ and ‘ballistic’ behaviour is primarily observed in a mesoscopic system, in which the physical dimensions of the system are restricted to the physical length scales of electrons – such as the mean free path length l_e , the phase coherence length l_ϕ , and the Fermi wavelength λ_F [15]. Due to the importance of these physical length scales, a brief discussion on each of them is as follows.

The electronic mean free path length l_e is determined by the quantity of imperfections in a mesoscopic system and as shown by Equation 1.2, it is directly dependent on the mean free time between the electron scattering events, τ and Fermi velocity, v_F . It is important to note here, that the mean free path length of electrons does not influence the destruction of phase coherence. For metallic systems, l_e is generally in the order of nanometres whereas for highly conductive semiconductor heterostructures it is considerably larger (in the order of $10\ \mu\text{m}$) [16].

$$l_e = v_F \tau \quad (1.2)$$

As opposed to impurity scattering, the electron scattering events from electron-phonon interactions are in general inelastic and therefore leads to phase incoherence. Since the occurrence of these events is rare at low temperatures, the phase coherence

length l_ϕ between these events can be determined by assuming diffusive transport due to impurity scattering between two phase destroying events.

$$l_\phi = \sqrt{D\tau_\phi} \quad (1.3)$$

where, τ_ϕ is the phase coherence time or mean free time between two phase randomising events and D is the diffusion constant that contains only the impurity scattering which does not destroy phase coherence.

The Fermi wavelength or the de Broglie wavelength of electrons at the Fermi edge λ_F has been a key length scale for studying ‘size quantization’ in semiconductor heterostructures [2, 17-23].

$$\lambda_F = h/\sqrt{2m^*E_F} \quad (1.4)$$

where, m^* denotes the effective electron mass (which is 0.068 m_e for GaAs) and E_F the Fermi energy. Usually, for GaAs based heterostructures, the Fermi wavelength can be as large as 100 nm, and hence can be comparable to the at least one dimension of the mesoscopic device. This realisation makes the wave character of the electrons become more important, because the electron density of states is quantised in the restricted direction according to the allowed standing-wave modes, which changes the dimensionality of the system. For example, size quantization in only one direction results in the electron system being confined to two dimensions, normally referred as ‘quantum films’ or ‘two-dimensional electron systems’. Size quantization effects on conductivity have been fundamental to research on mesoscopic electron transport during the last two decades [24-27]. Further work, involving quantum confinement in a second spatial direction, resulting in one-dimensional motion of electrons (‘quantum wires’) has also revealed an enormous amount of information related to ballistic transport [28-38].

Figure 1.2 illustrates the ‘size quantization’ for two- and one-dimensional electron systems.

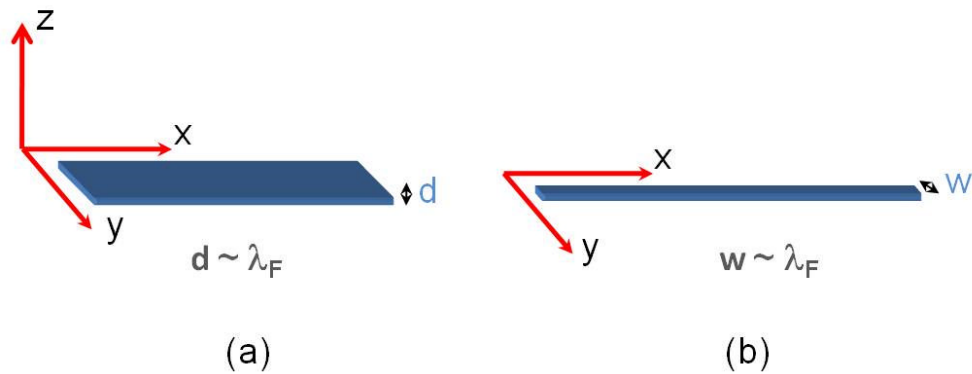


Figure 1.2 Demonstration of ‘size quantization’, as the dimensions of the electron system become comparable to the Fermi wavelength λ_F , resulting in (a) two-dimensional and (b) one-dimensional electron systems.

All the work presented in this thesis is based on observing picosecond time resolved electron transport properties in these mesoscopic systems, with consideration of the fundamental physical length/time scales of charge particles as discussed above.

1.4. Two-dimensional electron systems

(2DES)

A two-dimensional electron system (2DES) is the simplest type of mesoscopic system commonly used for researching the fundamental physics of condensed matter electron transport. It was first employed in the form of a Si MOS-FET transistor by W. Shockley and G. L. Pearson [39]. A schematic illustration of the Si MOS-FET transistor is shown in Figure 1.3.

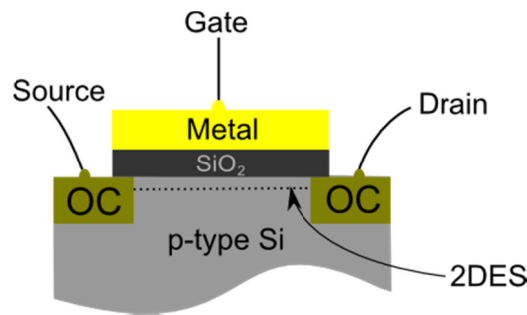


Figure 1.3 Schematic of a two-dimensional electron system formed in a Si MOS-FET. The two ohmic contacts (OC) formed on the bulk Si act as source and drain, while the metal electrode formed on SiO₂ layer acts as gate.

As shown in Figure 1.3, a p-type doped Si chip (with doping density $N_D \sim 10^{21} \text{ m}^{-3}$) is electrically contacted using two ohmic contacts acting as source and drain. A metal electrode referred as a gate is patterned on to the Si chip overlapping the two ohmic contacts. This metal contact (gate) is separated from the Si by a SiO₂ layer, making a Schottky contact (metal-on-semiconductor) of a very high resistance.

The voltage applied to the metal electrode creates band bending to accumulate carriers at the SiO₂ – Si interface thereby creating a thin inversion layer of charge carriers. The ‘inversion’ refers to the opposite polarities of free carriers accumulated at the interface and the carriers in the bulk material due to doping. Hence, an electron system is generated with electron motion confined to the order of λ_F in the perpendicular direction. Since the Fermi wavelength of the confined electrons with the doping densities used ($\lambda_F \sim 20 \text{ nm}$) was comparable to the dimensions of the electron system in the direction of confinement, it was possible to observe size quantization effects in the conductivity of the inversion layer.

The Si MOS-FET based 2DES systems provided an excellent foundation in for observing size quantization effects in the electron systems, however they were found to be unattractive for studying further quantum mechanical effects in the 2DES, due to

strong coulomb scattering from the charged impurities at the oxide-semiconductor interface [24, 40, 41]. This problem led to research on the growth of high quality 2D electron systems, which were required not only from the perspective of understanding applied physics but also from the perspective of understanding fundamental physical science.

The development in growth techniques of pure crystalline semiconductors using Molecular Beam Epitaxy (MBE) over the previous few decades has allowed the formation of ultra-high quality 2DESs between two III-V compound semiconductor interfaces, for example using modulation doped GaAs/Al_xGa_{1-x}As heterostructures [17, 42-48]. A typical choice of x is 0.3. The formation of these heterostructures together with their energy band structure and measured electron transport properties are discussed below.

1.4.1. 2DES in GaAs/Al_xGa_{1-x}As heterostructure

Since undoped GaAs and Al_xGa_{1-x}As are very similar compound semiconductor structures but with different band gap energies (E_g for GaAs ~ 1.4 eV and E_g for Al_xGa_{1-x}As ~ 2 eV), it allows parent doping impurities to donate their free carriers into a separate close-by structure but, as will be shown, it also allows the scattering of free carriers from the resulting ionized impurities to be minimised. A sequential process illustrating the formation of a 2DES at a GaAs/AlGaAs heterojunction is shown in Figure 1.4 [49]. As shown in Figure 1.4 (b), in contrast to a Si MOS-FET based 2DES, the free electrons are provided by the doping layer of integrated Si-donors inside the AlGaAs, while the bulk GaAs remains undoped. A ‘modulated doping’ technique first demonstrated by Dingle [50] is typically used for incorporating Si donor atoms in the AlGaAs layer. For this technique, most of the doping electrons are thermally excited into the conduction band, while as little as ~ 10 % contributes to the free carriers confined in the triangular

quantum well (Figure 1.4c). The positive charge of ionized donor impurities in the AlGaAs and the negative charge of the free carriers trapped at the interface build up a charge dipole, resulting in the band structure shown in Figure 1.4 (c).

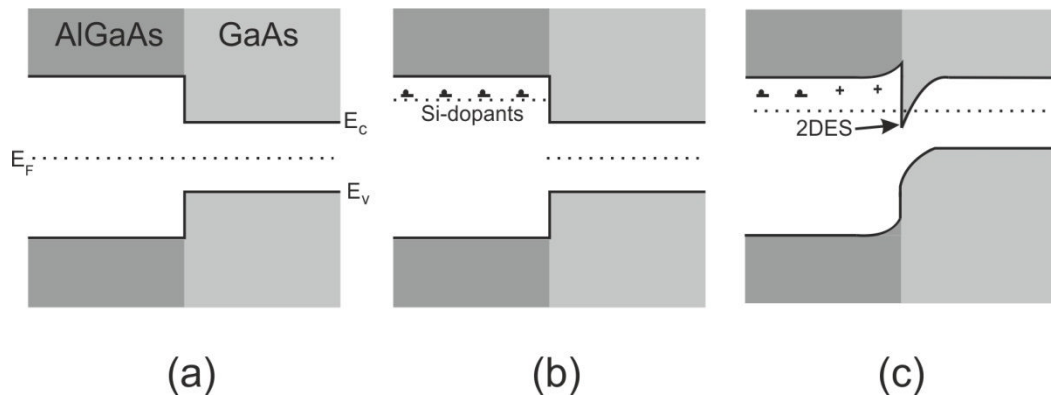


Figure 1.4 Energy band across the GaAs/AlGaAs heterostructure. (a) for the undoped scenario, (b) after n-type doping of AlGaAs with Si dopants, and (c) resulting band structure after 2DES formation at the heterojunction, with the Fermi energy at equilibrium across the GaAs/AlGaAs structure.

It was demonstrated by Stormer *et al* [51], that an additional undoped AlGaAs spacer layer can be introduced between the modulation Si-doped AlGaAs layer and the GaAs layer having the 2DES at the interface, to reduce the dominant ionized impurity scattering experienced by the free electrons in the 2DES. An illustration of such a modified heterostructure to achieve high electron mobilities is shown in Figure 1.5.

An added advantage of using a GaAs/AlGaAs heterojunction for creating a 2DES is that there is very little lattice mismatch between the two crystal structures resulting in very negligible strain induced defects (i.e. dislocations) in the 2DES. Hence the electrons undergo much less scattering subjected to the interface as compared to the oxide-semiconductor interface in a Si MOS-FET.

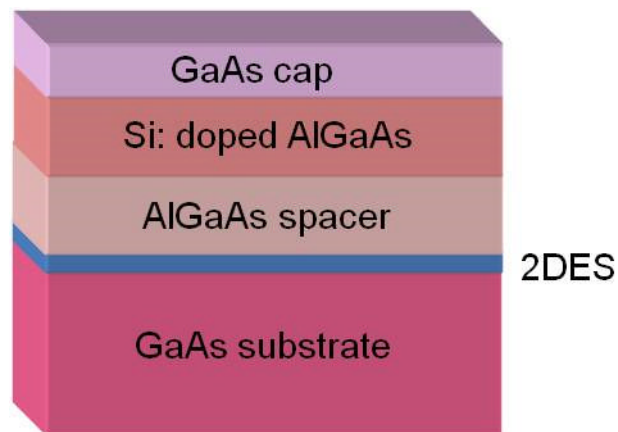


Figure 1.5 Schematic of a MBE grown GaAs/AlGaAs heterostructure having 2DES confined at the heterojunction. The addition of the undoped AlGaAs ‘spacer’ layer between the Si-doped AlGaAs and GaAs layer reduces the impact of ionized scattering on the confined charge carriers.

In recent years, the optimization of layer sequences and composition of $\text{Al}_x\text{Ga}_{1-x}\text{As}$ layers, together with modified doping techniques has resulted in 2DESs with carrier concentrations of $\sim 10^{11} \text{ cm}^{-2}$ having remarkable low-temperature electron mobilities from roughly $5 \times 10^3 \text{ cm}^2/\text{Vs}$ in 1977 to $36 \times 10^6 \text{ cm}^2/\text{Vs}$ by 2008 [52]. Correspondingly, it has allowed the physical length scales of electron transport, such as mean free path length l_e to be increased to the order of millimetres. These advances in the improvement of the electron mobility in the 2DES over the past few decades as compiled by Schlom *et al* [53] and presented in Figure 1.6, promises to enable the study of quantum effects which have been previously immeasurable in earlier materials.

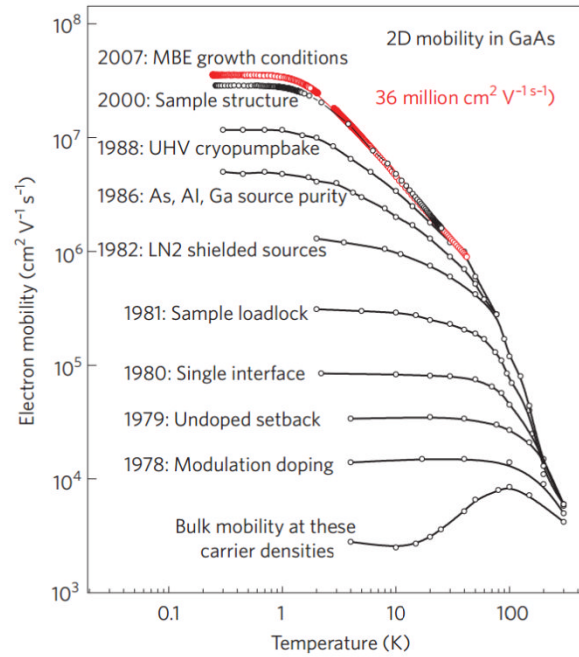


Figure 1.6 Progress in improving carrier mobility in 2DESs, up to the present record of 36,000,000 cm^2/Vs , together with the information on the technical modifications and innovation required for GaAs/AlGaAs heterostructures, displayed for the last three decades [53].

1.4.2. Electron transport properties in a 2DES

As mentioned earlier, the transport properties of the electrons in a confined 2DES is greatly influenced by the ‘size quantization’ effect of the electron system, it is therefore essential to understand the distribution of the electron density of states in the 2DES that contributes to the electric current.

The width of the 2DES defined at the GaAs/AlGaAs heterojunction in the direction of layer growth is very thin and typically in order of ~ 10 nm, as shown in Figure 1.4 (c). This corresponds to Fermi wavelength of electrons λ_F confined in a 2D plane. For this reason, the energy of the electron density states that can exist within the 2DES are quantized into discrete levels (sub-bands). A schematic of the distribution of density of states in a 2DES is shown in Figure 1.7 (a), while Figure 1.7 (b) clearly

illustrates the influence of the λ_F and the boundary conditions of the 2DES on quantized discrete energy levels [54]. It is noted that for a typical 2DES, usually only a single sub-band is occupied.

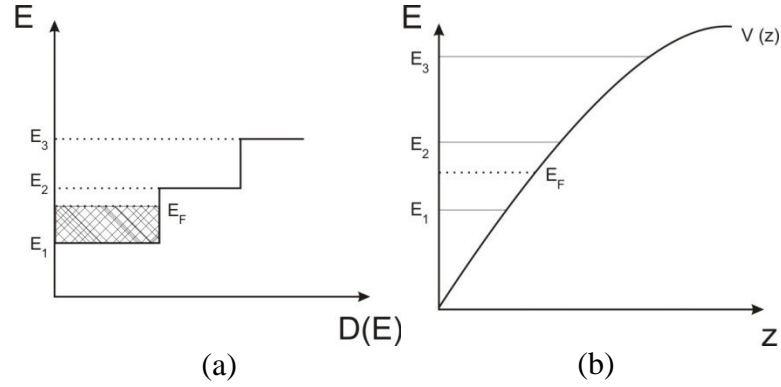


Figure 1.7 (a) Density of states for a 2DES. (b) Heterojunction interface showing quantized sub-band energies (E_1 , E_2 , E_3) and Fermi energy E_F , where $V(z)$ is the potential barrier controlling the boundary conditions of the 2DES.

The low-temperature transport properties of the electrons in the filled sub-band of the confined 2DES are examined usually through measurement of resistivity or conductivity under the effect of an in-plane applied electric field E and a perpendicular magnetic field B . This technique exploits the fact that the motion of electrons parallel to E is disturbed by the Lorentz force, which directs the electrons in a direction perpendicular to the direction of E , forcing them to execute circular orbital motion as a result. The resulting two-dimensional transport can be described in terms of a resistivity tensor, including a **diagonal component** (in the direction parallel to E):

$$\rho_{xx} = \frac{\sigma_{xx}}{\sigma_{xx}^2 + \sigma_{xy}^2} \quad (1.5)$$

and an **off-diagonal (Hall) component** (in the direction perpendicular to E):

$$\rho_{xy} = \frac{\sigma_{xy}}{\sigma_{xx}^2 + \sigma_{xy}^2} \quad (1.6)$$

where, σ_{xx} and σ_{xy} are the corresponding elements of the conductivity tensor.

A typical four-terminal Hall bar geometry patterned into the GaAs/AlGaAs heterostructure (see Appendix 1 for fabrication details) as shown in Figure 1.8, is used for resistivity tensor investigation under magnetic fields. The measurements are carried out by passing electric current (I) with current density j between Ohmic contacts S and D. The voltage between contacts A and B or A and C are then simultaneously measured to observe ρ_{xx} or ρ_{xy} .

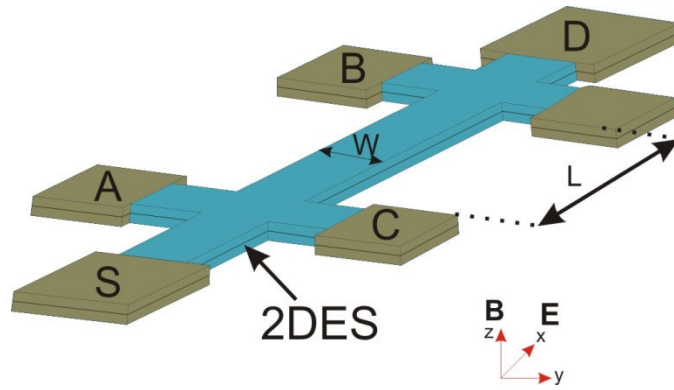


Figure 1.8 A four-terminal Hall bar geometry formed on GaAs/AlGaAs heterostructure containing the 2DES with source and drain ohmic contacts shown by S and D. The electron transport coefficients are measured using ohmic contacts A-D, under influence of electric E and magnetic fields B , with x , y and z axes showing their respective direction.

The diagonal resistivity tensors can be written in terms of the Hall bar device geometry and the longitudinal voltage can be written as,

$$\rho_{xx} = \frac{E_x}{j_x} = \frac{V_{AB}W}{LI_x} \quad (1.7)$$

where, $E_x = V_{AB}/L$ and $j_x = I_x/W$. Similarly the Hall resistivity evaluated considering the measured Hall voltage is given by,

$$\rho_{xy} = \frac{E_y}{j_y} = \frac{V_{AC}}{I_y} \quad (1.8)$$

where, $E_y = V_{AC}/W$ and $j_x = I_x/W$.

In the classical case of a 2D electron transport within small applied magnetic fields, i.e. where Boltzmann's approximation is valid, the above expressions for resistivity tensors shows the diagonal resistivity to be independent of the magnetic field and Hall resistivity to be linearly dependent on the magnetic field. Subsequently, the transport properties that characterize the 2DES such as sheet density n_s and carrier mobility μ_e can be calculated using,

$$n_s = B/e\rho_{xy} \quad (1.9)$$

and

$$\mu_e = R_H/\rho_{xx} \quad (1.10)$$

where, R_H is the Hall coefficient, given by $1/n_s$.

1.4.3. The quantum Hall Effect

The study of quantum mechanical behaviour of the 2DES at high magnetic fields resulted in the discovery of the quantum Hall effect, which was highly significant in the field of solid state experiments [1]. Figure 1.9 shows an illustration of the quantum Hall effect measured for a 2DES at temperatures < 24 mK, having sheet density n_s of $1.7 \times 10^{11} \text{ cm}^{-2}$ and electron mobility μ_e , of $1.2 \times 10^6 \text{ cm}^2/\text{Vs}$. It was found that in strong magnetic fields, ρ_{xy} does not increase proportionally with B but forms plateaux at quantized values of h/ie^2 , where i is an integer, and ρ_{xx} is not constant but oscillates and vanishes to zero where the plateaux appear in the Hall resistivity.

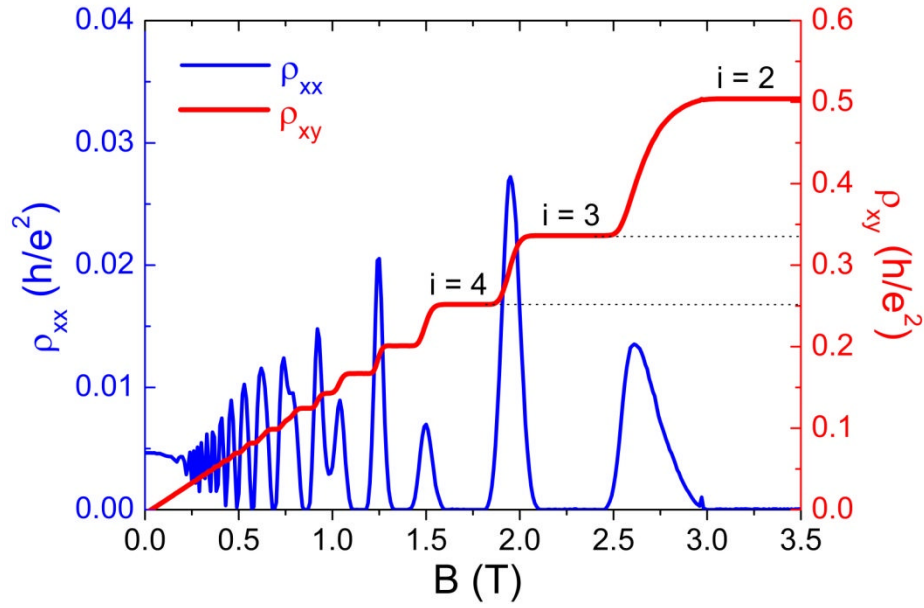


Figure 1.9 The Quantum Hall effect measurement using the Hall bar geometry at $T < 24$ mK, showing the Hall resistivity ρ_{xy} getting quantized at values of h/e^2 and the Shubnikov-de Haas oscillations occurring in the diagonal resistivity ρ_{xx} .

This quantum behaviour of the electron transport can be understood by considering the effect of perpendicular magnetic fields on the density of states of the 2DES. In the presence of a magnetic field, the energy spectrum of the lowest filled subband is no longer continuous as observed for zero magnetic fields (seen in Figure 1.7) but divided into several discrete energy levels as illustrated in Figure 1.10. These discrete energy levels, known as Landau levels (LLs) [54] are energy separated by $\hbar\omega_C$, where ω_C is the cyclotron frequency of the circular orbital motion of electrons in the 2DES and it is given by,

$$\omega_C = \frac{eB}{m^*} \quad (1.11)$$

Hence, when the Fermi energy is in between LLs, there is no longitudinal conduction current, as a result the diagonal resistivity vanishes to zero with Hall resistivity showing a plateau. When the Fermi energy is pinned at a LL, the current

flows, and the diagonal resistivity rises correspondingly, with the Hall resistivity showing a linear increase.

It is also important, as shown in Figure 1.10, that at high magnetic fields, each of these LLs can split further into two separate energy levels due to spin degeneracy, indicating spin up and spin down. The process is commonly known as ‘spin splitting’ of LLs.

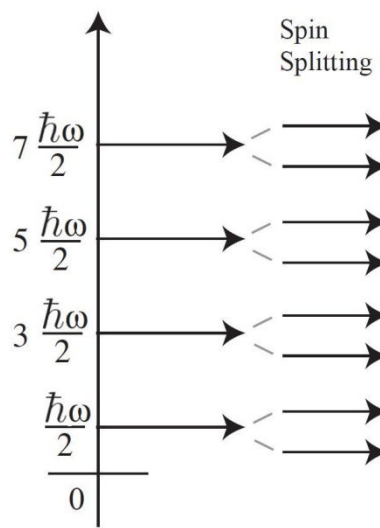


Figure 1.10 Energy spectrum of the 2DES under magnetic fields, demonstrating the occurrence of LLs and spin splitting, taken from reference [54]. The spectrum shown here is considered for an ideal case (i.e. disorder free system).

Due to the distribution of the energy spectrum for the density of states under finite magnetic fields, the overall carrier density n_s of the 2DES is contributed to by a number of filled LLs up to the Fermi energy. It can be derived by considering the interdependence of the resistivity tensor elements due to the two dimensional motion of electrons, given by,

$$\rho_{xx} = \frac{\sigma_{xx}}{\sigma_{xx}^2 + \sigma_{xy}^2} \quad \rho_{xy} = \frac{\sigma_{xy}}{\sigma_{xx}^2 + \sigma_{xy}^2} \quad (1.12)$$

considering that ρ_{xx} drops to zero when ρ_{xy} shows a plateau at h/e^2 , and using Equation 1.9, we obtain

$$\frac{h}{ie^2} = \frac{B}{en_s} \quad (1.13)$$

and consequently

$$n_s = i \frac{eB}{h} \quad (1.14)$$

Hence, the number of filled LLs up to the Fermi energy, indicated by the filling factor, can be determined by the carrier density. The effect of increasing magnetic field causes the Fermi energy to move through successive LLs as the higher energy LLs depopulate. The process is illustrated in Figure 1.11. It is noted that, for disordered systems (i.e. with impurities) the LLs are generally broadened and considered to have a Lorentzian shape, in contrast to the one shown for ideal systems in Figure 1.10.

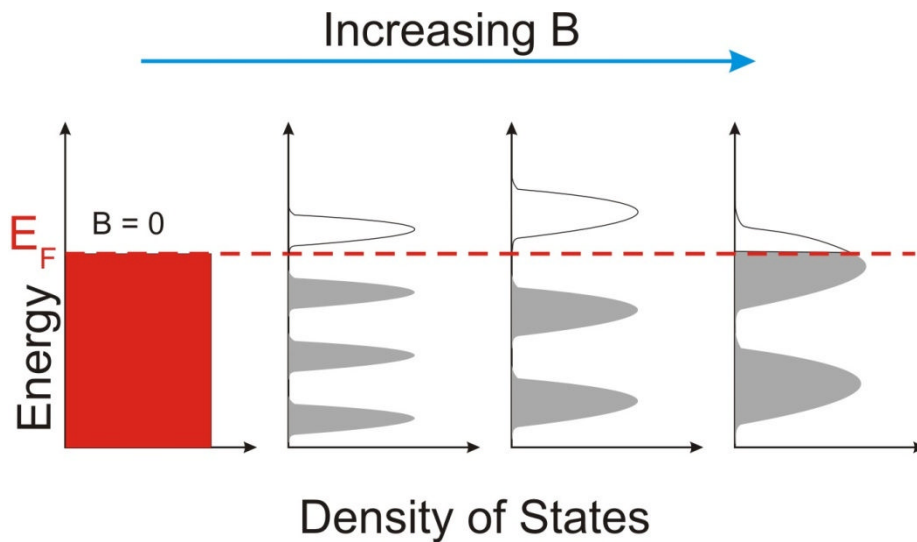


Figure 1.11 Illustration of the density of states in a 2D electron system for increasing magnetic fields. At $B = 0$, there is a uniform density of states. At finite magnetic field, discrete LLs are formed and separated by $\hbar\omega_c$. The LLs are delta functions in the ideal case, but are broadened due to disorder in the system. As the magnetic field further increases the Fermi level passes through successive LLs.

1.5. THz time-domain spectroscopy

Over recent years, pulsed THz time-domain spectroscopy (THz-TDS) has been a well-established technique for studying molecular vibrations in various crystals [3, 5, 55]. Also, having a key advantage of coherent generation and detection of pulsed THz radiation using a pump-probe scheme, THz-TDS has also been a powerful tool in studying carrier dynamics in semiconductor nanostructures with picosecond time scale resolution [7, 8].

In addition, the energy/frequency range of THz radiation encompasses many types of resonant absorption by charged particles in low dimensional solid state nanostructures - such as two-dimensional electron systems (2DESs) [56], quantum wires [2], carbon nanotubes [57, 58] and single- and bi-layer graphene [59]. This makes THz time-domain spectroscopy systems ideal for studying frequency dependent physical phenomena in these structures, such as carrier resonances and intraband transitions. The techniques that are typically used to perform these measurements are the free-space THz-TDS and the on-chip waveguide spectroscopy method, in which picosecond time scale electromagnetic pulses can be directly coupled from an adjacent waveguide to the nanoscale device under test (NDUT). So, the measured transmitted signal will in general contain the features corresponding to the resonant absorptions in the nanoscale devices.

A detail discussion on THz generation and detection in both the free-space THz-TDS and the waveguide spectroscopy systems is given in the following sections.

1.5.1. THz generation and detection

The generation and detection of THz electromagnetic radiation based on photoconductivity or optical non linearity of the medium is discussed here, since these

two methods are primarily used in THz sources and detectors based on femtosecond pulsed lasers.

Photoconductive switching is the most common and effective approach used for coherent generation and detection of ps pulses, in which a semiconductor surface is illuminated by using a train of femtosecond laser pulses (with above-band gap pulse energy) [60-62]. As initially demonstrated by Auston [63], the THz is generated by acceleration of photo-induced electrons and holes in a semiconductor. An electric field is applied across the semiconductor by means of metal electrodes fabricated on the semiconductor surface. As soon as a portion of a femtosecond infra-red laser pulse (referred to as the pump beam) is focused onto the semiconductor in the gap between the electrodes, the photo-induced carriers accelerate under the applied electric field. The electromagnetic field of the resulting transient current generated, radiates in the THz frequency range.

The relation between the radiating electric field and the change in the photocurrent density is given by,

$$E_{rad}(t) \propto \frac{dJ(t)}{dt} \quad (1.15)$$

and

$$J = e [nv_e + pv_h] \quad (1.16)$$

where, E_{rad} , is the electric field of the THz radiation, J is the total current density, n and p are the electron and hole densities, v_e and v_h are their corresponding net drift velocities. The radiation pulse from this transient current can propagate either on a transmission line or in free space. Figure 1.12 shows the schematic of a typical semiconductor based

photoconductive antenna used for THz generation and radiation in free space TDS systems [62, 64].

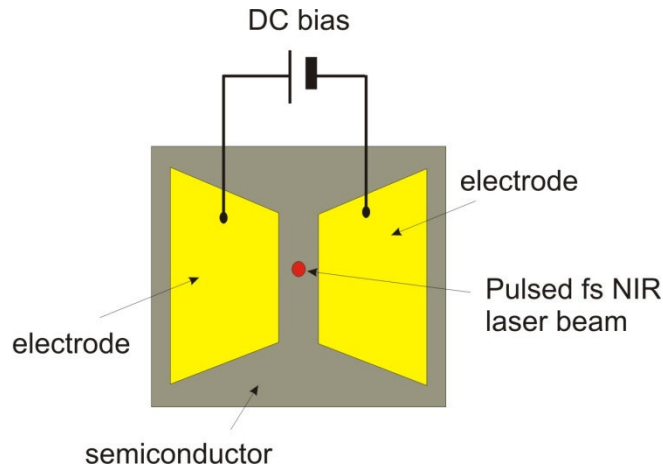


Figure 1.12 Schematic of the dipole-like photoconductive switch used for emission of free space pulsed THz radiation.

Since the THz electric field generated is directly proportional to the duration of the current transient (Equation 1.15), it is essential to consider the limitations on the current transient caused by the carrier lifetimes of the semiconductor used. The conventional semiconductor materials used for THz photoconductive switches are MBE-grown GaAs and silicon-on-sapphire. However, the carrier lifetime in these materials are relatively long (in order of 5-10 ps) [65] and so not very suitable for emission of THz-bandwidth pulses.

The carrier lifetimes can be significantly reduced in MBE grown GaAs by reducing the growth temperature (forming what is known as low-temperature-grown GaAs, or LT-GaAs) [65, 66]. The LT-GaAs is epitaxially grown at temperatures ~ 200 °C as compared to standard GaAs growth temperatures ~ 600 °C. This introduces point defects in the GaAs lattice which creates low-lying donor states below the conduction band edge. The recombination rate of electrons and holes is consequently increased, reducing the average carrier lifetime to as low as 90 fs [67]. On the other

hand, the large number of donor states available for electrons makes the resistivity of the LT-GaAs unacceptably low, allowing electron conduction even in the absence of optical excitation. It was found by Gupta *et al* [66] that the post-growth annealing of LT-GaAs at high temperatures of ~ 600 °C reduces the number of point defects, thereby increasing the resistivity. With properties like high resistivity, short carrier lifetime, and high carrier mobility; LT-GaAs is considered to be an ideal semiconductor material for photoconductive generation of THz radiation with a sub-picosecond time duration.

The portion of the femtosecond near infra-red laser pulse used for THz detection is usually referred to as the probe beam. Similarly to the photoconductive generation process of THz electromagnetic transients, the photoconductive detection can be realized by using the same working principle of the photoconductive antenna. In this case, the probe beam which is time delayed with reference to the pump beam generates photocarriers in the detector switch. However, the THz electric radiation field which hits the detector switch in coincidence with the probe laser pulses then accelerates the laser-induced photocarriers to produce a train of photocurrent pulses. A series connected lock-in amplifier measures this generated photocurrent signal, which consecutively can be used to extract the THz electric field amplitude.

An alternative method of detection of the THz radiation using electro-optic sampling in a non-linear material has been widely used for free space THz-TDS systems [68, 69]. The electro-optic (EO) detection employs the linear EO effect (also known as Pockel's effect), where a birefringence in the non-linear material (such as ZnTe, GaP, and GaSe) is created upon application of a bias electric field. For the THz detection scheme, the electric field of the incident THz radiation acts as this bias field. The induced birefringence causes a change in polarisation of the infrared probe beam (from circular to elliptical) propagating through the crystal at the same instance. The

orthogonal components of the probe beam are then separated by passing it through a quarter wave plate and a Wollaston prism as shown in Figure 1.13. The intensity of each component is then measured using a pair of balanced photodiodes, where the generated output current is proportional to the THz electric field.

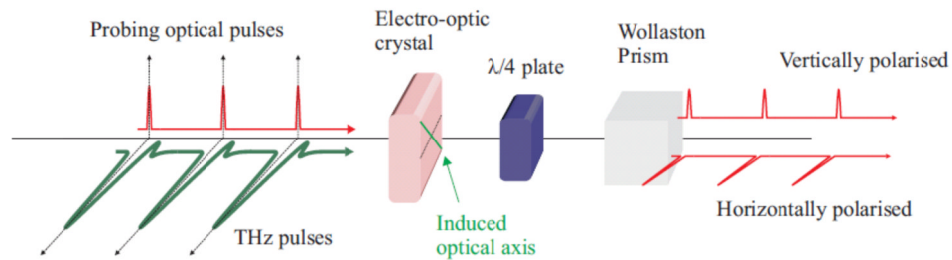


Figure 1.13 Electro optical detection of the THz pulses using the Pockels effect [12]. The quarter wave plate is labelled $\lambda/4$.

The main advantage of using EO detection of THz electric fields is its time resolution, which is primarily limited only by the time duration of the optical laser pulse. Thinner EO crystals with good phase matching properties between the THz radiation and the optical pulse have been used to detect spectral components at frequencies exceeding 135 THz [70].

1.5.2. Free space THz spectroscopy systems

The pump-probe technique used in free space THz-TDS systems for THz generation and detection using photoconductivity and optical non-linearity is discussed here. A schematic representation of a typical THz-TDS system consisting of a photoconductive emitter and an electro-optic crystal as a detector is shown in Figure 1.14.

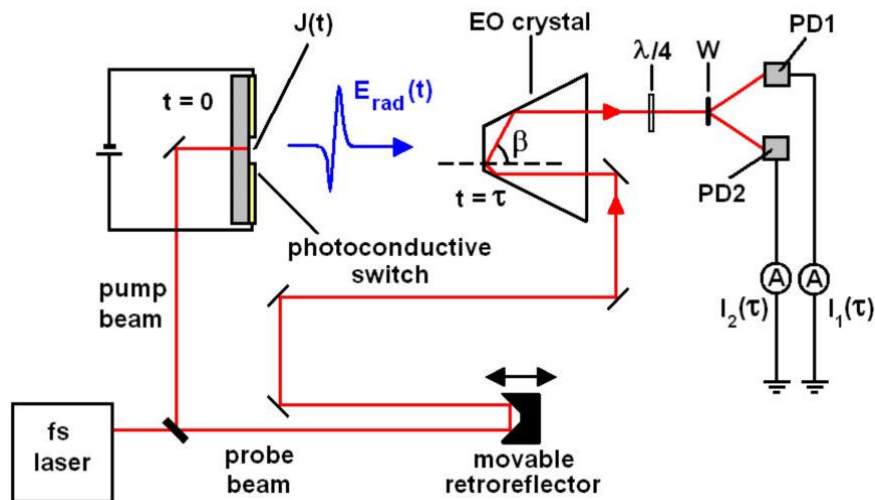


Figure 1.14 Example of a free-space THz time-domain spectroscopy, showing the THz generation using a photoconductive antenna and the THz detection using an electro-optic crystal, taken from reference [71]. The internal reflection of the electro-optic crystal shows the probe beam propagating at an angle β to the THz beam in the crystal. The quarter wave plate is labelled $\lambda/4$, and the Wollaston prism is labelled W.

A femtosecond pulsed laser beam from a mode-locked laser having a pulse duration of at a wavelength of 800 nm is split into two parts – a pump beam and a probe beam. The pump beam is focused onto the photoconductive emitter switch. The probe beam, introduced at a defined time by means of an optical delay line (retroreflector) is then used to electro-optically sample the generated THz radiation by using an electro-optical crystal. [69, 72, 73]. As shown in Figure 1.14, the polarised probe beam from the electro-optic crystal is then passed through a quarter-wave plate (indicated by $\lambda/4$) to make it circularly polarised before being split into its orthogonal components by the Wollaston prism (indicated by W). The intensity of each component is then independently measured using photodiodes. The relative difference in the polarization components measured through two photodiodes yields a relative measure of the instantaneous THz electric field. The frequency spectra obtained from the time-domain THz pulses measured using free space THz-TDS systems typically ranges from 0.3 – 8 THz.

It is important in the THz-TDS systems to have an efficient coupling between the emitter and the detector. A common configuration practised, consists of using a pair(s) of parabolic mirrors to guide the THz radiation in the free space from the emitter to the detector. The arrangement often includes a midpoint in the confocal planes between the emitter and the detector, making it ideal for THz imaging and spectroscopy purposes of various samples. An example of such an arrangement used in a free space THz-TDS system for spectroscopy analysis of molecular vibrational modes is shown in Figure 1.15 [55]. As shown, the THz radiation generated using a LT-GaAs photoconductive emitter passes through explosive samples under test and then detected electro-optically.

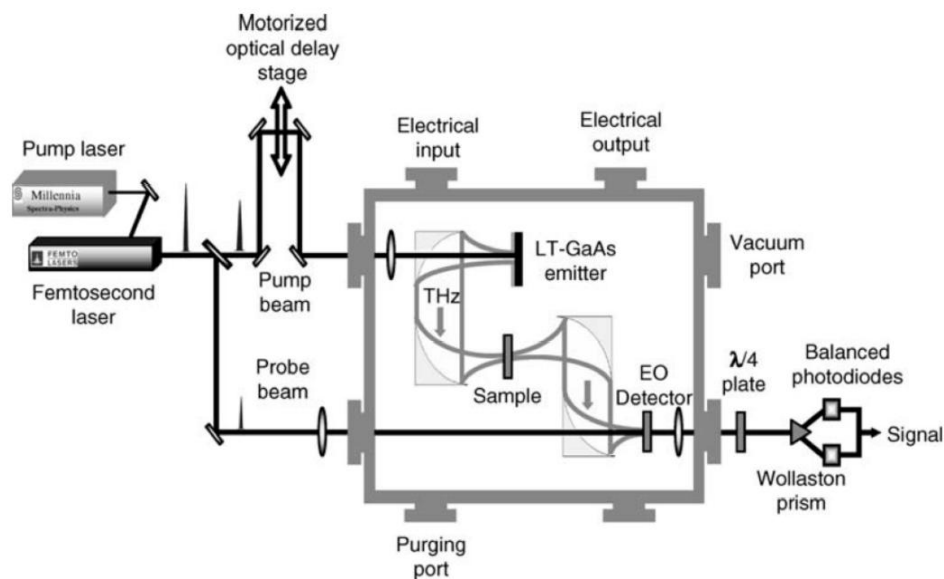


Figure 1.15 Example of a free-space THz-TDS system employing pairs of parabolic mirrors to guide the propagating THz radiation through various ‘sample’ under test, taken from reference [55]. The propagating THz waves are enclosed in a nitrogen-purged box to avoid absorption by water content in the surrounding atmosphere.

1.5.3. THz waveguide spectroscopy systems

The strong absorption of THz radiation by water in humid environment has been a big limiting factor in terms of bandwidth of free space THz-TDS systems and feasibility of

using THz frequencies. They are often purged with dry air or nitrogen gas to isolate THz radiation from water absorption [74]. Also, although having the benefit of a wide bandwidth spanning several THz, free-space systems are usually not efficient in coupling THz radiation in and out of nano or microscale structures. The relatively large wavelength of the THz beam ($\lambda \sim 100\mu\text{m}$) makes it incapable of focusing to a diameter less than few hundreds of microns without losing frequency components at or below 1 THz. The addition of waveguides in THz-TDS systems is considered to be a very important development in spectroscopy research [75, 76]. The mode of propagation of THz radiation on waveguides is fundamentally different to free-space propagation of THz radiation, and the field pattern can take a form that offers useful advantages over free-space waves for spectroscopy applications.

Recent advances included “free-standing waveguides”, having a straight, bare metal wire as a waveguide, with the intention of coupling free space THz waves into the waveguide so that they propagate along the waveguide surface [76-78]. As THz waves couple into the metal wire, the THz electric field pulse dislocates charge carriers in the metal wire on a picosecond time scale resulting into a disturbance of carriers propagating along the surface of the wire. The associated electro-magnetic field created along the metal wire is the guided THz wave. A similar technique was adopted by Walther *et al* [79], where the THz pulses propagating along the metal wire waveguide was used to perform molecular spectroscopy of lactose powder dispersed on top of the metal wire. As shown in the schematic, the THz pulses are generated by a photoconductive switch at one end of the metal wire and detected at the other end by electro-optic sampling in a ZnTe crystal.

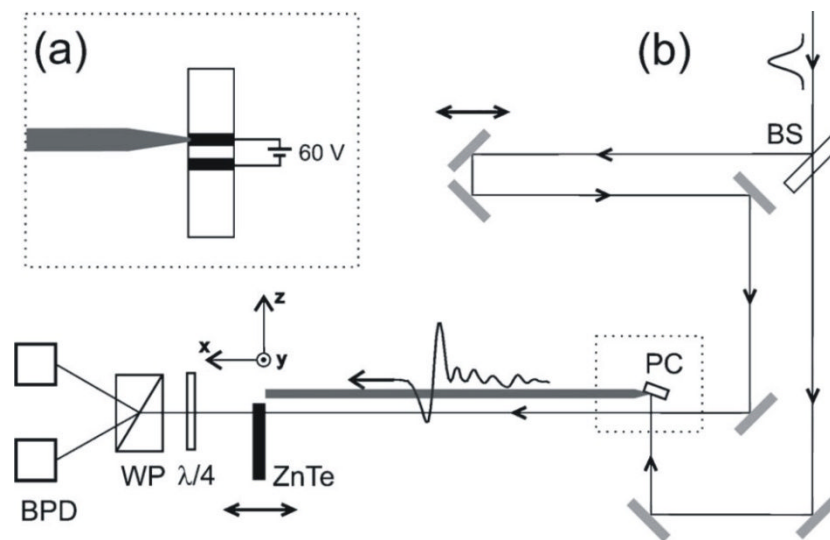


Figure 1.16 Example of THz-TDS system using free-space coupled metallic wire waveguide, taken from reference [79]. (a) Side view of the photoconductive emitter with the metallic wire tip connecting the positive electrode. (b) The schematic of the experimental setup used (BS represents beam splitter, PC represents photoconductive switch emitter, WP represents Wollaston prism, and BPD represents balanced photodiodes).

The reported technique is considered to be a compact and a novel form of THz spectroscopy setup with high sensitivity for molecular resonant absorption analysis. However, the large loss in coupling of free space THz radiation with the waveguides was a major limitation of the approach. This has been a strong motivation behind the development of techniques that allow in plane integration of THz sources and detectors with the waveguides.

1.6. On-chip THz-TDS systems

On-chip THz systems have been an active area of development while THz technology has advanced over the last decade. In contrast to the free space coupled waveguides, it allows generation and detection of THz radiation to be coupled locally with the planar transmission lines lithographically patterned on one chip. Also, as most of the propagating evanescent field of the THz radiation is contained within the host dielectric

substrate, it avoids absorption of THz radiation by water content present in the atmosphere. This method allows highly sensitive, spatial resolution detection of the evanescent field of the THz radiation, promising new capabilities for THz spectroscopy and imaging of various materials [80-82]. A detailed review of on-chip THz-TDS systems are given in this section, since it is this technique used in the project for ps pulse interaction of low-dimensional semiconductor systems.

1.6.1. On-chip THz generation and detection

For on-chip THz pulse generation and detection, a similar photoconductive excitation and detection mechanism as discussed in section 1.5.1 for free space THz-TDS systems is primarily used. The photoconductive semiconductor material (such as LT-GaAs) used for patterning on-chip THz emitters and detectors can either form the substrate for the overlaid waveguides [83], or can be epitaxially transferred onto a separate substrate, using an epitaxial lift-off and film transfer process [84, 85].

Figure 1.17 shows an illustration of the photoconductive switch (Auston switch) operation used for on-chip THz generation. Similar to the technique discussed previously for free space photoconductive emitter (in section 1.5.1), the generation and recombination of photocarriers in the semiconductor under applied electric field produces a picosecond time scale current transient, which is then directly coupled with the integrated transmission line.

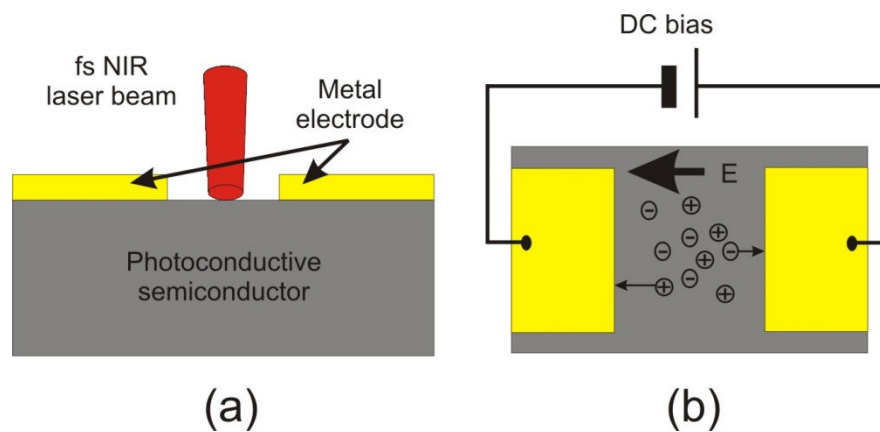


Figure 1.17 Illustration of ps time scale electrical transient generated using a photoconductive switch for on-chip THz systems. (a) 2D cross section of a typical photoconductive switch, with NIR laser beam illuminating the switch gap and (b) photogenerated charge separation in the applied DC electric field.

Figure 1.18 shows a typical example of the switch region defined between the metal electrode and the centre conductor of an integrated on-chip coplanar waveguide overlaid on a LT-GaAs photoconductive substrate. The property of the photoconductive region, defined as ‘switch region 1’ in Figure 1.18 is usually characterised in terms of photocurrent generated across the pump switch as a function of applied bias and laser power. The generated ps electrical transient propagating along the waveguide can be delivered to desired locations in order to perform time resolved experiments of the NDUT. A similar photoconductive switch pair can then be used to detect the current transients at various distances along the waveguide.

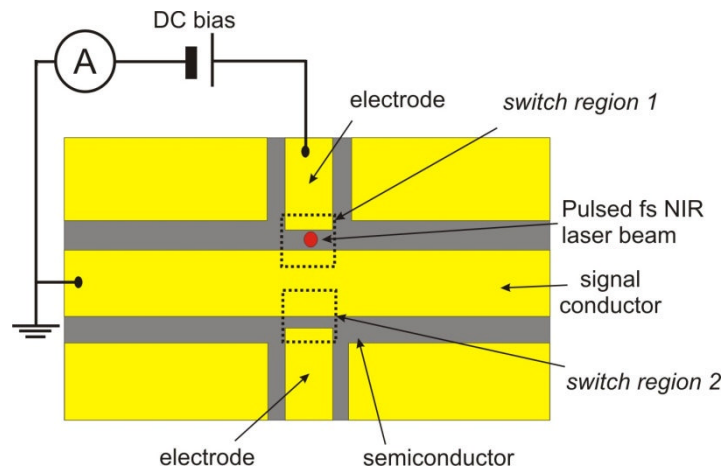


Figure 1.18 Schematic representation of a pair of photoconductive switch region defined between the metal electrodes and the integrated signal conductor of the CPW. The experimental configuration is also shown for measuring the characteristics of a switch region in terms of photocurrent generated across applied bias.

1.6.2. Waveguide geometries

The different geometries of planar transmission lines that have been demonstrated for on-chip transmission of signals at THz frequencies and THz-TDS absorption spectroscopy applications, include microstrip lines [86], slot lines [87], coplanar waveguides (CPW) [88] and planar Goubau lines [89]. A brief review on each of these transmission lines including the structure of the transmission lines and the property of field propagation pattern is as discussed, defining the underlying reasons behind the final choice of the transmission line used for this project.

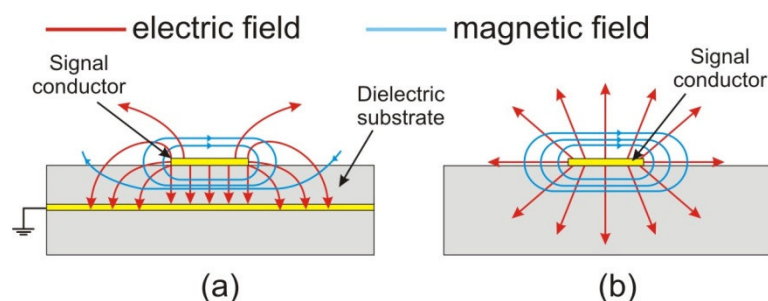


Figure 1.19 2D cross section of (a) the microstrip line, and (b) the planar Goubau line. Also shown are the electric and magnetic fields surrounding an electrical pulse as it propagates along the signal conductor.

Microstrip lines

Microstrip lines have been extensively used in microwave circuits with its operation pushing into the THz frequency range. As shown in Figure 1.22 (a), it consists of a signal conductor and a ground plane separated by a dielectric where the electric field is mostly concentrated, with some fraction in the air above. This as a result, having a quasi-transverse electromagnetic (quasi-TEM) mode of electromagnetic field propagation along the microstrip line [90]. Having a low-permittivity dielectric placed between the two conductors has allowed the evanescent field of microstrip lines to be used for THz-TDS absorption spectroscopy of polycrystalline materials up to 1.2 THz [82]. The main drawback of the microstrip lines for its application in this project, is the complexity in its fabrication and integration of a ground plane within the LT-GaAs based photoconductive heterostructure grown using MBE.

Planar Goubau lines

The planar Goubau line structure is very similar to that of microstrip lines, having a single conductor on the dielectric substrate with a difference of having no ground planes, as shown in Figure 1.22 (b). The electromagnetic field propagation mode supported in this case is only a quasi-transverse magnetic (quasi-TM) mode, with a radial electric field propagating along the waveguide. This mode of propagation makes transmission along the Goubau lines lossy at low frequencies, but with much lower attenuation experienced by propagation of THz frequency components [91]. The recent demonstration of increase in bandwidth of planar Goubau lines up to 1.5 THz and its application for spectroscopy of overlaid polycrystalline materials by Russell *et al* [92], made it a promising choice of planar transmission line for the work in this project. Although, for planar Goubau lines, the field extends much further than on e.g. microstrip

lines, so is more prone to interference. As a result, it is not suited for the particular work carried out in this project.

Coplanar transmission lines

Another planar waveguide geometry which has been widely popular for THz frequency applications are coplanar transmission lines [88, 93], due its simple structure of having a both signal conductor and ground conductor in the same plane. The tightly confined quasi-TEM mode of field propagation along the waveguide makes them a very attractive geometry for absorption spectroscopy applications of various materials including quantum confined systems [10].

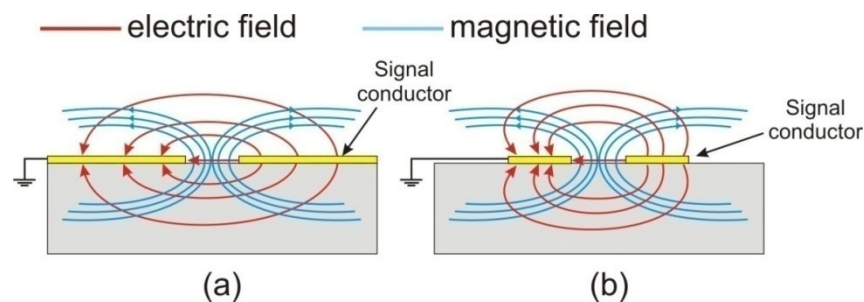


Figure 1.20 2D cross section of (a) the coplanar slot line, and (b) the coplanar strip line. Also shown the electric and magnetic fields surrounding an electrical pulse as it propagates along the signal conductor.

Considering the structure of the planar waveguide, the coplanar transmission lines are further sub-categorized into coplanar slot lines (CPSlot), coplanar strip lines (CPStrip) and coplanar waveguides (CPW). The geometry of CPSlot and CPStrip lines are shown in Figure 1.23 (a) and (b), are the simplest form of coplanar transmission line. They have a similar structure that consists of only a signal conductor and a ground plane overlaid on the same surface of the dielectric substrate material with the electric field confined between them. The primary difference between CPSlot and CPStrip line is the

variation in the confined field pattern due to the physical dimensions of the two conductors.

A coplanar waveguide (CPW) is a coplanar transmission line consisting of three conductor geometry, with two ground planes separated by a gap on either side of the signal conductor. As opposed to the single mode of propagation observed in other waveguide geometries, the coplanar waveguide has an ability to support two different quasi-TEM modes depending on the symmetry of the electric field on either side of the signal conductor. The modes are referred to as the odd mode (also known as symmetric mode) as shown in Figure 1.24 (a), or the even mode (also known as asymmetric mode or slot line mode) as shown in Figure 1.24 (b).

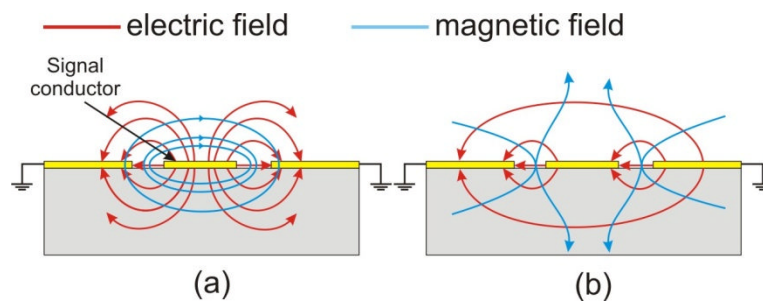


Figure 1.21 2D cross section of the CPW structure including the signal conductor and the ground planes. It also illustrates (a) the symmetric mode and (b) the anti-symmetric mode for the transverse propagating electric and magnetic fields.

With key advantages such as ease of design, fabrication and integration of waveguide geometry with the LT-GaAs photoconductive material and having flexibility of preferential excitation of different quasi-TEM modes, the CPW geometry was used for the on-chip THz-TDS work discussed in this thesis. Since the efficient transmission of THz pulses along the CPW is important for the experiments in this project, it was essential to understand the fundamental characteristics of CPWs as a transmission line. A brief review of transmission line theory of CPW is discussed in the following section.

1.6.3. Transmission line theory for coplanar waveguides

The properties of any transmission line (for TEM wave propagation) can be understood by considering a lumped element model represented by a two wire line. Due to symmetry of the electric field propagation in three conductor CPW, the lumped element model of the CPW can also be represented using an equivalent two conducting line geometry. Figure 1.22, shows a lumped-element circuit model of a short piece of CPW having length Δx .

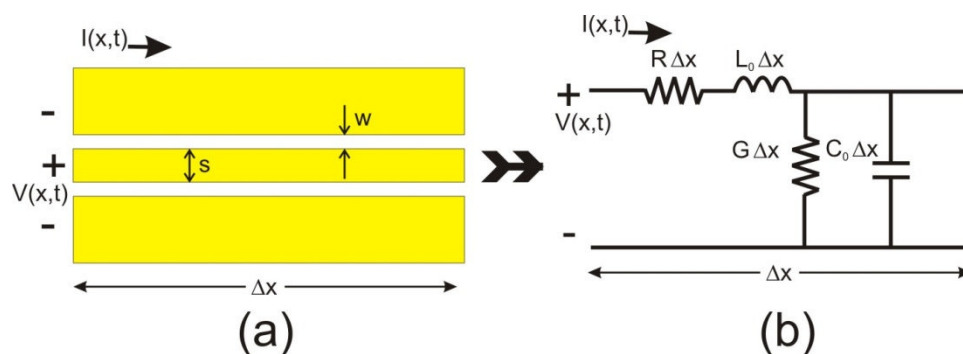


Figure 1.22 (a) Aerial view of a short length (Δx) coplanar waveguide, showing the physical geometry dimensions, and (b) an equivalent two wire line lumped element circuit model representing the three terminal coplanar waveguide. The single ground conductor in the lumped element model represents both the ground planes of the CPW.

As shown in the lumped element circuit model, the series resistance per unit length (labelled R) represents the losses in the transmission line due to the finite conductivity of each of the metal conductors. Whereas, the shunt conductance per unit length (labelled G) between the metal conductors represents the non-zero conduction in the dielectric. The circuit element labelled L_o represents the self-inductance in the line caused by the propagating electrical signal, and the circuit component labelled C_o represents the capacitance caused by the close proximity of the parallel conducting surfaces. The propagation constant (also known as damping coefficient) γ , which shows the effect of these lumped elements on the propagating high frequency signal is given by,

$$\gamma(f) = \sqrt{(R + j\omega L_o)(G + j\omega C_o)} = \alpha(f) + j\beta(f) \quad (1.17)$$

where, $\alpha(f)$ mainly represents the attenuation in the signal due to the radiation, conductor and dielectric losses and $\beta(f)$ determines the degree of dispersion a signal experiences.

An important fundamental entity for considering transmission line properties in terms of signal propagation is the overall impedance representation of the transmission line, also known as the characteristic impedance Z_o , which can be written as,

$$Z_o = \frac{V_o}{I_o} \quad (1.18)$$

considering the lumped element circuit model representation and the propagation constant, the characteristic impedance can be re-written as,

$$Z_o = \frac{R + j\omega L_o}{\gamma} \quad (1.19)$$

Considering the physical geometry of the CPW (as shown in Figure 1.22) and the dielectric substrate used, the characteristic impedance Z_o of a CPW is given by [94],

$$Z_{CPW} = \frac{120\pi}{\sqrt{\epsilon_{eff}(f)}} \frac{K'(k)}{K(k)} \quad (1.20)$$

where, ϵ_{eff} is the effective permittivity depending on the permittivity of the dielectric material used ϵ_r and $K(k)$ is the integral of the CPW geometry defined constant k .

$$\epsilon_{eff} = \frac{1+\epsilon_r}{2} \quad k = \frac{s}{s+2w} \quad (1.21)$$

and,

$$K'(k) = K\sqrt{1-k^2} \quad (1.22)$$

The characteristic impedance Z_o of a CPW as described above, determines the capability to propagate signals in either direction, however is essential to understand the effect on the properties of signal propagation (i.e. signal reflections) when the characteristic impedance of the line changes. Considering the on-chip waveguide technology used in this project for measuring properties of nanoscale devices with different characteristic impedances, it is especially important to understand the effect of waveguide discontinuities. These discontinuities can be quantified by the reflection coefficient.

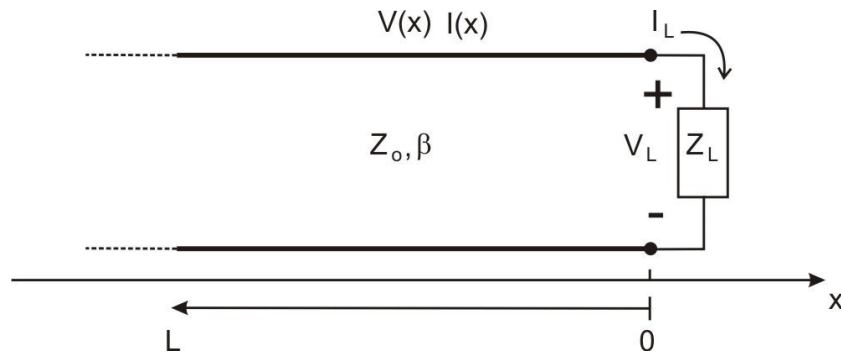


Figure 1.23 Example of a lossless transmission line terminated with a load impedance Z_L .

Figure 1.23 shows a lossless transmission line (in this case a CPW) terminated with an arbitrary load impedance Z_L , where $Z_L \neq Z_o$. The inequality between Z_o and the ratio of voltage to current at the load results in excitation of a reflected wave with an appropriate amplitude. The amplitude of the reflected signal normalised to the amplitude of the incident signal is known as the reflection coefficient, Γ [95]

$$\Gamma = \frac{Z_L - Z_o}{Z_L + Z_o} \quad (1.23)$$

where, $\Gamma = 0$ for $Z_L = Z_o$, $\Gamma = 1$ for an open circuit termination, and $\Gamma = -1$ for a short circuit termination. It is observed that the polarity of the reflection coefficient relates directly with the phase polarity of the reflected signal [96].

1.6.4. Pump Probe measurement

The pump-probe arrangement similar to free space THz-TDS systems is used for on-chip THz pulse generation and detection of propagated pulses along the waveguide. As shown in Figure 1.24, a portion of the fs near infrared laser beam (NIR, $\lambda \sim 800$ nm) is used to excite LT-GaAs based pump photoconductive switch in order to generate a ps time scale current transient, while the time delayed probe beam is used to sample the current transient at various points along the waveguide.

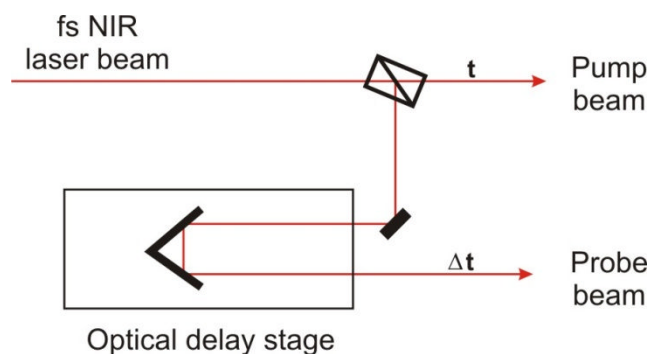


Figure 1.24 Pump-probe arrangement used for on-chip THz-TDS systems.

In order to determine the transmission characteristics of an on-chip waveguide, two different arrangements were mainly used in this project. Both enabled the terahertz pulse to be sampled before and after propagating along the waveguide.

The geometry that is used for the terahertz pulse generation and time resolved sampling before and after travelling along the transmission line (in this case, a coplanar waveguide) is shown in Figure 1.25. As shown, the electrical transient generated using a pump switch is sampled before propagating along the transmission line by aligning the time delayed probe beam at switch region on the same side of the waveguide and adjacent to the pump switch region (displayed as position 1). Whereas, the propagated pulse along the waveguide is detected by illuminating the switch region at position 2 with the probe beam.

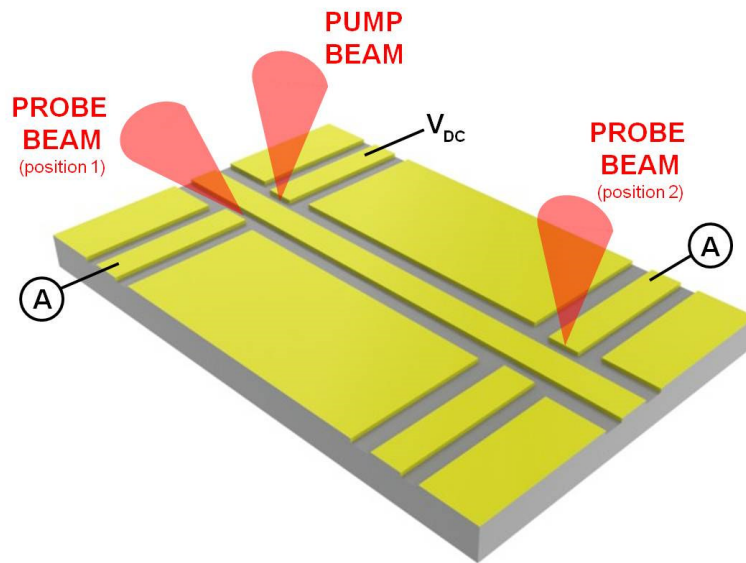


Figure 1.25 Example of a pump-probe arrangement for on-chip generation and detection of THz pulses. A DC voltage bias is applied across the pump switch gap. The electrical transient generated with the pump beam, is launched on to the on-chip waveguide and can be sampled before and after propagation along the waveguide using probe beam at position 1 and 2 respectively.

The pulse measurement before and after propagation along the waveguide also allows the velocity of the guided pulse v_p to be calculated, as shown in Figure 1.26. The probe beam is first aligned at position 1 at an angle θ to the waveguide axis, to measure the pulse before propagation along the signal conductor. It is then repositioned to position 2 for measuring the pulse after propagation along the waveguide. The pulse velocity can be derived by considering the time delay between the peaks of the pulses measured in each position ($\Delta t = t_{\text{position 2}} - t_{\text{position 1}}$) and the distance travelled by the pulse (length of the waveguide, L).

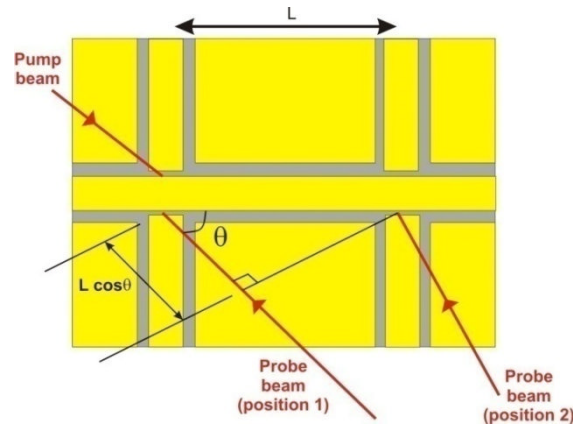


Figure 1.26 Diagram of the procedure used for extracting propagating pulse speed by measuring the pulses before and after propagation (position 1 and 2 respectively), along the active length of (L) of the on-chip waveguide. The diagram illustrates the change in the probe-beam path length by a distance $\sim L \cos \theta$ when it is transferred from position 1 to position 2, or vice-versa.

However as illustrated in Figure 1.26, it is important to consider the change in the beam path lengths during this process, as the probe beam was aligned on switch position 1 for measuring the pulse before propagation and then aligned to switch position 2 for measuring the pulse after propagation. Considering this modification the pulse speed can be calculated by,

$$\Delta t = \frac{L}{V_P} + \frac{L \cos \theta}{c} \quad (1.24)$$

1.7. THz-TDS studies of 2DES

Since the discovery of the quantum Hall effect, the high frequency or time-resolved ultrafast measurements that are sensitive to the physical time scale of electron transport are widely used to study dynamic properties of 2DES. The pulsed THz techniques, including free space and on-chip systems, have shown potential for spectroscopy studies of 2DES with the observation of fundamental physical phenomena such as cyclotron resonance (absorption due to cyclotron motion of electrons) [97], magneto plasmon

resonance [10] and ballistic electron transport [98]. In free space THz-TDS systems, transmission and reflection measurements through thin 2DES structures placed in optical access cryostats, has allowed extraction of spectroscopic information of the 2DES. Also, the advancement in polarisation sensitive free space THz transmission systems has allowed investigation of the optical Hall effect in the quantum Hall regime [9], which gave some potentially useful insights into the dynamic behaviour of electron conductivity of 2DES.

The on-chip THz technique has an advantage of having much longer lengths of interaction as compared to the free space THz systems, since the evanescent field of the propagating pulses can be directly coupled with the incorporated 2DES within the dielectric substrate or superstrate of the on-chip waveguide. In addition, the difficulty of THz coupling into the cryostats used for free space spectroscopy studies of 2DES at cryogenic temperatures can be avoided using on-chip THz systems. An illustration of such a system with integrated on-chip coplanar waveguide with photoconductive switch regions and the 2DES superstrate as 'NDUT' is shown in Figure 1.27. The change in transmission properties such as loss and dispersion within the waveguide can be used to extract the properties of the 2DES.

An on-chip time-resolved measurement system similar to the one shown in Figure 1.27 with small variation, successfully demonstrated the use of gold coplanar strip (CPStrip) lines for measuring high frequency 2DES conductivity as a function of magnetic field [10]. The CPStrip with integrated photoconductive switches was fabricated on a multilayer substrate consisting of the LT-GaAs photoconductive layer, with fringing fields of the THz radiation capacitively coupling to the 2DES employed as superstrate. The measurements revealed plasmon resonances in the 2DES resulting from the geometry of the 2DES strip.

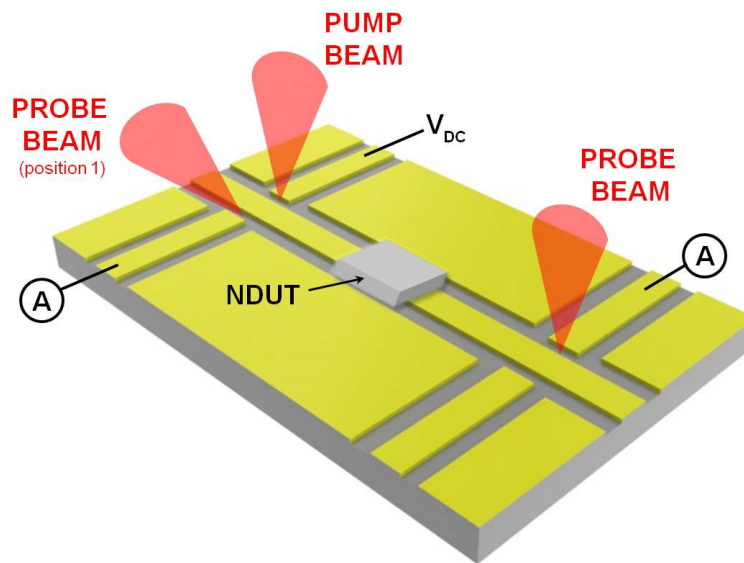


Figure 1.27 Similar pump-probe arrangement as shown in Figure 1.25, for generation and sampling of THz pulses along an on-chip waveguide. In this case, the evanescent field of the propagating pulses along the waveguide is used for spectroscopy of the nanoscale device under test (NDUT).

Alternatively, a direct electrical coupling of ps time scale pulses from on-chip waveguides into the 2DES using a flip-chip bonding process has revealed ps time resolved ballistic electron transport, as demonstrated by Shaner and Lyon [98]. The reported measurements showed accurate time of flight of electrons to be extracted by magnetic focusing of the ps time scale electrical current transients.

The work presented in this thesis will concentrate on the improvements in the integration methods used for interacting ps time scale pulses propagating along the waveguides with the nanoscale devices such as the 2DES. With the aim of enhancing on-chip THz generation, propagation and detection techniques in cryogenic environments and under presence of high magnetic fields, this work has clear significance for advancing picosecond time resolved studies of nanoscale devices.

Chapter 2: On-chip THz waveguide and its integration with 2DES

2.1. Introduction

For picosecond (ps) pulse interaction studies of a 2DES at cryogenic temperatures and under magnetic fields, as demonstrated later on this thesis, it was essential to incorporate both the on-chip THz waveguide and the 2DES in close proximity.

The first purpose of this chapter is to present characteristic measurements of the on-chip THz coplanar waveguides, independent of any integration with the 2DES. Following this will be a detailed discussion on the implementation of various techniques demonstrated in the literature for incorporating THz waveguides in close proximity with the 2DES, including in each case a consideration of their suitability for this project.

Finally, the optimization and development of the integration method chosen for this work will be presented, including detailed characterisation measurements of the integrated waveguide devices.

2.2. Characterisation of on-chip THz waveguides

This section describes the operation of the on-chip coplanar waveguide devices using TDS, which are used to study various integration methods with 2DES structures as discussed later on this chapter. The planar waveguide structure consisted of a metal strip formed on a LT-GaAs heterostructure substrate grown using MBE. Figure 2.1 (a) shows the schematic of the GaAs based heterostructure used as a substrate for the overlaid CPW. As shown in the schematic, a 400 nm AlAs optical barrier layer was first grown on top of the semi-insulating GaAs substrate at ~ 600 °C, followed by a low-temperature growth of the 2 μm thick LT-GaAs photoconductive material at ~ 215 °C. Before defining switch regions on top of the LT-GaAs surface, for on-chip THz generation and detection, the structure was annealed in-situ at ~ 550 °C for 15 minutes to increase the LT-GaAs resistivity [99].

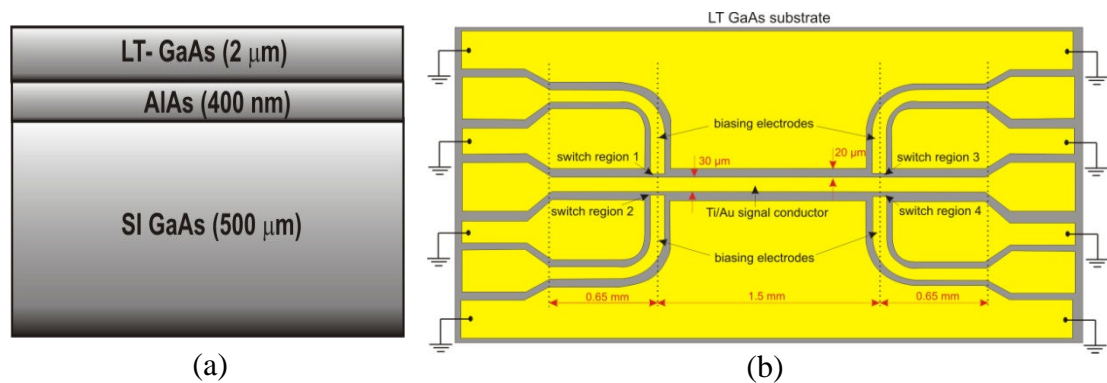


Figure 2.1 (a) Schematic of the SI-GaAs based heterostructure, containing the LT-GaAs photoconductive layer grown on top of the optical barrier (AlAs), using MBE. (b) The overlaid CPW device design consisting of the four switch regions coupled with the Ti/Au signal conductor and ground planes.

The pattern of the metal coplanar waveguide with four integrated photoconductive switch regions as shown in Figure 2.1 (b), was fabricated on top of the LT-GaAs surface using conventional UV lithography followed by thermal evaporation

of a 20/200 nm thick Ti/Au layer. The centre Ti/Au strip acted as signal conductor, with ground planes placed on either side in close proximity. The two pairs of photoconductive switch regions defined on either side of the signal conductor were used to generate and detect ps electrical transients, before and after propagation along the 1.5 mm ‘active region’ of the waveguide. The 0.65 mm long parasitic region of signal conductor, i.e. the region between the switch regions and the line termination, was defined to delay the resulting time-domain reflections.

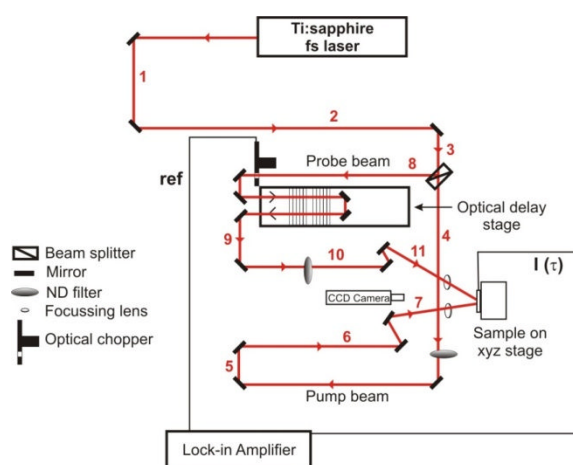


Figure 2.2 Diagram of the on-chip waveguide measurement setup operating at room temperature. The beam from the Ti:sapphire laser was split into pump and probe beams using the beam splitter. The pump beam was passed along paths 4-7, before being focussed onto the sample. The probe beam was optically modulated and passed along an optical delay line via paths 8-11, before being focussed onto the sample.

The THz-TDS system diagram for operating on-chip THz coplanar waveguides is shown in Figure 2.2. As shown, the laser beam from the Ti:sapphire laser (centre wavelength 800 nm, pulse duration 100 fs and, repetition rate of 80 MHz) was split into pump and probe beam using a beam splitter. The two beams were aligned using various mirrors and were focused very precisely onto switch gaps using focusing lenses. The pump beam was focused onto the pump switch to generate THz pulses, while the probe beam was used to detect the pulse by focusing on the probe switch. The probe beam was reflected through a reflector mounted on a motorized translation stage, in order to

control the time delay τ between the two pulsed beams. Also the pulse train was modulated by mechanically chopping the beam at ~ 3 kHz, and the lock-in amplifier measuring the detected current transient $I(\tau)$ from the detection switch was tuned to this modulation frequency.

The electrical transport properties of the switch gap regions defined on LT GaAs material were first observed in terms of the photocurrent generated across the switch gap, with respect to the DC bias applied at the metal electrode. The experimental configuration used for this measurement is illustrated in Chapter 1, Section 1.6.1 and shown in Figure 1.18. The current-voltage measurements carried out for the one of the pump-probe switch regions with varying optical beam intensity are shown in Figure 2.3. Figure 2.3 (a) shows the I-V characteristics for the switch region 1, and Figure 2.3 (b) shows the I-V characteristics of the switch region 3.

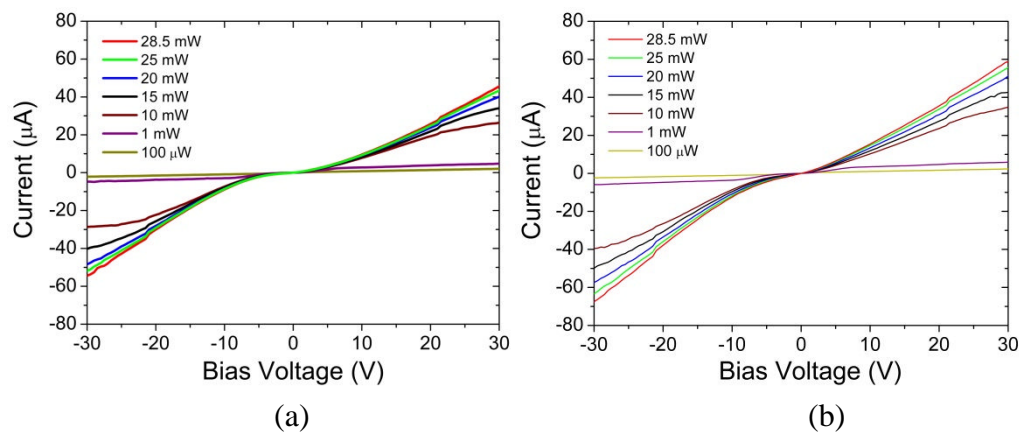


Figure 2.3 DC characteristics measured in terms of current versus applied voltage at varying laser powers, for (a) pump and (b) probe photoconductive switch gap defined on either side of the waveguide.

The I-V characteristics for both the switch regions under different illumination intensities (using ND filters) showed a relatively ohmic behavior. At low voltages there was a slight non linearity which was expected due to charge screening of electrons [100]; also the metal-semiconductor contact formed in the switch region was a Schottky

contact rather than an ohmic. The generated photocurrent variation with increasing beam powers at identical bias voltages showed a linear response, with dark resistance (under no illumination) across the switch gap measured to be $\sim 500 \text{ M}\Omega$.

Following the switch characterisation, the pulse transmission measurements were carried out for observing the CPW properties overlaid on LT-GaAs substrate. The pump-probe arrangement used for measuring the generated and transmitted pulses is identical to the one illustrated in Chapter 1, Section 1.6.4, and as shown in Figure 1.25. The pump and probe beam powers for these measurements were kept identical to 10 mW, with the pump switch (switch region 1) biased at 20 V. A time-domain measurement of the generated pulse undertaken with the probe beam focused at the switch region 2 (as shown in Figure 2.1 (b)) is demonstrated in Figure 2.4.

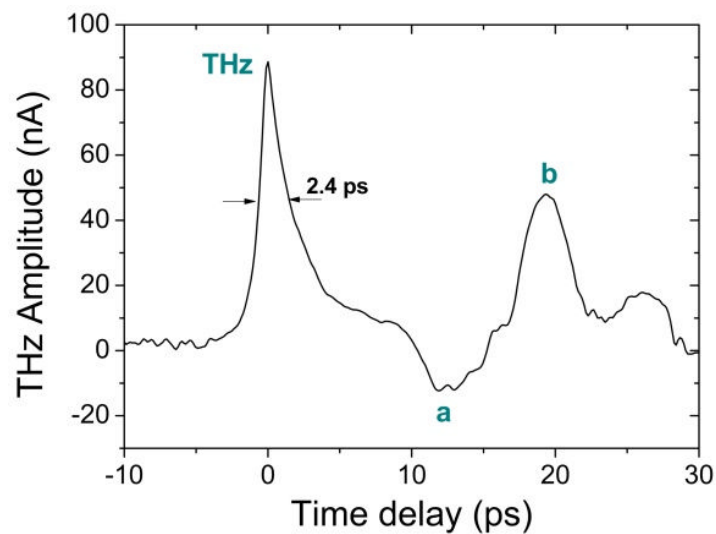


Figure 2.4 The time-domain scan of the generated THz pulse using switch region 1 as the source and switch region 2 as the detector. The main THz peak with time duration of 2.4 ps is followed by the two time delayed reflection peaks, a and b.

The time-domain pulse scan as shown, consists of the main THz pulse peak with time duration of 2.4 ps (measured using Full Width Half Maximum), followed by secondary oscillations a and b. For the CPW device design used, these oscillations were

expected to arise from the reflections of the main pulse from the grounded ends of the conductor. The accurate origin of these reflections was determined by considering the time delays between the THz peak and each reflected signal. Using the calculated phase velocity, the distance travelled by each reflection was determined, and the origin inferred from the CPW device geometry. Figure 2.5 shows the demonstration of the pulse path required for generating time-domain reflections following the main pulse.

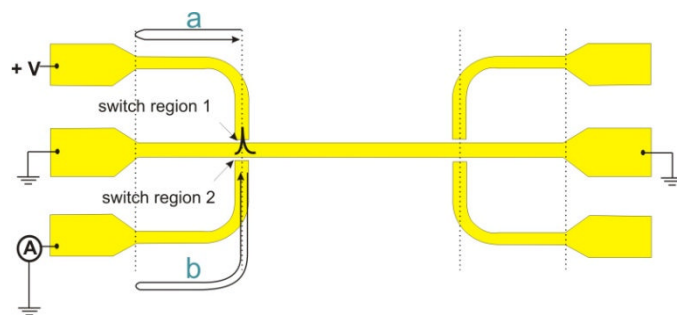


Figure 2.5 Demonstration of the pulse paths required to generate the two time-domain reflections peaks, a and b (in Figure 2.4), following the generated THz pulse peak.

The time-domain scan of the pulse after transmission along the 1.5 mm active region of the CPW was then measured, using identical beam power and pump switch bias as used for the measurement of the generated pulse. For the pump-probe arrangement in this case, the probe beam was focused at switch region 3 with pump beam focused on switch region 1. Since the CPW device geometry under test was symmetrical, the characteristic features of the transmitted signal were found to be similar to the main signal (i.e. the main THz pulse with secondary reflections) and are shown in Figure 2.6. However, a clear demonstration of attenuation and dispersion of the pulses was seen after propagating along the CPW on LT-GaAs dielectric substrate.

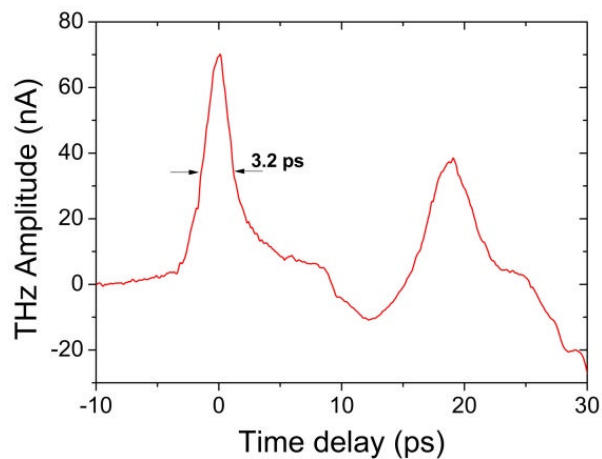


Figure 2.6 Example of the time-domain pulse transmitted along the 1.5 mm coplanar waveguide, measured using switch region 1 as the source and switch region 3 as the detector. The FWHM was measured to be 3.2 ps.

The time-domain THz pulse signal was then converted into the frequency domain by performing a Fast Fourier Transform (FFT) of the data points around the THz pulse peak, thereby allowing analysis of the frequency components contained within the time-domain signal. Figure 2.7 shows the normalised FFT of the measured transmitted THz signal, revealing the usable bandwidth of ~ 400 GHz for the CPW devices used, with a resolution of 50 GHz.

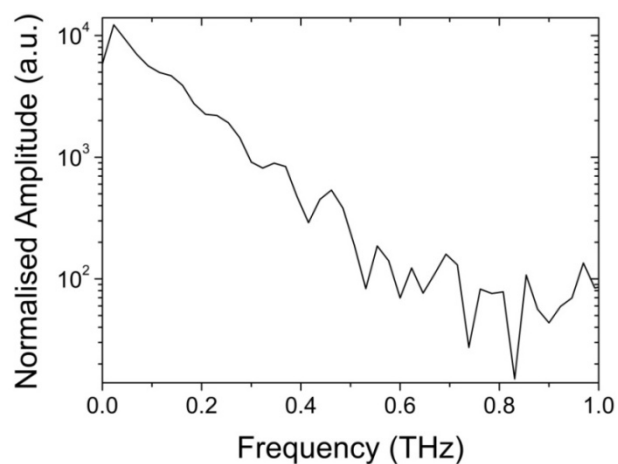


Figure 2.7 Fast Fourier Transform performed on the THz peak seen in Figure 2.6, showing the usable frequency bandwidth of the CPW devices up to ~ 400 GHz with peak signal-to-noise ratio of $\sim 100:1$.

Both the time-domain and frequency domain analysis of the THz pulse measurement propagating along the CPW showed a reasonable performance in terms of pulse peak amplitude and frequency bandwidth. Therefore, the demonstrated CPW device design on the LT-GaAs heterostructure was used for implementing various techniques to integrate a 2DES, as discussed in the next section.

2.3. Integration of on-chip THz waveguides and 2DES

This section describes various experimental arrangements carried out for incorporating 2DES and THz pulse transmitting waveguides, which can allow observation of picosecond timescale response of the mesoscopic system at cryogenic temperatures. Since the THz generation and detection is carried out using switches patterned on photoconductive material, it was essential to have the photoconductive material with integrated waveguide in close proximity to the GaAs/AlGaAs heterostructure containing the 2DES.

The system integration techniques discussed here involved both external post-processing integration of multiple chips (i.e. after sample fabrication), and pre-processing (i.e. before sample fabrication) methods. The first method limits the sensitivity in picosecond pulse coupling to the 2DES, while the second has a greater sensitivity owing to incorporating both the photoconductive layer and the 2DES on one single chip.

2.3.1. Flip-chip technique

The flip-chip approach exploits the propagating evanescent fields above an on-chip waveguide to perform spectroscopic measurements of an overlaid superstrate material. It has been previously used in on-chip THz technology to study molecular signatures of a wide range of materials [81, 82]. The first demonstration of picosecond time resolved electron transport measurements in low-dimensional electron systems [101] used the flip-chip method for integration of on-chip THz waveguides and the 2DES. It consisted of an on-chip THz CPW fabricated on one chip brought in close proximity with a separate GaAs/AlGaAs heterostructure chip containing the 2DES. Figure 2.8 (a) shows the schematic of the chip containing the waveguide overlaid on the host dielectric substrate (in this case sapphire), with integrated LT-GaAs photoconductive material capable of generation and detection of ps timescale electrical transients. The schematic structure of the GaAs/AlGaAs heterostructure formed on a separate chip containing the 2DES is shown in Figure 2.8 (b). Since the 2DES is formed close to surface of the heterostructure, it is flipped and then overlaid on the on-chip waveguide.

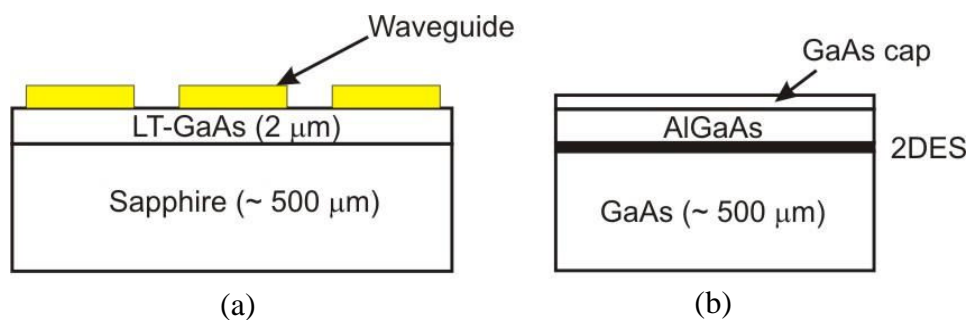


Figure 2.8 Illustration of the two separate chips used for ‘flip-chip’ integration technique. Where, (a) shows the chip containing the sapphire substrate with the photoconductive material and the overlaid CPW. (b) shows the chip containing the GaAs substrate with the GaAs/AlGaAs heterostructure containing the 2DES grown on top.

The flip-chip substrate assembly method has an advantage of allowing spectroscopy of the 2DES to be carried out by either capacitively coupling the electric field of the propagating ps timescale pulses to the 2DES or by direct electrical coupling

of the signal through the electrical contacts patterned on the 2DES. A brief discussion on the representation of each of these methods is given below.

2.3.1.1. Evanescent field coupling

The flip-chip method of capacitively coupling the evanescent fields of the ps pulse to the 2DES allows absorption spectroscopy without making direct electrical contact. A pictorial representation of the evanescent field coupling method is shown in Figure 2.9, with a CPW used for propagating ps timescale pulse generated and detected using integrated photoconductive switches.

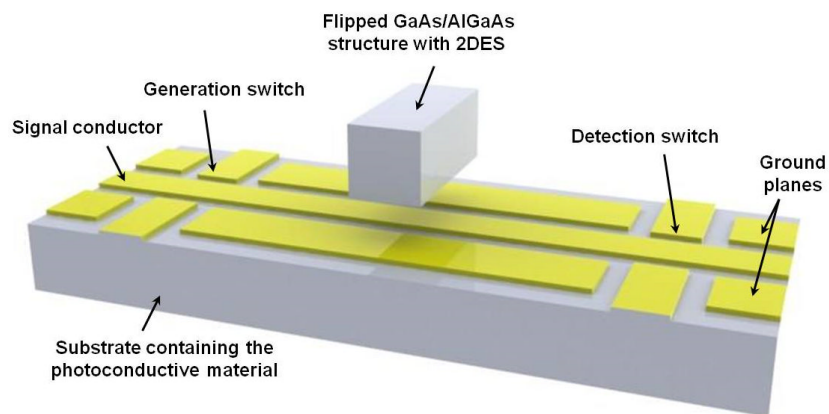


Figure 2.9 Graphical illustration of the ‘flip-chip’ approach, showing coupling of the propagating pulse along the CPW with the flipped GaAs/AlGaAs heterostructure chip containing the 2DES. The integrated generation and detection photoconductive switch shows the location points for pulse launch and detection.

The setup showing implementation of the technique demonstrated in Figure 2.9 by E. Shaner [10], for waveguide spectroscopy of the 2DES is shown in Figure 2.10. The Ti/Au CPW pattern fabricated using lift-off technique on the epilayer substrate, with pump and probe laser beams delivered to the launch (L) and detection (D) points on the waveguide, is shown in Figure 2.10 (a). Figure 2.10 (b), shows the illustration of the flipped 2DES chip epoxied (non-conductively) to the waveguide, with the substrate containing the LT-GaAs photoconductive layer on sapphire. It is noted, since the surface

of the waveguide together with switch regions was covered with the 2DES chip as a superstrate, the optical excitation using pump and probe fs laser pulses was made through the via holes in the silicon layer forming the base of the integrated chip.

Although the sensitivity of the ps pulse measurement through the 2DES was limited by the evanescent field coupling configuration, it did successfully demonstrate measurement of ps pulse interactions with the 2DES. Hence, an analogous example reproducing this method was demonstrated in this project.

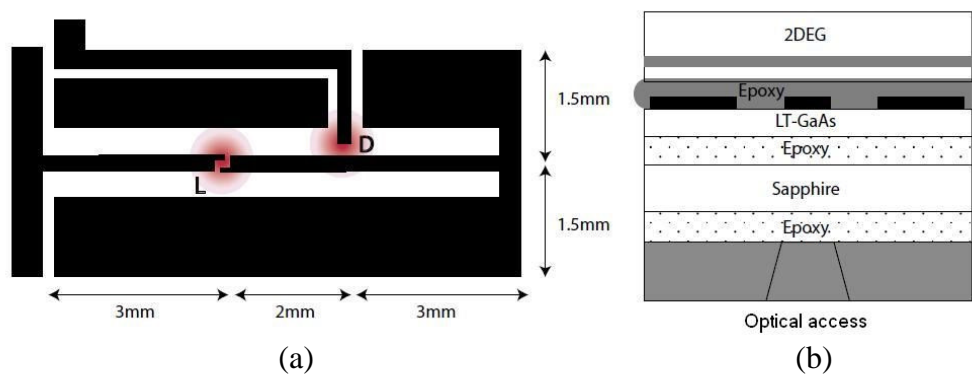


Figure 2.10 Experimental arrangement showing the demonstration of ‘flip-chip’ evanescent field coupling technique, taken from reference [10]. (a) shows the geometry of the CPW used, with the location points for ps pulse generation and detection along the CPW shown by L and D. (b) The configuration of the integrated structure used, showing the 2DES chip flipped and epoxied to the waveguide chip.

A similar ‘flip-chip’ experimental configuration previously established at Leeds for sub-wavelength THz imaging, using on-chip waveguides based on BCB (benzocyclobutene) dielectric [71], was used for interacting the evanescent fields propagating along the CPW devices with a 2DES superstrate. Figure 2.11 shows the experimental arrangement used for room temperature interaction between a flipped 2DES sample and a CPW device fabricated on the LT-GaAs heterostructure.

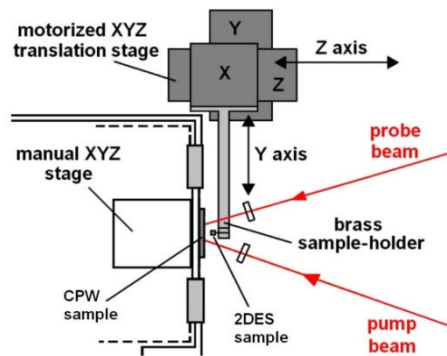


Figure 2.11 Diagram of the experimental arrangement for evanescent field coupling of on-chip CPW with the 2DES, taken from reference [71].

As shown in the schematic, the 2DES sample containing the GaAs/AlGaAs heterostructure on GaAs substrate, similar to one illustrated in Chapter 1, Section 1.4 (shown in Figure 1.5) was cleaved and glued to a custom-designed brass sample holder using GE (general electric) varnish. The computer-controlled 3-axis motorized stage attached to the sample holder was used to sequentially move the 2DES sample along the z-axis. In doing so, the sample was brought in close proximity with the CPW device, with the surface plane-parallel to the waveguide. This process was carried out by avoiding any obstruction to the pump and probe laser beams focussed on to the generation and detection photoconductive switches. The measured time-domain spectra of the pulse transmitted along the CPW with the 2DES sample surface in full contact, and at several separation distances from the CPW surface is shown in Figure 2.12.

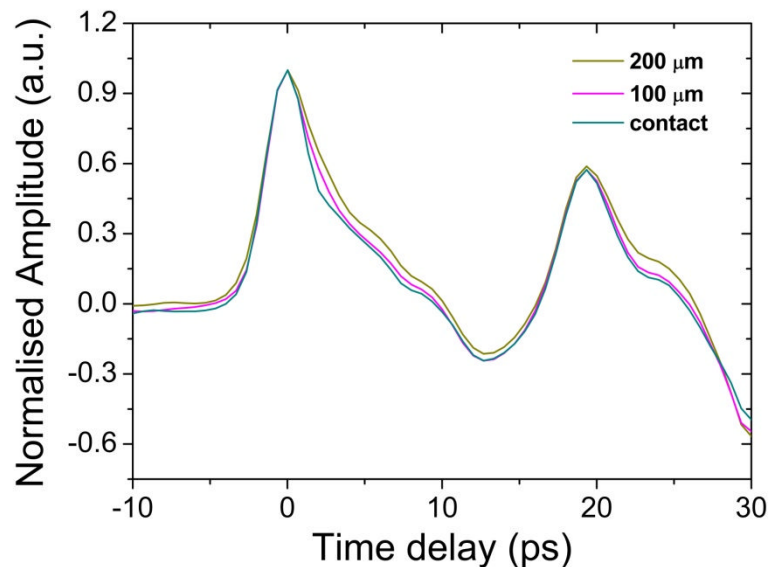


Figure 2.12 Experimental data showing the time-domain scans of the transmitted pulse measured after propagation along the 1.5 mm active length of the CPW (as shown in Figure 2.1 (b)), with the flipped 2DES chip in close proximity distances and in full contact with the waveguide surface.

From the data shown in Figure 2.12, at first instance, no significant change was observed in terms of attenuation or dispersion of the transmitted pulses upon interaction with the 2DES sample in close proximity. This can be explained by considering the 2D cross-section of the evanescent field propagating along the CPW. A large proportion of this field was mostly being concentrated in the GaAs substrate due to its high dielectric permittivity ($\epsilon_{\text{GaAs}} = 12.9$) [102], hence resulting in relatively weak interaction with the 2DES.

Considering the limited sensitivity of the evanescent coupling method for the 2DES interaction measurement, together with complications in system integration in much smaller sample volumes in cryogenic environments; the flip-chip coupling method in this case was found to be not suitable for the absorption spectroscopy of the overlaid 2DES structure.

2.3.1.2. Direct electrical coupling

An alternate method using ‘flip-chip’ configuration for measuring ps timescale electron transport in 2DES involves direct coupling of pulses along the waveguide into the 2DES through electrical contact made between the 2D electron layer and the waveguide.

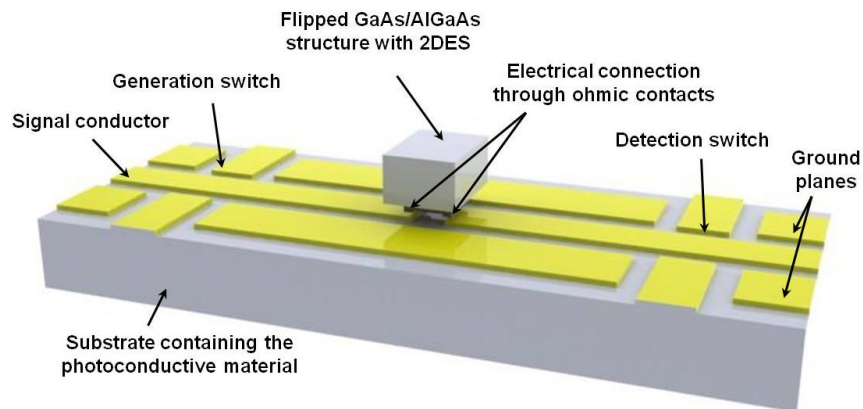


Figure 2.13 Graphical illustration of the ‘flip-chip’ approach, showing direct electrical coupling of the propagating pulse along a CPW with the flipped GaAs/AlGaAs heterostructure chip containing the 2DES. The electrical connection is made through the direct contact between the signal conductor and the ohmic contacts. The integrated generation and detection photoconductive switch shows the location points for pulse launch and detection.

Figure 2.13 illustrates the ‘flip-chip’ configuration with electrical bonding between the 2DES and the on-chip waveguide. As shown, the ps timescale pulses generated and propagating along the signal conductor of the CPW are coupled into the flipped 2DES sample through electrical connections formed between the signal conductor and the ohmic contacts formed to the 2D electron layer. A similar electrical connection is then used for the pulse transmitted through the 2DES to be coupled back onto the signal conductor and detected using the detection switch region.

The experimental implementation of the ‘flip-chip bonding’ technique was also established by E. Shaner [98], where ps time-resolved ballistic transport in the 2DES was observed using transverse magnetic field focusing of the injected pulse at cryogenic temperatures. Figure 2.14 shows the schematic of the CPW device used, with the 2DES

chip having four ohmic contacts ‘flip-chip’ bonded for electrical connection with the waveguide.

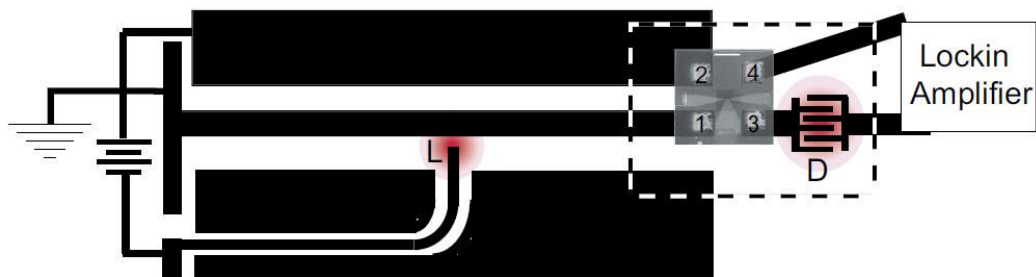


Figure 2.14 Experimental configuration previously established for demonstrating the ‘flip-chip’ arrangement to electrically couple the ps pulses travelling along the CPW with the flipped 2DES chip, taken from reference [98]. The four ohmic contacts formed on the flipped 2DES chip surface are directly bonded to the signal conductor and the ground planes of the CPW. The location points for ps pulse generation and detection along the CPW shown by L and D respectively.

This integration approach was found to be much more sensitive for time-resolved electron transport measurements in the 2DES; however the integration of the CPW with the 2DES chip by electrically connecting the ohmic contacts on flipped 2DES carefully to the CPW would require micron accuracy flip-chip bonders. Hence, it was not employed in this particular work.

2.3.2. Three-chip substrate assembly technique

Another post fabrication approach for integration of on-chip THz waveguides with the 2DES was recently demonstrated by D. Maryenko [103]. It followed the accomplishment of a reflection-free ps timescale electrical pulse propagation along a CPW, which was overlaid onto two separate ErAs:InGaAs photoconductive material chips and electrically connected between the interface (at cryogenic temperatures and under magnetic fields) [93].

The technique established was referred to as a ‘three-chip substrate assembly’, since the substrate chip containing the 2DES was assembled between the two

photoconductive material substrate chips. The CPW pattern was then aligned and electrically connected across the three-chips. Figure 2.15 shows the graphical illustration of the three-chip substrate assembly technique.

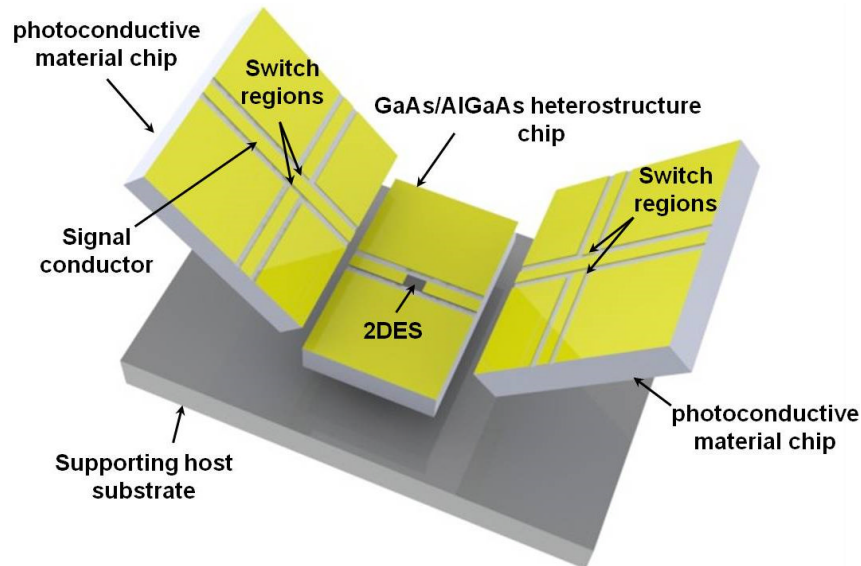


Figure 2.15 Graphical illustration of the ‘three-chip substrate assembly’ method, showing the ‘post-fabrication’ assembly of the CPW overlaid on three different chips onto a supporting host substrate. The left and right chips contain the photoconductive switch gaps for THz generation and detection, whereas the chip in the middle contains the active 2DES device coupled with the signal conductor of the CPW.

As shown, the 2DES device was fabricated on a GaAs/AlGaAs heterostructure with a subsequent formation of CPW electrically connecting the ohmic contacts on the 2DES. In parallel to this processing, the CPW with integrated photoconductive switches was separately formed on a photoconductive material substrate. Thereafter the chip with the CPW on the photoconductive material is cleaved and placed on either side of the chip containing the ‘active’ 2DES device. All the three chips were placed and glued on a separate host Si substrate. The coplanar waveguide was then aligned at the interface between the separate chips and the signal conductor and ground planes were electrically contacted by applying conductive silver epoxy. The advantage of this technique over flip-chip configuration is that it provides flexibility with the ‘active device’ under test;

i.e., it can be used to interact ps pulses with more confined quantum systems such as 1D quantum wires or 0D quantum dots instead of just a 2DES, provided the dielectric constant of the active material is comparable to the photoconductive material.

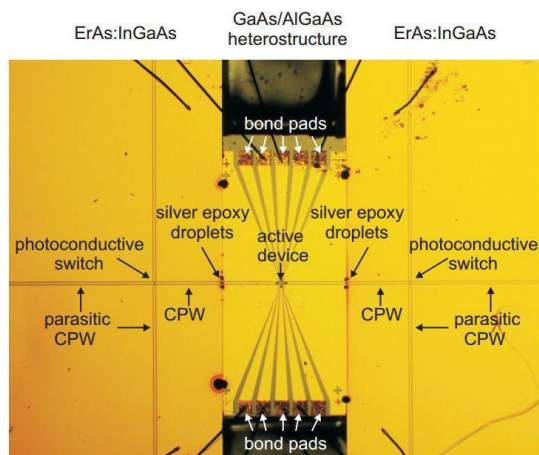


Figure 2.16 Optical image of an integrated device using three-chip substrate assembly method for coupling on-chip CPW with a 2DES device, taken from reference [103]. The left and right chips containing the photoconductive switches are fabricated from the ErAs:InGaAs photoconductive material, while the central chip containing the 2DES is fabricated from a GaAs/AlGaAs heterostructure.

The successful demonstration of three-chip substrate assembly method by D. Maryenko is illustrated in Figure 2.16. It is seen from the schematic that the left and right chips are fabricated from ErAs:InGaAs photoconductive material and contain the photoconductive switches. The central chip is fabricated from a GaAs/AlGaAs heterostructure containing the 2DES. Also as demonstrated, the electrical connection of the CPW between chips after aligning the ground planes and centre conductor is carried out using silver epoxy droplets. This method did allow ps pulse coupling with the 2DES device, however the experimental results showed no strong evidence of ps time-resolved electron transport.

In this current project, the multiple chip substrate assembly technique was also attempted in order to integrate the 2DES with on-chip THz coplanar waveguides.

Initially, the CPW device fabricated on LT-GaAs photoconductive material substrate, as shown in Figure 2.17 (a) with CPW active region of 1.5 mm, was cleaved from the middle, re-assembled and glued onto a host Si substrate (no inclusion of the chip with 2DES). Figure 2.17 (b) shows an optical image of the re-assembled CPW device, with signal conductor and ground planes of the CPW electrically connected using conducting silver epoxy.

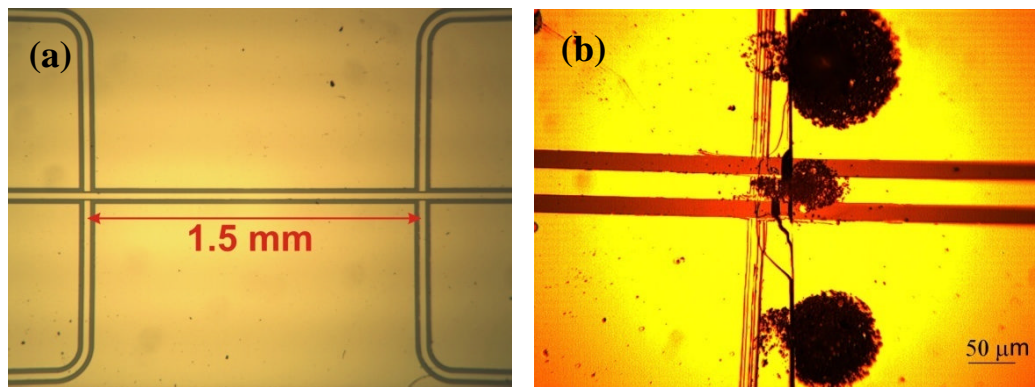


Figure 2.17 Optical microscopic image of the CPW device geometry implementing ‘multiple-chip assembly’ technique. (a) shows the image of a continuous CPW device with integrated generation and detection photoconductive switch gaps on a single LT-GaAs substrate chip. (b) shows the image of an interface between multiple CPW sections (after cleaving and re-assembling of the continuous CPW device). The CPW sections including the integrated generation and detection photoconductive switch gaps on multiple LT-GaAs substrate chips were electrically connected using a conductive epoxy.

The pulse transmitted along the active region of the CPW was measured before and after the multiple chip assembly process. Figure 2.18 shows the comparison of the time-domain pulse scan after propagation along a continuous CPW sample and along a CPW across multiple chips. A clear demonstration of a transmitted pulse with no reflection occurring from the multiple chip interface was noted, resembling the pulse propagated along a continuous CPW on a single chip.

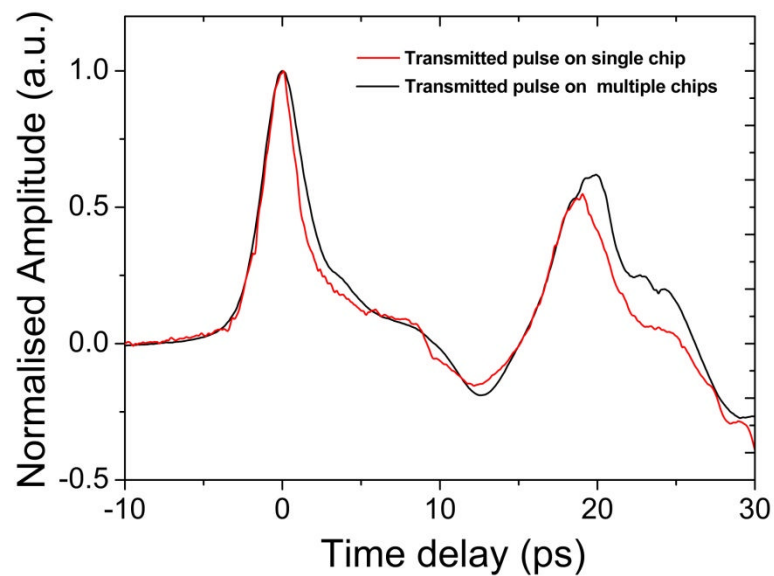


Figure 2.18 Experimental data showing the comparison between the transmitted pulse measurements along a CPW overlaid on a single LT-GaAs substrate chip and along a electrically connected multiple CPW sections overlaid on two different LT-GaAs substrate chips.

However, the successful application of this integration method was limited to the cleaving and re-assembly of the same chip. With the inclusion of the third (separate chip), the assembly of the three chips was found to be difficult. The reason was that any dislocations or roughness at the interface of the two separate chips (e.g. the central 2DES chip and photoconductive material chip) cleaved independently would be more prominent as compared to the re-assembly of the same chip cleaved in two halves. The presence of these dislocations would cause a finite gap ($\sim 1\text{-}5\ \mu\text{m}$ wide) at the interface of the separate dielectric substrate chips, as illustrated in Figure 2.19, thereby preventing reflection-free pulse propagation through multiple chips.

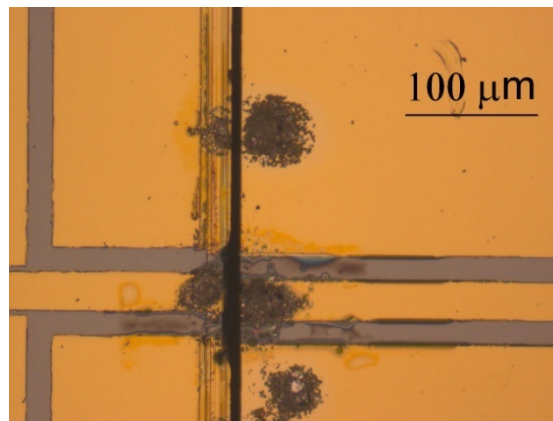


Figure 2.19 Optical microscopic image of the interface between CPW sections cleaved and re-assembled from the separate GaAs substrate chips. The image shows the resulting finite gap between the two chips due to presence of interface dislocations.

A major drawback of this method for integrating 2DES with on-chip waveguides was the poor yield and repeatability of device fabrication, which was in turn largely dependent on the post-fabrication multiple chip assembly. And so, it was decided against using this integration approach.

2.3.3. Epitaxial transfer method

After attempting several previously established techniques by other research groups for incorporating the 2DES with on-chip waveguides, two alternate methods were proposed in this work, which had not been demonstrated before and were expected to allow successful incorporation of both 2DES and THz waveguide on a single chip.

The first method was based on the principle of epitaxial lift-off and transfer process of ultra-thin films onto an arbitrary dielectric substrate. Figure 2.20 shows a layer-by-layer view of the integrated device design based on the epitaxial transfer method. As shown, both the 2DES and the LT-GaAs photoconductive material films, initially grown on a GaAs substrate using MBE, can be separately lifted-off and transferred onto a host substrate (in this case quartz). Since quartz has a comparatively

low dielectric permittivity ($\epsilon_{\text{quartz}} \sim 2.3$), and has already been established as a suitable substrate for THz bandwidth on-chip waveguides, it was chosen for this work [92].

The subsequent processing of the ohmic contacts on the 2DES mesa, followed by overlaying the CPW with integrated switch regions, would enable pulse interaction measurements on a single chip.

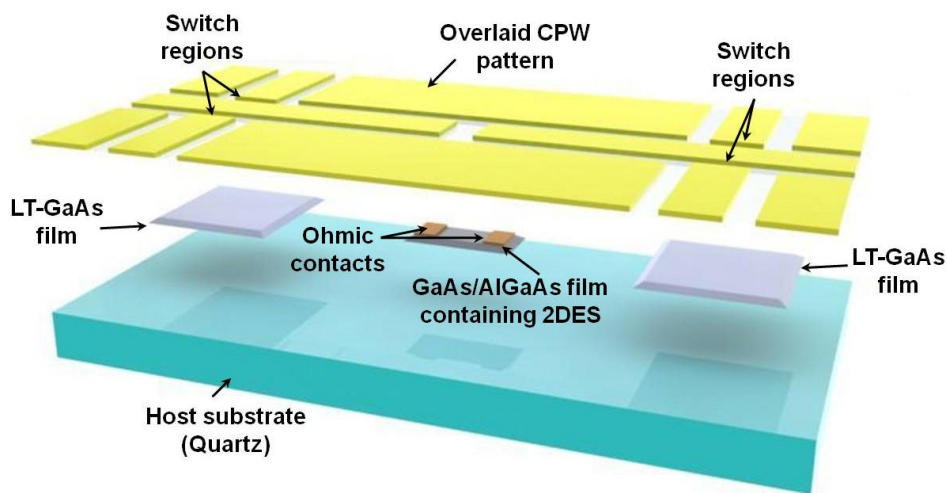


Figure 2.20 Layer-by-layer view of the implementation of the epitaxial transfer method, for integrating ultra-thin films of the LT-GaAs photoconductive layer and 2DES on a host substrate (quartz). The electrical coupling of the 2DES with the overlaid on-chip CPW is carried out via ohmic contacts formed on the film containing the 2DES. While the LT-GaAs films are used defining switch regions for generation and detection of propagating ps timescale pulses.

The likelihood of this integration approach was firstly based on the initial demonstration of epitaxial lift-off and transfer of thin LT-GaAs photoconductive films ($< 1 \mu\text{m}$) [84, 85], with dimensions of 4 mm x 2 mm. In this demonstration, the multilayer heterostructure containing the thin film on top of the AlAs release layer was initially grown on a GaAs substrate using MBE. The thin photoconductive film was then lifted-off from the rest of the substrate by selectively etching away the release layer using a dilute hydrofluoric (HF) solution. The etch selectivity in HF solution was found to be ($\sim 10^7$) for $\text{Al}_x\text{Ga}_{1-x}\text{As}$ (with $x > 0.6$) alloy as compared to $\text{Al}_x\text{Ga}_{1-x}\text{As}$ (with

$x < 0.4$). This allowed the integration of the thin film onto a separate dielectric substrate using covalent bonding.

Another independent experiment showed successful operation of a 2DES, following epitaxial lift-off and transfer of the GaAs/AlGaAs heterostructure layers containing the 2DES onto a quartz substrate [104, 105]. Both of these experiments encouraged the idea of the epitaxial transfer method being implemented in this work for integrating both the photoconductive layer and the 2DES on one single chip.

The schematic of the heterostructures independently grown using MBE for implementing epitaxial transfer process are shown in Figure 2.21. The GaAs/AlGaAs heterostructure containing the 2DES grown on top of the AlAs release layer is illustrated in Figure 2.21 (a), whereas Figure 2.21 (b) shows the layer structure of a heterostructure containing the LT-GaAs photoconductive layer on top of the AlAs release layer.

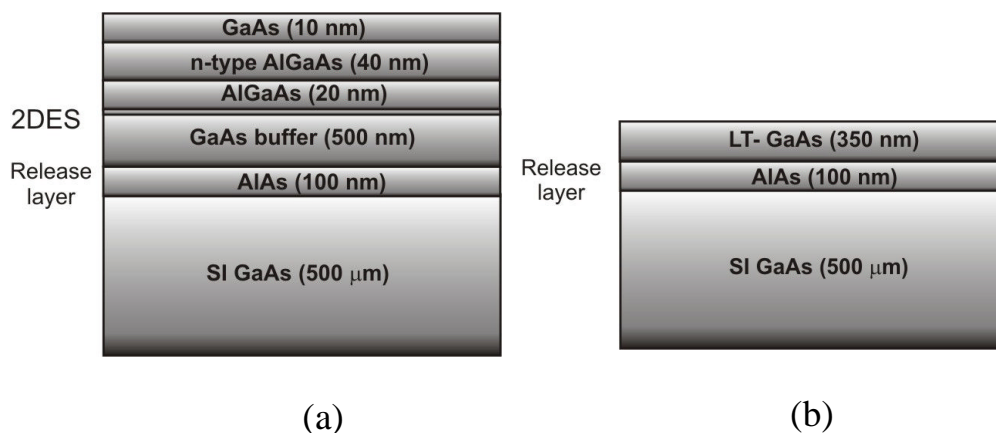


Figure 2.21 Schematic of the MBE grown layer structures used for the epitaxial lift-off and transfer of (a) GaAs/AlGaAs heterostructure containing the 2DES, and (b) LT-GaAs photoconductive layer. The incorporation of the AlAs release layer shown in both structures aids the epitaxial lift-off process.

Two chips were first cleaved to the dimensions of 4 mm x 4 mm from the LT-GaAs heterostructure, while a single chip cleaved to the dimension of 3 mm x 3mm from the GaAs/AlGaAs heterostructure was used. The dimensions were initially chosen

for aiding the handling of the chips. For selectively etching the AIAs release layer, as described earlier, a dilute hydrofluoric (HF) acid solution was used, with a dilution concentration of HF:H₂O ~ 1:10. Also, in order to assist the handling of the ultra-thin epilayers (from both the structures) during the transfer and integration process onto the quartz substrate, a layer of black wax (or Apiezon wax) was coated on the top surface of the heterostructure. The bonding of the epilayers with quartz took place via van der Waals forces.

After the bonding of both the GaAs/AlGaAs and the LT-GaAs epilayers onto the quartz substrate, the film surfaces observed optically showed a high occurrence of micro-cracking. An example of the micro-cracks across the surface of the transferred LT-GaAs film is shown in Figure 2.22. A similar observation was seen for the transferred GaAs/AlGaAs epilayers containing the 2DES.

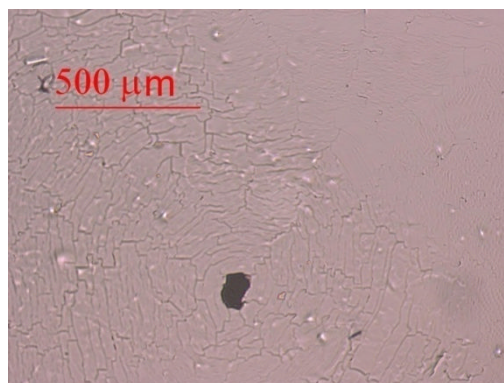


Figure 2.22 Optical microscopic image demonstrating the micro-cracking of the LT-GaAs film after epitaxially transferred from the MBE structure and covalently bonded onto a quartz substrate.

The key reason for the micro-cracking of the transferred epilayers was found to be the creation of byproducts from the chemical reaction between the etching solution and AIAs release layer [106], especially the gaseous H₂. The gas bubbles trapped in the area between the epilayer and the substrate cause surface tension in the epilayer film, thereby resulting in micro-cracks. The consistency of substrate cracking was seen across

several attempts with the 2DES and LT-GaAs epilayer transfer processes. Also, the presence of layer cracking was very critical for functioning of the 2DES, and therefore required a lot more research work to be carried out in terms of optimizing the overall fabrication process (i.e. etching solution concentration, the physical dimensions of the lifted-off epilayer, the temperature during the etching process and the handling technique of the epilayers during the transfer process). Due to time constraints in the project, this method was not considered to be a viable option for successful integration of the 2DES and the LT-GaAs photoconductive material on one chip.

2.3.4. Monolithic integration technique

The second method proposed and established here for incorporation of the 2DES with the on-chip waveguides involved a novel scheme, demonstrating a monolithic integration of an epitaxially grown LT-GaAs photoconductive layer with the 2DES. Since both LT-GaAs and GaAs/AlGaAs based 2DES have a similar lattice structure, it allows the epitaxial integration of two layers on the GaAs substrate without changing the lattice parameter of the structure.

However, the difference in epitaxial growth temperatures of the LT-GaAs and the 2DES poses a great difficulty in achievement of the monolithic approach. The optimum epitaxial growth temperature of the LT-GaAs photoconductive layer is widely known to be ~ 200 °C [65, 107, 108], (for excitation of ps lifetime carriers), also shown in Figure 2.23. This growth temperature is comparatively much lower than the conventional growth temperatures of a GaAs/AlGaAs based 2DES [44]. As a result, the epigrowth of the 2DES on the same wafer will effectively change the properties of the LT-GaAs (assuming the LT-GaAs layer is grown first).

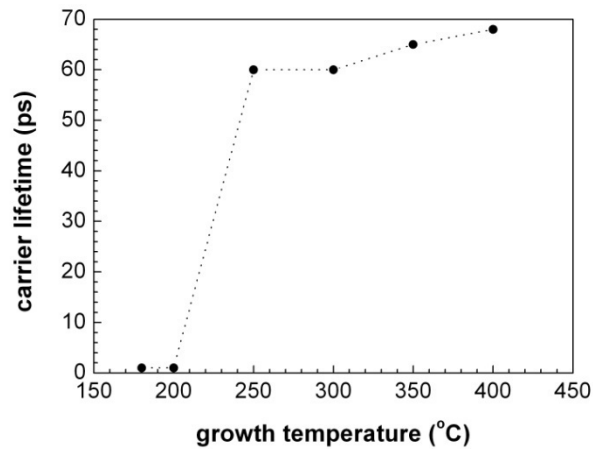


Figure 2.23 Typical dependence of the photo-generated carrier lifetime on the MBE growth temperature for as-grown (un-annealed) LT-GaAs photoconductive layer, taken from reference [65].

On the other hand, the successful implementation of this technique shows numerous advantages; most importantly, unlike the previous integration methods discussed, the coupling of THz waveguides with the active ‘2DES’ device is only dependent on processing of the structure (i.e. selective etching and overlaying metal contacts). Therefore, it avoids any ‘post-fabrication integration’ processes which could result in decreasing the overall functioning device yield. Also, having the 2DES coupled with the waveguide overlaid on the same substrate allows more efficient and low loss electric field coupling of the propagating ps timescale pulses, resulting in high sensitivity for observing electron transport.

The following sections discuss the application in this project of the monolithic approach for integration of the 2DES and LT-GaAs photoconductive layers. Individual characterisation data and optimization of the performance of each layer is given below.

2.4. First generation of monolithic integrated structures

The first generation of the monolithic integrated structure demonstrated in this work consists of a GaAs/AlGaAs epilayer sequence first grown on top of the semi-insulating (SI) GaAs substrate, followed by the subsequent growth of LT-GaAs photoconductive layer. A similar monolithic integration scheme was presented earlier at Leeds [109], showing free-space THz emission from a photoconductive semiconductor switch grown on the same wafer as the 2DES. Also, the low temperature electron transport characteristics separately measured in the 2DES were not compromised by the integrated photoconductor. The detailed layer structure grown on the SI substrate for the first generation integrated structures is as shown in Figure 2.24.

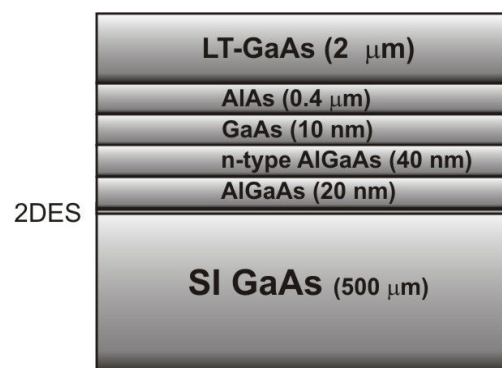


Figure 2.24 Schematic of the MBE grown layer structure used for the first generation monolithic integration of the LT-GaAs photoconductive layer with the 2DES heterostructure.

It is noted from the schematic that the first layer sequence consists of a conventional 2DES GaAs/AlGaAs heterostructure, containing the 20 nm undoped AlGaAs spacer layer, followed by a 40 nm Si-doped AlGaAs layer and a 10 nm GaAs cap layer. A 400 nm AlAs optical barrier layer was then grown followed by a subsequent growth of a 2 μm LT-GaAs photoconductive layer. The growth temperature

across all the layers was ~ 600 °C, with the exception of the LT-GaAs layer, which was grown at ~ 215 °C. The wafer was then annealed in situ at 530 °C for 15 minutes, to increase the LT-GaAs resistivity.

Before individually investigating the properties of the LT-GaAs and the 2DES layers integrated monolithically using MBE, the conduction band profile of the structure shown above was simulated using a Poisson-Schrodinger 1D numerical solver to determine the carrier distribution as a function of depth into the wafer at cryogenic temperatures (~ 4 K). The simulation result is shown in Figure 2.25.

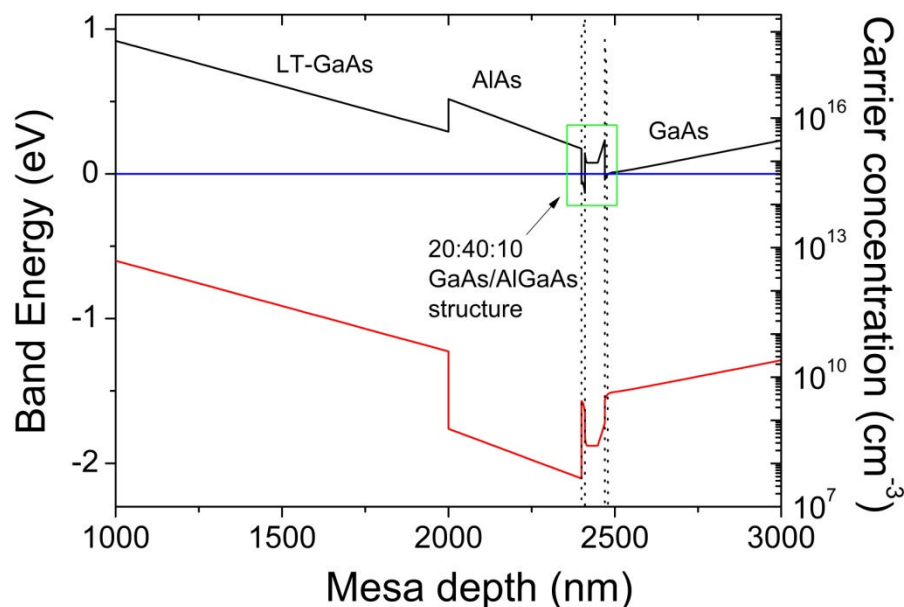


Figure 2.25 Simulated conduction band profile showing the distribution of carrier concentration across the layer structure for the first generation monolithic integration of LT-GaAs layer on top of the 2DES heterostructure.

It is noted that in addition to the 2DES forming at the GaAs/AlGaAs heterojunction interface, a second electron system in parallel to the 2DES was induced at the AlAs-GaAs cap layer interface. This resulted from the conduction band bending below the Fermi energy near the AlAs-GaAs cap layer interface. The second electron

layer in parallel to the 2DES could act as a very low resistance parallel conducting layer, thereby affecting the properties of both the LT-GaAs and the 2DES layers.

The subsequent sections show characteristic measurements for the first generation integrated structure, independently showing the ps pulse transmission properties using the LT-GaAs based CPWs and the low-temperature electron transport properties in the 2DES.

2.4.1. Characterisation of photoconductive layer

Since the photoconductive layer was located at the top of the integrated layer structure, the quality of the LT-GaAs layer was characterised first using ps pulse generation and transmission pulse measurements on CPW devices. The LT-GaAs based CPW device geometry used for integrated structures were identical to ones previously characterised in section 2.2 (for LT-GaAs structure without the 2DES).

The properties of the switch region defined on the LT-GaAs for generation and detection of ps timescale electrical transients were tested in terms of generated current across the switch gap with respect to the applied bias. Figure 2.26 shows the I-V measurement carried out across one of the four identical switches integrated with the CPW overlaid on the integrated structure surface. The inset of the Figure shows a comparable I-V measurement previously carried out across an identical switch geometry overlaid on the reference structure (i.e. LT-GaAs heterostructure without the 2DES). As noted from Figure 2.26, the photocurrent generated across the switch gap on LT-GaAs with 2DES underneath was comparable to the photocurrent generated across the photoconductive switch gap structures without the 2DES.

However, the contribution of the low-resistance parallel conducting layer induced at the AlAs-GaAs cap interface within the integrated structure (as seen in Figure

2.25) was clearly observed in terms of dark current measurement. The dark resistance of the photoconductive switch gap on the integrated structure was measured to be $\sim 2 \text{ M}\Omega$. This was much lower than the $\sim 500 \text{ M}\Omega$ dark resistance measured earlier for the photoconductive switch material without the 2DES structure.

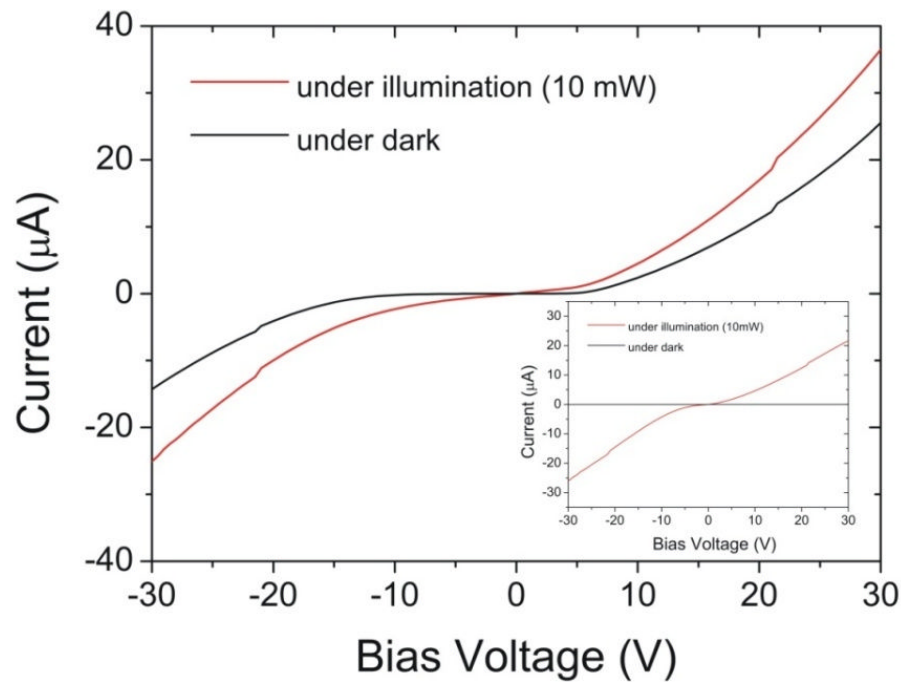


Figure 2.26 Main figure: the DC characteristics of one of the four switch gaps defined on the surface of the monolithically integrated LT-GaAs layer, measured in terms of current generated with respect to the applied bias in dark and illumination conditions. Inset: the DC characteristics of the switch gap defined on the surface of the reference structure (i.e. containing the LT-GaAs with no 2DES, as shown in Figure 2.1(a)) under similar conditions.

The pulse generation and transmission measurements were then carried out to observe carrier lifetimes and intensity of ps timescale electrical transients generated using the LT-GaAs layer within the integrated structure. Figure 2.27 shows the generated (input) and the transmitted (output) pulse measurement performed using pump-probe arrangement. The pump-probe beam powers throughout the measurement were kept at 10 mW with switch bias of 20 V applied at the pump switch.

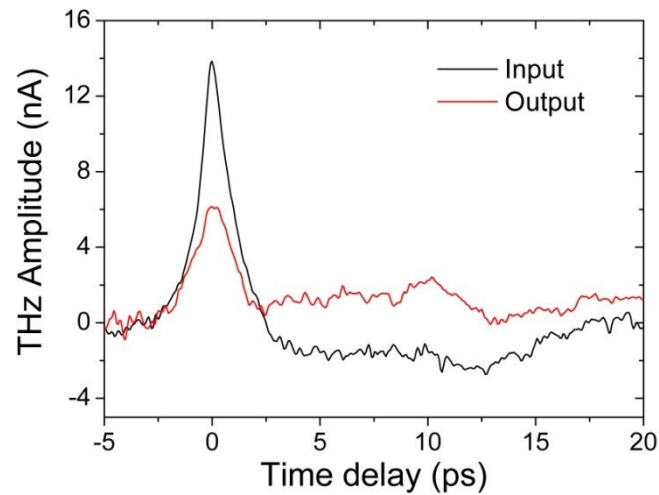


Figure 2.27 Experimental data of the THz pulses propagating along the CPW defined on the surface of the monolithically integrated LT-GaAs layer. The measurement show the time-domain ps pulse comparison observed at the input of the device (prior to the propagation down the CPW) and the device output.

The time-domain THz signal amplitudes observed (for input and output pulses) along the CPW demonstrated a poor performance of the LT-GaAs photoconductive layer within the integrated structure (having 2DES and low-resistance conducting layer in parallel) as compared to the LT-GaAs structure demonstrated earlier without the 2DES heterostructure (discussed in section 2.2). A tabulated comparison of the measured LT-GaAs photoconductive layer properties between the LT-GaAs structures with and without the 2DES is shown in Table 1.

LT-GaAs structure	Dark current amplitude at 20 V switch bias (μA)	Generated photocurrent amplitude at 20 V switch bias (μA)	Transmitted THz peak amplitude at 20 V switch bias (nA)	Signal-to-noise ratio	Transmitted pulse duration (ps)
First generation integrated structure (LT-GaAs with 2DES)	12.6	18.5	6	20:1	3
Reference LT-GaAs structure (with no 2DES)	0.059	13.5	70	500:1	3.2

Table 1 LT-GaAs heterostructure and ps timescale transport properties measured from transmitted pulses along the CPW.

The deterioration and correspondingly poorer signal-to-noise ratio of the transmitted THz signal along the CPW patterned on integrated structure was anticipated due to the presence of the parallel conducting layer (at AlAs-GaAs cap interface). The low-resistance layer in close proximity to the waveguiding surface acts as a lossy ground plane, thereby attenuating or preventing the transmission of THz frequency electrical transients.

The properties observed for the LT-GaAs photoconductive material monolithically grown above the 2DES were found not to be ideal for integrating on-chip waveguides due to the transmission properties of the overlaid waveguide being affected by the unwanted formation of the electron system in close proximity.

2.4.2. Characterisation of 2DES

After observing the properties of the LT-GaAs photoconductive layer, the transport properties of the monolithically integrated 2DES were then independently characterised using Hall bar measurements. From the LT-GaAs characterisation, the parallel conducting layer realized at the AlAs/GaAs cap interface was found to affect the LT-GaAs properties as a photoconductive material. Hence, in order to observe the electron transport properties of the 2DES independently from the low-resistance parallel conducting layer, it was essential to selectively remove the latter without changing the properties of the 2DES. This was carried out by selective etching of the overlying LT-GaAs and AlAs layers. Since the Fermi energy of the structure is pinned at the mid-gap, the etching process will result in raising the conduction band edge above the Fermi energy, thereby resulting in depopulation of the unwanted electron layer induced in parallel to the 2DES. The Hall bar geometry as illustrated in Chapter 1, Section 1.4 and as shown in Figure 1.8, was then fabricated on top of the exposed GaAs/AlGaAs

heterostructure surface (see Appendix 1-2, for selective etching and Hall bar fabrication details).

To assess the carrier transport co-efficients such as sheet density n_s and carrier mobility μ , magneto resistance measurements in the quantum Hall regime were then carried out at 1.4 K. Figure 2.28 shows the observed diagonal and Hall component of 2DES resistivity using a typical four-terminal resistance measurement configuration. Using Equation 1.9 and 1.10 which shows the dependence of electron transport coefficients on the measured resistivities, the sheet density of the 2DES was found to be $1.57 \times 10^{11} \text{ cm}^{-2}$ with electron mobility of $70.5 \times 10^3 \text{ cm}^2/\text{Vs}$.

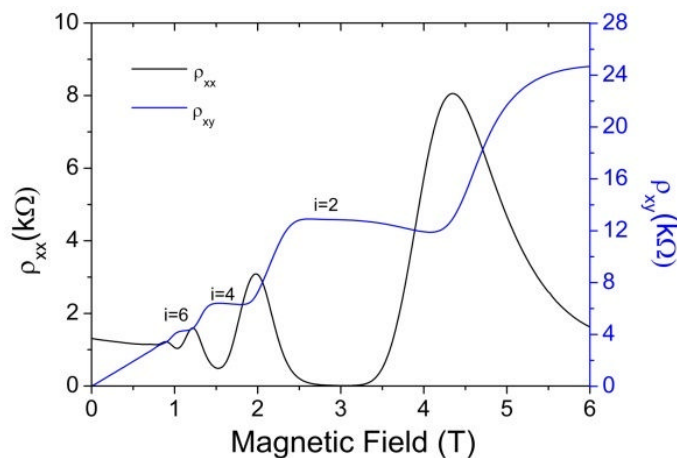


Figure 2.28 Experimental data for the dark measurement of Hall (ρ_{xy}) and diagonal (ρ_{xx}) resistivity of the first generation monolithically integrated 2DES, taken using a four-terminal Hall bar device configuration at 1.4 K.

The transport properties of the 2DES were re-measured to observe its dependence due to photo excitation. Figure 2.29 shows the four-terminal resistivity measurement at 1.4 K after illumination with 800 nm wavelength radiation (using a LED). As demonstrated earlier by Reed *et al* [110], both the measured diagonal and Hall component of the 2DES resistivities showed decrement by illuminating the Hall bar

sample. The altered sheet density and carrier mobility were found to be $3.44 \times 10^{11} \text{ cm}^{-2}$ and $295 \times 10^3 \text{ cm}^2/\text{Vs}$.

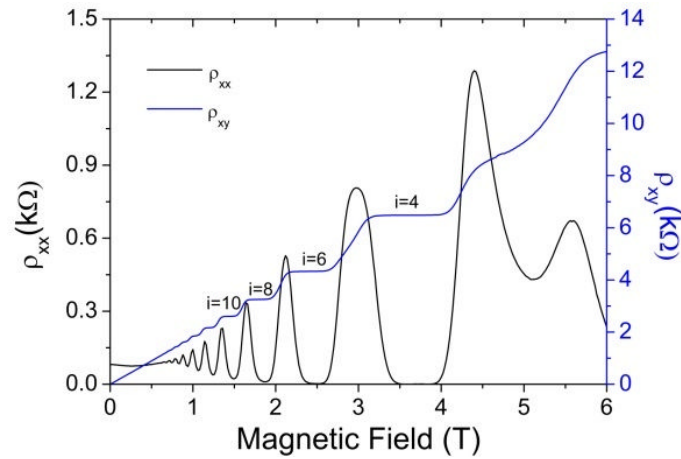


Figure 2.29 Experimental data for the light (after illumination) measurement of Hall (ρ_{xy}) and diagonal (ρ_{xx}) resistivity of the first generation monolithically integrated 2DES, taken using a four-terminal Hall bar device configuration at 1.4 K.

The 2DES properties confined within the integrated structure (after etching the top LT-GaAs and AlAs layers) showed similar sheet density and carrier mobility to a second reference GaAs/AlGaAs heterostructure grown to identical design but without the LT-GaAs-AlAs layers grown on top, thereby demonstrating uncompromised performance of the 2DES by the integrated growth approach.

To summarize the performance of the first generation monolithically integrated structure, both the 2DES and the LT-GaAs properties were found to be affected by the formation of a parallel low-resistance conducting layer, which was unintentionally induced during the integrated growth process. However the 2DES properties assessed after the removal of the overlaid layers showed uncompromised performance.

2.5. Second generation of monolithic integrated structures

Following the full characterisation of the first generation integrated structure containing both the 2DES and the LT-GaAs; a second generation heterostructure with modifications in the order of the layer structure was proposed and grown using MBE. Figure 2.30 shows the detailed schematic of the epitaxially grown layer structure.

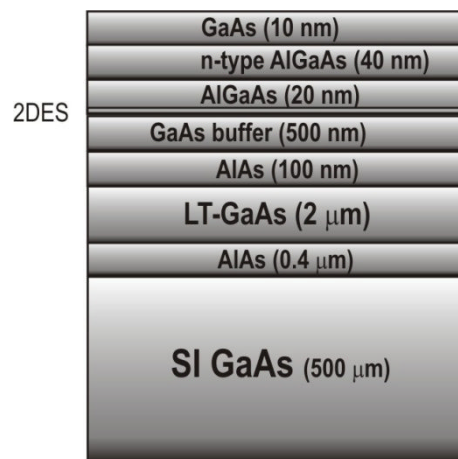


Figure 2.30 Schematic of the MBE grown layer structure used for the second generation monolithic integration of the LT-GaAs photoconductive layer with the 2DES heterostructure.

As shown for this generation of the integrated structure, the LT-GaAs photoconductive layer with the AlAs optical barrier layer is grown first on the SI GaAs substrate, followed by the epitaxial overgrowth of the GaAs/AlGaAs heterostructure containing the 2DES. This modification was carried out in order to avoid forming an additional conducting electron layer in close proximity to the 2DES and the LT-GaAs. The conduction band profile simulation results for the second integrated structure design, illustrating the carrier distribution as a function of depth into the wafer, is shown in Figure 2.31. It is clearly noted from the carrier distribution that the parallel

conducting electron layer that was observed in the previous generation (as shown in Figure 2.25) has now been eliminated by the modified layer structure.

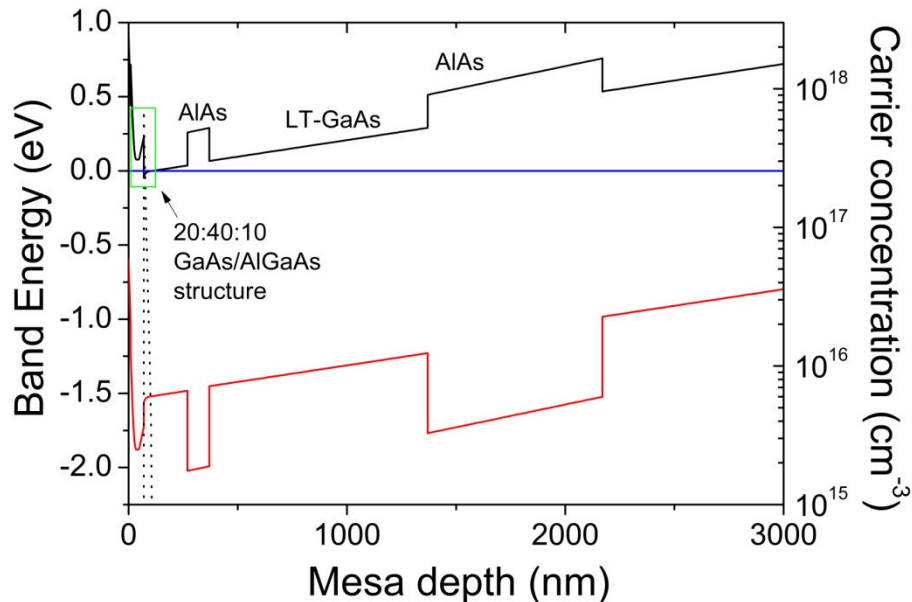


Figure 2.31 Simulated conduction band profile showing the distribution of carrier concentration across the layer structure for the second generation monolithic integration of LT-GaAs layer below the 2DES heterostructure.

However, the MBE growth process for successful monolithic integration of the 2DES on top of the LT-GaAs layer proved to be more complicated than the previous structure due to the temperature variation through the growth process. Since, the 2 μm thick LT-GaAs layer was grown on 400 nm AlAs layer at 215 $^{\circ}\text{C}$, the following high temperature growth (~ 600 $^{\circ}\text{C}$) of the 2DES heterostructure on top effectively annealed the LT-GaAs, thereby increasing the carrier lifetimes in the photoconductive layer.

Also a direct dependence of the growth and the structural properties of the LT-GaAs layer on the crystallinity of the overgrown layers were observed, as previously demonstrated in the literature [111-113]. It was found that the lattice parameter of the over layer structure changes depending on the growth temperature and critical thickness d_c of the LT-GaAs layer. Growth of an LT-GaAs layer with thickness greater than d_c can

cause a polycrystalline formation of the 2DES heterostructure. Previous estimations of d_c are of the order of 0.1-3 μm for the LT-GaAs layers grown at low-temperatures $\sim 200^\circ\text{C}$ [112].

After several growth iterations of the monolithic integrated structure, the growth temperature and the thickness of the LT-GaAs layer were optimized to avoid polycrystalline growth of the 2DES heterostructure above and also to maintain photo-generated carrier lifetimes in ps timescales.

2.5.1. Characterisation of 2DES

In this generation of the integrated structure, as the 2DES was easily accessible through the top surface, the electron transport properties of the 2DES was first characterised using standard four-terminal Hall bar measurements. As before, the Hall bar geometry together with the ohmic contacts was fabricated on top of the GaAs cap surface.

The magneto resistance measurement in the quantum Hall regime carried out at 1.4 K demonstrating the behavior of the diagonal and Hall resistivity is shown in Figure 2.32. The sheet density and carrier mobility extracted from the 2DES resistivity measurements under dark conditions were found to be $3.65 \times 10^{11} \text{ cm}^{-2}$ and $500 \times 10^3 \text{ cm}^2/\text{Vs}$. The corresponding sheet density and mobility measured from magneto resistance measurements after illumination (as shown in Figure 2.33) were found to be $6.3 \times 10^{11} \text{ cm}^{-2}$ and $900 \times 10^3 \text{ cm}^2/\text{Vs}$.

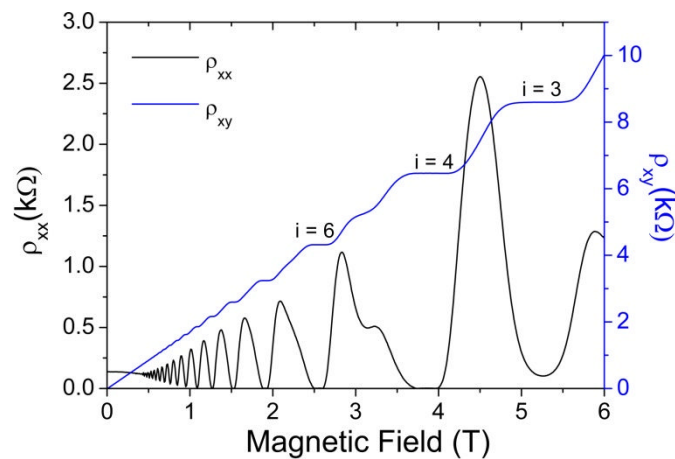


Figure 2.32 Experimental data for the dark measurement of Hall (ρ_{xy}) and diagonal (ρ_{xx}) resistivity of the second generation monolithically integrated 2DES, taken using a four-terminal Hall bar device configuration at 1.4 K.

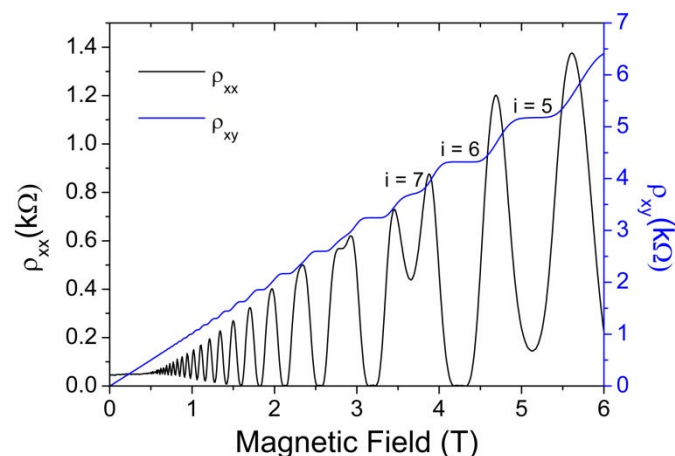


Figure 2.33 Experimental data for the light (after illumination) measurement of Hall (ρ_{xy}) and diagonal (ρ_{xx}) resistivity of the second generation monolithically integrated 2DES, taken using a four-terminal Hall bar device configuration at 1.4 K.

The transport coefficient measurements for the monolithically integrated 2DES above the LT-GaAs photoconductive layer showed a six-fold increase in carrier mobility as compared to the 2DES confined in the previous monolithic integrated structure. In this particular case, the performance of the 2D electron layer was also found to be considerably better than the reference GaAs/AlGaAs based 2DES with no monolithically integrated LT-GaAs layer. Hence, the 2DES in the second generation

monolithic integrated structure was found to be ideal for ps timescale electron transport studies using integrated on-chip waveguides.

2.5.2. Characterisation of photoconductive layer

For the second generation integrated structure, in order to characterize the monolithically integrated LT-GaAs properties as a photoconductive layer, it was essential to expose the LT-GaAs surface by selectively etching away the overlying layers (the details of the selective etch process is shown in Appendix 3). Following the removal of the overlying structure, the CPW design geometry as shown earlier in Figure 2.1 (b) was overlaid on top of the exposed LT-GaAs surface.

The I-V characteristics of one of the four identical photoconductive switch gaps used for ps pulse generation and detection propagating along the CPW are shown in Figure 2.34. The inset of the Figure shows a comparable I-V measurement previously carried out across a identical switch geometry overlaid on the reference structure (i.e. LT-GaAs heterostructure without the 2DES).

Under similar bias and illumination conditions, a clear similarity was seen in terms of the photocurrent amplitude generated in the LT-GaAs photoconductive switch gap based on structures integrated with or without the 2DES. Also the dark resistance of the LT-GaAs switch after removing the overlaid 2DES was found to be very similar ($\sim 550 \text{ M}\Omega$) to that of the LT-GaAs switch based on the reference structure ($\sim 500 \text{ M}\Omega$).

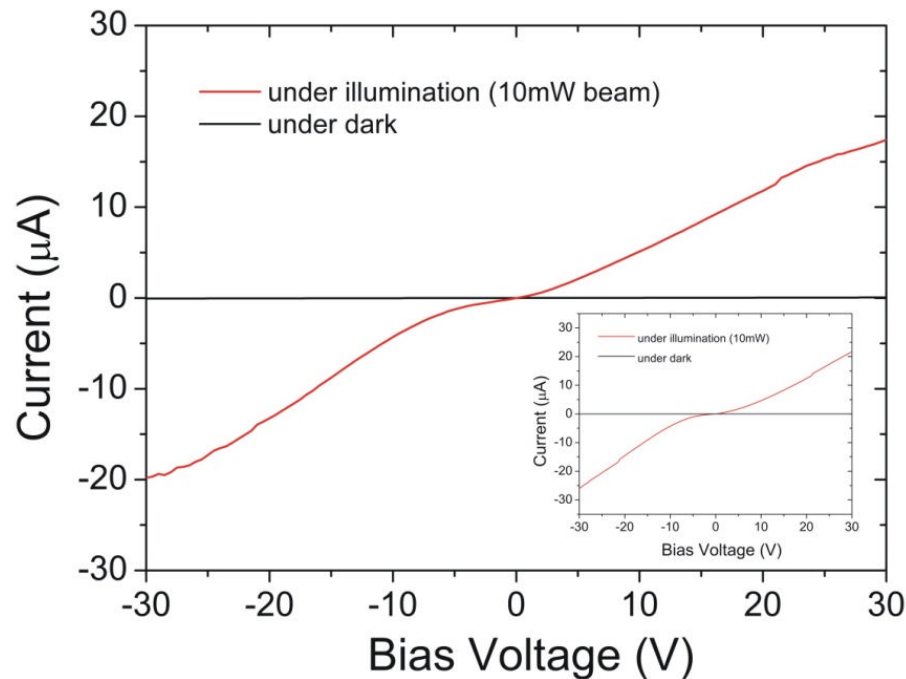


Figure 2.34 Main figure: the DC characteristics of one of the four switch gaps defined on the exposed surface of the monolithically integrated LT-GaAs layer, measured in terms of current generated with respect to the applied bias in dark and illumination conditions. Inset: the DC characteristics of the switch gap defined on the surface of the reference structure (i.e. containing the LT-GaAs with no 2DES, as shown in Figure 2.1(a)) under similar conditions.

The following ps pulse generation and transmission measurements were then carried out to characterize the properties of the CPW. As before, the pump-probe beam powers throughout the measurement were kept at 10 mW with switch bias of 20 V applied at the pump switch. Figure 2.35 shows the generated (input) and the transmitted (output) pulse measurement performed using the pump-probe arrangement. As shown, the input THz peak amplitude was measured to be ~ 120 nA with pulse duration of 2.4 ps, while the output pulse peak amplitude was measured to be 94 nA with pulse duration of 3.8 ps.

The input and output pulse measurements showed a great resemblance to the signals observed with a similar geometry CPW based on the reference structure with no 2DES.

The comparison of these properties, as tabulated in Table 2, showed uncompromised performance of the LT-GaAs photoconductive layer for on-chip THz generation and detection after its monolithic integration with the 2DES.

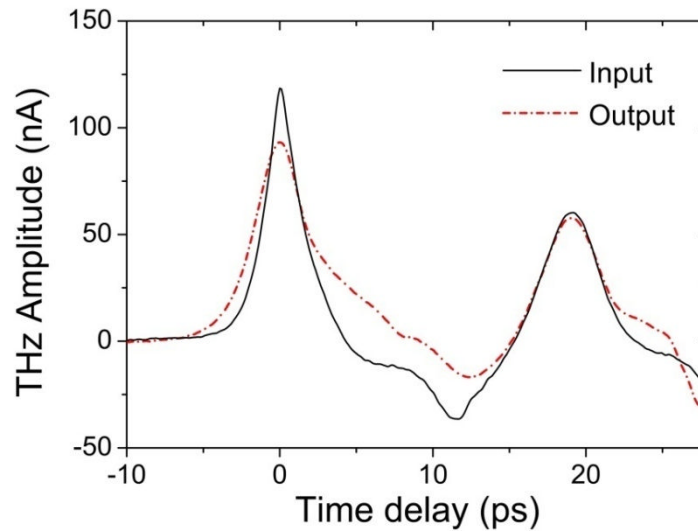


Figure 2.35 Experimental data of the THz pulses propagating along the CPW defined on the exposed surface of the monolithically integrated LT-GaAs layer. The measurement show the time-domain ps pulse comparison observed at the input of the device (prior to the propagation down the CPW) and the device output.

LT-GaAs structure	Dark current amplitude at 20 V switch bias (μA)	Generated photocurrent amplitude at 20 V switch bias (μA)	Transmitted THz peak amplitude at 20 V switch bias (nA)	Signal-to-noise ratio	Transmitted pulse duration (ps)
Second generation integrated structure (LT-GaAs with 2DES)	0.055	18.5	90	500:1	3.8
First generation integrated structure (LT-GaAs with 2DES)	12.6	18.5	6	20:1	3
Reference LT-GaAs structure (with no 2DES)	0.059	13.5	70	500:1	3.2

Table 2 LT-GaAs heterostructure and ps timescale transport properties measured from transmitted pulses along the CPW.

2.6. Summary

This chapter has given a brief overview of the performance of LT-GaAs photoconductive material within on-chip THz CPWs using THz-TDS. The characteristic measurements showing the performance of the LT-GaAs photoconductive layer for on-chip THz generation and detection, together with the ps pulse transmission properties of the overlaid CPW were consequently understood prior to integration with a 2DES.

A detailed discussion on the execution of various methods that permits incorporation of on-chip THz CPWs in close proximity with the confined electron system was also presented. Initial implementations of previously established methods in the literature were not found to be ideal due to the overall complexity in the ‘post-fabrication’ assembly and also the limited sensitivity achieved in interacting the electric field of the ps pulses travelling along the waveguide with the adjacent 2DES.

Out of the two methods that were later proposed and implemented to overcome the complexity issues in the assembly of the THz waveguides with the 2DES, the monolithic integration approach showed the greater potential for application in this work. The properties of the monolithic approach, such as ‘pre-fabrication’ assembly of the LT-GaAs with the 2DES, allows the on-chip THz waveguides with photoconductive switches to be processed with the in-plane adjacent 2DES. This significantly increases the sensitivity of the ps timescale measurement of the 2DES as compared to previous methods demonstrated in the literature. Also, the independent characterisation of both the LT-GaAs and the 2DES layers allowed the optimization of their performances by modifying the monolithic growth parameters, thereby successfully achieving an undiminished performance following monolithic integration of both layers.

The material covered in this chapter completes the necessary background for the remainder of this thesis, which will describe an investigation of the characteristics of on-chip THz CPWs at cryogenic temperatures and under magnetic fields and their application to studying ps timescale electron transport in a 2DES using the established monolithic integrated structures.

Chapter 3: THz generation and detection at Milli-Kelvin temperatures and under magnetic fields

3.1. Introduction

This chapter will describe the first attempts within this project to perform on-chip THz spectroscopic measurements at milli-Kelvin temperatures and in high magnetic fields. The methodology follows that described in Chapter 2, where a coplanar waveguide is used to support the propagation of THz electrical pulses. In order to obtain quantitative information about the 2DES from ps pulse interaction measurements using planar waveguides, it was first necessary to understand the pulse transmission properties of the waveguides without the 2DES present under similar environments. This was achieved by using a LT-GaAs substrate for the coplanar waveguide, which is relatively non-conductive and which supported the propagation of conventional waveguide modes [114]. The THz waveguides were first characterised at room temperature by the pulsed THz-TDS technique described in Chapter 2, Section 2.2. However for milli-Kelvin measurements, the NIR laser beams were coupled to standard optical fibers inserted into the dilution fridge, to illuminate the photoconductive switches. This technique removed any need for optical access windows for the laser beams. Section 3.2 describes in detail the experimental setup and methodology used to perform these measurements. This

work also gave rise to a new technique for dynamic imaging of the photoconductive switches, the results of which are also presented.

3.2. Experimental setup

This section briefly outlines the operation of the $^3\text{He}/^4\text{He}$ dilution refrigerator. Details about the experimental setup used for on-chip THz transmission measurements, including the use of optical fibers, are also described, followed by a description of structure and geometry of the coplanar waveguide devices used for this work.

3.2.1. $^3\text{He}/^4\text{He}$ dilution refrigerator

The conventional cryostats achieving operation temperatures in the range 300 K to 1 K utilize liquid cryogens such as ^4He . Pumping on ^4He enables temperatures down to about 1 K to be reached [115]. The P-T phase diagram of ^4He is shown in Figure 3.1.

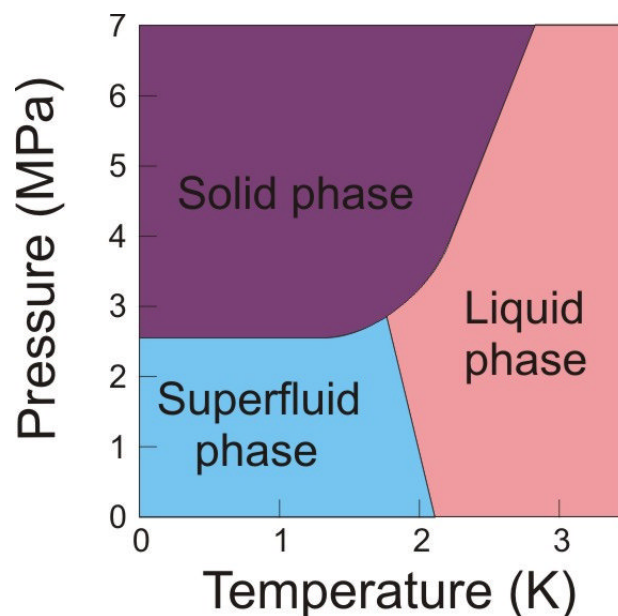


Figure 3.1 P-T phase diagram of ^4He .

The lighter isotope of helium, ^3He , is used only to achieve the lowest temperatures in this range; it is very scarce and highly expensive. The dilution refrigerator takes advantage of the peculiar low-temperature behavior of the ^3He - ^4He mixtures. When a mixture of two stable isotopes of helium is cooled below a tri-critical temperature, it separates into two phases. The concentration of ^3He in each phase depends upon the temperature. Since the enthalpy of the ^3He in the two phases is different, the evaporation of ^3He from the concentrated phase into the dilute phase provides the cooling power of the dilution fridge. The phase diagram of ^3He - ^4He mixtures is shown in Figure 3.2 [115].

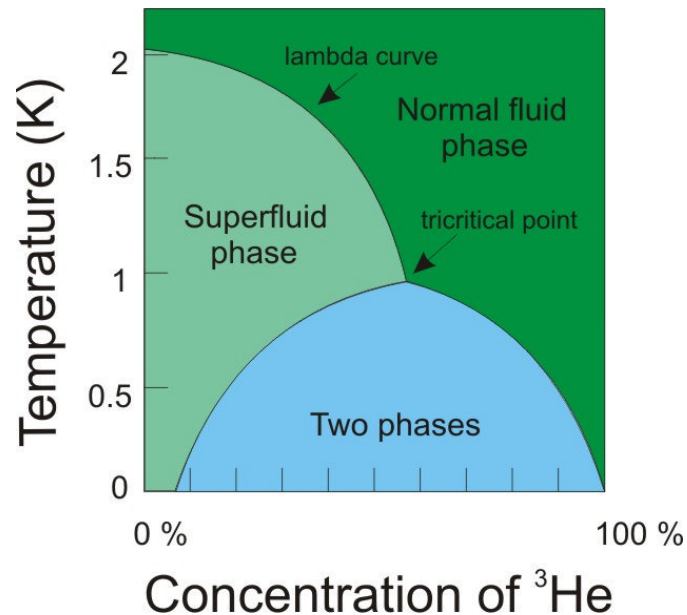


Figure 3.2 Phase diagram for ^3He - ^4He mixtures.

The concentrated phase is rich in ^3He and lighter than the dilute phase (^4He). The concentrated phase of the mixture composes mainly liquid ^3He , and the dilute phase consists of ^3He gas. The ^4He which composes majority of the dilute phase is inert, so the ^3He gas moves through the liquid ^4He without interaction. The formation of ^3He gas from the ^3He liquid takes place at the phase boundary in the mixing chamber of dilution

fridge. This process continues to work even at the lowest temperatures, as the equilibrium concentration of ^3He in the dilute phase is finite as the temperature approaches absolute zero.

The dilution refrigerator that is used for this work is shown in Figure 3.3. It consists of an integrated pulse tube cooler, a gas handling system and a compressor for the pulse tube. With cooling power of over $200\ \mu\text{W}$ at temperature of $100\ \text{mK}$, it can reach a base temperature $< 10\ \text{mK}$. The integrated superconducting cryo-free magnet can reach high fields up to $12\ \text{T}$.

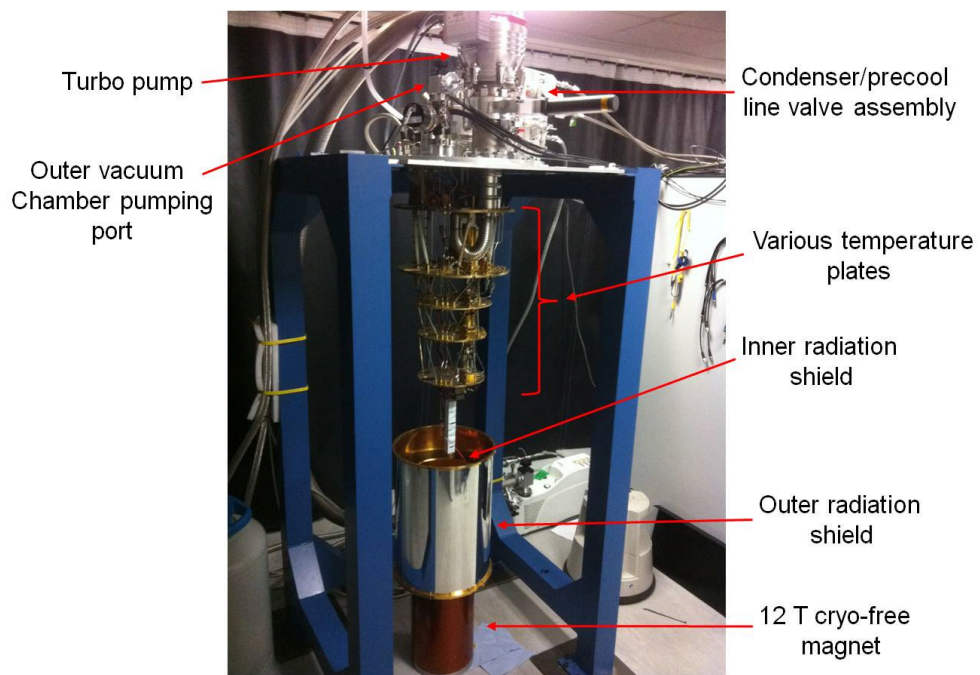


Figure 3.3 Oxford instruments DR 200 cryo-free dilution refrigerator.

During the pre-cooling procedure, the pulse tube cooler is used to condense the $^3\text{He}/^4\text{He}$ mixture into the dilution unit. It does not cool the mixture sufficiently to form the phase boundary but simply to bring it to $1.2\ \text{K}$. In order to get phase separation, the temperature should fall below the tri-critical point at $0.86\ \text{K}$. This cooling is provided by the still; it cools the incoming ^3He before it enters the heat exchangers and the mixing

chamber. Gradually, the rest of the dilution unit is cooled to the point where phase separation occurs. Figure 3.4, indicates the different critical temperature regions inside the dilution unit. It is important for the operation of the dilution refrigerator that the ^3He concentration and the volume of the mixture is chosen correctly, so that the phase separation occurs inside the mixing chamber.

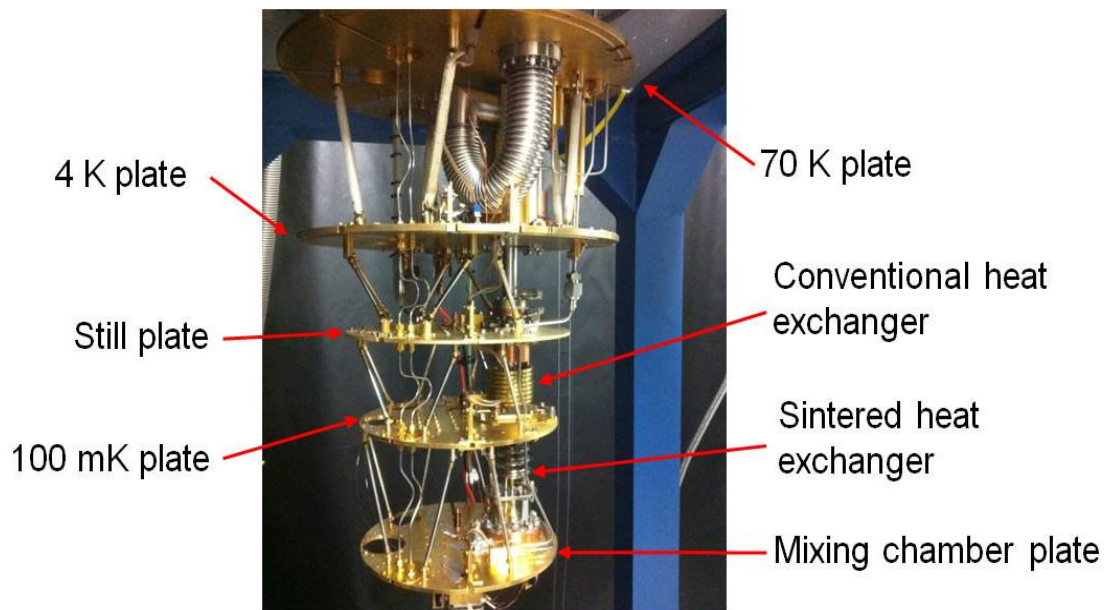


Figure 3.4 Diagram of various critical temperature plates inside the dilution unit.

For continuous operation, the ^3He must be extracted from the dilute phase to prevent saturation and resupplied to concentrated phase keeping the system in dynamic equilibrium. The ^3He is pumped away from the liquid surface in the still, which is typically maintained at 0.6-0.7 K, and the ^3He leaving the mixing chamber is used to cool the returning flow of concentrated ^3He in a series of heat exchangers. In the regions where the temperature is below 50 mK, conventional counter flow heat exchangers are not very efficient and so special sintered heat exchangers are used for this purpose as shown in Figure 3.4.

A room temperature vacuum pumping system is used to remove the ^3He from the still and compress it before passing it through impurity removing filters and cold traps (at 77 K). The gas is returned to the cryostat, where the mixture is pre-cooled by the pulse tube cooler. Primary impedance is used to maintain high enough pressure for the gas to condense.

The experimental apparatus is mounted on the mixing chamber plate (shown in Figure 3.4), ensuring that it is in good thermal contact with the dilute phase. For the experiments carried out at higher temperatures, the mixing chamber can be warmed by applying heat directly to the mixing chamber.

3.2.2. Photonic crystal fibers

The key reason for using optical fiber coupling for photoconductive sampling in dilution fridge is to avoid the need for optical access windows, which would admit 300 K black body radiation and cause unwanted thermal loading. The access window materials that transmit at the laser wavelength $\lambda = 810$ nm are transparent to large portions of the thermal black body spectrum that peaks near $10\ \mu\text{m}$. For example, the thermal loading from a 300 K black body looking through a 1 cm radius quartz window at 77 K is calculated to be 7 mW [116]. Hence optical fibers are a suitable alternative for laser radiation coupling in this work.

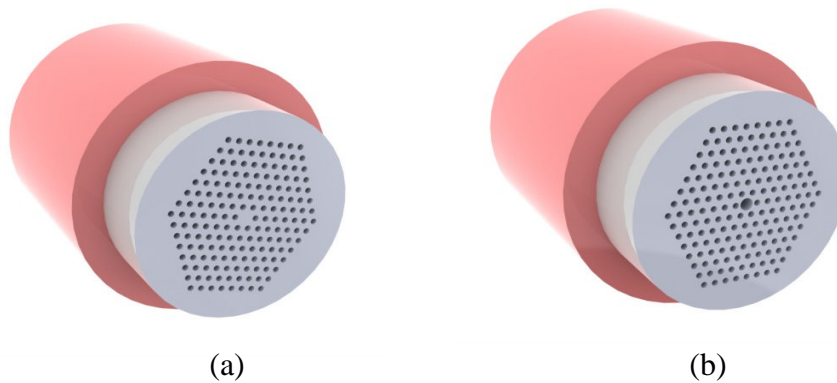


Figure 3.5 Cross-section schematic, showing structure of (a) Solid core and (b) Hollow core optical fibers.

At first, both solid core silica and hollow core fibers were considered. The schematic of the structure of these fibers is shown in Figure 3.5. Both of these fibers offered important properties such as single-mode transmission and extreme non-linearity. The solid core fibers are similar to conventional fibers, typically known as high index guiding fibers, guide light in a solid core, usually pure silica. Total internal reflection is caused by the lower refractive index in the air-filled region. On the other hand, hollow core fibers typically known as low index guiding fibers, guide light by the photonic bandgap (PBG) effect. The periodic microstructure in the fiber cladding results in a photonic bandgap, where light of certain wavelengths cannot propagate; hence the light is confined to the low index core as the PBG effect makes propagation in the microstructured cladding region impossible.

For this work, the transmission properties of each of these fibers, including optical beam intensity and dispersion of spectral components, were tested independently using an interferometric autocorrelation measurement. The system diagram of the experimental arrangement is shown in Figure 3.6. As shown in the schematic, the pulsed NIR laser beam from the Ti:sapphire laser is passed along through a pair of neutral density (ND) filters via paths 1-4 and focused into the central core of the fiber with a diameter of $\sim 6 \mu\text{m}$. For preliminary tests, a 1 meter long fiber was used, and its ends were carefully sheathed and cleaved for beam coupling. The optical power of the laser beam was kept limited to 10 mW in order to avoid causing damage to the central core. Also, a half-wave plate retarder is used in order to overcome polarization dispersion in the optical fibers, resulting from the finite refractive index of the optical medium. The coupling ends of the fiber were mounted on a linear x direction translation stage in order to optimize beam coupling from the focusing lens.

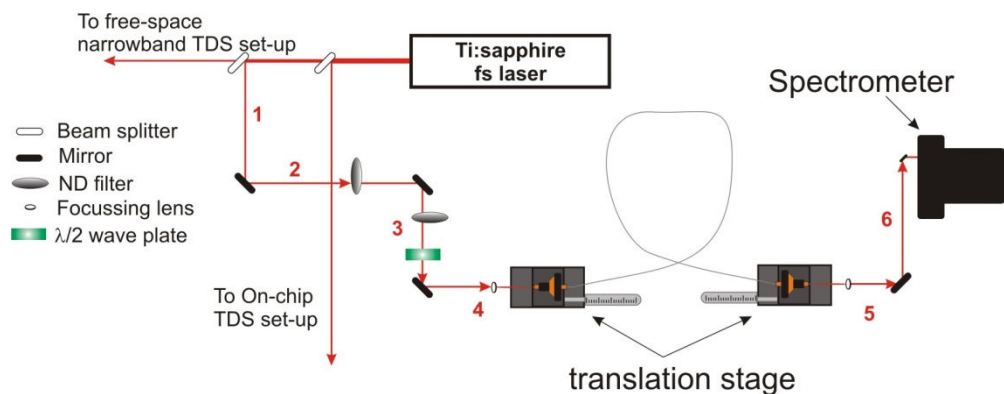


Figure 3.6 Diagram of optical setup used for testing optical fibers.

The efficiency of coupling in both solid core and hollow core fibers after careful alignment was measured to be around 70 %. The pulse duration measured through a 1 m long zero dispersion, single mode hollow core fiber is shown in Figure 3.7. The pulse duration measured after travelling through the fiber was compared directly with the

autocorrelation of the free space femtosecond laser pulse. It was demonstrated for hollow core fibers that the transmitted pulse duration of the laser beam with centre wavelength of ~ 810 nm was not affected; this result was found to be consistent for fiber lengths up to 10 m. As a result, using hollow core fibers for guiding laser beam pulses in the cryostat would not require any external dispersion compensation.

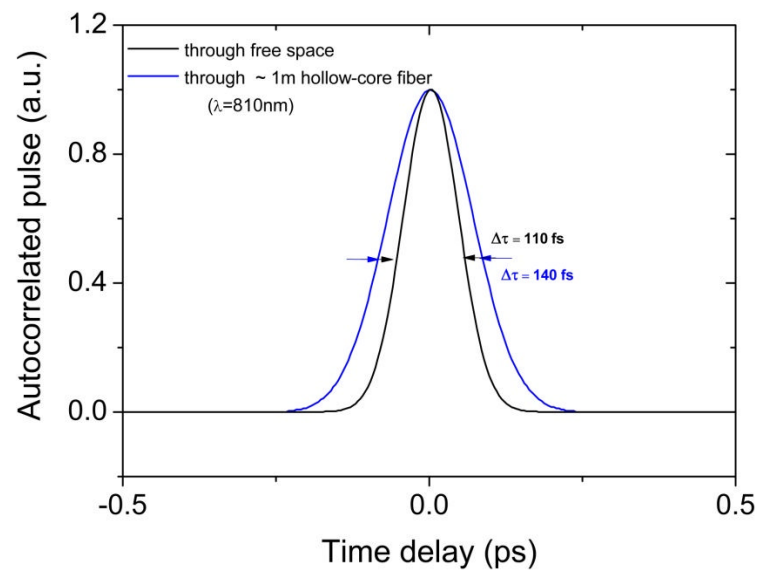


Figure 3.7 Experimental data showing the comparison of pulse duration at $\lambda \sim 810$ nm, between a free space laser pulse and a transmitted laser pulse through a ~ 1 m long hollow core fiber.

However, the zero dispersion property of the hollow core fiber was found to be wavelength dependent. The refractive index of the periodic microstructure in the fiber cladding would alter for different wavelengths, thereby deviating the pulse dispersion from a zero value [117]. A clear demonstration of the pulse being dispersed is seen in Figure 3.8, when the centre wavelength was altered from ~ 810 nm to ~ 780 nm.

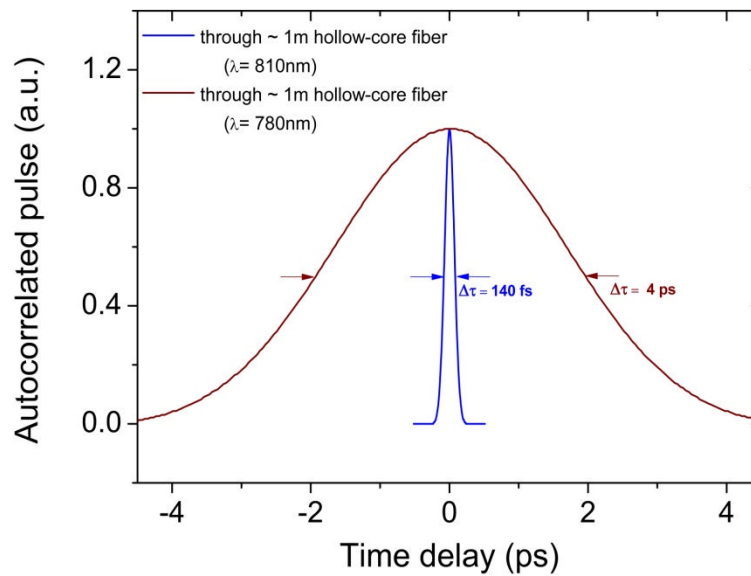


Figure 3.8 Experimental data showing the comparison of laser pulse durations for transmission through a ~1 m long hollow core fiber at two different wavelengths ($\lambda \sim 780$ and 810 nm).

The 1 m long hollow core fiber was then replaced by similar length solid core silica fiber. Figure 3.9 shows the transmitted pulse duration measured through the fiber and compared with a free space femtosecond laser pulse. The refractive index of the solid core silica glass induces negative dispersion on laser pulses at ~810 nm wavelength. This meant that the longer wavelengths travel faster than the shorter wavelengths, as a result causing optical pulses of high bandwidth to broaden in time. It was noted that the dispersion of pulse duration was strongly dependent on the length of the solid core fiber (for both wavelengths, $\lambda = 780$ nm and $\lambda = 810$ nm). This material dispersion is acceptable for experiments where relatively long pulses (several picoseconds) are used, however for the shorter pulses used for this work (~100 fs) this material dispersion was undesirable. In order to compensate for this dispersion, a Grating Dispersion Compensator (GDC) was required.

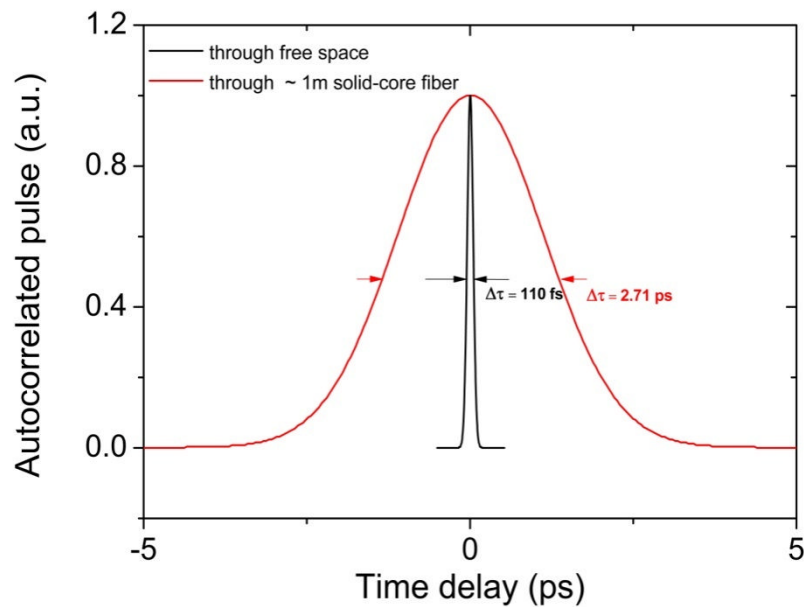


Figure 3.9 Experimental data showing the comparison of pulse duration at $\lambda \sim 810 \text{ nm}$, between a free space laser pulse and a transmitted laser pulse through a $\sim 1 \text{ m}$ long silica core fiber.

After studying the transmission properties of both types of optical fibers at room temperatures, hollow core fibers seemed an obvious choice to be used for guiding pulses in the cryostat, as they do not require external dispersion. However, when the tests were repeated at operating temperatures down to 77 K , it was observed that the hollow core fibers underwent physical contraction, which seriously affected the transmission properties. Conversely, the transmission properties of the solid core fibers remained unchanged at cryogenic temperatures. As a result, the solid core fibers were chosen for the purposes of this work. A GDC was designed for optimizing the pulse duration at the fiber's end.

The GDC used in the experimental setup as shown in Figure 3.10, employed 'Littrow' pulse compression, which uses two precisely designed blazed gratings. These gratings are usually fabricated by moulding the epoxy coated glass substrate. The first grating acts as a diffraction grating which separates out the wavelengths according to the grating relation as shown below in Equation 3.1, where m refers to the diffracted order,

d is the grating spacing, α is the incident angle with respect to the normal, and β is the diffracted angle.

$$m\lambda = d(\sin\alpha + \sin\beta) \quad (3.1)$$

Typically, only first-order diffraction from the Littrow arrangement is considered for dispersion compensation, as the power is diffracted preferentially into the first order. The wavelengths of the input pulse (~100 fs) are spread spatially and re-collimated by a second grating. The pre-chirped output pulse envelope is broadened in time (~25 ps). The natural (negative) dispersion of the silica core then recompresses the pulse. Using this technique, the subsequent pulse duration measured after passing through 10 m of solid core optical fiber was found to be reduced below ~300 fs. The main advantage of using the GDC is that it provides flexibility in using variable lengths of fiber, as the output pulse width is easily tuneable through the positioning of the second grating.

3.2.3. On-chip THz-TDS system

In order to operate THz coplanar waveguides at milli-Kelvin temperatures, an on-chip THz-TDS setup similar to the setup used for room temperature characterisation was used, as shown in Figure 3.10. The use of optical fibers is helpful to implement the pump-probe sampling measurements in a cryogenic environment with high magnetic fields. A pair of 10 m long solid core silica optical fiber was used to guide the pump and probe beams into the sample space of the dilution refrigerator. The horizontally polarized beam from the pulsed infrared Ti:sapphire laser (centre wavelength 800 nm, pulse duration 100 fs, repetition rate 80 MHz) was pre-chirped using GDC in order to compensate for the pulse dispersion in the fibers.

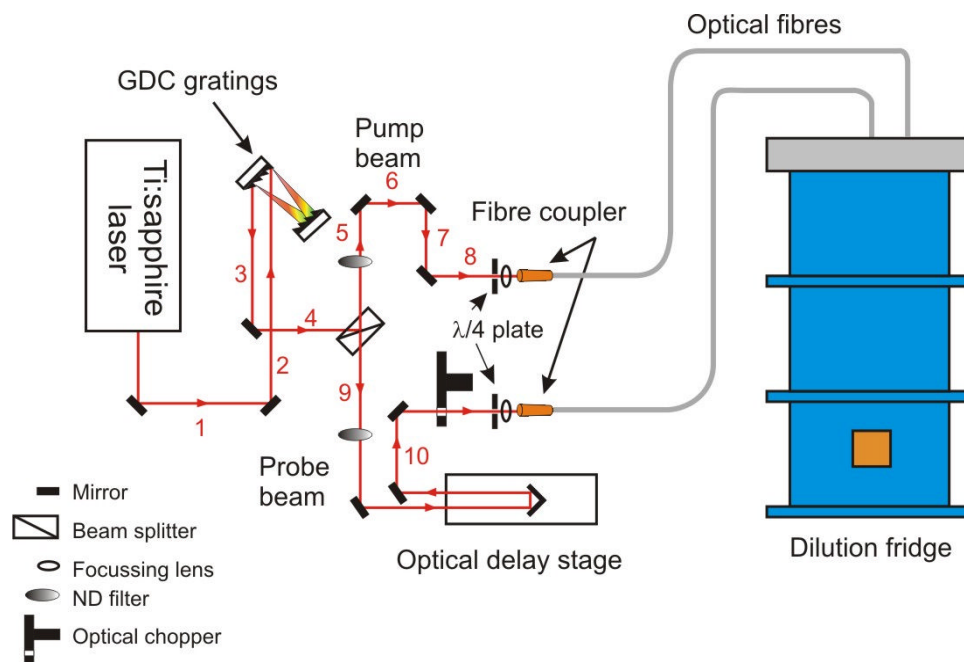


Figure 3.10 System diagram of THz-TDS used for operating on-chip waveguides at cryogenic temperatures. The 100 fs laser pulses from Ti:sapphire laser are beam split and compressed before being channelled down two optical fibers for accessing the dilution fridge.

The laser beam was then passed along a 45° angle beamsplitter as shown via paths 1-4 in Figure 3.10, where it is split into pump and probe sections. The pump beam passed along paths 5-8, and was focused directly onto central core of the optical fiber. The probe beam was passed along an optical delay line via paths 9-10 and through an optical chopper. It was then focused onto the central core of an identical optical fiber. The pair of optical fibers guiding pump and probe beams were coupled into the refrigerator through a top-access insert and were carried all the way to the mixing chamber plate.

Previous on-chip THz transmission studies at cryogenic temperatures by E. Shaner [98] demonstrated a method for gluing optical fibers directly to the photoconductive switches. This fixed arrangement of the fibers was trialed within this project, and worked satisfactorily at room temperature; however, at liquid helium

temperatures the thermal contraction during cooling caused misalignment of the laser beams and strongly affected the photoconductive excitation.

In order to avoid these limitations, a novel approach was demonstrated in this work. A cryogenic sample holder consisting of brass ferrules, free-space optics and piezo-electric stages was custom designed in order to focus the pump and probe beams from the optical fibers onto the appropriate photoconductive switches of the coplanar waveguide device. This technique enabled dynamic control over positioning of laser beams with sub-micron accuracy. The cryogenic sample holder used is shown in Figure 3.11 [83].

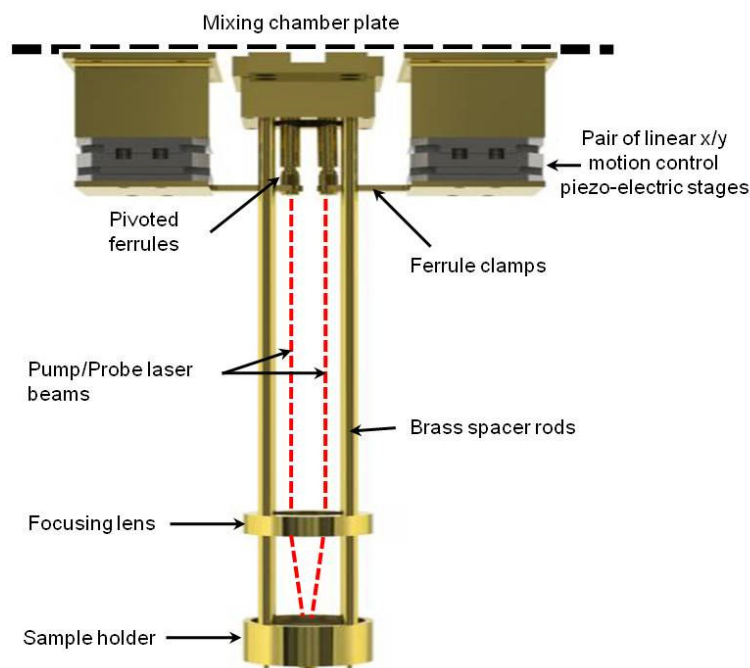


Figure 3.11 Illustration of the cryogenic sample holder used, together with the two pairs of piezoelectric stages for positioning and alignment of free space laser beams.

The fibers guiding the dispersion-compensated pump and probe beams are coupled inside brass ferrules which are pivoted at the bottom of the mixing chamber plate of the dilution refrigerator, around 30 cm above the on-chip THz system. An

aspherical lens fixed at the end of each of these ferrules is used to collimate the laser beams, while the free end of the ferrules is connected to two sets of crossed, linear piezo-electric stage pairs (one pair for each ferrule) via brass clamps as shown in Figure 3.11. This allowed micron-precision control in translating the laser beams across the plane of the sample surface. In order to maximize the optical excitation efficiency, the collimated pump and probe beams were focused onto the photoconductive switches using a focusing lens placed at a fixed height above the on-chip system.

3.2.4. On-chip THz waveguide devices

The transmission characteristics of THz microstrip and Goubau lines have already been explored extensively both at room temperatures and at low-temperatures by the present group at Leeds [4, 118]. However these transmission lines require a low dielectric permittivity substrate (e.g. quartz or BCB) and also the transfer of thin LT-GaAs films onto these substrates to enable photoconductive generation and detection.

The choice of the substrate for the present work was a 500 μm -thick GaAs wafer, which has a relative permittivity of ~ 12.9 for frequencies between 0.3-2.0 THz (much larger than quartz or BCB), hence it was more appropriate to use a coplanar waveguide as the transmission line. The GaAs substrate was used in this work, as LT-GaAs can easily be monolithically integrated onto it using MBE. The layers of this monolithic heterostructure are shown in Figure 3.12.



Figure 3.12 Schematic of LT-GaAs/AIAs/GaAs photoconductive heterostructure grown using MBE.

The metal coplanar waveguide was fabricated on the surface of the LT-GaAs photoconductive layer using UV lithography followed by thermal evaporation of a 20/200 nm thick Ti/Au layer. The centre Ti/Au strip acted as a signal conductor, and on both sides in close proximity, ground planes were placed. These ground planes guided the picosecond pulse of charge which was generated and detected by the photoconductive switches. The basic design for each device studied in this chapter is based on the parallel pump and probe layout described in Chapter 1, Section 1.6 and as shown in Figure 1.25. A total of four probe arms (or biasing electrodes) were integrated into the design, forming two pairs of photoconductive switches, to allow input and output measurements to be made. The length of the ‘active region’ of the CPW, also regarded as the length of transmission line between two switches was 1.2 mm, while its width was 30 μm. The ground plane separation from the signal conductor and electrodes was 20 μm, resulting in 50 Ω characteristic impedance for the waveguide (as calculated using Equation 1.20). The parasitic region of the transmission line was kept 2.48 mm. Using the phase velocity formulation as discussed in Chapter 1, Section 1.6, the parasitic region should considerably delay the pulse reflections from transmission line discontinuities, thereby giving an expected time-window of ~40 ps for THz pulse measurements.

Figure 3.13 shows one of the CPW device designs studied here (Sample 1). The enlarged view of the photoconductive switch (PCS) regions is shown in the inset, showing the separation gap between the transmission line and the biasing electrodes was $5\ \mu\text{m}$.

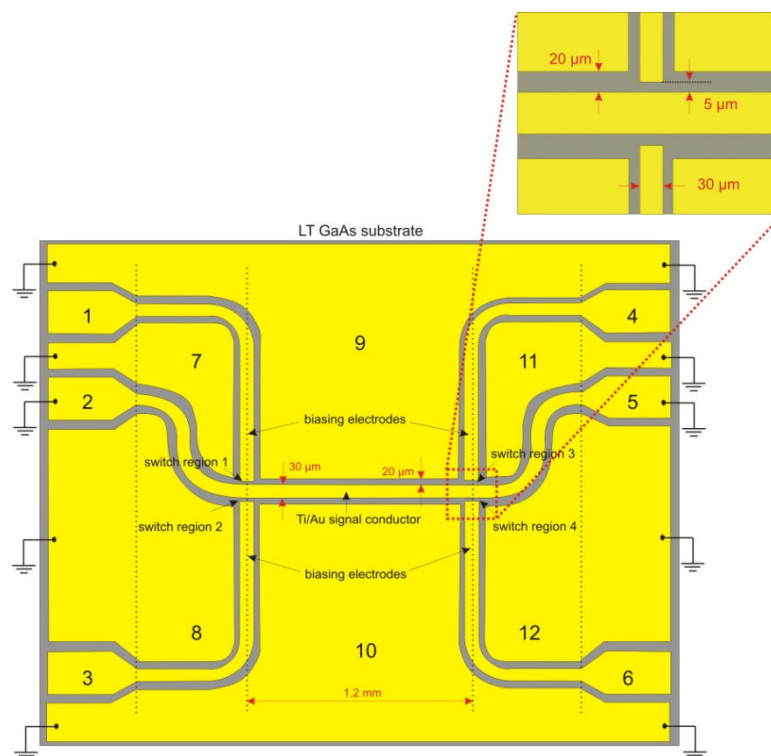


Figure 3.13 Main figure: Diagram of a THz coplanar waveguide device (Sample1) used in this work, containing a transmission line between contact pads (2 and 5) and four converging biasing electrodes defining simple PCS gap regions. Inset: Enhanced view of one of the four switch regions showing dimensions of the switch gap, transmission line and probe arms.

An alternative design of PCS geometry consisting of an interdigitated metal-semiconductor configuration was also studied for understanding the effect of switch geometries on the generation and detection of ps timescale electrical transient. As shown in Figure 3.14, a second CPW device design (Sample 2) was also investigated, employing an interdigitated arrangement of photoconductive switch (IPCS) gaps for the pulse detection switches. This work was undertaken in order to understand the effect of switch geometries on the amplitude and shape of the THz pulses, both at room and

cryogenic temperatures. Previous theoretical modelling studies of PCS gap geometries have shown a direct comparison between a simple PCS and IPCS gap [119].

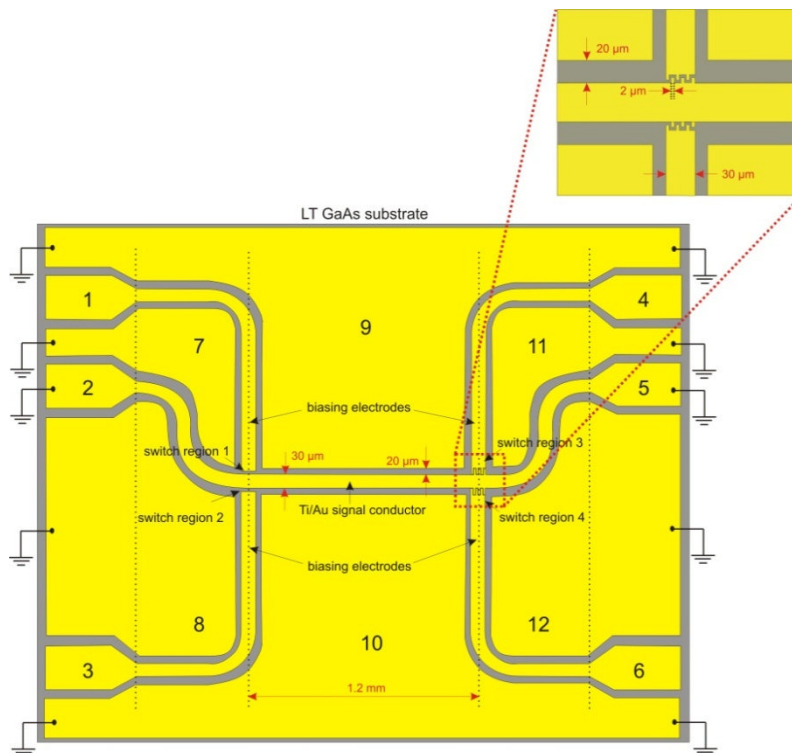


Figure 3.14 Main figure: Diagram of a THz coplanar waveguide device (Sample2) used, containing a transmission line between contact pads (2 and 5) and four converging biasing electrodes defining two simple PCS gap regions (pump switch) and two IPCS gap regions (probe switch). Inset: Enhanced view of one of the IPCS pairs showing dimensions of the switch gap, transmission line and probe arms.

As shown in the inset of Figure 3.14, for switch regions 3 and 4, the simple 5 μm switch gap between the transmission line and the biasing electrode is replaced with pair of interdigitated fingers. The dimensions of the finger width and gap spacing were kept identical to 2 μm.

The next two sections provide a detailed study of the operation of the two CPW device designs at both room and cryogenic temperatures. The comparison between simple PCS and IPCS gap characteristics is also discussed.

3.3. On-chip THz transmission studies at room temperature

The operation of the THz CPW devices was first examined at room temperature. This work also involved a consideration of the DC properties of PCSs integrated with waveguides, as they play an important role in the generation and detection of THz electrical transients. The LT-GaAs based photoconductive switches on two independent devices were thoroughly characterised on the basis of photo-carriers generated across the switch at both room and cryogenic temperatures.

3.3.1. DC characterisation of photoconductive switches

The biasing arrangement for measuring DC current across one of the switch region is similar to the one demonstrated in Chapter 1, Section 1.6 and as shown in Figure 1.18. The dark current measurements (with no laser beam focussed on the switch region) were measured to be negligible (in order of nA) due to the high dark resistivity of LT-GaAs. The photocurrent measurement at varying bias voltages on both pump and probe switches for varying laser beam intensity is shown in Figure 3.15(a) and 3.15 (b) for Sample 1, and Figure 3.16(a) and Figure 3.16(b) for Sample 2. The observed responses showed ohmic behaviour as expected [120]. The inset shows the response of current across the switch region with varying beam power at constant bias of 30 V, which was also found to be linear.

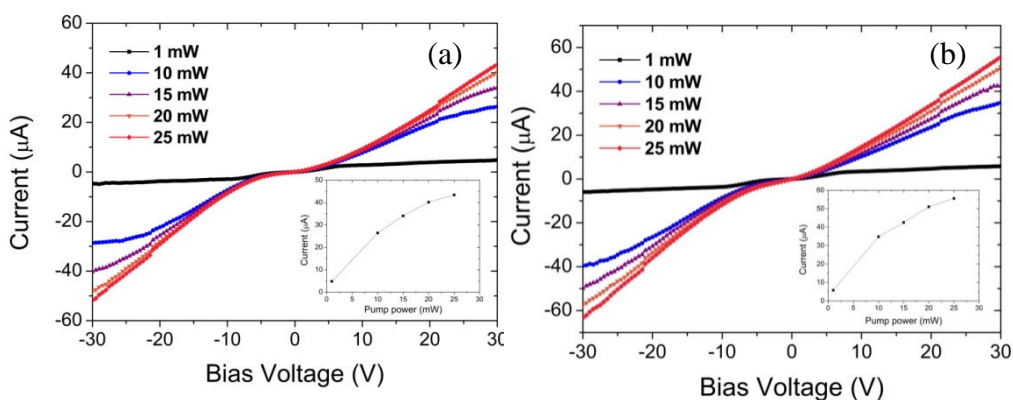


Figure 3.16 Main figure: Current versus applied voltage for Sample 1, for (a) the pump switch and (b) probe switch at varying laser powers. Inset: Current achieved at 30 V for each power.

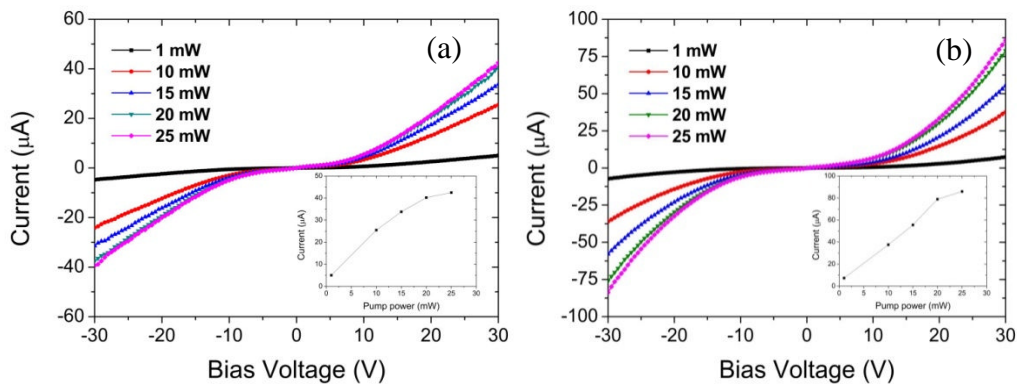


Figure 3.15 Main figure: Current versus applied voltage for Sample 2, for (a) the simple PCS gap pump switch and (b) IPCS gap probe switch at varying laser powers. Inset: Current achieved at 30 V for each power.

As shown in Figure 3.15, both pump and probe switch with simple PCS geometry for Sample 1 show similar photocurrent generation for equal biasing and illumination conditions, thereby demonstrating equal carrier generation across each switch. However for Sample 2, it is noted from Figure 3.16, that the photocurrent generated across the probe switch with IPCS geometry was ~ 1.5 times that across the pump switch with simple PCS geometry under equal biasing and illumination conditions. This result can be explained by the fact that the electric field density generated by applying bias to the switch is larger for IPCS because the smallest distance between the interdigitated electrodes is $2\ \mu\text{m}$, much smaller than the $5\ \mu\text{m}$ gap for the simple PCS geometry of the pump switch.

3.3.2. Input pulses

Having characterised the properties of PCS under varying biases and laser beam powers, the THz pulse transmission experiments were carried out on two devices using a room temperature THz-TDS setup. The pump and probe beam were set to the same powers (10 mW) in order to achieve equal carrier generation across each PCS on the device. Initially the generated (input) THz pulse was measured using two adjacent switch regions on either side of the transmission line. The position of the pump and probe beams together with bias arrangement is similar to one demonstrated in Figure 3.18. Both pairs of switch regions (1-2, 3-4) were tested in order to show reproducibility for generating and detecting THz pulses with similar amplitude and pulse shape.

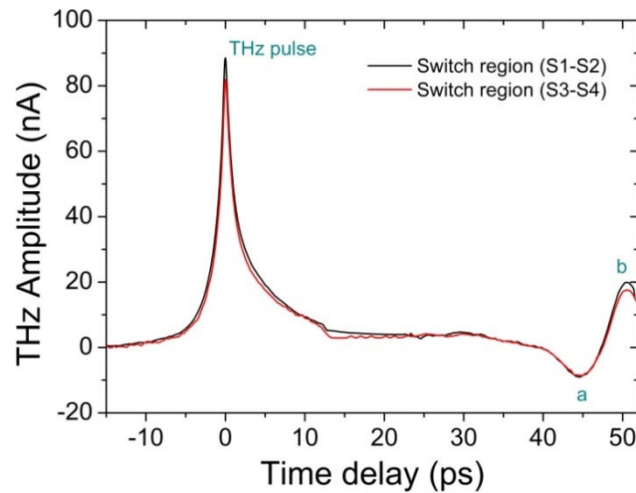


Figure 3.17 Comparison of the generated THz pulse scans for both pairs of switch regions on Sample 1 showing the two main reflection peaks.

Figure 3.17 shows the single THz pulse scan generated and detected using both adjacent switch pairs on Sample 1 with a 30 V pump bias voltage applied. The first peak identified as the THz pulse is followed by several other reflections which are explained with reference to reflections within the waveguide geometry. It is noted that the generated THz pulse shape (with FWHM ~ 2 ps) and pulse amplitude using both simple PCS switch pairs on Sample 1 are very similar, as expected, thereby showing a good reproducibility of generation and detection of the pulses across all switch pairs. The two reflection features labeled as ‘a’ and ‘b’ in Figure 3.17 are readily identifiable by considering the calculated pulse propagation velocity of $1.24 \times 10^8 \text{ ms}^{-1}$, (using Equation 1.24). In Chapter 1, Section 1.6, it was shown that the reflections occurring from a short circuit undergo a 180° phase inversion, whilst reflections from open circuits retain their original phase. The origin of the two reflections from the discontinuities in the waveguide is demonstrated in Figure 3.18.

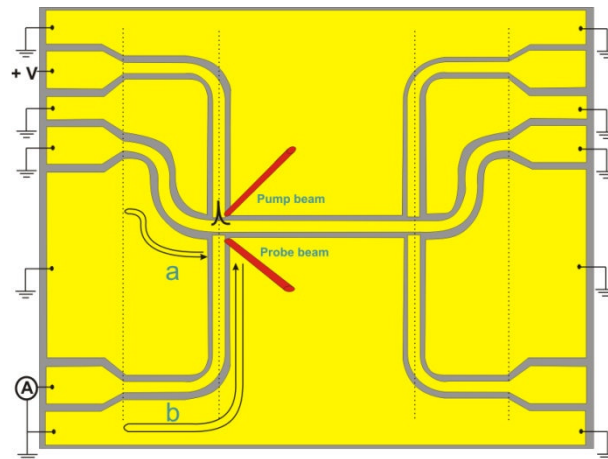


Figure 3.18 Demonstration of the pulse paths required for the origin of the two subsequent reflections a and b, following the main generated THz pulse.

For a positive-polarity THz pulse, the first subsequent reflection (labeled a) is negative in sign since it undergoes a single reflection from a short circuit interface of the transmission line as shown in Figure 3.17. The second reflection (labeled b) in the pulse scan is identified as arising from the open circuit interface of the 3.36 mm-long probe electrode connected to the lock-in amplifier for pulse measurement. This propagation path of the pulse is only possible when the resistance of the switch becomes relatively low during each laser illumination pulse, and also when the characteristic impedance of the biasing electrodes and the transmission line are similar.

On the other hand, under a similar bias voltage (30 V) and illuminated power density of laser beams (10 mW), the input pulse measurement on Sample 2 showed a great influence on the photoconductive switch gap topology over the generated electrical pulse shape and amplitude. Figure 3.19 shows the single THz scan using both adjacent simple PCS pairs (S1-S2) and IPCS pairs (S3-S4).

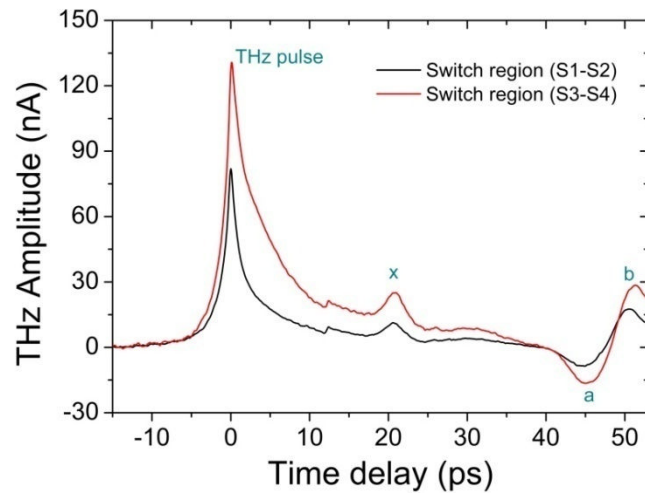


Figure 3.19 Comparison of the generated THz pulse scans for both pairs of switch regions (SPCSs and IPCSs) on Sample 2 showing the two main reflection peaks. Also shown added reflections ‘x’ occurring between different geometries of pump and probe switch.

It is noted that the electrical pulse peak generated and detected is almost twice that for the IPCSs even when identical pump bias voltage and beam power density is used for both geometry switch pairs. This result was expected, as the photocurrent generated across IPCSs was also almost twice that generated across simple PCSs. The device design of Sample 2 was identical to Sample 1, apart from the difference in switch geometry used. At first glance, the single scan of the THz pulse on Sample 2 reveals similar features following the main peak (i.e. reflections generated from the transmission line geometry-labeled ‘a’ and ‘b’). An added small reflection feature observed in the pulse scan (labeled ‘x’) is identified as the reflection arising from having two different switch geometries on either end of the transmission line, each presenting a different impedance.

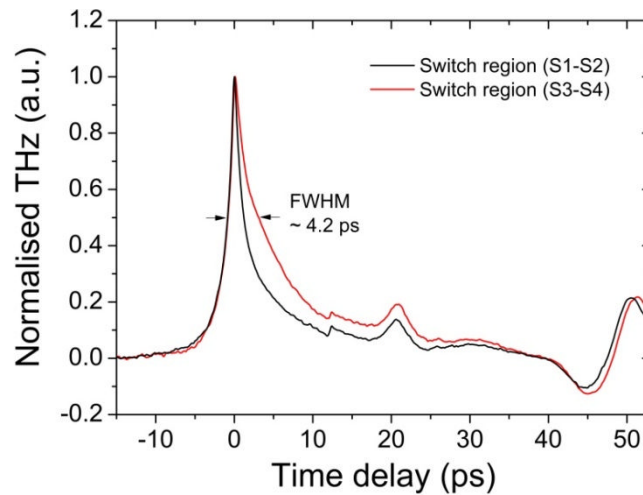


Figure 3.20 Normalised generated THz pulse scans for Sample 2 using both pairs of switch regions (SPCSs and IPCSs), showing the variation of FWHM of the THz pulse with respect to the switch pair geometry used.

Figure 3.20 shows a comparison of the normalised input pulses generated and detected by simple PCSs and IPCSs. It is shown that the FWHM is broader for the IPCS (~4 ps as compared to ~2 ps for the simple PCSs). This is attributed to the increase in the switch gap capacitance for smaller gap IPCS geometry as compared to the larger gap simple PCS geometry.

3.3.3. Output pulses

The response of the transmitted (output) THz pulses on CPW devices reveals important properties of the THz interconnect. Since both the THz CPW devices under test were symmetrical, the overall response of the detected pulse was expected to be the same as the input pulses (i.e. the main pulse peak with secondary reflections). However the output pulse shape, detected after transmission along the waveguide, is affected by attenuation and dispersion arising from the dielectric substrate. The biasing and illumination arrangement used for output THz pulse measurements is identical to that described in Chapter 1, Section 1.6.4 and as shown in Figure 1.25. To detect the output pulse, the pump beam is focused on one of the pump switch regions (switch region 1)

and the probe beam is focussed on one of the probe switch regions (switch region 3). The pump and probe beam powers were maintained at 10 mW each, and 30 V bias applied at the pump switch. Since both the devices have an identical transmission line design, the signal exhibits the same reflection features originating from specific points on the transmission line (as discussed in section 3.3.2). It is important to note that for output THz pulse measurements on Sample 1, a simple PCS is used for detection of the pulse, while for Sample 2, an IPCS gap is used. Figure 3.21 shows the comparison of THz pulse scans for Samples 1 and 2.

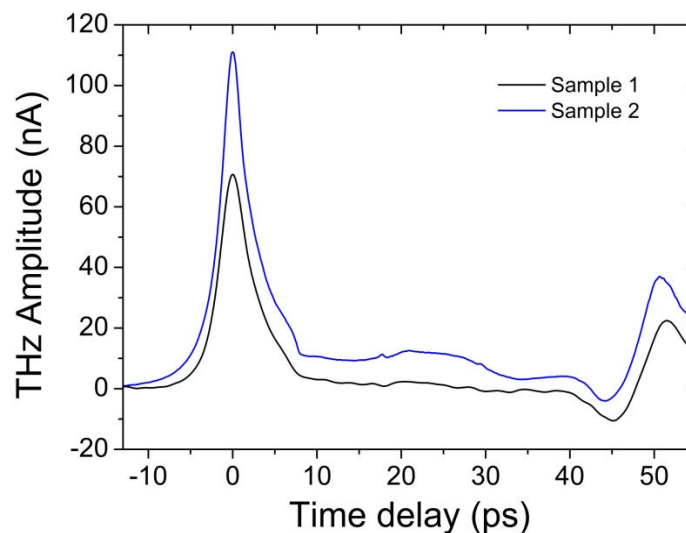


Figure 3.21 Example of a pulse transmitted along the 1.2 mm coplanar waveguide for Samples 1 and 2, using switch region 1 as the source and switch region 3 as the detector in both cases.

At first instance, the time-domain output THz pulse scans for both devices showed a strong similarity, since they are mainly influenced by the identical ‘active region’ of the waveguide. It was also observed that the detected output pulse amplitude for Sample 2 was almost twice that for Sample 1, owing to the use of the IPCS gap for detection. The FWHM of transmitted pulses on both the devices was found to be identical (~ 4 ps), indicating very similar dispersion. In order to perform transmission

measurements at cryogenic temperatures, much lower laser beam powers ($< 5\text{mW}$) were required, in order to avoid thermal loading of the fridge. Therefore, while still operating at room temperature, the SNR for the transmitted pulses was carefully observed while using similarly low laser powers.

Figure 3.22 shows the transmitted pulse scans obtained on Sample 2 by varying both pump and probe beam powers simultaneously to 1 mW, 2 mW, 5mW and 10 mW. The inset shows the effect of the laser power on the magnitude of the THz signal measured at the output switch.

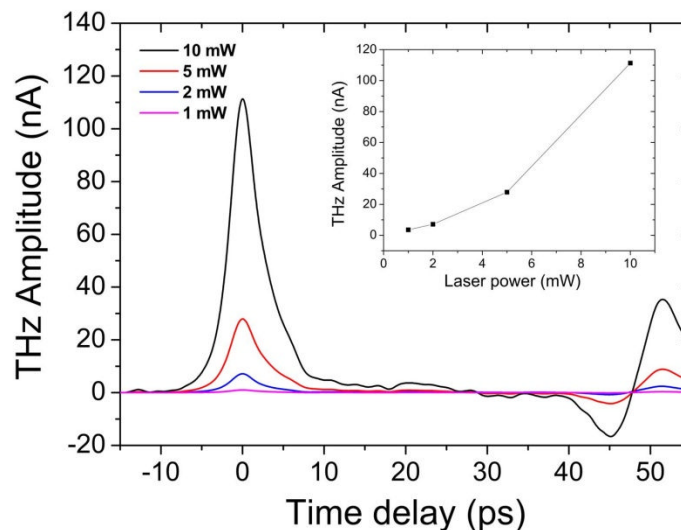


Figure 3.22 Main figure: Transmitted THz pulse scans for Sample 2 at varying pump and probe beam powers. Inset: Variation of transmitted pulse peak amplitude with respect to beam powers.

The time-domain signal was then converted into the frequency domain by performing an FFT of the data points around the THz peak. Figure 3.23 shows a comparison of the spectrum of frequency components contained within the transmitted pulse, for both devices. It reveals that for both Samples 1 and 2, the usable bandwidth for allowing analysis on frequency components is up to at least 500 GHz, and the frequency resolution achieved on these devices was close to 10 GHz. The overall room

temperature transmission properties of both waveguide devices were considered suitable for further investigation at cryogenic temperatures and within magnetic fields.

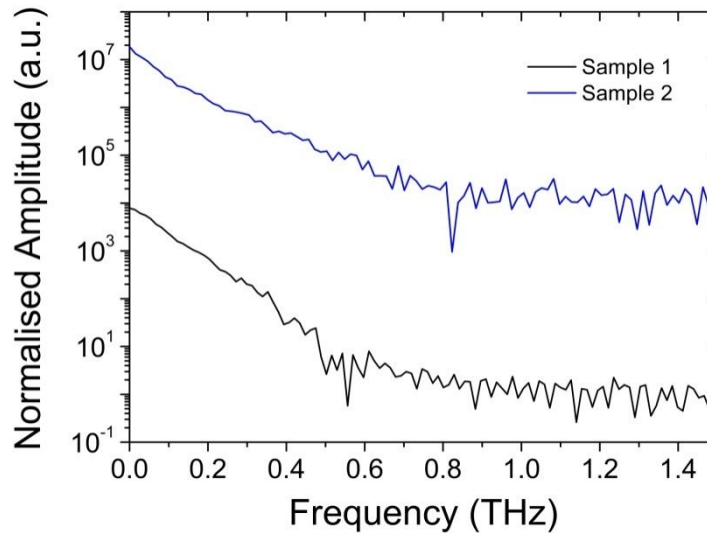


Figure 3.23 Fast Fourier transform of the transmitted time-domain signals shown in Figure 3.21 for Sample 1 and 2.

3.4. On-chip THz transmission studies at cryogenic temperatures and under magnetic fields

In room temperature on-chip TDS systems, laser beam powers up to 10 mW or higher can be used for generating and detecting THz pulses; however this is not possible for low-temperature measurements performed in the dilution refrigerator. The optical laser beam power is limited by two major factors; first, the cooling power of the dilution refrigerator, which is generally around 200 μ W for reaching operating temperatures of \sim 100 mK (for the DR 200 system used). Secondly, the power handling capacity of optical fibers is also limited. Owing to these challenges, cryogenic photoconductive sampling with LT-GaAs photoconductors was previously unproven at sub-Kelvin

temperatures. Sample 2 was chosen for the cryogenic temperature measurements in this work, owing to its higher sensitivity for THz signal detection as demonstrated in room temperature characterisation.

3.4.1. DC characterisation and dynamic imaging of photoconductive switches

Following room temperature characterisation, the CPW device was placed in the cryogenic sample holder shown in Figure 3.11. Several cool-down runs with the cryogenic sample holder were carried out in order to make sure that the cooling power of the dilution fridge was sufficient to reach the base temperature of < 10 mK (with laser beams switched off). The optical intensity of pump and probe beams were set to 2 mW throughout these measurements to achieve minimal thermal loading. A bath temperature of 100 mK (measured at the mixing chamber plate using a RuO₂ thick film resistor) was achieved, limited solely by the thermal loading from the laser beams. Following careful alignment of both collimated pump and probe beams on appropriate switches on the CPW device using x-y piezo electric stages, the DC I-V characteristics of the switches were measured. Figure 3.24 shows the DC current passing through the switch regions at varying bias voltages. Each current measurement was repeated on pump and probe switches for varying magnetic fields. The behaviour of both simple PCS and IPCS on Sample 2 observed at cryogenic temperatures was identical to its properties measured at room temperature as shown in Figure 3.16 (a) and (b).

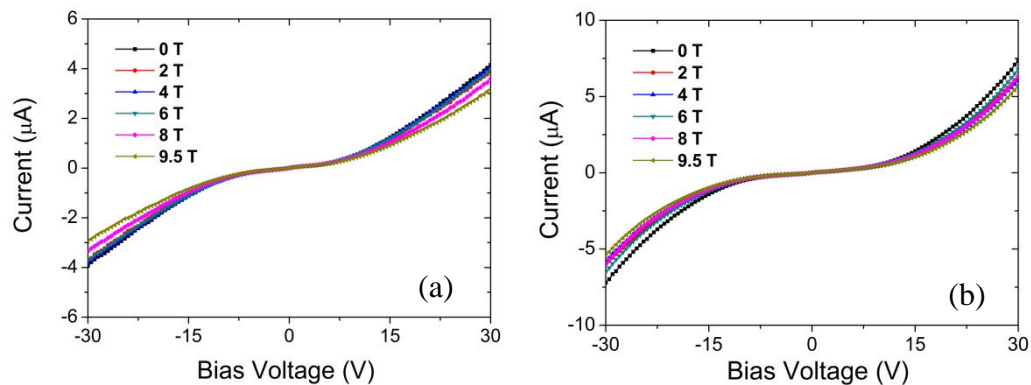


Figure 3.24 Current versus applied voltage for Sample 2 for (a) the pump switch and (b) the probe switch taken at 100 mK and varying magnetic fields.

The variation of magnetic field revealed a striking feature in terms of its dependence on switch region characteristics. As discussed by Zamdmer *et al* [9], the ‘sub-linear’ behaviour of current at lower biases is mainly dependent on the mobility of photo-generated carriers. However, the ‘super-linear’ behaviour of the photocurrent at higher biases is found to be strongly dependent on the combination of photo-generated carriers and additional carriers excited from the lower energy As donor states due to high density electric fields. This effect is commonly referred as localised electron heating or impact ionization within the switch region [121, 122]. It was clear from the Figure 3.24 that the ‘sub-linear’ region of the generated photocurrent across both switch regions was independent of the magnetic field; however, a slight decrease in the photocurrent density with increasing magnetic fields was observed for ‘super-linear’ current region. This dependence was attributed to the overall carrier transit time between photoconductive switch gap exceeding the photo-generated carrier lifetimes due to the cyclotron motion resulting from magnetic fields. This magnetic field dependence on the PCS gap characteristics has also been reported in literature [93]. Since the ‘sub-linear’ photocurrent region at lower switch biases was found to be independent of magnetic

fields, it was decided to use low pump switch bias of 5 V for on-chip THz transmission experiments undertaken in presence of magnetic fields.

As discussed in section 3.2.3, an added advantage of the setup used for this work over setups used in previous research work, was the ability to dynamically control the position of collimated laser beams with micron-precision across the sample surface, using a pair of x-y piezo electric stages and the pivoted fiber ferrules. This allowed imaging of the active region of the PCS in terms of the photocurrent generated, while raster scanning the pump laser across the switch gap. Figure 3.25 shows such an image of the pump switch regions at a temperature of 200 mK and at 0 T and 9.5 T magnetic field, as shown in (a) and (b) respectively.

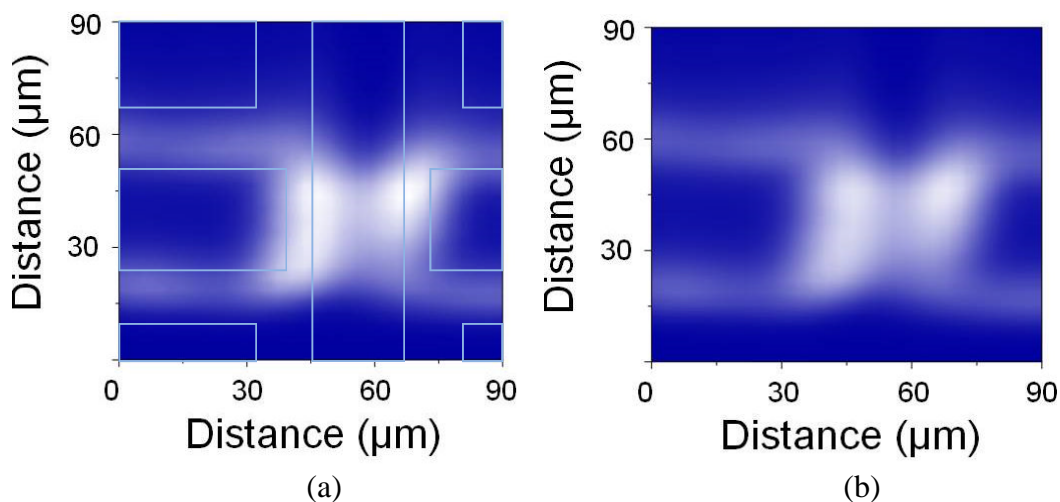


Figure 3.25 The photocurrent image map of the pump switch pair (light regions showing higher current) taken at (a) 200 mK, 0 T and, (b) 200 mK, 9.5 T. The comparison between the actual physical switch pair geometry design on the sample and its photocurrent image map is also shown.

3.4.2. Transmitted THz pulses

The first experimental results of the THz pulse transmission through CPWs at $< 1\text{K}$ temperatures are discussed here. Following the photocurrent imaging of the PCS, the positions of the stages were fixed to align the pump and probe beams on the corresponding switches. The transmitted pulses were measured at both temperatures

down to 100 mK and in varying magnetic fields. The measurements were expected to be identical to the room temperature characterisation results as discussed in section 3.3, since the attenuation and dispersion characteristics of the waveguide were expected to be independent of temperature and magnetic field.

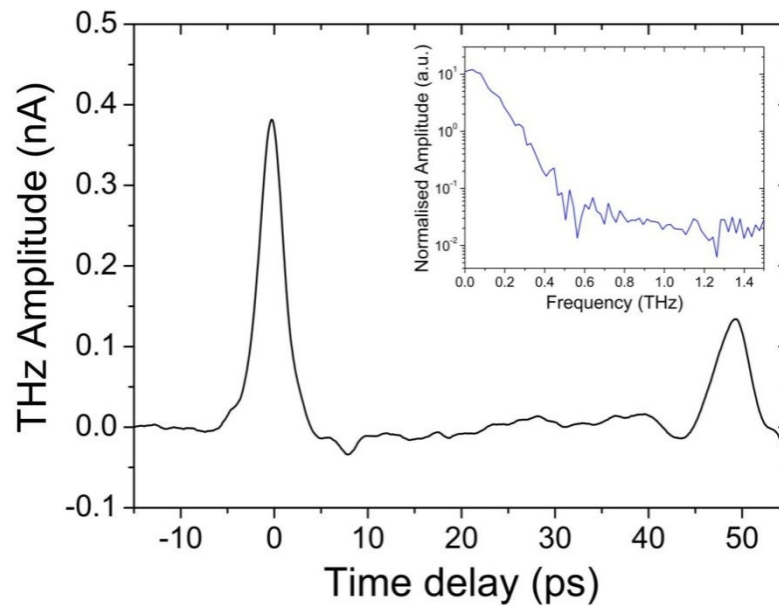


Figure 3.26 Main figure: Experimental measurement of a transmitted pulse along the CPW (Sample 2) taken at 100 mK and 0 T. Inset: FFT of the portion of the time-domain signal before first reflection.

The pump and probe beam powers were maintained at 2 mW each, and a 5 V pump switch bias was used. Figure 3.26 shows a transmitted THz pulse measured at 100 mK and at 0 T field. It is noted that since the laser beam intensity used here is considerably lower than that in the room temperature characterisation, the amplitude of the THz pulse was correspondingly much reduced. Also the subsequent reduction of the pump bias voltage to 5 V resulted in a reduction in the FWHM from 4 ps (as measured at room temperature for a 30 V pump bias) to 3 ps. The inset of Figure 3.26 shows the spectrum of frequency components contained within the transmitted pulse.

The transmitted pulse data was then obtained for varying magnetic fields between 0 and 9.5 T. Figure 3.27 shows output pulse scans taken at intervals of 1 T from 0 to 9 T. The output pulse shape and amplitude, including the reflection features were found to be completely independent of varying magnetic fields, as expected. These results confirmed the suitability of these waveguides for subsequent excitation and measurement of the THz-frequency electrical transients in a 2DES.

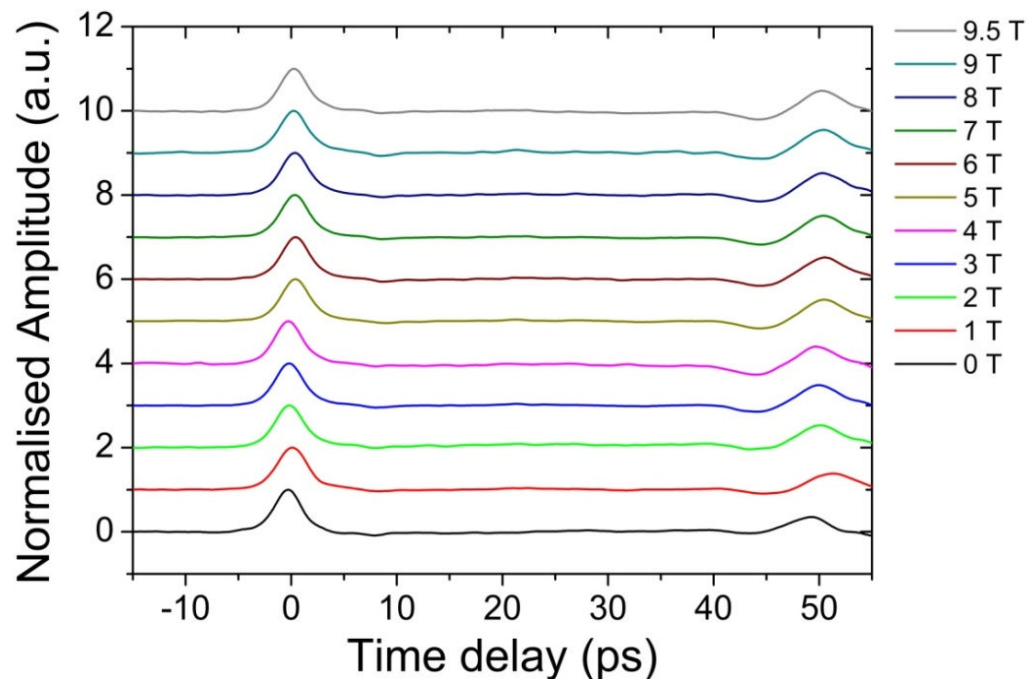


Figure 3.27 The normalised amplitude time-domain spectra of the transmitted pulse taken at 100 mK and varying magnetic fields from 0 – 9.5 T offset by 1 unit per trace.

Using the successfully demonstrated method of imaging the PCS gap by means of the generated photocurrent (see section 3.4.1), the transmitted THz pulse amplitude was continually monitored at the detected switch, while precisely moving the position of the pump beam over the switch region. This allowed generation of a directly comparable image map based on the THz pulse amplitude.

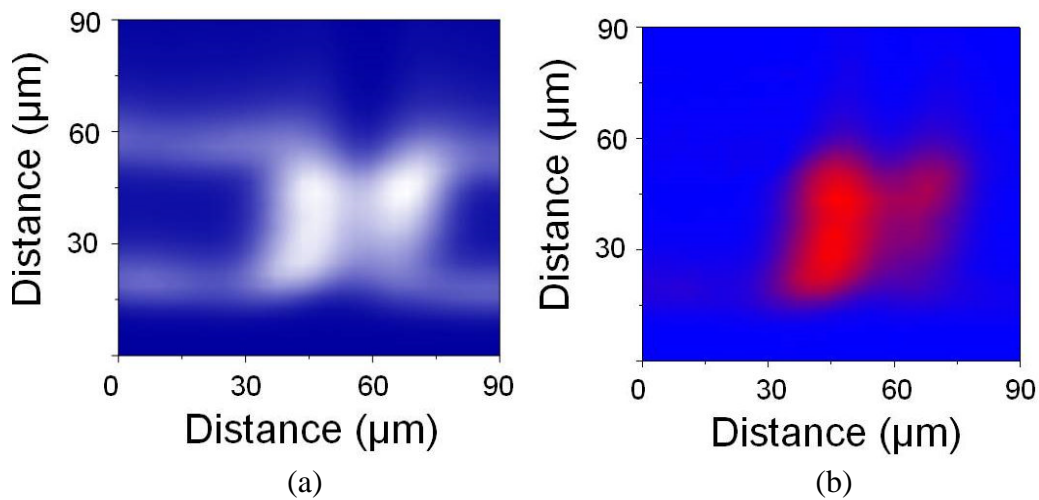


Figure 3.28 (a) The photocurrent image map of the pump switch pair (light regions showing higher current) and, (b) the corresponding image map based on the transmitted THz pulse amplitude (red regions showing peak transmitted pulse amplitude detected). Data were taken at 200 mK and 0 T.

Figure 3.28 shows the images based on (a) generated photocurrent and (b) output THz pulse peak amplitude, measured at 200 mK and 0 T magnetic field. Figure 3.29 shows the corresponding images measured in a magnetic field of 9.5 T.

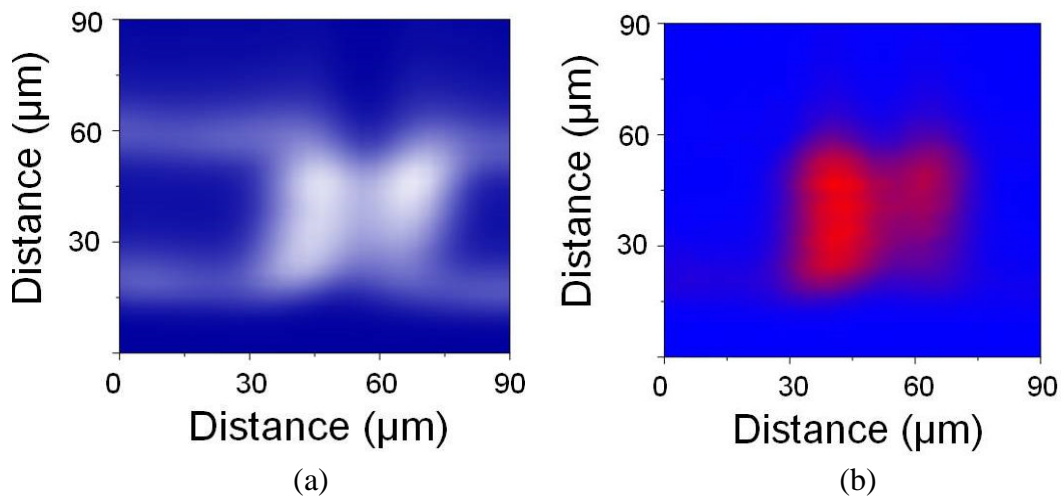


Figure 3.29 (a) A photocurrent image map of the pump switch pair (light regions showing higher current) and, (b) the corresponding image map based on the transmitted THz pulse amplitude (red regions showing higher peak transmitted pulse amplitude detected). Data were taken at 200 mK and 9.5 T.

3.5. Summary

In this chapter, the geometry and room temperature transmission characteristics of two CPW devices with different PCS geometries (simple PCS and IPCS) have been presented, showing the significance of different switch gap geometries for the measured DC current-voltage characteristics, THz pulse amplitudes and THz pulse shapes.

Also, this chapter has demonstrated a previously unexplored method of THz generation and detection using CPWs at sub-Kelvin temperatures and in magnetic fields, establishing a good basis for integration of the waveguides with nanoscale devices. The most important properties of the CPWs, such as attenuation and dispersion caused by the dielectric substrate, were shown experimentally to be independent of magnetic field, thereby confirming the suitability of this technique for excitation and time-resolved detection of THz-frequency electrical transients in a 2DES.

The ability to create a photocurrent image map of the THz generation switch region at cryogenic temperatures and in magnetic fields was demonstrated by raster-scanning the laser beams across different regions of the PCS. A novel method was also demonstrated whereby a corresponding image map was simultaneously generated based on the peak amplitude of the transmitted THz pulse. The work undertaken here represents a novel approach for performing pump/probe magneto-spectroscopy measurements with on-chip waveguides at cryogenic temperatures.

A summary of this chapter has been published as reference [83].

Chapter 4: THz interaction with a 2DES between 300 K and 4 K

4.1. Introduction

This chapter discusses time-resolved measurements of picosecond electron transport in the 2DES under varying temperatures between 4 K and 300 K. These measurements were performed to develop a quantitative understanding of how pulse propagation through a 2DES is affected by temperature-related changes in the conductivity. Also, this work proved to be a convenient intermediate step on the way to the subsequent measurements at sub-Kelvin temperatures and high magnetic fields, which will be discussed further on in Chapter 5.

Two different approaches for interacting picosecond pulses with the 2DES will be presented in this chapter. For both methods, the waveguide substrates containing the LT-GaAs and 2DES layers are formed from the optimised monolithic integrated wafer structure discussed in Chapter 2.

4.2. 2DES integrated THz waveguides and experimental techniques

The two different methodologies for THz-frequency excitations of the 2DES allowed either ‘transmission spectroscopy’ or ‘reflection spectroscopy’ of the 2DES to be performed at both room and cryogenic temperatures. The details of the coplanar

waveguide devices used for testing both methods and the experimental setup used in these measurements are discussed below.

4.2.1. Pulse injection waveguide devices

The first technique was based on the direct injection of picosecond current pulses into a 2DES through ohmic contacts. The injection and subsequent measurement of the pulses was achieved using a coplanar waveguide deposited on the surface of the heterostructure. As shown in the schematic diagram of the pulse injection device in Figure 4.1, the 2DES was selectively etched away to leave a 100 μm -long strip, and AuGeNi ohmic contacts were formed at each end. The centre conductor of the CPW guiding the picosecond pulses overlapped the (source-drain) ohmic contacts, which were annealed beforehand to make electrical contact with the 2DES situated 70 nm below the surface. The current pulses were transmitted into and out from the 2DES by these ohmic contacts, and then propagated to the detection region at the other end of the transmission line, where they were sampled using on-chip THz-TDS. The ‘sub-mesa’ shown in the schematic was formed to aid the process of selectively etching away the LT-GaAs photoconductive material; this is explained in a greater detail in the following section.

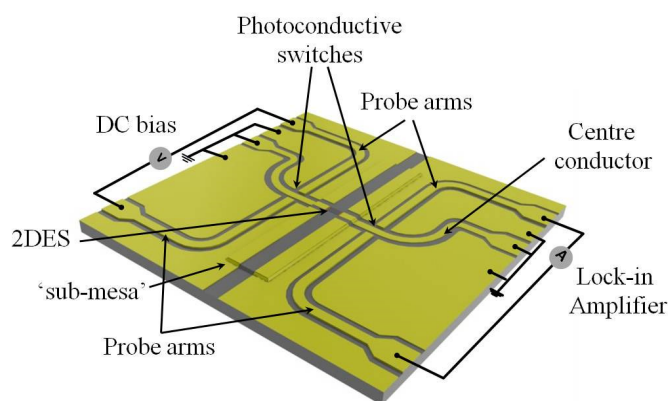


Figure 4.1 Schematic of ‘picosecond pulse injection’ device with 2DES embedded into coplanar waveguide with probe arms defining regions for photoconductive excitation of exposed LT-GaAs layer.

4.2.1.1. Device fabrication

The layout of the monolithic integrated heterostructure grown using MBE used for device fabrication is shown in Figure 4.2 (a). In order to expose the LT-GaAs photoconductive layer surface to define THz generation and detection switch regions on either side of the rectangular mesa containing the 2DES, it was necessary to chemically etch the layers grown above. This was systematically carried out using a selective wet chemical etch for different layers using Shipley S1813 photoresist as a protective layer.

In the first etch procedure, a dilute citric acid etch ($C_6H_8O_7 : H_2O_2$ with a volume ratio 3:1) was used to etch the overlaid 2DES layers which terminated at the AlAs etch stop layer (100 nm thick). This etch-stop layer was then removed using a hydrofluoric acid etch ($HF : H_2O$ with a volume ratio 1:10), revealing the smooth LT-GaAs surface on either side of the ‘sub-mesa’ containing the 2DES, as shown in Figure 4.2 (b). Since both the wet etch procedures used gave anisotropic etch profiles[123], it was essential to create a larger 300 μm wide and 3.5 mm long ‘sub-mesa’ to support the ‘super-mesa’ of 100 μm width and 30 μm length, as shown in Figure 4.1. The ‘super-mesa’ strip containing the confined 2DES was then defined from the sample surface to a depth of ~ 100 nm using a subsequent dilute sulphuric acid etch ($H_2SO_4 : H_2O_2 : H_2O$ with a volume ratio 1:8:71) procedure, as shown in Figure 4.2 (c). Owing to the width of the centre conductor for the overlaid CPW being chosen as 30 μm , the width of the super-mesa was kept the same to ensure a continuous overlap between CPW-2DES interface.

Ohmic contacts formed from AuGeNi alloy were then deposited by thermal evaporation across the edge of the etched smaller mesa to define source and drain contacts. As shown in Figure 4.2 (d), these contacts were diffused laterally to make contact with the electron layer situated 70 nm below the sample surface using ex-situ thermal annealing at 430° C for 80 seconds under a nitrogen atmosphere. For the final

step, the coplanar waveguide with centre conductor, ground planes and bias electrodes for defining switch regions was overlaid using conventional UV lithography followed by thermal evaporation, as shown in Figure 4.2 (e). The THz waveguide consists of a 20/250 nm-thick Ti/Au strip with the centre conductor overlapping the ohmic contacts defined on the 2DES ‘super-mesa’. This relatively thick metal waveguide strip was used to avoid conductor losses induced by the skin effect [124] as well as possible breakage of the metal running over multiple defined mesas.

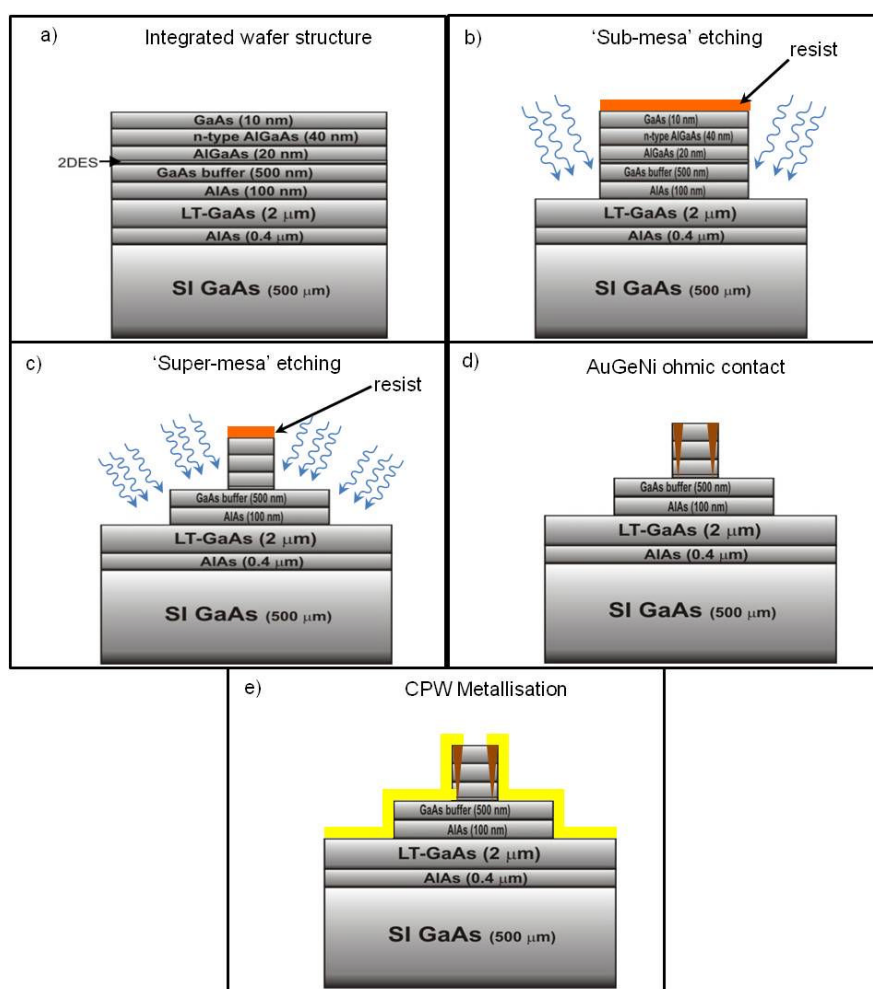


Figure 4.2 Schematic diagram showing the main stages of fabrication for the picosecond pulse injection devices (a) Monolithic integrated structure grown using MBE. (b) ‘sub-mesa’ etching. (c) 2DES ‘super-mesa’ etching. (d) AuGeNi metallisation for Ohmic contact. (e) CPW metallisation.

Figure 4.3 shows the complete design of pulse injection waveguide devices with integrated 2DES ‘super-mesa’ coupled with the centre conductor of the CPW through ohmic contacts. It also shows the four defined switch regions used for measuring picosecond time-scale pulses before and after transmission through the 2DES.

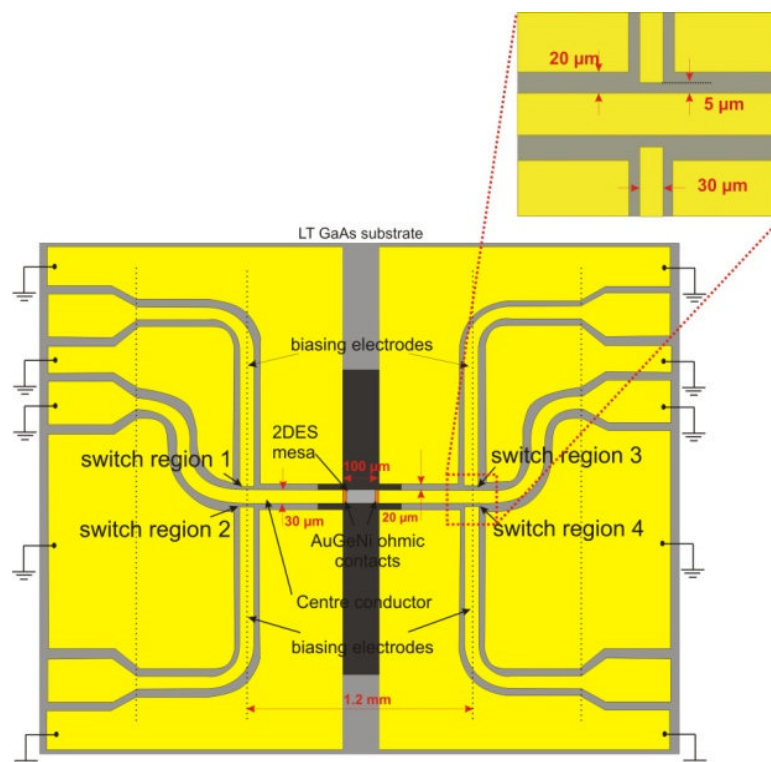


Figure 4.3 Main figure: Diagram of the THz CPW device fabricated, containing the 2DES strip integrated in the signal conductor and four biasing electrodes defining PCS gap regions. Inset: Detailed view of one of the four switch regions.

4.2.1.2. Lumped element model

For pulse injection waveguide devices, the transmission of the picosecond pulses through the 2DES is highly dependent on the conductivity of the electron layer since this determines its impedance. Therefore, the behaviour of the 2DES connected to the transmission line was modelled as a lumped element circuit, as shown in Figure 4.4.

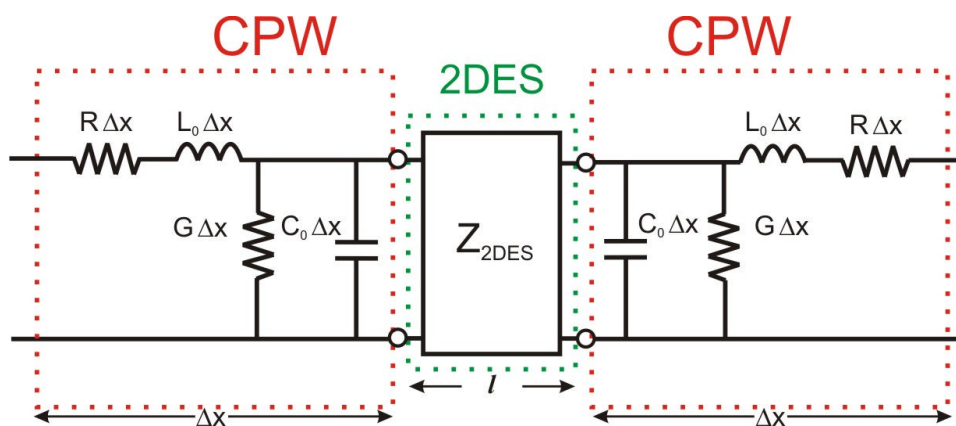


Figure 4.4 A lumped element circuit model representation of the 2DES integrated with coplanar waveguide for picosecond pulse injection.

A standard lumped circuit element representation is used for the CPW which forms a transmission line for picosecond pulses injection into the 2DES, and for carrying the transmitted pulse back from the 2DES to the detection region (as previously discussed in Chapter 1, Section 1.6.3). The short 2DES region electrically connected to the centre conductor of the coplanar waveguide through the source-drain ohmic contacts can be modelled as a mismatched load Z_{2DES} connected between the CPW regions [95]. The conductance of the 2D electron layer was related to the real part of the impedance of the 2DES region, as shown by Equation 4.1. Where, w is the width and l is the length of the 2DES strip.

$$Re[Z_{2DES}] = R = \frac{1}{\sigma} \left(\frac{l}{w} \right) \quad (4.1)$$

This resistive element representing the resistance of the 2DES is greatly dependent on temperature. At room temperature, the electron transport in the 2DES is diffusive due to electron-phonon scattering and so the mean free length of the electrons l_e is much smaller than the 2DES mesa length L ($l_e \ll L$). As a result the conductivity of the electron layer is low; thereby it appears as a relatively large resistive element when compared to the characteristic impedance of the transmission line ($\sim 50 \Omega$). This results

in impedance mismatch between the transmission line and the 2DES strip, resulting in greater reflection from the CPW/2DES interface than pulse injection. However, at cryogenic temperatures most of the electron-phonon scattering is suppressed, and the electron transport in the 2DES becomes ballistic with a mean free length l_e of the electrons exceeding the length of the mesa L ($l_e \gg L$). This means the resistivity of the 2DES strip becomes more comparable to the characteristic impedance of the transmission line ($\sim 50 \Omega$), resulting in more efficient pulse injection and transmission through 2DES region. A full spectrum of pulse injection and transmission studies at varying temperatures through 2DES is discussed in section 4.3.

4.2.2. Capacitive coupling waveguide devices

The second method presented here for THz frequency excitation of 2DES involved capacitively coupling the electric field of the propagating electromagnetic wave on the CPW with the 2DES laterally situated in close proximity (~ 70 nm below sample surface). This approach is particularly useful in understanding the behaviour of magneto conductivity of the 2DES layer at high frequencies, as demonstrated recently [125]. Figure 4.5 shows a illustration of a capacitively coupled waveguide device. As shown, a continuous metallic coplanar waveguide is deposited on the sample surface. The transmission line of characteristic impedance $\sim 50 \Omega$ directly connects the generation and detection photoconductive switches. Once again, a ‘sub-mesa’ is formed to selectively expose the LT-GaAs photoconductive material.

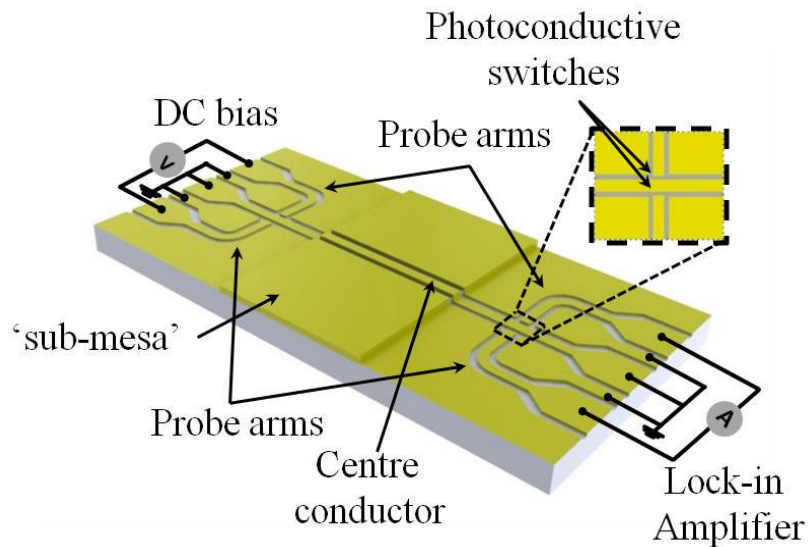


Figure 4.5 Schematic of ‘capacitive coupling waveguide’ device with active region of the CPW overlaid on the sub-mesa containing the 2DES system located ~ 70 nm below.

4.2.2.1. Device fabrication

The MBE grown monolithic integrated heterostructure containing the LT-GaAs and 2DES layers used for device fabrication was same as the one used for fabricating picosecond pulse injection devices (shown in Figure 4.6 (a)). The surface of the heterostructure was chemically etched to a depth of about 670 nm using the ‘Sub-mesa’ etch procedure as described and shown in Figure 4.6 (b). This step exposed the LT-GaAs surface on either side of the rectangular mesa containing the 2DES as shown in Figure 4.5, for defining photoconductive switch regions. Finally, the pattern of the CPW with continuous centre conductor and ground planes was lithographically defined and then formed from a 20/250 nm-thick Ti/Au layer deposited on the surface using thermal evaporation as shown in Figure 4.6 (c).

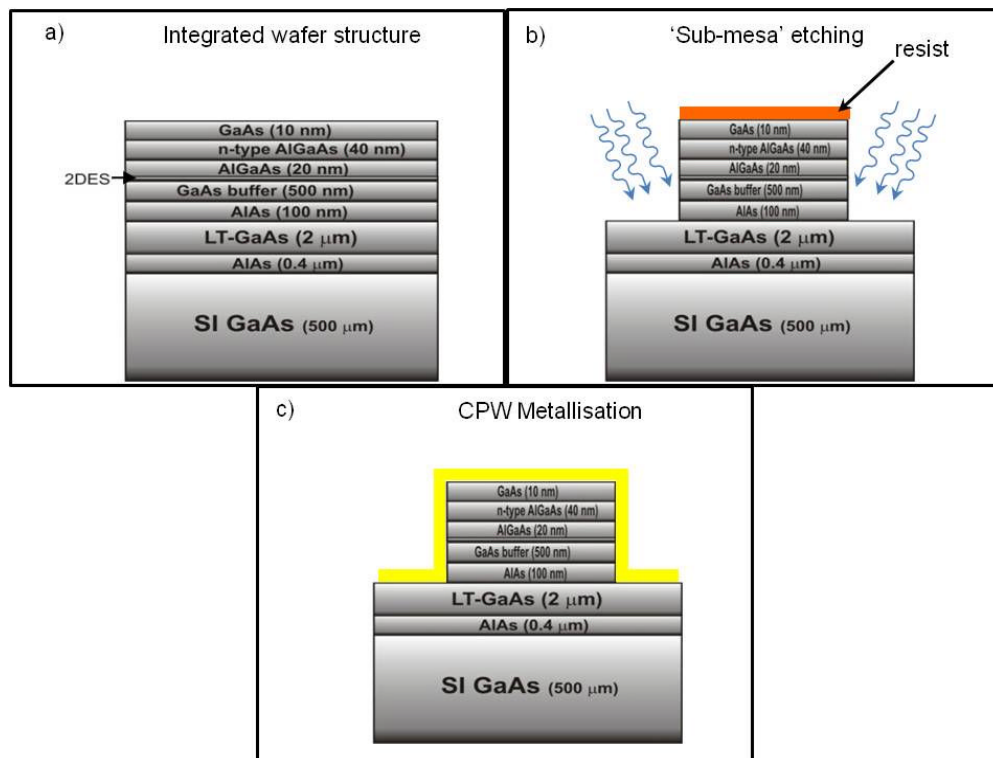


Figure 4.6 Schematic diagram showing the main stages of the capacitive field coupling CPW device fabrication. (a) Monolithic integrated structure grown using MBE. (b) ‘sub-mesa’ etching. (c) CPW metallisation.

Since there were no electrical connections to the 2D electron layer, the 2DES was characterised separately using Hall bar devices. The QHE measurements performed on a Hall bar sample from the same wafer at 1.2K gave a carrier density of $3.5 \times 10^{11} \text{ cm}^{-2}$ and a mobility of $500,000 \text{ cm}^2\text{Vs}^{-1}$. The detailed Hall Effect experiments under magnetic fields including Shubnikov-de Haas oscillations were carried out on a Hall bar device from the same wafer structure (as discussed in Chapter 2, Section 2.5.1).

4.2.2.2. Lumped element model

For capacitive coupling waveguide, no direct electrical contact was made between the transmission line and the 2DES, in contrast to the pulse-injection approach. However the transmission of pulses on the CPW in this case is strongly dependent on the conductivity of the 2DES layer, due the interaction between the propagating electric field and the

2DES. Once again, a lumped circuit element model is used to model the behaviour, as shown in Figure 4.7.

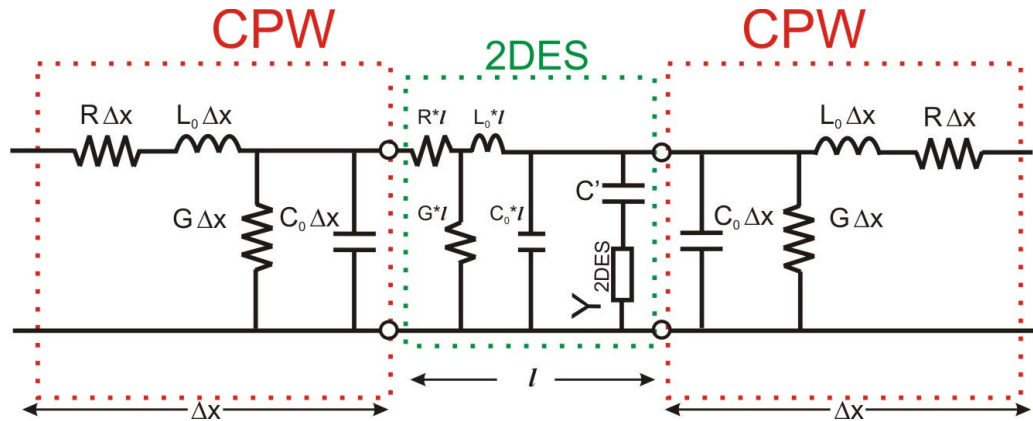


Figure 4.7 A lumped element circuit model representation of capacitively coupled waveguide overlaid on top of the 2DES layer.

In this case the conductivity of the 2DES is represented by a real part of the shunt admittance element (Y_{2DES}), for the portion of the CPW overlaid on top of the sample surface containing the 2DES (i.e. CPW on ‘sub-mesa’) [125, 126]. The value of the shunt admittance can be related directly to the conductivity of the electron layer as shown in Equation 4.2.

$$Re[Y_{2DES}] = G = \frac{1}{R} = \sigma \left(\frac{l}{w} \right) \quad (4.2)$$

This indicates at room temperatures with lower conductivity of the 2DES layer, the shunt conductive element should not greatly affect the propagating THz signal travelling on the CPW above. However, at cryogenic temperatures as the conductivity of the 2DES increases, the highly conducting electron layer will capacitively absorb the transmitted signal propagating along the overlaid metal CPW. The consequent variations in the insertion loss of the transmitted THz signal are directly related to the changing conductivity, thereby allowing ‘attenuated total reflection spectroscopy’ of the

conductivity of the 2DES layer to be performed. Experimental studies carried out using the technique described here are discussed in section 4.4.

4.2.3. Experimental setup

An identical pump-probe on-chip THz-TDS setup was used as for the room temperature characterisation of CPW devices discussed in Chapter 2 and as shown in Figure 2.2. A schematic layout of the setup used for THz pulse transmission measurements through 2DES at varying temperatures is shown in Figure 4.8.

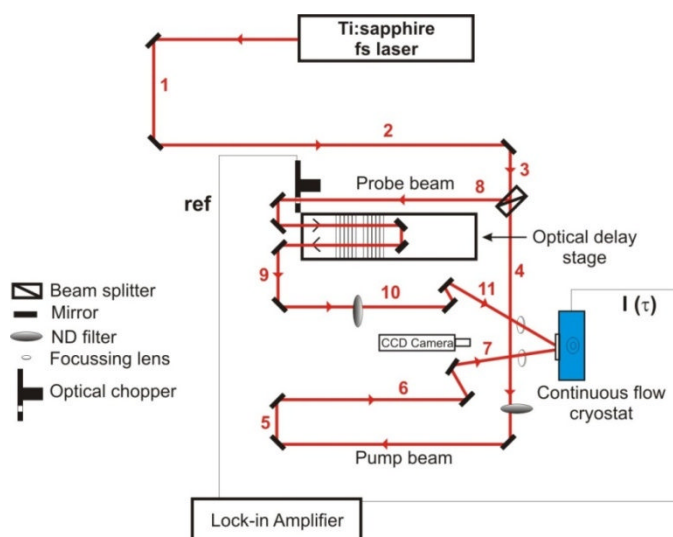


Figure 4.8 System diagram of THz-TDS used for operating 2DES integrated THz waveguides at cryogenic temperatures using continuous He flow cryostat.

As shown in Figure 4.8, the transmission measurements at both room and cryogenic temperatures (down to 4 K) were performed with the waveguide device mounted in the continuous flow cryostat behind transparent quartz windows to allow direct comparisons between different temperature conditions. The pump beam passed along the paths 4-7 and was focussed through the quartz windows onto the pump-photoconductive switch. The probe beam passed through a time delayed path 8-11 using

an optical delay stage before focussing through the quartz windows onto the probe-photoconductive switch.

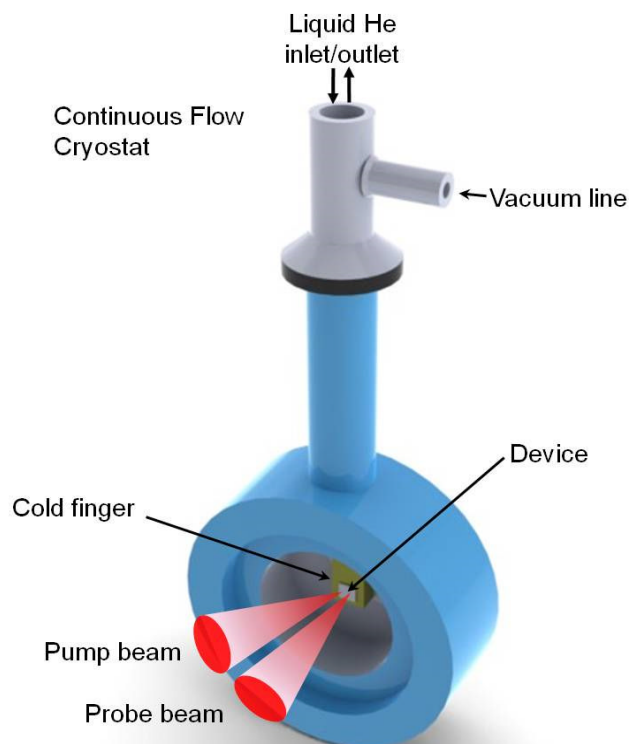


Figure 4.9 Schematic diagram of the THz waveguide device mounted within the continuous flow cryostat, with optical access provided by transparent quartz windows.

Figure 4.9 shows the schematic layout of a CPW device mounted within a continuous flow cryostat on a cold finger attached to the probe with electrical connections. The transparent quartz windows provide optical access for both pump and probe beams to be aligned on PCS regions. A reduction of 15 % in optical beam intensity was revealed for both pump and probe beams after transmission through the quartz windows due to multiple reflections of the laser beams at the window interface. Also, the varying temperature measurements on CPW devices were carried out while pumping the vacuum line of the cryostat, as shown in Figure 4.9.

4.3. Picosecond pulse injection in 2DES

In order to obtain quantitative information about the 2DES using pulse injection waveguide device as discussed earlier, a reference device was also fabricated with a break in the CPW replacing the 2DES. Figure 4.10 (a) shows an optical microscope image of a 100 μm strip of 2DES mesa integrated into the gap of the centre conductor, with electrical connection made through ohmic contacts. While Figure 4.10 (b) shows an identical reference device made in parallel with no integrated 2DES strip (skipping the 2DES mesa processing shown in Figure 4.2 (c) and (d)). Discontinuous ground planes were also introduced in order to suppress direct coupling of the pulse across the centre conductor gap.

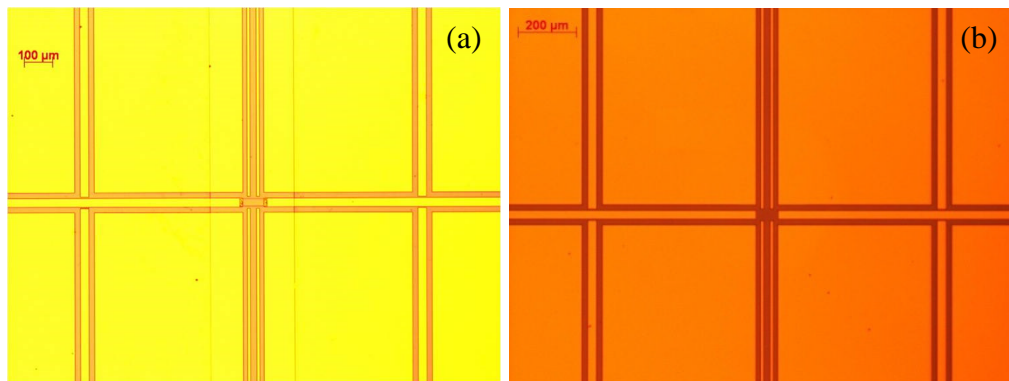


Figure 4.10 (a) Microscope image of a pulse injection device with integrated 100- μm -long 2DES strip. (b) Microscope image of a reference device with 100 μm long gap.

Measurements of picosecond times-scale pulses before and after transmission on both devices at varying temperatures from 300 K to 4 K are reported below. From the comparative pulse transmission studies on both integrated waveguide structures with and without 2DES, it was expected to see a clearly distinguishable contribution from the conductivity of the electron layer.

4.3.1. Input pulses

As described earlier, for both of the pulse-injection devices fabricated, the 2DES mesa strip or a gap integrated with the centre conductor acts as a series lumped element with mismatched impedance compared with that of the CPW transmission line. For example, the measured room temperature resistance of the 2DES strip of $30\ \mu\text{m}$ width and $100\ \mu\text{m}$ length was $\sim 5\ \text{k}\Omega$, while the reference device with a similar sized gap in the centre conductor acted as an open circuit. In order to study the behaviour of reflections arising from these mismatch conditions and the efficiency of THz pulse transmission from the generator to the detector, it was essential to observe the “input” THz pulses on one side of the transmission line. Figure 4.11 shows the room temperature (300 K) input pulse scan measured for the ‘reference device’ with $100\ \mu\text{m}$ long gap in the centre conductor, by focusing pump and probe beams of identical beam powers (10 mW) at switch regions 1 and 2 respectively as shown in Figure 4.3. The pump switch (switch region 1) was biased at 30 V.

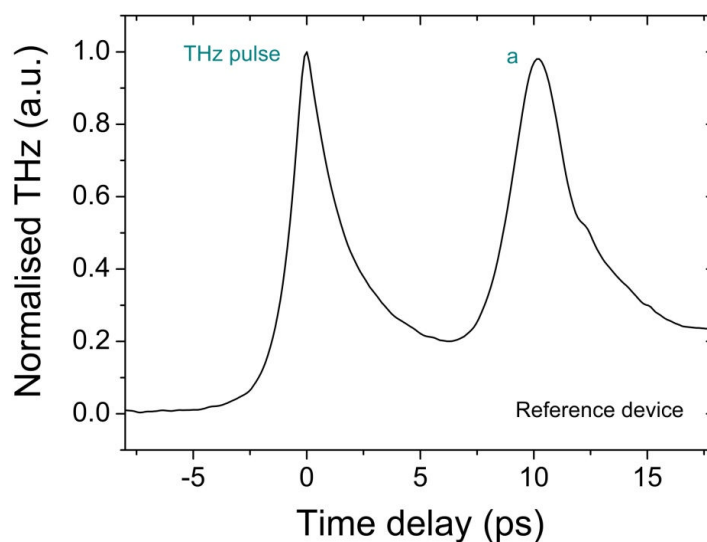


Figure 4.11 Experimental data of the generated THz pulse scan for the reference device taken at 300 K, showing the secondary reflection ‘a’ arising from the integrated gap.

It was observed in the normalised time-domain input THz pulse scan, that the first peak identified as the THz pulse was followed first by an identical amplitude reflection (labelled as 'a'). This reflection feature in the time-domain was readily identifiable using the pulse propagation velocity of $1.24 \times 10^8 \text{ ms}^{-1}$ (as evaluated earlier). The origin of the reflection from the discontinuity in the transmission line is illustrated in Figure 4.12.

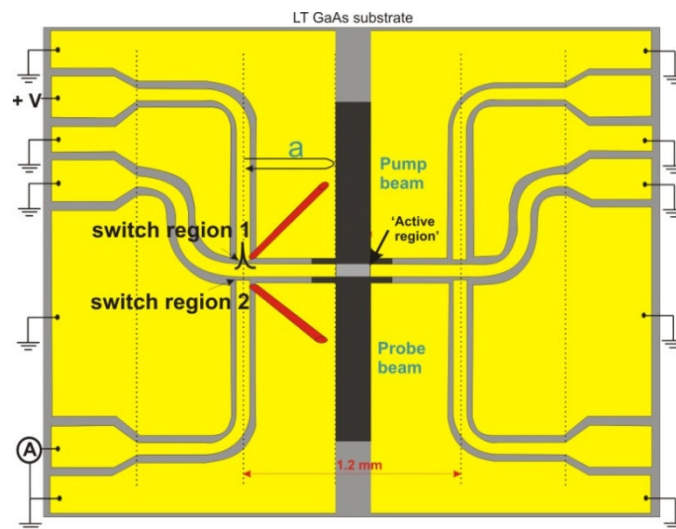


Figure 4.12 Demonstration of the pulse path required for the origin of the reflection 'a', following the main generated THz pulse.

In a reference device where the 'active region' in the centre conductor corresponds to a gap, the positive THz pulse generated at the pump switch undergoes a single reflection from the open circuit interface of the gap in the transmission line due to impedance mismatch. The propagation path of this reflection feature is identified as 'a'. It is noted, that the reflection feature retains the original phase of the main THz pulse owing to its reflection from an open circuit interface (as discussed in Chapter 1, Section 1.6.3). In addition, since the impedance mismatch due to the gap interface in the transmission line was impervious to varying temperatures, the amplitude of the reflection was expected to remain unchanged.

For the actual pulse injection device with integrated 2DES mesa strip ‘active region’, the input THz pulse scan measurement showed an similar result to the reference device at room temperatures. Figure 4.13 shows the normalised input THz pulse measured using switch region 1 as pump switch and switch region 2 as a probe switch. The main THz pulse generated was followed by a similar time-domain reflection feature labelled ‘a’ as seen for the reference device. This was because the 2DES mesa strip, having a resistance of $\sim 5 \text{ k}\Omega$ at room temperature, acts as high impedance lumped element as compared to the transmission line with characteristic impedance of 50Ω . However since the resistivity of the 2DES strip decreases with decreasing temperatures, a drop in the amplitude of the pulse reflection from the 2DES interface was then expected.

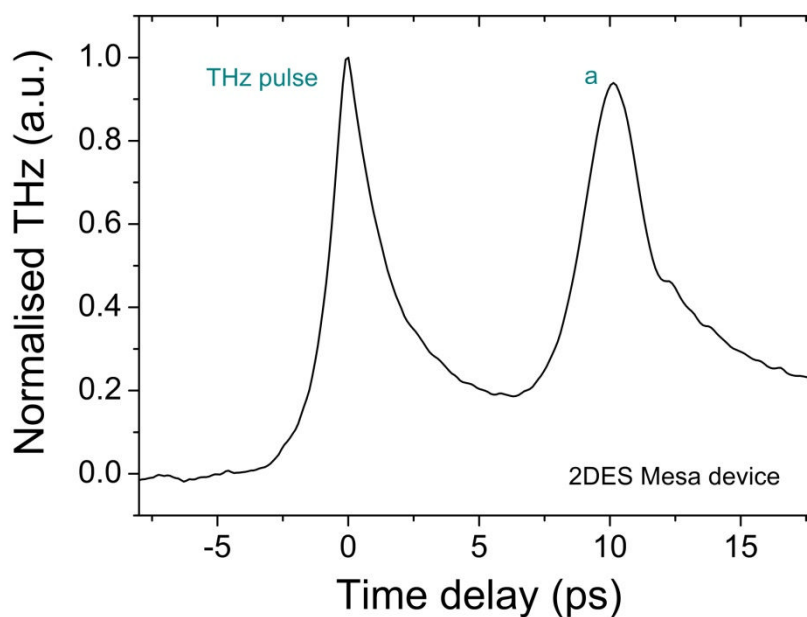


Figure 4.13 Experimental data of the generated THz pulse scan for the 2DES Mesa device taken at 300 K, showing the secondary reflection ‘a’ arising from the integrated 2DES-CPW interface.

A full set of input THz pulse measurements was undertaken for both the reference and the pulse injection CPW devices at varying laser powers and pump switch

biases. The variation in the main THz pulse peak and the reflection peak amplitude for varying laser powers and pump switch bias voltages is shown in Figure 4.14 (a) and (b) respectively.

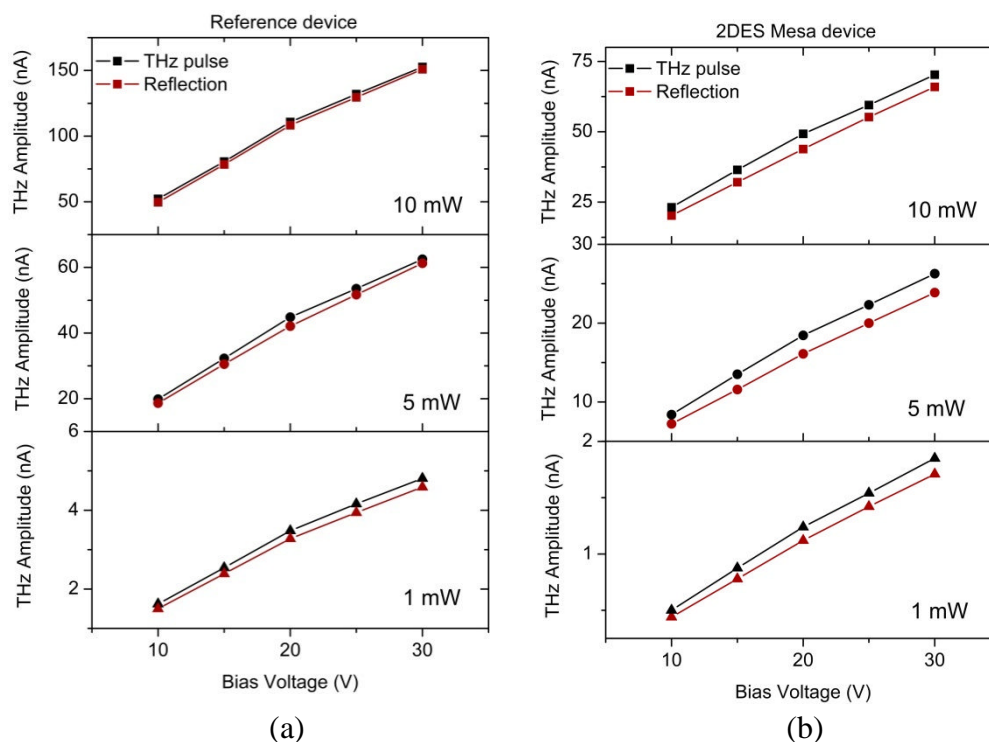


Figure 4.14 Peak amplitudes of incident and reflected pulses for (a) reference device and (b) 2DES mesa device at different biases and beam powers.

Firstly, a decrease in THz amplitudes was observed for pulse injection devices having integrated 2DES mesa as compared to the reference device with no 2DES, which was attributed to degradation in the quality of the exposed LT-GaAs photoconductive layer by post-2DES mesa processing. Secondly, for both devices, a linear response was seen in the increase of peak THz amplitudes with respect to increasing laser beam intensities and switch biases. This behaviour was previously demonstrated for continuous microstrip transmission lines with LT-GaAs used as emitter and detector of THz radiation [118].

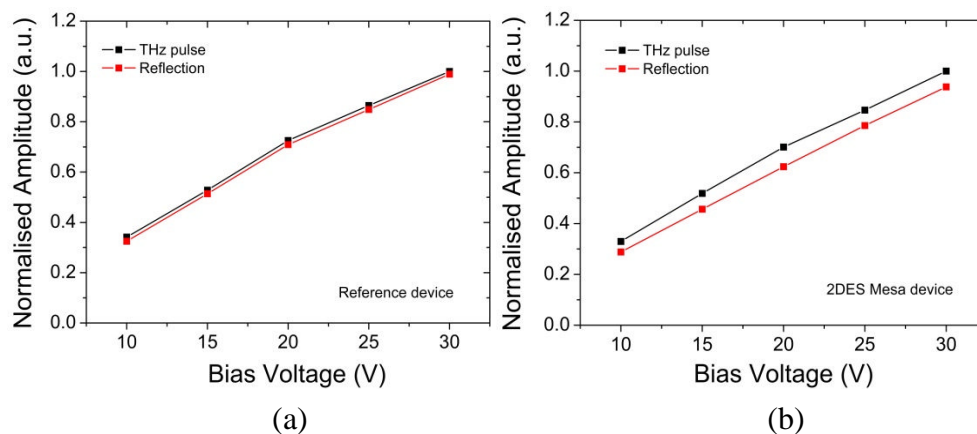


Figure 4.15 Normalised pulse peak amplitude comparison between the THz pulse and the reflection for (a) reference device and (b) 2DES mesa device.

Furthermore, for identical beam powers, if we consider the relative decrease in the reflected THz amplitude peak with respect to the generated THz pulse peak, we see a marginally smaller drop in the reference device as compared to the pulse injection device as shown in Figure 4.15 (a) and (b). This clearly suggests that as the impedance of the 2DES mesa is much smaller than the gap (open circuit) impedance, and a small amount of THz pulse energy couples into the 2DES mesa and gets transmitted even at room temperatures, thereby showing a larger decrease in the amplitude of reflection pulse peak.

Input pulse measurements for both devices were then carried out for varying temperatures by cooling the device mounted in the cryostat using a continuous flow of liquid helium. A PID (proportional-integral-derivative) temperature controller linked with the thermocouple mounted on the cold finger was used to precisely control the temperature of the device. Figure 4.16 shows the input pulse measurements carried out at different temperatures for the ‘reference device’. It was observed that the THz pulse peak and the reflection feature from the open circuit interface of the gap remain unaltered with varying temperatures, as expected. The beam powers of 10 mW and pump switch bias of 30 V were kept constant throughout these measurements, and the

alignment of the position of the beams was optimised at every temperature, in order to compensate for thermal contraction of the cold finger.

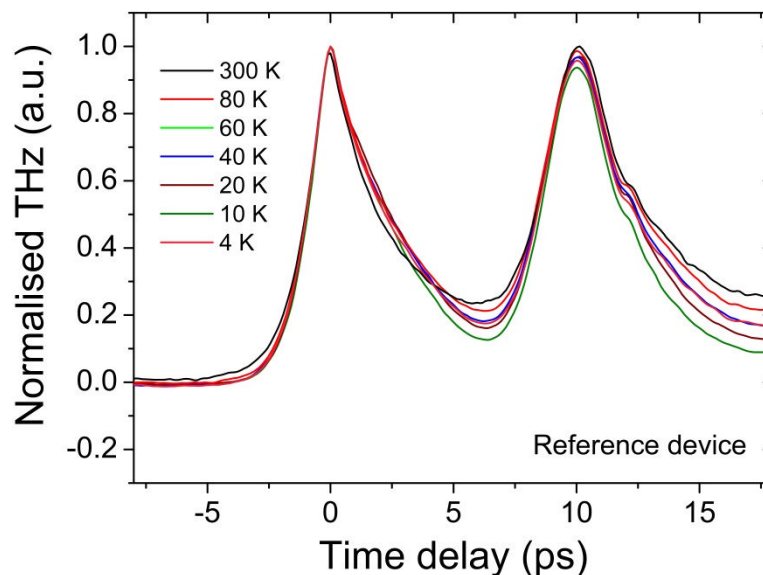


Figure 4.16 Comparison of the normalised generated THz pulse scans for the reference device, measured at varying temperatures, using switch region 1 as source and switch region 2 as detector.

The input THz pulse measurements for the CPW injection device with 2DES mesa integrated with the centre conductor at varying temperatures is shown in Figure 4.17. The most striking observation from Figure 4.17 is that the amplitude of the reflected THz signal from the 2DES drops with decreasing temperature, as the 2DES conductivity increases. As explained earlier, the electron transport in the 2DES becomes ballistic at low temperatures, the measured resistance of the 2DES mesa drops from $\sim 5 \text{ k}\Omega$ at room temperatures to $\sim 200 \text{ }\Omega$ at cryogenic temperatures, and hence it is anticipated that more THz pulse energy should couple into the 2DES and gets transmitted.

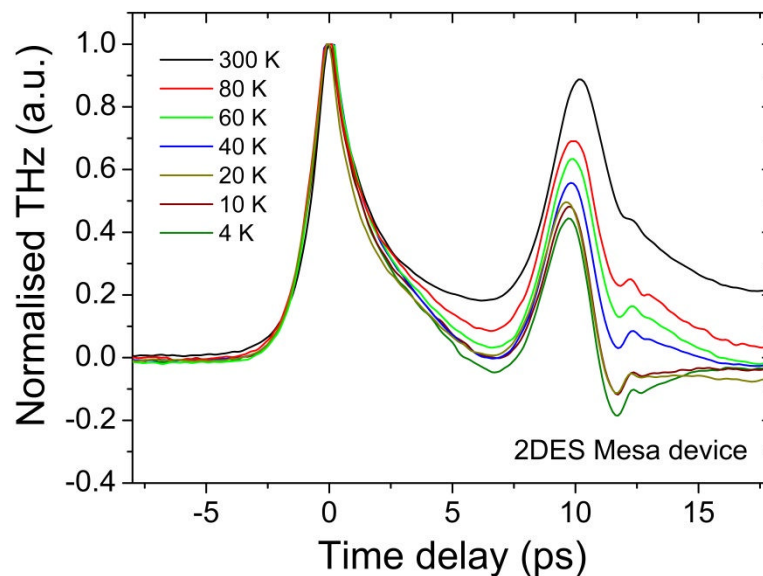


Figure 4.17 Comparison of the normalised generated THz pulse scans for the 2DES mesa device, measured at varying temperatures, using switch region 1 as source and switch region 2 as detector.

The reflection pulse amplitude plot with decreasing temperatures as shown in Figure 4.18 clearly shows that for the reference device the reflection peak remains impervious to changing temperatures, in contrast to the results for the 2DES mesa device.

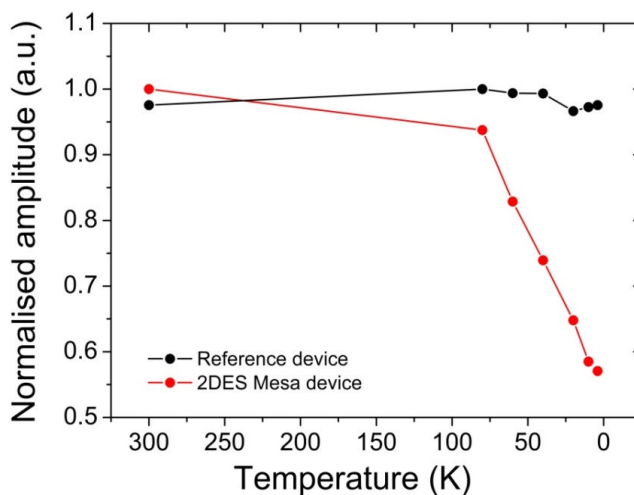


Figure 4.18 Comparison of the first reflection amplitude seen in the reference device and the pulse injection device as a function of temperature

4.3.2. Transmitted pulses

The pulses transmitted through the ‘active region’ of both CPW integrated devices are examined at different temperatures. In the same way as for the input pulse measurements, the pump and probe beams were set at beam powers of 10 mW and the pump switch was biased at 30 V. Figure 4.19 shows the alignment position of the pump and probe beams, and the arrangement used for applying bias to the switches.

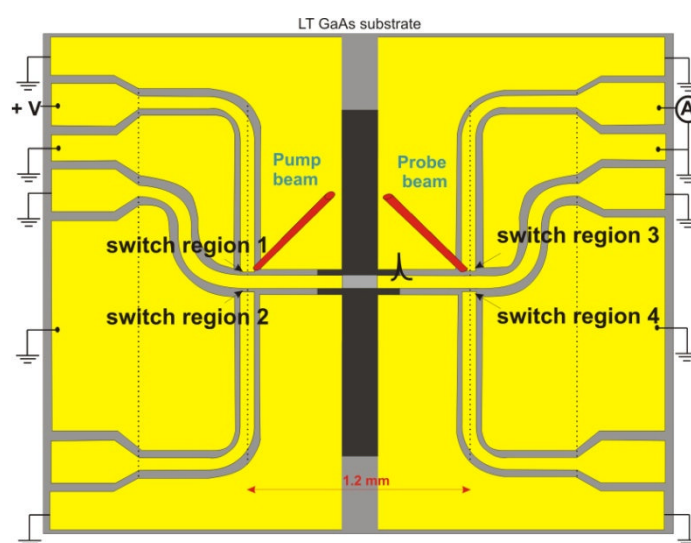


Figure 4.19 Setup for measuring transmitted pulses, showing the bias arrangement and the alignment of pump and probe beams.

The transverse electric field patterns for the guided THz pulses consists of two possible modes of pulse propagation, which depend on the symmetry of the electric field direction in the gaps either sides of the centre conductor. The mode with symmetrical electrical field pattern is described as the ‘odd mode’ as shown in Figure 4.20 (a) while the one with anti-symmetrical field pattern is referred as the ‘even mode’ Figure 4.20 (b).

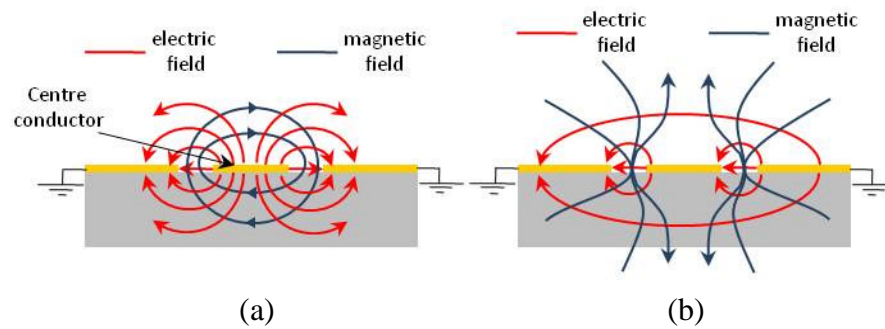


Figure 4.20 2D cross-section of the CPW, showing (a) the odd mode and (b) the even mode for the transverse propagating electric and magnetic fields.

Typically, for the THz pulse generated from a single photoconductive switch region on one side of the transmission line, the propagating pulse along the CPW has a field pattern consisting of a superposition of both these modes. A measurement of such a transmitted pulse in the reference device with a gap in the centre conductor and ground planes is shown in Figure 4.21, for varying temperatures.

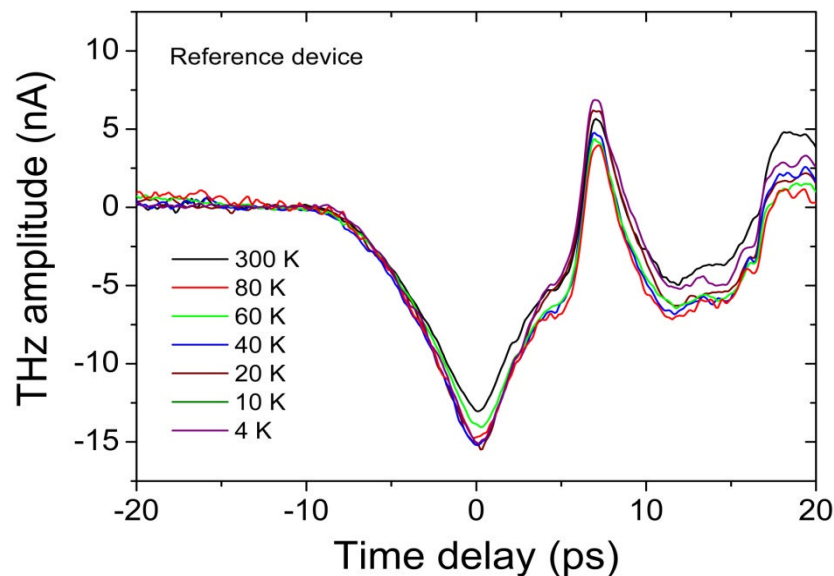


Figure 4.21 Comparison of transmitted pulses along the reference device with integrated gap, measured at different temperatures using switch region 1 as the source and switch region 3 as the detector.

The measured transmitted pulse in this case was expected to consist of mainly the even mode owing to its field pattern [127]. The ‘open circuit’ representation of the

gap in the centre conductor and the ground planes suppresses a large amount of the direct coupling power coming from the odd-mode, however the more strongly radiating even mode does get directly coupled through the integrated gap due to the shape of its field pattern.

Further analysis on the transmitted pulses on the reference device at varying temperatures was carried out by preferentially exciting both the odd and even modes as using a method previously demonstrated for photo-conductively excited coplanar waveguides [114, 128]. The preferential odd mode excitation was performed by applying equal bias voltages (V_1 and V_2) across the switch gap regions 1 and 2 as shown in Figure 4.19 ,while simultaneously illuminating both switches with the pump laser beam, and the even mode excitation was carried out by applying opposite polarity voltages ($V_1 = -V_2$).

Figure 4.22 shows examples of the pulse transmitted along the reference device, with preferential excitation of the odd and even modes. In each case the pulse was launched using pump beam power of 20 mW and detected using 10 mW. For odd mode excitation, +30 V was applied across both switch gaps 1 and 2, while for even mode excitation +30 V was applied to switch region 1 and -30 V applied to switch region 2. A direct comparison of the amplitudes of the two modes shows that the discontinuities in the centre conductor and the ground planes suppresses considerably the direct coupling of the odd mode, hence confirming that the transmitted pulse measured across the reference device consists mainly of the direct coupled even mode across the centre-conductor gap.

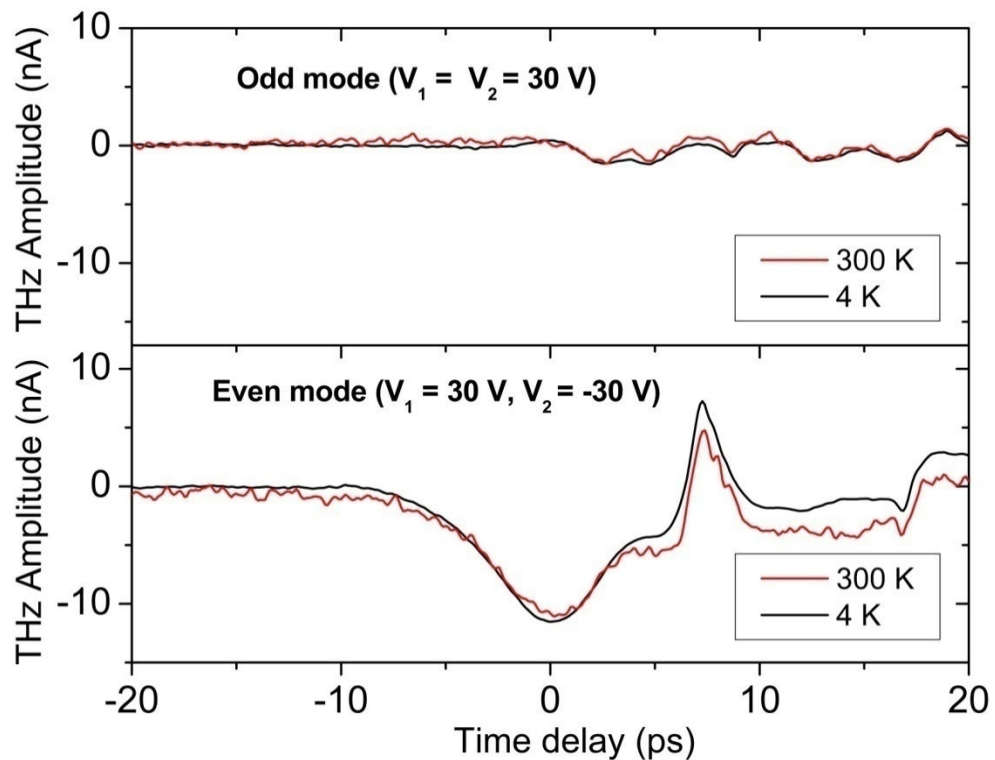


Figure 4.22 Examples of pulses transmitted through the CPW with integrated gap, with odd mode and even mode preferentially excited. The transmitted pulse scans measured at 300 K and 4 K are shown.

The measurement of the pulse transmitted through the 2DES strip for CPW injection device taken at room temperature is shown in Figure 4.23 (a). The propagating pulse in this case consists of superposition of both modes, as a single photoconductive switch was used for generation. The resemblance seen in the transmitted pulse shape for CPW coupled with 2DES (shown in Figure 4.23 (a)) and for the CPW with integrated gap at room temperatures (shown in Figure 4.21) suggested that the ‘high impedance’ representation of the 2DES strip at room temperatures also suppresses a large amount of direct coupling power coming from the odd-mode, as a result the measured transmitted pulse is likely to arise mostly from the direct coupling of the even mode.

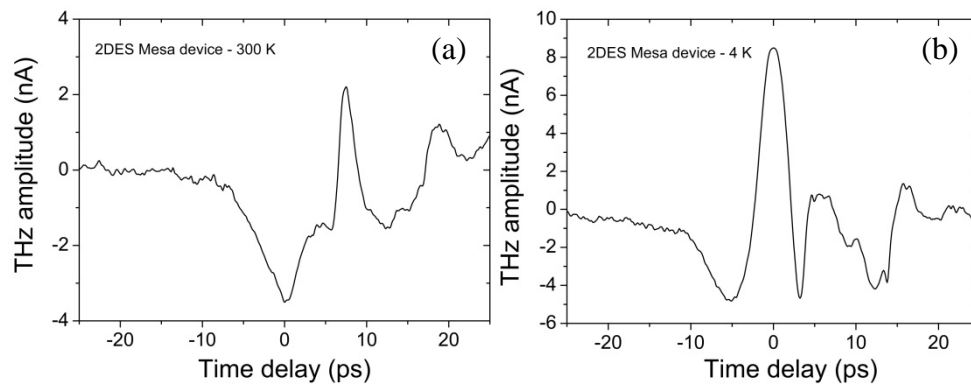


Figure 4.23 Example of transmitted pulses along the CPW device with integrated 2DES strip, measured at (a) 300 K and (b) 4 K, using switch region 1 as the source and switch region 3 as the detector.

The input pulse measurements on the CPW injection device shown in Figure 4.17 at low temperatures suggested the increase in the conductivity of the electron layer leads to more THz radiation being coupled and transmitted through the integrated 2DES region. The measurement of the pulse transmitted through the 2DES at 4 K as shown in Figure 4.23 (b) suggests that the odd-mode power coupling through the 2DES layer is now more prominent due to change in the transmitted pulse shape and increase in transmitted THz amplitude. This dependence of the 2DES conductivity on the transmitted pulses is clearly illustrated by preferentially exciting odd and even modes separately. Examples of the pulses transmitted along the CPW coupled with 2DES strip with preferential excitation of different modes are shown in Figure 4.24. The comparison of the transmitted pulses using preferential odd-mode excitation at 300 K and 4 K temperatures shows a striking dependence of the 2DES conductivity on the transmitted pulse amplitude with varying temperatures, whereas the directly coupled even-mode component of the electromagnetic radiation remains unchanged against varying temperatures. It confirms that as the 2DES conductivity increases the odd mode coupling and transmission of the THz pulse through the 2DES also increases. These

results are in qualitative agreement with theoretical predictions and the experimental results reported for preferential mode excitation in CPW [114].

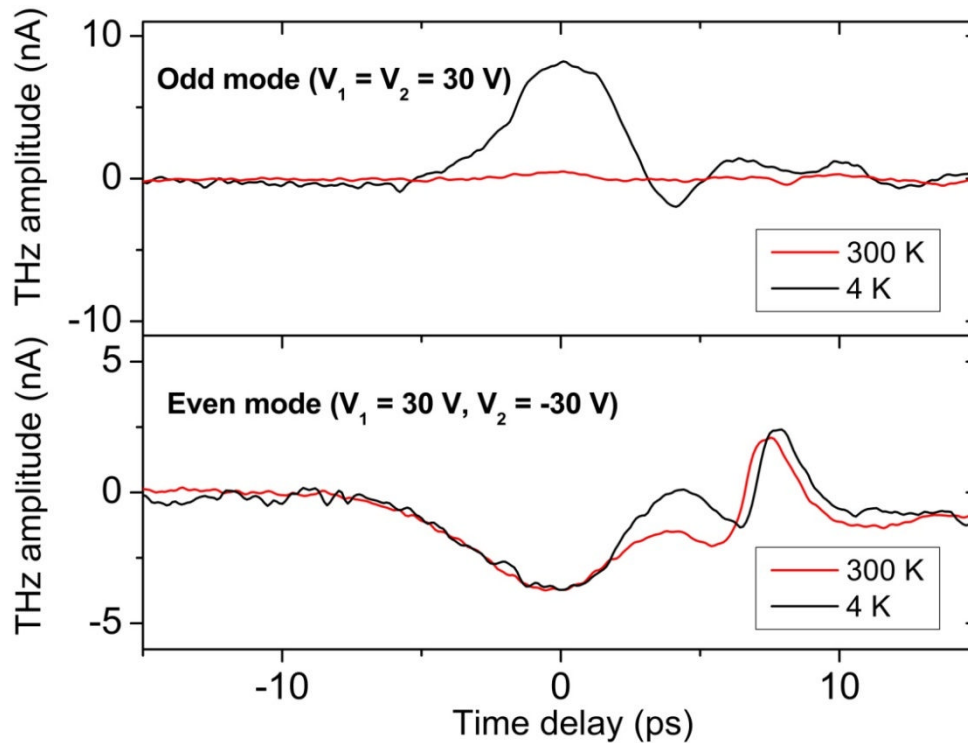


Figure 4.24 Examples of pulses transmitted through the CPW with integrated 2DES, with odd mode and even mode preferentially excited. The transmitted pulse scans measured at 300 K and 4 K are shown.

A direct comparison of the transmitted pulse peak amplitude while preferentially exciting the odd-mode for the reference device with integrated gap and for the injection device with integrated 2DES strip at varying temperatures is shown in Figure 4.25, demonstrating the rise in the transmitted pulse for injection device as the conductivity of the 2DES layer increases. Whereas, for the reference device with discontinuities in ground planes and centre conductor, the transmitted pulse amplitude remains unchanged with varying temperatures.

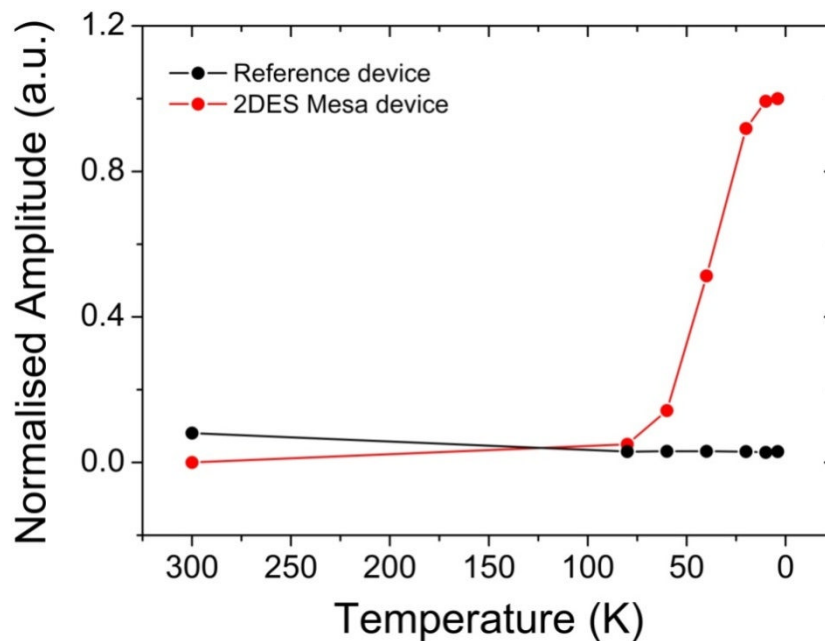


Figure 4.25 With odd mode preferentially excited, the transmitted pulse amplitude variation with decreasing temperatures compared for the reference device and the 2DES mesa device. For a direct comparison, the transmitted pulse amplitude data set shown is normalised to the maximum amplitude observed between both the devices.

4.4. Waveguide spectroscopy of 2DES

As discussed earlier, an alternative approach undertaken in this work to study picosecond time-resolved electron transport in 2DES involved waveguide spectroscopy using THz coplanar waveguides as reported previously by E. Shaner [101]. The THz electric field propagating along the waveguide can capacitively interact with the 2DES, thereby allowing the conductivity behaviour of the 2DES to be extracted as described in section 4.2.2. In addition, measuring the interaction between the picosecond timescale pulses with the 2DES acting as a dielectric layer can lead to a more thorough understanding of the origin of collective 2D plasmon resonances in the electron layer.

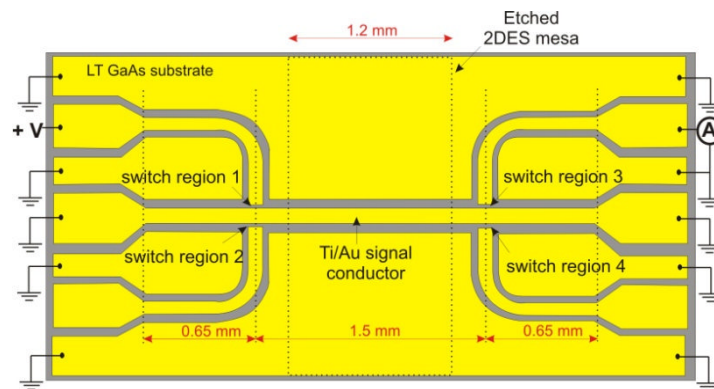


Figure 4.26 Diagram of the capacitive field coupling THz CPW device, containing active region of the signal conductor and ground planes overlaid on top the 1.2 mm long ‘sub-mesa’ containing the 2DES.

Figure 4.26 shows the complete design of the coplanar waveguide devices. The waveguide geometry used consists of a 30 μm wide centre conductor with 20 μm gap between the ground planes on either side. The active region of the waveguide (i.e. the region between the PC switches) was 1.5 mm long and overlaid on top of the 1.2 mm long defined 2DES mesa. The integrated photoconductive switches for THz generation and detection were patterned on the exposed LT-GaAs surface. The preliminary experiments for waveguide spectroscopy of the 2DES using ‘capacitively coupled waveguide devices’ at room and cryogenic temperatures are discussed below.

4.4.1. Room temperature device characterisation

Using the THz-TDS setup as discussed in section 4.2.3 and shown in Figure 4.8, waveguide spectroscopy was performed on the 2DES. First with the capacitively coupled waveguide devices mounted in the continuous flow cryostat, pump/probe pulse measurements were performed at room temperatures (300 K). Figure 4.27 shows the generated pulse before propagation along the waveguide measured by focusing pump and probe beams of identical beam powers (10 mW) at switch regions 1 and 2 respectively. The pump switch was biased at 10 V.

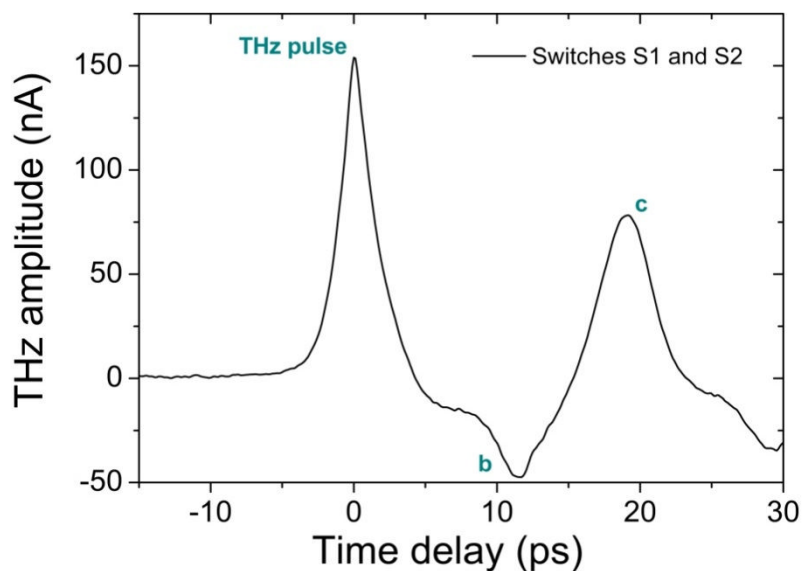


Figure 4.27 Example of an input pulse measured for a capacitive coupling waveguide device at 300 K, using switch region 1 as source and switch region 2 as detector.

The time-domain THz pulse scan consists of the main THz pulse with a FWHM of ~ 2.4 ps followed by secondary reflections 'b' and 'c', identified to be arising from the discontinuities in the transmission line. The propagation path of these reflection features is demonstrated in Figure 4.28.

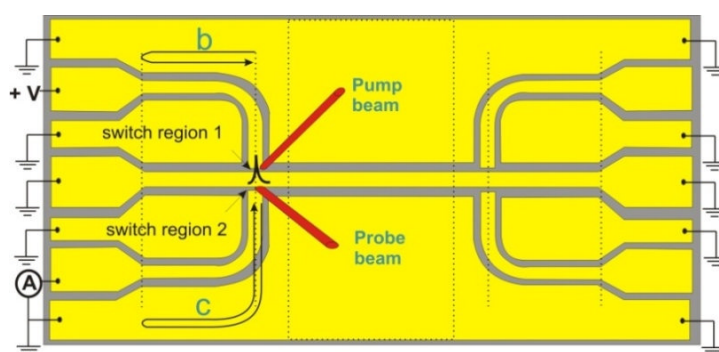


Figure 4.28 Schematic of the pulse path creating secondary reflections 'b' and 'c', following the main generated THz pulse.

Since the parasitic regions of the waveguide in this CPW device pattern were much shorter than the CPW device pattern used for picosecond pulse injection experiments, the time delay between the THz pulse and secondary reflections was much shorter, thereby reducing the resolution of the CPW frequency spectra. The pulse transmitted along the waveguide with active region overlaid on top of the 2DES was then measured by probing at switch region 3, and the time-domain pulse scan obtained is shown in Figure 4.29.

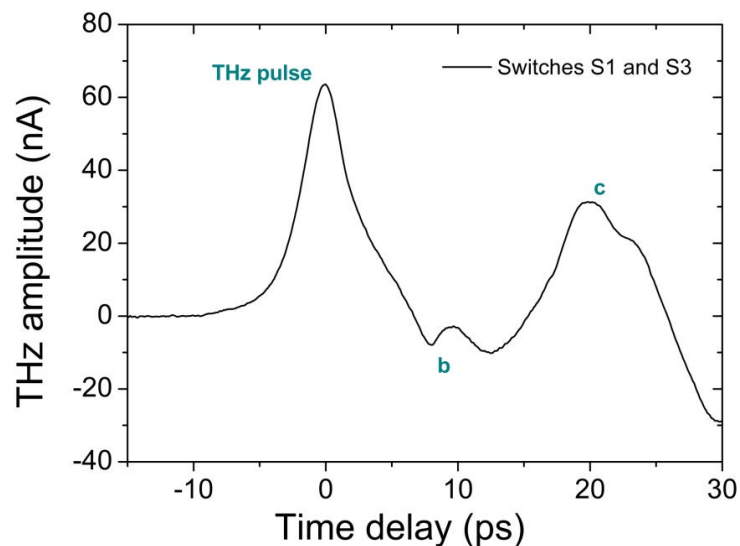


Figure 4.29 Example of a transmitted pulse measured for capacitive coupling waveguide device at 300 K, using switch region 1 as source and switch region 3 as detector.

It was observed from the transmitted pulse scan that the pulse shape was identical to the generated pulse as shown in Figure 4.27, with the main THz pulse peak with a FWHM of ~ 3.9 ps followed by secondary reflection in the time-domain signal. As understood from section 4.2.2, the conductivity of the 2DES layer is very low at room temperatures, so the impact of the 2DES acting as a shunt conductance element on the transmitted pulses propagating along the waveguide above would be negligible. Hence the attenuation observed in the transmitted pulses is mainly due to the frequency dependent conductor loss $\alpha_{cond}(\omega)$,

$$\alpha_{cond}(\omega) = Re \left[\frac{Z_s(\omega)}{Z_0} \right], g \text{ in } \frac{db}{mm} \quad (4.3)$$

where Z_s is the surface impedance of the Au conductor used and g is an additional geometrical factor [129]. Waveguide loss is discussed in more detail in Chapter 1, Section 1.6.3. Also, the pulse broadening results mainly from the frequency dependent loss cause by dielectric GaAs substrate, having effective permittivity of ϵ_{eff} ,

$$\epsilon_{eff} = \frac{1}{2} (\epsilon_{GaAs} + 1) \quad (4.4)$$

4.4.2. 2DES spectroscopy at cryogenic temperatures

The pulses transmitted along the CPW were then measured as the operating temperature of the device was systematically reduced to the base temperature of the continuous helium flow cryostat (4 K). Figure 4.30 shows the comparison of the normalised time-domain pulse scan observed for pulses transmitted along the CPW overlaid on top of the 2DES mesa at temperature intervals of 20 K from 120 K to 4 K.

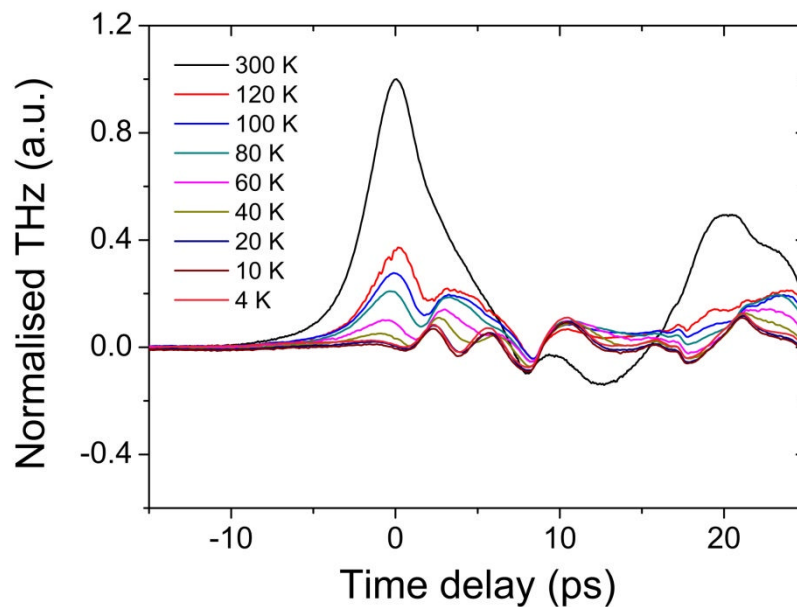


Figure 4.30 Comparison of time-domain transmitted pulse scan measured at varying temperatures on capacitive field coupling device.

Examining Figure 4.30, the amplitude and pulse shape of the picosecond time-resolved pulse has been altered by effectively increasing the conductivity of the 2DES with decreasing temperature. As expected, with increase in conductivity of the 2DES, the portion of the propagating signal being absorbed by the electron layer increases.

This attenuation in the transmitted signal due to 2DES can be understood as shown in [130], if $V(t, 0)$ is considered to be the generated time-domain waveform. The propagating waveform along the waveguide overlaid on conductive substrate at a point z is $V(t, z)$, is given by,

$$V(t, z) = F^{-1}[F\{V(t, 0)\} \exp\{-\Upsilon(f)z\}] \quad (4.5)$$

where, $F\{\cdot\}$ denotes the Fourier transform of $\{\cdot\}$, and $F^{-1}[\cdot]$ the inverse Fourier transform of $[\cdot]$, and $\Upsilon(f)$ the damping coefficient given by [131],

$$\Upsilon(f) = \alpha(f) + j\beta(f) = \frac{f}{c} \sqrt{\epsilon_{eff}(f)} = \sqrt{Z(f)Y(f)} \quad (4.6)$$

The parameters $\alpha(f)$ and $\beta(f)$ of the damping coefficient $\Upsilon(f)$ are the frequency dependent attenuation and phase factors of the voltage signal. Where, $\alpha(f)$ mainly arises from the radiation, conductor and dielectric losses and $\beta(f)$ determines the degree of dispersion a signal experiences. For a highly conductive plane such as a 2DES layer located in close proximity to the CPW, the dielectric loss dominates the damping coefficient, considering the amount of the electric field mode residing in the 2D electron layer. Hence from Equation 4.2, 4.5 and 4.6, it can be understood that the 2DES in parallel with the CPW acts as shunt admittance, thereby reducing the amplitude of the transmitted signal. The variation of the transmitted pulse peak with reducing temperatures, i.e. increasing 2DES conductivity, is shown in Figure 4.31.

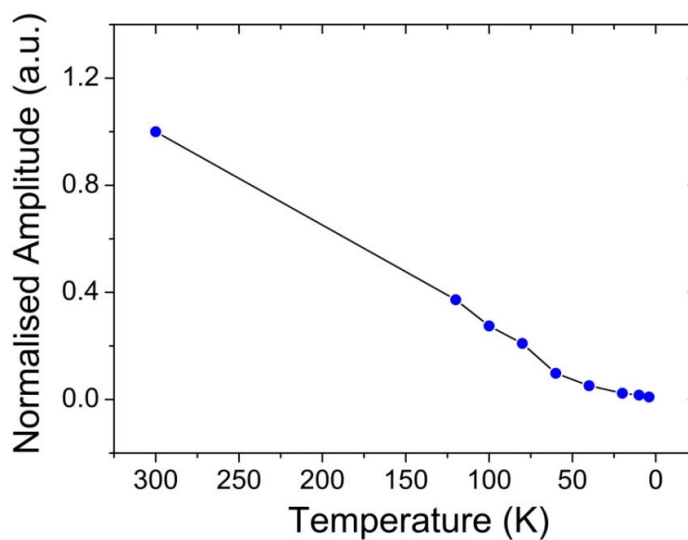


Figure 4.31 Variation of transmitted pulse amplitude with decreasing temperatures or increasing 2DES conductivity.

The data also show low amplitude oscillations observed in the time-domain transmitted signal at 4 K, as shown in Figure 4.32. These oscillations were tentatively attributed to a standing wave being created within the 2DES mesa of length 1.2 mm as shown in Figure 4.26.

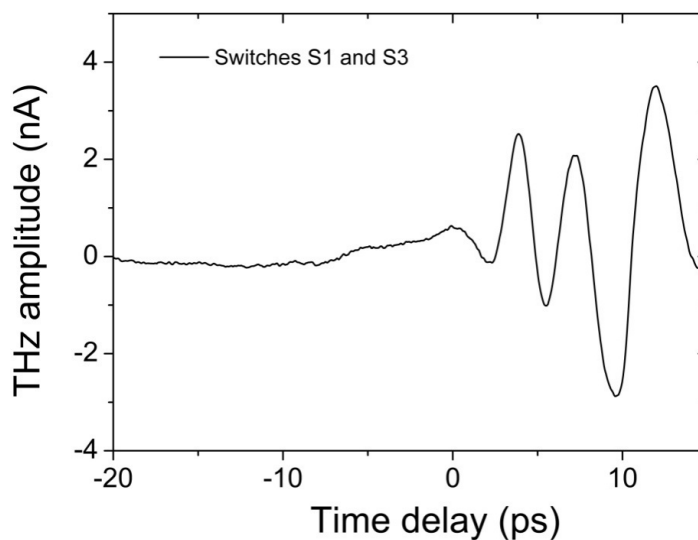


Figure 4.32 Example of a time-domain pulse transmitted along the CPW on capacitive coupling device at 4 K, using switch region 1 as source and switch region 3 as detector.

Considering the electric field propagation along the CPW patterned over 2DES mesa at low temperatures, the conductive 2DES layer below the CPW acts as a secondary ground plane located in close proximity to the signal (centre) conductor, consequently creating a transmission medium similar to lossy microstrip line for sustaining a standing wave. The fundamental frequency of the standing wave is governed by the length of the 2DES mesa and is given by,

$$f = V_P / 2\lambda = 51.67 \text{ GHz} \quad (4.7)$$

where, V_P is the pulse propagation velocity along the CPW and λ is the length of the 2DES mesa along the CPW.

To further characterise the frequency of the standing wave being created in the 2DES mesa, a frequency domain analysis was implemented. Figure 4.33 shows the Fourier transform amplitude of the signals displayed in Figure 4.30 at various temperatures. To produce a clean transform, a rectangular window was first applied to the data to cut off the data beyond 10 ps (i.e. before the first reflection occurring due to waveguide discontinuity).

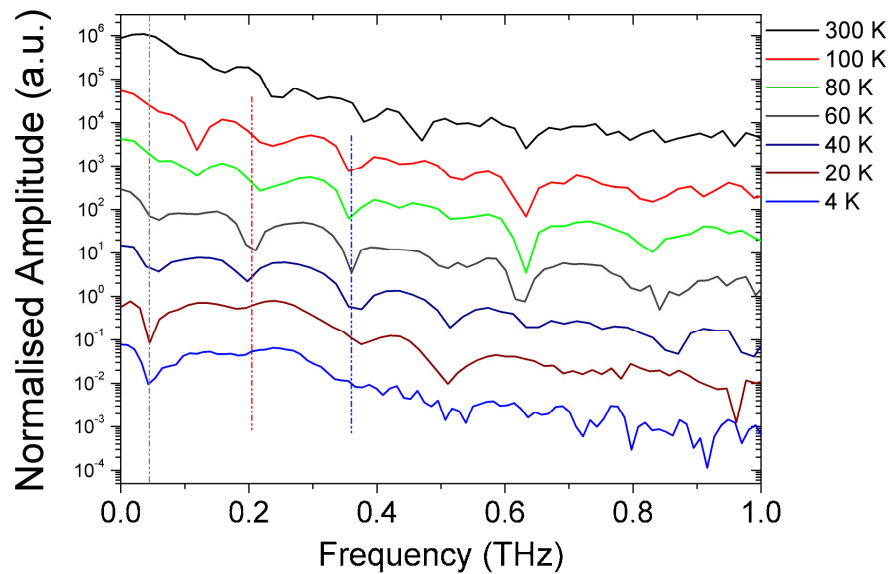


Figure 4.33 Frequency spectrum comparison of the transmitted time-domain signals observed at varying temperatures and as shown in Figure 4.30. The (grey) dashed line corresponds to the fundamental frequency of the standing wave, with resonance frequencies of the second and third order harmonics shown by (red and blue) dashed lines.

The frequency spectra shown for the transmitted pulses at low temperatures clearly shows absorption at frequency corresponding to the fundamental frequency of the standing wave created within the 2DES mesa. Also, the absorption at frequencies corresponding to the higher harmonics of the fundamental frequency of the standing wave was also observed. It is noted, that the frequency resolution of the measurement was limited due to the short time delay between the main pulse and the secondary reflections and can be easily improved in future generation devices.

4.5. Summary

This chapter has examined the effect of interaction between ultra-short timescale pulses with a highly conductive 2D electron layer. The capability of THz waveguides for spectroscopy of 2DES at varying temperatures has been demonstrated.

The transmission spectroscopy work discussed using ‘picosecond pulse injection waveguides’, shows the direct electrical measurement of transport through the electron layer at picosecond timescales by integrating the 2DES into the signal conductor of the waveguide. It clearly illustrates the transmission of picosecond pulses through a short strip of 2DES as the conductivity of the electron layer increases by decreasing temperatures. On the other hand, the waveguide spectroscopy of the 2DES was also established by using ‘capacitive coupling waveguides’, where the electric field from the propagating pulses capacitively interacted with the 2D electron layer. The behaviour of 2DES conductivity against varying temperatures was understood in terms of transmitted pulse shape and amplitude.

The work shown in this chapter provides a very good platform for understanding ballistic transport and charge density perturbation (plasmons) in 2DES at picosecond time scales under magnetic fields, which will be the subject of the following chapter.

The work presented in this chapter formed the basis of several publications, listed on page 187.

Chapter 5: THz interaction with 2DESs at milli-Kelvin temperatures and under magnetic fields

5.1. Introduction

Having established CPW-based techniques for interacting THz radiation with 2DESs at cryogenic temperatures, work was undertaken subsequently to investigate the response of the system under magnetic fields, which is the subject of this chapter. It is understood that high frequency electrical characterisation of a 2DES under magnetic fields permits the study of important physical phenomena such as cyclotron resonance and magneto plasmons [11, 24, 132, 133]. Firstly, analytical modelling of high frequency phenomena observed in a confined 2D electron layer under influence of magnetic fields will be presented. The rest of the chapter will be devoted to experimental measurements of picosecond pulse propagation through the 2DES under magnetic fields at milli-Kelvin temperatures. The results presented here represent an important step in improving the capabilities for studying quantum-confined ballistic electron transport on a picosecond timescale. Further details of the CPW devices, having capabilities of simultaneous DC and picosecond characterisation of the 2DES, will also be presented.

5.2. Analytical modelling of THz pulse interactions with confined 2DES

The electron velocities within the 2DES is much slower than the typically measured THz signal propagation times (typically a few ps) over similar length scales. Hence, the electrons entering from one end of the coupled 2DES (source) are not the same ones that leave the other end (drain). The electromagnetic field associated with the charge carriers instead affects adjacent electrons, allowing the disturbance to propagate along the mesa at the speed of an electromagnetic wave. In effect, putting an electron at one end of a conductive 2DES causes one to come out the other end. This resulting non-equilibrium in the charge density of 2DES causes plasmon excitation of the 2DES. The origin and behaviour of these plasmonic oscillations under magnetic fields for the geometry of the 2DES used for this work is as discussed.

If we assume ballistic transport in the 2DES (i.e. negligible scattering), the picosecond pulses injected into the 2DES cause electrons to move beyond their equilibrium positions in the initially electro-neutral 2DES, due to inertia. As a result charge density fluctuations are created along the confined layer. As shown in Figure 5.1, if a band of electrons with length L is shifted by a small distance δx in the X-direction under the influence of an electric field E , a charge density fluctuation has been created. This extra charge induces an electric field, which drives the electrons along its direction to compensate for the initial charge. The repeating process causes a plasma oscillation, and the collective excitations of charge carriers in a 2DES are called 2D (bulk) plasmons [134].

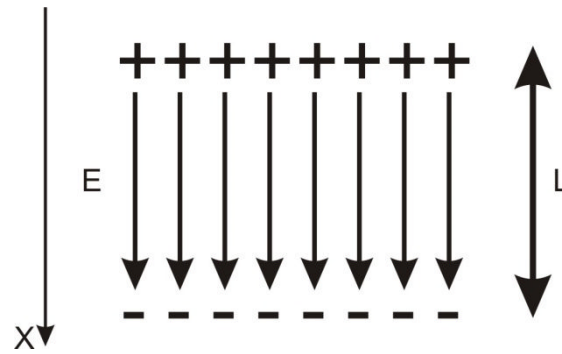


Figure 5.1 Charge fluctuation in a 2DES of length L , created by primary applied electric field E .

As demonstrated by F. Stern [135], the 2D plasmon dispersion in the long wavelength limit for a confined 2DES can be modelled using,

$$\omega_p^2(k) = \frac{ne^2}{2m^*\epsilon\epsilon_0} k_1 k_2, \quad (5.1)$$

where ω_p describes the frequency of the collective charge oscillation in a 2DES with charge density n , dielectric permittivity ϵ and effective mass m^* at a wave vectors k_1 and k_2 oriented in a 2D plane. The allowed values for the wave vectors depend on the physical dimensions of the 2D electron layer, and are given by,

$$k_1 = \frac{i\pi}{w} \qquad k_2 = \frac{i\pi}{l} \quad (5.2)$$

where, w is the width of the 2DES, l is the length of the 2DES and i is an integer representing the number of plasmon oscillation modes.

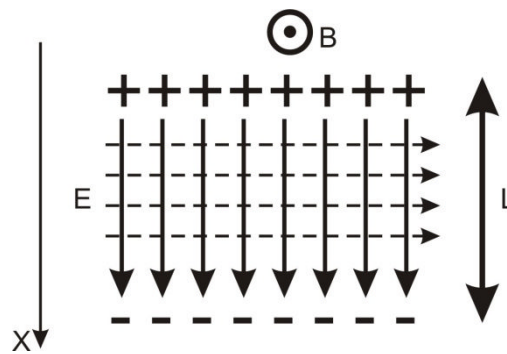


Figure 5.2 Charge fluctuation in a 2DES of length L , created by an externally applied electric field E and also external magnetic field B perpendicular to the 2DES.

However, in presence of a perpendicular magnetic field, the plasmon excitations in the 2DES are also governed by the cyclotron motion of electrons. Figure 5.2 shows an illustration of the modified charge density fluctuations under a magnetic field. This leads to a resultant dispersive mode which is influenced by both the plasmon oscillations and the cyclotron motion of electrons in a 2DES [136]. The resultant bulk magneto plasmon resonance frequency, ω_{bmp} as a function of magnetic field B , can be modelled using,

$$\omega_{bmp}^2(B) = \omega_p^2(k) + \omega_c^2 \quad (5.3)$$

where ω_c , as discussed in Chapter 1, Section 1.4.3, corresponds to the cyclotron resonance frequency and is given by,

$$\omega_c = eB/m^* \quad (5.4)$$

Considering the pulse injection waveguide device described in the previous chapter (as shown in Figure 4.1), the THz pulses are electrically channelled directly to the $30 \mu\text{m}$ wide and $100 \mu\text{m}$ long 2DES. The bulk magneto plasmon modes generated under magnetic field by the ps-timescale pulse injection into the 2DES, were modelled using a MatLab program based on Equations 5.1 – 5.4. The physical properties of the 2DES (such as sheet density, n_s) required for the simulation were determined by performing QHE measurements under magnetic field on a Hall bar sample fabricated

from the same wafer as discussed in Chapter 2, Section 2.5.1. The values of n_s were found to be $3.5 \times 10^{11} \text{ cm}^{-2}$ in dark conditions and $6 \times 10^{11} \text{ cm}^{-2}$ under illumination (using a 800 nm red LED). The observation of magneto plasmon resonances in the 2DES under illumination was crucial to provide understanding of the influence of 800 nm radiation on the electron density of the 2DES, as similar wavelength radiation is used for photoconductive THz generation and detection in LT-GaAs-based photoconductive switches used in all devices presented in this thesis.

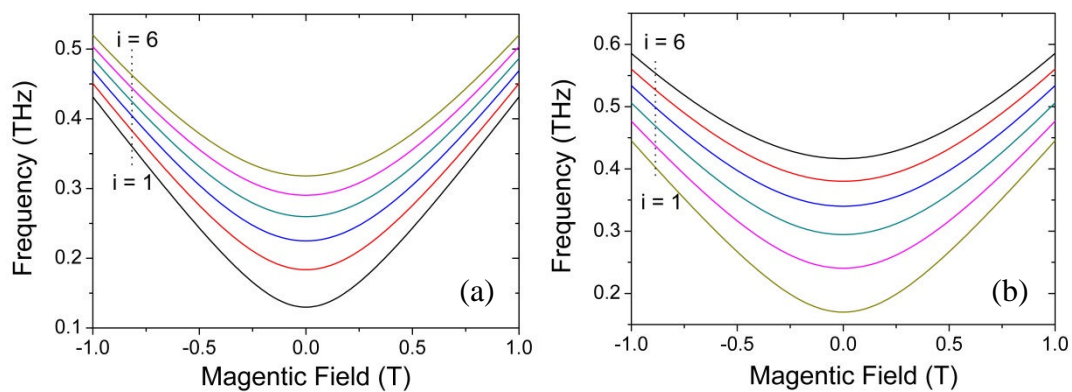


Figure 5.3 Analytical simulations showing the first six magneto plasmon modes ($i = 1...6$) in a 2DES with a fixed confinement width of ($x \text{ um}$), for different charge densities measured under (a) dark conditions (Sheet density, $n_s = 3.5 \times 10^{11} \text{ cm}^{-2}$) and (b) under illumination (Sheet density, $n_s = 6 \times 10^{11} \text{ cm}^{-2}$).

Figure 5.3 shows the MatLab simulation of the first six bulk magneto plasmons modes generated in the 2DES coupled to the THz CPW waveguide device, both (a) in the dark (b) when illuminated. From the simulation results shown, and considering Equation 5.3 and 5.4, it is noted that with increasing magnetic field, the resonance due to cyclotron motion of electrons in the 2DES dominates the resultant bulk magneto plasmon dispersion, as the dispersion modes observed due to 2D bulk plasmons is independent of magnetic fields ($\omega_c \gg \omega_p$). It is also observed that, a device of equal physical size, the frequency spacing between the bulk magneto plasmon resonances

modes increases as the charge density of the 2DES increases (achieved here by introducing extra carriers under illumination).

In addition, the influence of physical dimensions of the confined 2DES on the resulting magneto plasmons modes was also simulated. Figure 5.4 shows a comparison between the simulation of magneto plasmon resonance modes for a 2DES having charge density of $6 \times 10^{11} \text{ cm}^{-2}$ and two different confined electron layer size of (a) $30 \times 30 \text{ }\mu\text{m}$ and (b) $1 \times 1 \text{ mm}$. A clear dependence of the physical confinement of the 2DES on the frequency spacing of individual magneto plasmon modes was observed. It is also noted, as the 2DES confinement size increases, the spacing between the resonance modes decreases.

Hence, in bigger samples with larger 2DES confinement perimeter, it was found that the resonance features due to the cyclotron motion of electrons is the dominating dispersion mode in the 2DES, even at low magnetic fields, and masks the weaker bulk plasmon dispersion modes.

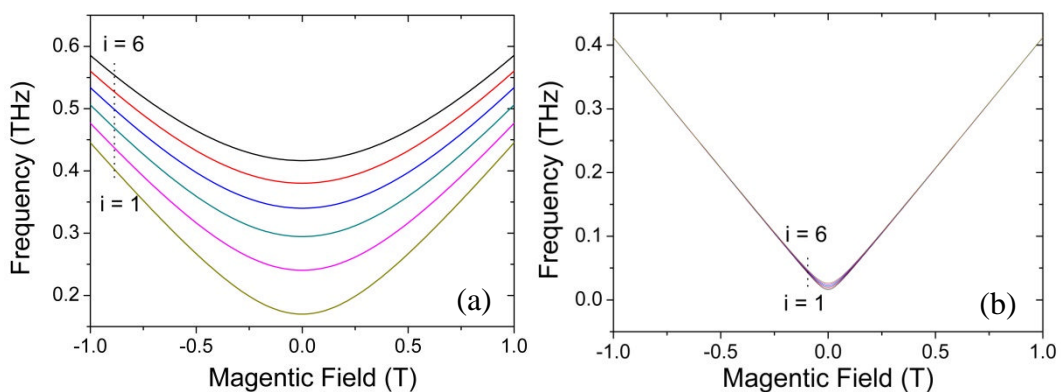


Figure 5.4 Analytical simulations showing the first six magneto plasmon modes in a 2DES, considering identical charge densities under illumination ($n_s = 6 \times 10^{11} \text{ cm}^{-2}$) with different 2DES confinement width of (x μm) (a) $30 \text{ }\mu\text{m}$ and (b) 1 mm .

The analytical simulations carried out in this work clearly show that the frequency of the magneto plasmons observed in a confined 2DES lie in the THz

frequency range and are therefore expected to interact with a THz pulse propagating along the coupled on-chip waveguide. For the pulse injection waveguide device used in this work, it was anticipated to see a resemblance between the bulk magneto plasmon frequencies derived from analytical simulations and any resonant absorption frequencies determined from the pulse injection measurements of the 2DES.

5.3. Picosecond pulse injection into a 2DES under magnetic field

This section presents the measurements of ps timescale pulse transmission through a 2DES at milli-Kelvin temperatures and under magnetic fields, using a dilution refrigerator. The on-chip THz-TDS setup, discussed in Chapter 3, Section 3.2.3, was used to implement pump-probe sampling measurements in a cryogenic environment. The sample was held at the centre of the 12 T magnet integrated into the dilution refrigerator, using the sample holder as shown in Figure 3.11. Ohmic contacts on either side of the 2DEG mesa, connected to the CPW centre conductor, allowed 2-terminal DC characterisation of the 2DES' transport characteristics under magnetic field [137], together with ps pulse transmission measurements.

5.3.1. DC characteristics of 2DES

The experimental arrangement used for observing DC transport properties of the 2DES coupled to the CPW centre conductor is shown in Figure 5.5. Two-terminal measurement geometry was used in order to measure the DC magneto conductivity of the 100 μm long and 30 μm wide 2DES strip. With the sample mounted in the cryogenic sample holder and the pump-probe laser beams off, the bath temperature was noted to be < 26.14 mK.

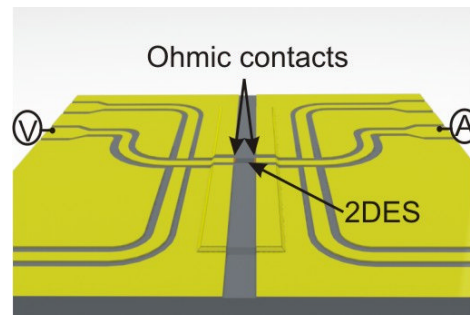


Figure 5.5 The experimental arrangement for measuring DC transport properties of the coupled 2DES with the centre conductor. The 2DES resistance is extracted by measuring the current under constant DC bias applied using a two-terminal geometry.

A contact resistance of 500Ω was measured across the centre conductor / 2DES mesa at cryogenic temperatures. As anticipated, owing to ballistic behaviour in the 2DES at low temperatures, the resistance value was considerably lower than the $5 \text{ k}\Omega$ measured at room temperature. The DC electrical current through the 2DES, measured by applying constant voltage of $100 \mu\text{V}$ to either side of the centre conductor and sweeping the external magnetic field, is shown in Figure 5.6.

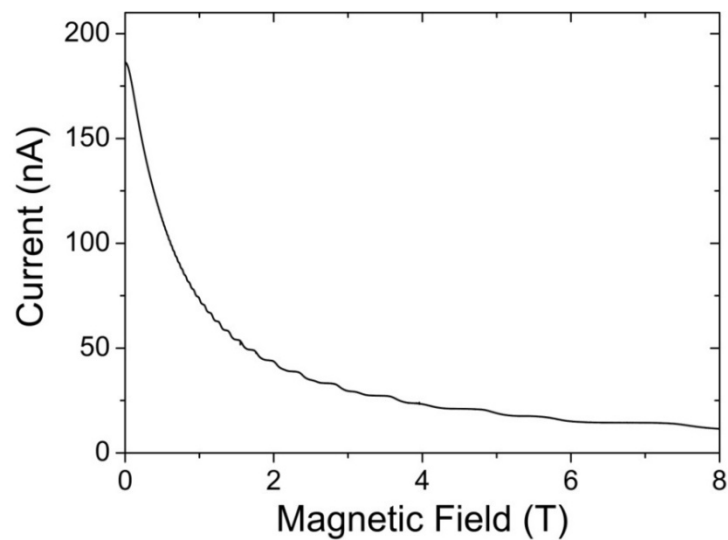


Figure 5.6 Current measured through a 2DES coupled with the centre conductor of a THz waveguide device, measured as a function of applied magnetic field.

The current measured under varying magnetic field showed direct dependence on the magneto conductivity of the 2DES, given by Equation 5.5, where j is the current density arising from carrier motion in the 2DES driven by an electric field E .

$$j = E\sigma_{2DES} \quad (5.5)$$

From the discussion of transport coefficients in a 2DES in Chapter 1, Section 1.4.2, due to the two dimensional nature of the motion of carriers, the 2DES conductivity tensor measured by the two-terminal conductance measurement technique is given by:

$$\sigma_{2DES} = \begin{pmatrix} \sigma_{xx} & \sigma_{xy} \\ \sigma_{yx} & \sigma_{yy} \end{pmatrix} \quad (5.6)$$

where σ_{xx} (σ_{yy}) represent the diagonal conductivity in the direction of E , and σ_{xy} (σ_{yx}) represents the Hall conductivity perpendicular to E . Figure 5.7 shows the behaviour of 2DES conductivity under magnetic fields.

The pronounced features of a Hall conductivity plateauing is clearly illustrated as the system approaches quantum Hall regime, while the diagonal conductivity represents the finite conductivity of the 2DES at zero magnetic fields.

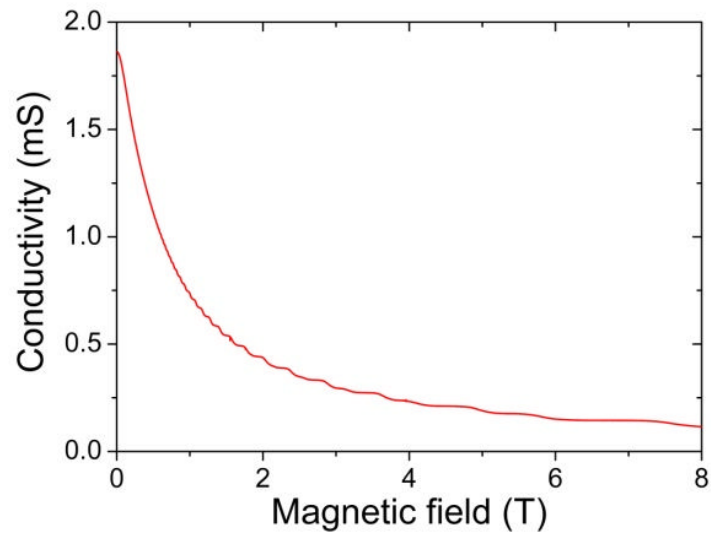


Figure 5.7 Two-terminal 2DES conductance measured as a function of magnetic field.

Since the 2DES resistivity tensor is an inverse matrix of σ , the resistance measurement of the 2DES at zero magnetic field should include only the diagonal resistance component and the contact resistance. After subtracting the zero field resistance, the resistance plot shown in Figure 5.8, which is dominated by the quantum Hall resistance, illustrates plateauing at precisely quantized integer values of $h/\nu e^2$ (where ν is an integer).

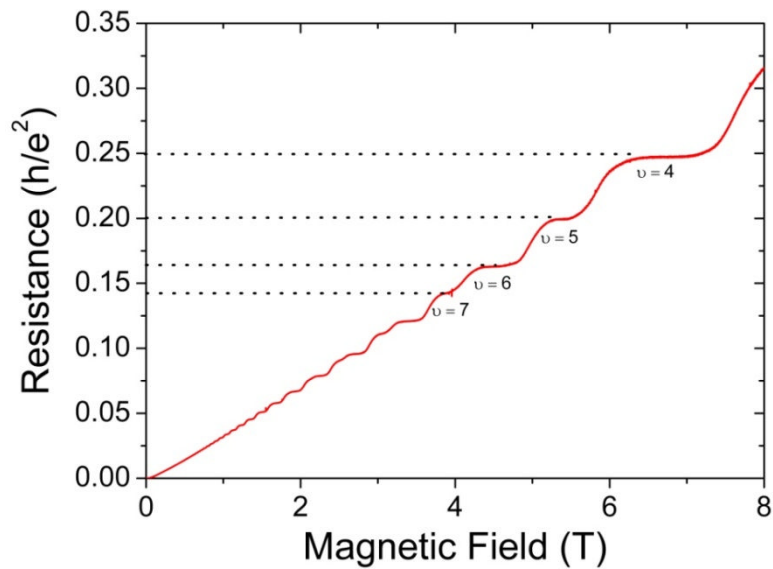


Figure 5.8 The Hall resistance measured from the 2DES coupled with the THz waveguide. Hall resistance is quantized at values of $h/\nu e^2$.

5.3.2. Sample temperature

For the DC transport measurements through the 2DES discussed in the previous section, the sample was placed in the cryogenic sample holder with no pump-probe laser beams illuminating the sample space.

In order to perform THz frequency transport measurements, the optical intensity of the pump-probe laser beams illuminating the PCS was kept to 4 mW. This increased the bath temperature to 400 mK due to thermal loading. However the actual temperature of the sample with the integrated 2DES (which influences the transport characteristics) cannot be accurately determined from the bath temperature or mounted thermometry devices.

It is suggested by Ma *et al* [137], in order to measure the sample temperature accurately, the temperature dependent transport characteristics of the 2DES, such as the amplitude of diagonal resistivity oscillations should be monitored. Owing to the two-terminal measurement setup, it was not possible to measure the weaker diagonal

resistivity component independently. The stronger Hall resistivity component of the 2DES was then observed while illuminating the photoconductive switches that are integrated on the sample.

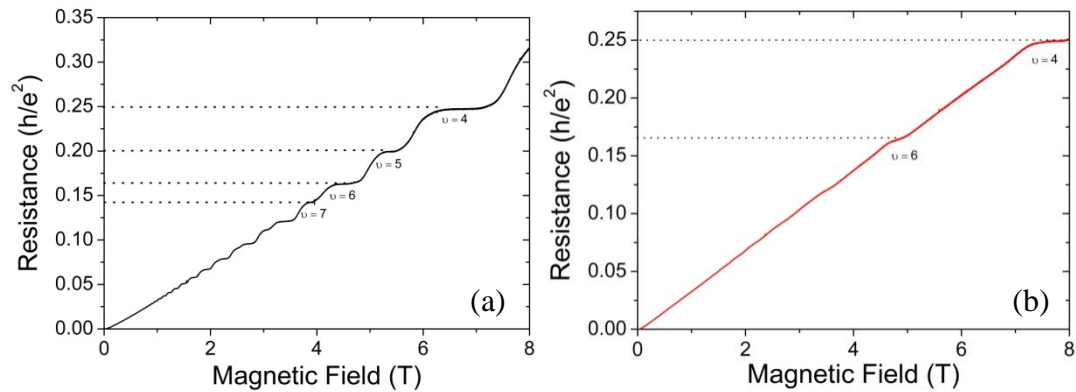


Figure 5.9 The Hall resistivity measured from the 2DES coupled with the THz waveguide (a) in the dark and (b) under illumination by an 800nm pump-probe laser beam arrangement. Hall resistance is quantized at values of $h/\nu e^2$.

The comparison of the Hall resistivity measured through the 2DES strip under dark and laser-illumination conditions is shown in Figure 5.9 (a) and (b) respectively. A significant change in the quantum Hall features were observed due to the influence of the scattered laser beams on to the charge density of the 2DES. The system degeneracy observed in the form of lower field quantum Hall features smearing out, suggested a distinct increase in the sample temperature under (~ 4 mW laser power) illumination conditions. This increase in the sample temperature under illumination conditions can be limited by considering optical excitation of PCS using lower optical beam power.

Also, four-terminal Hall bar geometry of the 2DES, as illustrated in Figure 5.10, is suggested to be coupled with THz CPW in the future. This will enable determination of both the Hall and diagonal 2DES resistance independently, required in order to determine accurately the sample temperature.

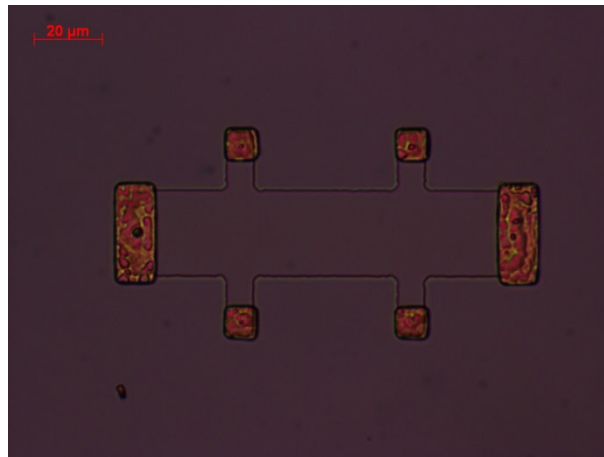


Figure 5.10 Hall bar configuration for coupling 2DES with THz CPW to perform *in situ* four-terminal quantum Hall characterisation.

5.3.3. Input pulses

After measuring the DC electron magneto transport properties of the 2DES integrated into the CPW, the corresponding THz frequency behaviour of same system was investigated. Both generated (input) and transmitted (output) pulses through the 2DES were measured, to obtain quantitative information about the 2DES magneto conductivity. The pump and probe laser beams with intensities of 1 mW were used for PCS excitation, while the pump switch was biased at 10 V. The operating bath temperature at the mixing chamber plate was noted to be 200 mK. As previously mentioned in Chapter 3, Section 3.4.1, the PCS photocurrent was optimised using piezoelectric stages to maximise THz generation and detection efficiency. The generated time domain pulse scan measured by illuminating adjacent photoconductive switch regions (1 and 2) at 200 mK and 0 T magnetic fields is shown in Figure 5.11.

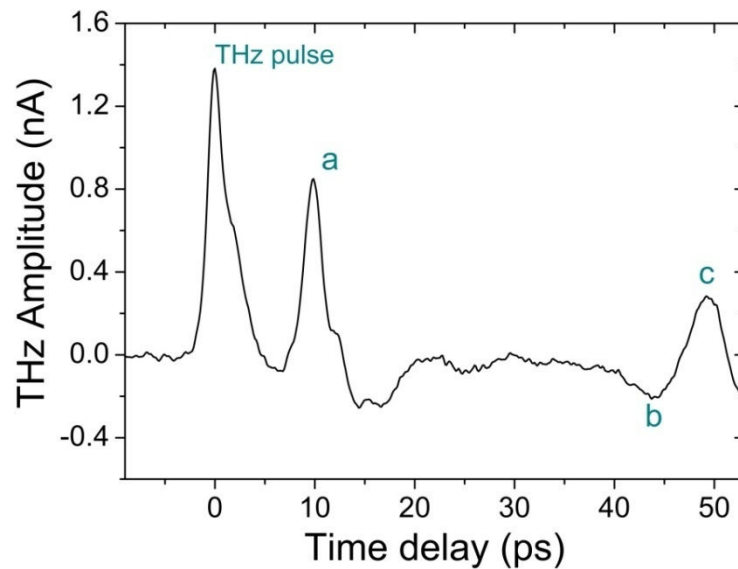


Figure 5.11 Experimental data of the generated THz pulse with secondary reflections for pulse injection device taken at 200 mK and 0 T magnetic field, using PCS 1 as the source and PCS 2 as the detector.

The input time domain pulse scan showed the main THz pulse peak, followed by several secondary reflections arising from waveguide discontinuities. Owing to the impedance mismatch between the CPW ($\sim 50 \Omega$) and the coupled 2DES strip ($\sim 200 \Omega$) at cryogenic temperatures, the first reflection, 'a', identified as originating from the CPW-2DES interface, showed no further decrease in amplitude relative to the generated pulse than was observed in the previous measurements carried out at 4 K (Chapter 4, Section 4.3.2). This observation was validated by comparing the measured contact resistance of the 2D electron layer both at 4 K and 200 mK, which was found to be identical. The two subsequent reflections, 'b' and 'c', were attributed to waveguide discontinuities, as discussed in Chapter 3, Section 3.3.2.

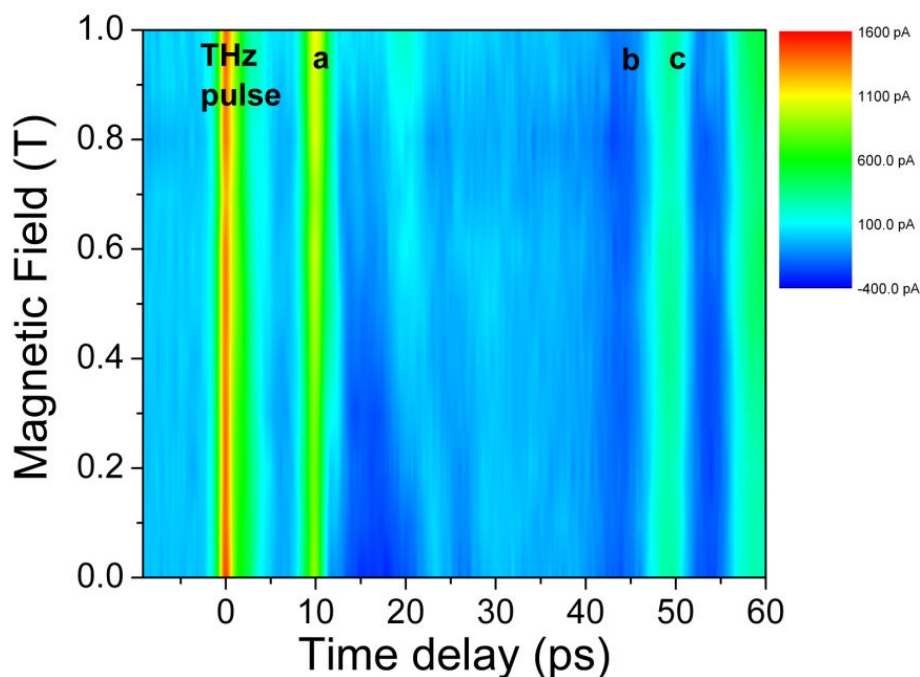


Figure 5.12 A contour plot of the time-domain generated pulse scan illustrating the behaviour of main THz pulse and secondary reflections with varying magnetic fields at 200 mK.

The magnetic field dependence on the input pulse was then investigated by sweeping the field from 0-1 T in 0.01 T steps. Figure 5.12 shows a contour plot of the time domain window observed for the generated pulse (as shown in Figure 5.11) at different magnetic fields. The THz pulse and the secondary reflections ‘b’ and ‘c’ were found to be not influenced by the external magnetic field. The reflection feature ‘a’, arising from the CPW-2DES interface, showed an increase in amplitude with increasing magnetic fields, as the impedance mismatch between the CPW and the 2DES increases. This may be explained by considering the two terminal DC transport measurements of the 2DES strip in Figure 5.7, which illustrated a decrease in the 2DES conductivity with increasing magnetic field. Also, as the two-terminal DC resistance of the 2DES increases to $> 1 \text{ k}\Omega$ after 1 T magnetic field no THz signal was expected to couple into the 2DES from the $50 \text{ }\Omega$ waveguide. For that reason, all the on-chip THz measurements with adjacent 2DES were performed up to 1 T.

The dependence of the proportion of THz pulse energy reflected from the 2DES strip on increasing magnetic field is more clearly presented in Figure 5.13. The higher resolution contour plot compares just the generated and reflected THz pulse amplitude across magnetic fields, shown in Figure 5.13 (a). The normalised peak amplitude comparison of the generated pulse and the reflected pulse with increasing magnetic fields is shown in Figure 5.13 (b). A clear illustration of increasing amplitude of the first reflected pulse is noted as the 2DES conductivity decreases with increasing magnetic field. This implies that a decreasing portion of the incident THz pulse energy will propagate through the 2DES owing to the quantum Hall behaviour of the 2D electron layer.

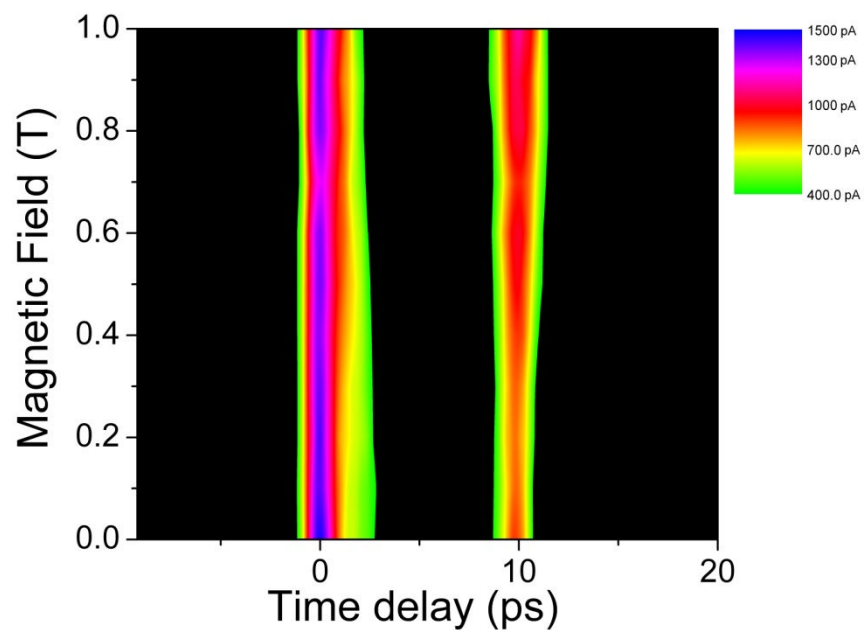


Figure 5.13 (a) A higher resolution contour plot showing the behaviour of the main generated THz pulse and the following time-domain reflection pulse from the CPW-2DES interface with increasing magnetic fields.

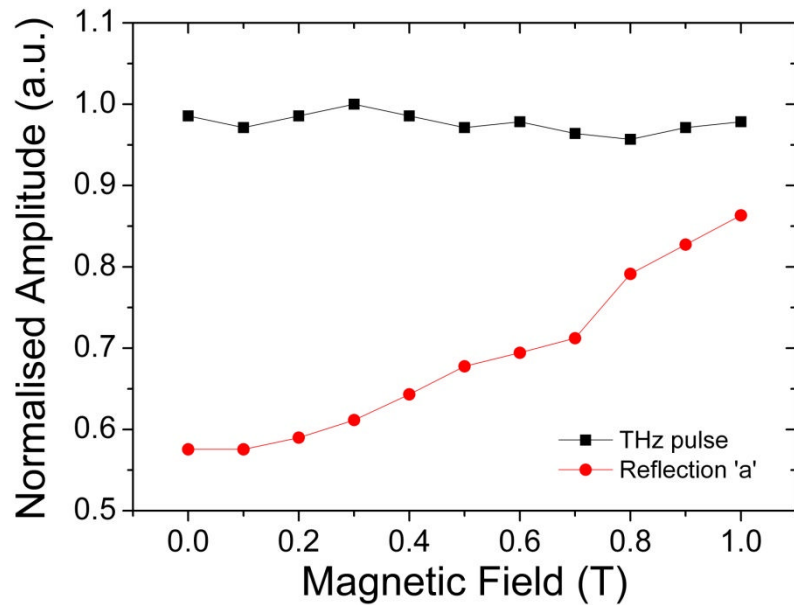


Figure 5.13 (b) A direct comparison of the trends observed between the generated THz pulse amplitude and the amplitude of the pulse reflected from the 2DES interface, for magnetic fields between 0-1 T.

5.3.4. Transmitted pulses

The transmission of picosecond timescale pulses through the 2DES was then examined under varying magnetic fields to detect the high frequency dynamic behaviour of the 2D electron layer. The beam alignment and PCS biasing setup for detecting transmitted pulsed was identical to the one demonstrated in Chapter 4, Section 4.3.2 and as shown in Figure 4.19. The pump and probe beams, each with optical intensities of 1 mW, were carefully aligned at switch regions 1 and 3 using piezoelectric stage pairs with pump switch (switch region 1) biased at 10 V. As mentioned in Chapter 4, Section 4.3.2; since a single PCS was used for THz pulse generation, the transmitted pulse scan observed through the 2DES in this case should consist of a superposition of both the odd and even guided modes.

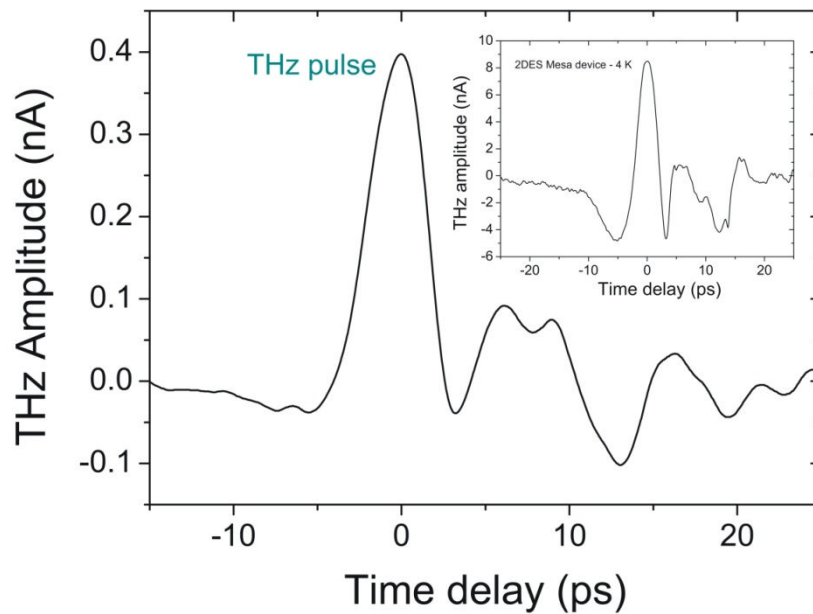


Figure 5.14 Main figure: Experimental data of the transmitted THz pulse propagated through the 2DES strip taken at 200 mK and 0 T magnetic field, using PCS 1 as the source and PCS 3 as the detector. Inset: Experimental data of the transmitted THz pulse propagated through the 2DES strip taken at 4 K, using PCS 1 as the source and PCS 3 as the detector.

Figure 5.14 shows the transmitted pulse scan observed at a bath temperature of 200 mK and at 0 T magnetic field. This result represents the lowest operating temperature THz pulse transmission through a semiconductor-based 2DES reported within the literature [138]. The inset shows a similar transmitted pulse measurement observed previously on the same 2DES-CPW injection device at 4K temperature in the continuous flow cryostat setup, using 10 mW optical beam powers and 30 V pump switch bias. It is noted for the time domain transmitted pulse scans taken at both 200 mK and 4 K temperatures, the main THz pulse is followed by several secondary, low amplitude reflections. These time-domain reflections are attributed to the impedance mismatch between the 2DES-CPW interface along the signal conductor and the 100 μm long discontinuity in the ground planes, as illustrated in Chapter 4, Section 4.3 and as shown in Figure 4.10.

Also as expected, since the 2DES conductivity remained unchanged from 4 K to sub-Kelvin temperatures, no further increase in the transmitted THz pulse amplitude was observed as compared to previous measurements at 4 K. However, as can be seen in Figure 5.14, there was a considerable reduction in the transmitted THz amplitude from ~ 8 nA to < 400 pA and correspondingly poorer signal-to-noise ratio, owing to the reduced pump-probe laser power. The power reduction, from 10 mW at 4 K to 1.0 mW at milli-Kelvin temperatures, may have masked further conductivity-related changes to the transmitted THz peak amplitude.

The effect of magnetic field on the time-domain transmitted pulses through the 2DES was then observed while sweeping the field from 0 – 1 T in 0.01 T steps. A clear dependence of the electron conductivity in the 2DES on the transmitted pulse shape and amplitude was observed, as demonstrated through a contour plot of the time-domain pulse window at varying magnetic fields (Figure 5.15). The plot shows the amplitude of the transmitted THz pulse diminishing with increasing magnetic field, corresponding to the decreasing DC conductance of the 2DES, and in agreement with the previous input pulse measurements.

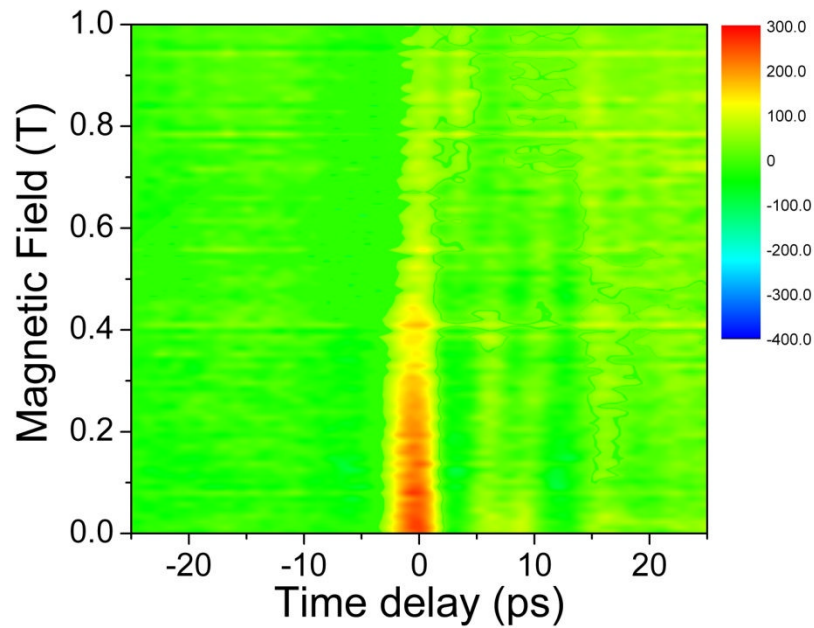


Figure 5.15 A contour plot of the time-domain transmitted pulse scan illustrating the behaviour of the main THz pulse peak (around 0 ps) and secondary reflections after propagating through the 2DES in varying magnetic fields.

A direct comparison between the transmitted THz signal amplitude as a function of magnetic field with the two-terminal 2DES strip conductivity is shown in Figure 5.16. The error bars fitted to the transmitted THz amplitude data shows the standard deviation from the previously measured DC conductivity of the 2DES. It was also observed that any low-field oscillations in the transmitted THz peak amplitude (resembling the oscillations observed in the two-terminal DC conductivity) as the system approaches the quantum Hall regime (solid line) were not apparent. This was attributed to the low transmitted THz power and correspondingly poor signal-to-noise ratio.

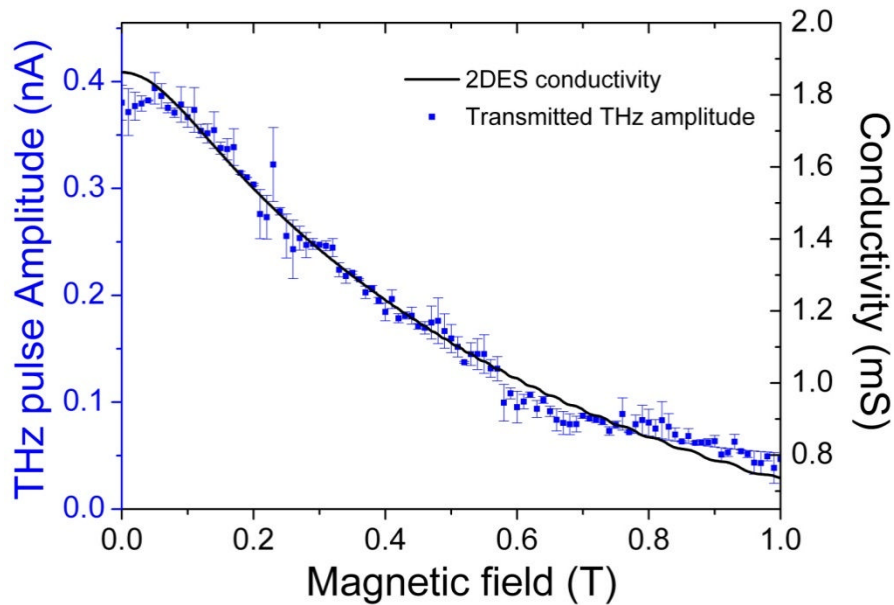


Figure 5.16 Comparison of the transmitted THz signal amplitude as a function of magnetic field (symbols) with the 2-terminal 2DES conductivity (line) measured at 200 mK temperature.

The time-domain transmitted pulse measured at 200 mK and 1 T magnetic field is shown in Figure 5.17, with the inset showing the transmitted pulse scan measured previously at 300 K on the same device. It is apparent that the transmitted pulse scan observed at increasing temperatures and increasing magnetic fields are very similar (the difference in the amplitude, as mentioned earlier, is attributed to different beam excitation powers at 200 mK and 300 K). This means that as the magnetic field increases, the consequence of increase in mismatch between the highly resistive 2DES and CPW interface is very similar to the increase in mismatch previously observed due to high operating temperatures as discussed in Chapter 4, Section 4.3.2. Also, as demonstrated previously through transmission of preferentially excited odd and even modes, it was found that the measured transmitted pulse with increasing magnetic fields consists mainly of the even mode electric field pattern, resulting from direct coupling between the centre conductor (bypassing the integrated 2DES).

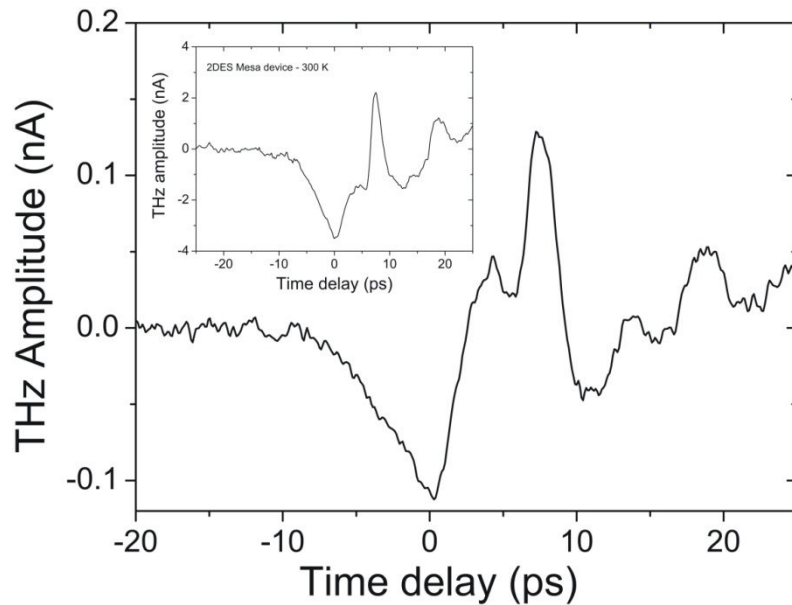


Figure 5.17 Main figure: Experimental data of the transmitted THz pulse propagated through the 2DES strip taken at 200 mK and 1 T magnetic field, using PCS 1 as the source and PCS 3 as the detector. Inset: Experimental data of the transmitted THz pulse propagated through the 2DES strip taken at 300 K, using PCS 1 as the source and PCS 3 as the detector.

In order to enable comparisons with the analytical modelling shown in section 5.2, a frequency domain analysis on the transmitted pulses was then implemented. The frequency spectra of the transmitted pulses obtained by performing Fast Fourier transforms on the time domain signals is displayed in Figure 5.18 at various magnetic fields. A direct comparison with occurrences of the magneto plasmon resonance in the 2DES region, theoretically modelled in section 5.2, is used to illustrate the expected positions of plasmonic features with respect to magnetic field. The behaviour of the first six plasmon resonance modes is illustrated.

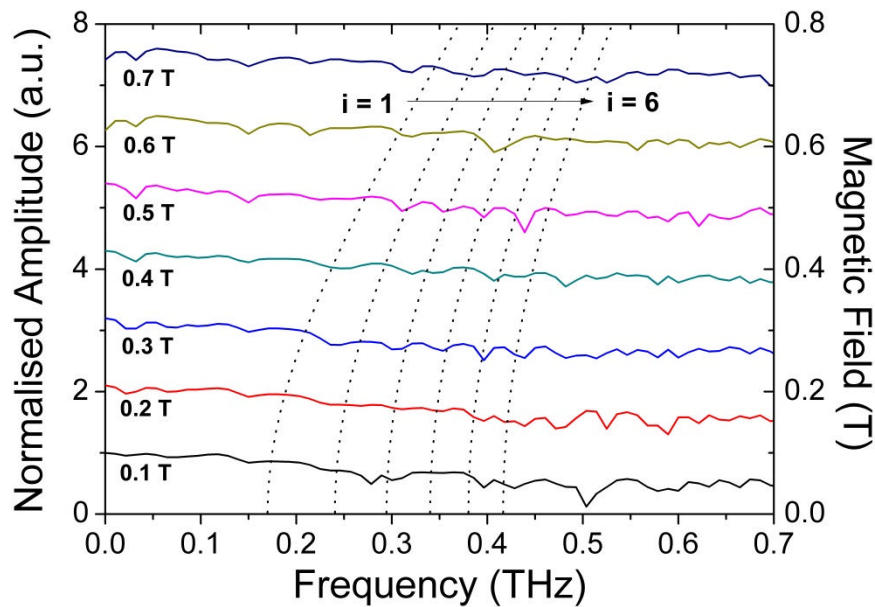


Figure 5.18 Frequency spectra of the time-domain transmitted pulses shown in Figure 5.15 at selected magnetic fields, normalised between 0 –1. Data offset by 1 for clarity. The dotted lines show the anticipated magneto plasmon resonance frequencies at corresponding magnetic fields, analytically modelled for the pulse injection device used.

From the comparison between measured results and the analytical modelling data shown in Figure 5.18, it was noted that the occurrence of magneto plasmon resonances in the strip of 2DES were not clearly observed in the frequency domain of the transmitted pulses at different magnetic fields. This was attributed to two limiting factors, as discussed below.

An important limiting factor was the poor frequency resolution of the pulse injection device. This was caused by secondary reflections in the time-domain transmitted pulse from the CPW-2DES interface and the discontinuity in the ground planes, as shown in Figure 5.14. The transmitted pulse measurement time window for a CPW of equivalent geometry, but without the coupled 2DES, measured at 100 mK temperatures (see Chapter 3, Section 3.4.2 and Figure 3.26) showed the time delay measured between the first reflection and the main transmitted THz peak to be ~ 40 ps, resulting in a frequency resolution of ~ 25 GHz. However, for measurement taken from

the pulse injection devices, the time delay between the first reflection and the transmitted THz peak was noted to be <10 ps, resulting in a relatively poor frequency resolution of >100 GHz. An additional drawback of having such a small time window before the secondary reflections is that, any distinctive ringing trailing the main transmitted THz pulse due to the presence of magneto plasmon resonances, as shown in previous experiments [10, 139], can easily be overshadowed by the presence of the secondary oscillations. To investigate further the high frequency ballistic transport in a 2DES, a higher frequency resolution device is required, including a longer time delay window between the transmitted pulses and secondary reflections to improve the sensitivity.

The considerably low transmitted THz power and its further reduction with increasing magnetic fields was also a limiting factor. Despite the limited information in the frequency spectra of the transmitted pulses, the measurements presented in this chapter have clearly demonstrated a controllable technique for picosecond time-scale excitation and detection of magneto transport in a quantum-confined electron system at sub-Kelvin temperatures.

5.4. Summary

In this chapter, the capability of on-chip THz CPWs to inject and measure picosecond time-scale pulses in a monolithically integrated 2DES, at milli-Kelvin temperatures and under magnetic fields, has been demonstrated for the first time. The frequency domain physical phenomena anticipated in the 2DES were modelled analytically using the physical properties of the 2DES in the experiments, and their comparison with experimental pulse injection measurements was presented and discussed.

The DC magneto conductance measurement of the integrated 2DES was demonstrated using a two-terminal technique. A clear prominence of Hall resistivity over diagonal resistivity was observed, with plateaus occurring in Hall resistivity at quantized integer values. Importantly, a spurious effect of scattered NIR radiation from the pump and probe laser beams causing electron heating in the adjacent 2DES was identified, by observing the degeneracy of the 2DES electron states. A four-terminal integrated 2DES Hall bar geometry as outlined in Figure 5.10, is proposed for future injection devices in order to accurately determine the level of degeneracy, and hence the sample temperature (through independent Shubnikov-de-Haas and Hall measurements).

The ability to sample both the input THz signal injected into the 2DES and the output THz signal transmitted along the 2DES was established at 200 mK and in magnetic fields of up to 1 T has been presented, which hitherto has not been demonstrated in the literature. A clear influence of the magnetic field dependent conductivity of the 2DES was observed on the time-domain injected and transmitted THz signals in terms of pulse shape and amplitude.

For observing frequency domain resonances in the 2DES due to THz pulse injection, a drawback of electrically coupling the 2DES with the CPW was identified in terms of the increasing impedance mismatch at the CPW-2DES interface under increasing magnetic fields. This restricted the picosecond magneto transport studies to conditions only where the resistance of the 2DES and the CPW design used for pulse coupling are of the same order. In order to resolve this dilemma, an alternative approach of capacitively coupling the electric field of the THz pulses propagating along the CPW with the 2DES located in close proximity as demonstrated in Chapter 4 could be used for future generation devices.

The on-chip techniques demonstrated in this work are an extremely important addition to the field of ultrafast magneto transport measurements through nanoscale devices. Consequently, the future investigation of fundamental physics and applications in this field look more feasible.

A summary of this chapter has been published as reference [138].

Chapter 6: Conclusions and Future work

6.1. Project overview

The motivation for the work demonstrated in this thesis was to perform picosecond time-resolved electron transport measurements in a 2DES. The use of on-chip terahertz waveguides for studying low-temperature interactions between picosecond timescale electrical pulses and a GaAs/AlGaAs based 2DES in presence of high magnetic fields is presented. In the course of this work, several novel device designs and experimental techniques were developed, which could lead to further technological applications.

In order to demonstrate generation and detection of THz pulses with ps time duration, optoelectronic excitation was carried out using photoconductive switches adjacent to a planar, on-chip CPW formed on an LT-GaAs substrate material. The characteristics of the CPW device measured at room temperatures showed electrical transients of ~ 3 ps duration in the time domain after propagation along the 1.5-mm-long waveguide, containing frequency components up to 400 GHz. The time and frequency domain pulse transmission properties of the on-chip CPW devices were found to be suitable for its integration with the 2DES.

The integration of a 2DES with a THz waveguide was initially carried out using ‘post-fabrication’ methods, with the 2DES and the THz waveguide fabricated on separate chips. These methods involved using either a flip-chip configuration or a three-chip assembly technique for sandwiching the two devices into a single structure. In the

later stages of the project, a novel monolithic integration approach using MBE was developed to address the limited sensitivity of the ps pulse to the overlaid 2DES, and to reduce the complexity of the fabrication process. After several modifications to the MBE growth process, the first ever successful concurrent demonstration of both low-temperature electron transport measurements showing the quantum Hall regime, and THz transmission measurements using on-chip CPW from the same structure, is presented. This approach indicates that neither the 2DES nor the photoconductive response of the LT-GaAs is compromised by the monolithic integrated growth approach.

The observation of the ultra-fast response of the 2DES integrated with the on-chip waveguides at cryogenic temperatures and under magnetic fields was another important aspect of this work which had not been matured. The few instances of similar measurements in the literature [98] involved the use of a complex and non-repeatable method for performing pump-probe measurements using optical fibres glued to on-chip waveguides at cryogenic temperatures (~ 4 K). By de-coupling the fibres from the waveguide surface, and collimating then re-focusing the free-space emission onto the optical switches, the system presented in this thesis offers a much more versatile and repeatable excitation technique. In addition, having the ability to control dynamically the positioning of the refocused laser spots on the device surface, an in-situ photocurrent imaging of the active switch region was demonstrated. Full characterisation of on-chip CPW devices with two different photoconductive switch geometries for generation and detection of ps timescale pulses were performed at sub-Kelvin temperatures and under magnetic fields. The experimental results demonstrated that the performance of on-chip CPWs based on LT-GaAs substrates experienced no adverse effects when exposed to cryogenic temperatures and magnetic fields. This emphasises one of the main

advantages of the cryogenic operation of the on-chip waveguides to be used for interacting ps pulses with the adjacent 2DES, using monolithic integrated structures.

To study the temperature dependence of ps pulse interactions with integrated 2DESs, two different device geometries were studied. The first geometry involved ps pulse injection directly into a 100 μm long and 30 μm wide 2D electron layer using via ohmic contacts patterned onto the 2DES and overlapping the CPW centre conductor. The second geometry involved capacitive coupling of the THz electric field to a submerged 2DES located in close proximity to the substrate surface. The on-chip THz-TDS measurements of pulse injection devices showed a distinct increase in the transmitted pulse amplitude as the conductance of the 2DES increased with decreasing temperatures, and hence the impedance mismatch between the CPW and 2DES mesa was reduced. Conversely, in measurements of capacitively coupled devices, an increase in attenuation of the transmitted THz signal was observed as the temperature was reduced. This occurs owing to the increasing conductivity of the submerged 2DES introducing a strong parasitic capacitance with the overlaid waveguide. The characterisation of both integrated device geometries with varying temperatures from (4 K to 300 K) showed successful ps pulse interaction with the conductive 2DES layer.

The capability of THz CPWs to inject and measure picosecond time-scale pulses in a monolithically integrated 2DES was then established at milli-Kelvin temperatures and under magnetic fields, which up until now has not been demonstrated in the literature. A clear dependence of the 2DES magneto resistance was seen on the behaviour of the transmitted THz pulse. In addition, analytical modelling was also presented to understand physical effects, including plasmon resonances in a confined 2DES upon ps pulse injection under magnetic fields. However, the experimental studies of ps time-resolved magneto transport properties in the 2DES were found to be limited

above 0.5 T magnetic fields due to an increasing impedance mismatch between the signal conductor of the CPW ($Z_{\text{CPW}} \sim 50 \Omega$) and the linearly increasing magneto resistance of the coupled 2DES (magneto resistance, Z_{2DES} found to be $> 1 \text{ k}\Omega$ for magnetic fields above 1 T). Additional design considerations are required to improve further the coupling of the metal-2DES transitions, before a clear observation of ps time-resolved electron transport in 2DES can be demonstrated.

6.2. Future Work

The work established in this thesis has shown a step forward in the use of on-chip guided wave THz systems in the study of the ultra-fast response of low-dimensional semiconductor nanostructures, by allowing measurement of their dynamic properties through ps timescale pulse interactions at cryogenic temperatures. However, there is still much room for subsequent development in this exciting technology, which will continue the work in this thesis. Some suggested points are discussed below:

6.2.1. Improvements and modifications in pulse injection geometry

The achievement of ps time resolved electron transport in the 2DES using pulse injection devices at sub-Kelvin temperatures and under magnetic fields was primarily limited to low-magnetic fields ($\sim 0.5 \text{ T}$). This was due to the impedance mismatch at the interface of a 50Ω characteristic impedance CPW and 2DES, which exhibited considerably larger magneto resistance (in the order of $\text{k}\Omega$) above 0.5 T. Therefore, suggested future work may involve designing CPW waveguide geometries with characteristic impedance corresponding to the magneto resistance of the 2DES at a chosen field of interest. The successful implementation will allow ps timescale measurements of higher magnetic field QHE, which is typically observed in steady state

measurements. In addition, this will also prevent any time-domain reflections from the metal-2DES interface following main THz pulse, thereby increasing the frequency resolution of the measurements essential to observe frequency domain plasmonic resonances.

The development in pulse injection technology for the coupled 2DES has the potential to allow probing of single nanostructures for the first time, using ps timescale current pulses. A quasi-1D electron system formed in a constricted GaAs/AlGaAs based 2DES is essentially predicted to be a THz frequency device, with the ability to support current propagation up to a cut-off frequency $> 1\text{THz}$ [140]. The pulse injection geometry developed in this work can allow investigation of this prediction and also allow observation of the change in dynamic conductivity of 1D and 0D electron systems arising from the interaction of ps pulses with strong carrier confinement. Figure 6.1 shows proposed device geometry to measure the ps response of (a) a 1DES and (b) a 0DES quantum dot system at cryogenic temperatures, using on-chip THz-TDS demonstrated.

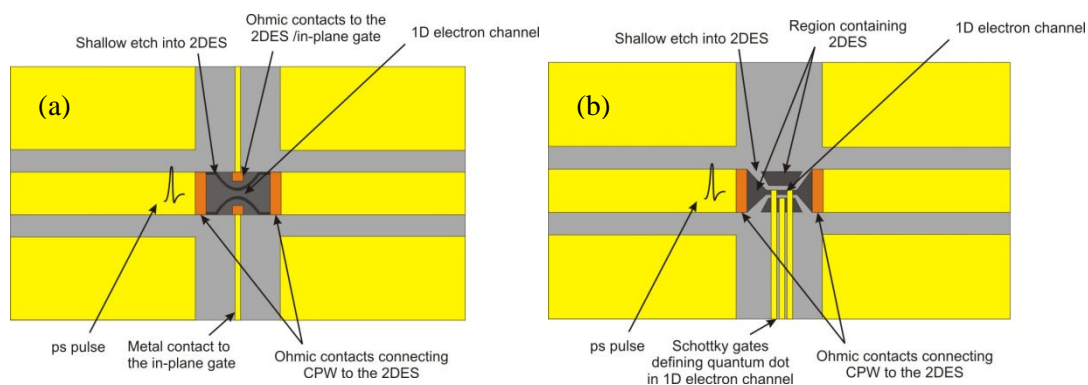


Figure 6.1 Schematic diagrams of CPW based devices designed to measure the ps response of (a) a 1DES and (b) a quantum dot system.

6.2.2. Measurement of ps pulse interaction using capacitive coupling geometry under magnetic fields

The dynamic magneto conductivity behaviour in the quantum Hall regime has also been frequently observed in a 2DES confined in a GaAs/AlGaAs heterostructure using an alternate method. This involves evanescent field coupling of the electromagnetic radiation propagating along a waveguide in close proximity to 2DES [10, 125]. Since no direct electrical contact is made between the CPW and the 2DES, it allows probing of the 2DES conductivity behaviour regardless of potential impedance mismatches between 2DES and CPW. As discussed in Chapter 4, the evanescent coupling of ps pulses propagating along a CPW with a 2DES in close proximity was also established as an alternate approach to probe the dynamic conductivity of the 2DES at cryogenic temperatures ranging from 4 K to 300 K. However due to time constraints in the project, these ps pulse interaction measurements using capacitive coupling devices are yet to be carried out using higher frequency resolution CPW device designs (as demonstrated in Chapter 3) and in presence of magnetic fields and at sub-Kelvin temperatures.

Publications and Conference Proceedings

C. D. Wood, **D. Mistry**, L. H. Li, J. E. Cunningham, E. H. Linfield and A. G. Davies. On-chip THz pulse spectroscopy techniques for measuring mesoscopic quantum systems. *Review of Scientific Instruments*, 84, 085101, 2013.

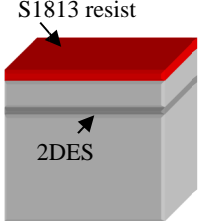
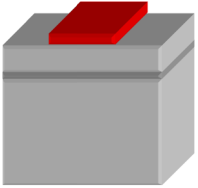
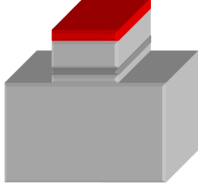
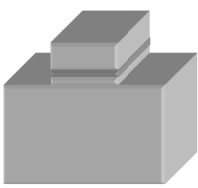
N. A. Doodoo-Amoo, K. Saeed, **D. Mistry**, L. H. Li, S. P. Khanna, E. H. Linfield, A. G. Davies, J. E. Cunningham. Non-universality in scaling exponents in quantum Hall transitions. *Physical Review B (submitted)*.

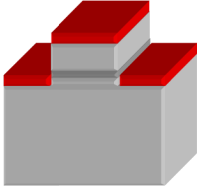
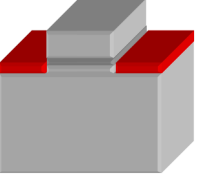
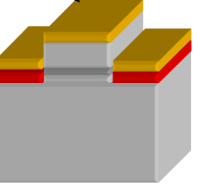
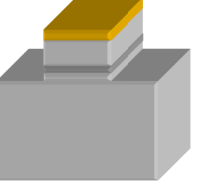
D. Mistry, C. D. Wood, L. H. Li, J. E. Cunningham, E. H. Linfield and A. G. Davies. On-chip THz pulse measurement of confined semiconductor systems at cryogenic temperatures. In *Conference Digest of International workshop on Optical Terahertz Science and Technology (OTST)*, Kyoto, (Japan), 2013.

D. Mistry, C. D. Wood, L. H. Li, J. E. Cunningham, E. H. Linfield and A. G. Davies. Monolithically integrated on-chip THz systems for picosecond time resolved electron transport in GaAs/AlGaAs heterojunctions. In *Conference Digest of UK Semiconductors*, Sheffield, (UK), 2012.

C. D. Wood, **D. Mistry**, L. H. Li, J. E. Cunningham, E. H. Linfield and A. G. Davies. On-chip THz generation and detection at Milli-Kelvin temperatures for the study of ultrafast phenomena in confined semiconductor systems. **Invited paper** in *Conference Digest of the Joint 38th International Conference on Infrared and Millimeter waves (IRMMW)*, Wollongong, (Australia), 2012.

Appendix 1: Hall bar fabrication

	Resist spin	Photolithography	Etching	Resist strip
Hall bar mesa fabrication	 <ul style="list-style-type: none"> • Sample cleaning using acetone and IPA. • Blow dry using nitrogen. • Shipley 1813 photoresist coating at 5000 rpm for 30 seconds. 	 <ul style="list-style-type: none"> • Soft bake S-1813 at 115 °C for 60 seconds. • Expose the sample using UV radiation. • Develop the pattern using MF 319 followed by DI H₂O rinse. 	 <ul style="list-style-type: none"> • Hall bar mesa etch using an etchant solution of H₂SO₄:H₂O₂:H₂O mixed at 1:8:71. • 100 nm mesa etch at an etching rate of ~600 nm/minute followed by DI H₂O rinse. 	 <ul style="list-style-type: none"> • Resist strip using quick rinse in acetone followed by IPA rinse. • Blow dry using nitrogen.

	Resist spin	Photolithography	Ohmic evaporation	Lift-off and annealing
Ohmic contact fabrication	 <ul style="list-style-type: none"> • Sample cleaning using Acetone and IPA. • Blow dry using nitrogen. • Shipley 1813 photoresist coating at 5000 rpm with a step value of 4 for 30 seconds. 	 <ul style="list-style-type: none"> • Soft bake S-1813 at 115 °C for 60 seconds • Expose the sample using UV radiation. • Develop the pattern using MF 319 followed by DI H₂O rinse. 	 <ul style="list-style-type: none"> • Deposition of 150 nm thick AuGeNi alloy layer, using thermal evaporation at a rate of ~1 Å/seconds under vacuum pressure of ~10⁻⁶ mBar. 	 <ul style="list-style-type: none"> • Metal lift-off process by soaking the sample in acetone for > 2 hours. • Diffusion of AuGeNi metal using in-situ annealing at temperatures ~430 °C.

Appendix 2: Selective etch for first generation integrated structure

Selective etch process		
Resist spin	<ul style="list-style-type: none"> • Sample cleaning using acetone and IPA. • Blow dry using nitrogen. • Shipley 1813 photoresist coating at 5000 rpm for 30 seconds. 	<p>S1813 resist</p> <p>LT-GaAs</p> <p>AlAs</p> <p>2DES</p>
Photolithography	<ul style="list-style-type: none"> • Soft bake S-1813 at 115 °C for 60 seconds. • Expose the sample using UV radiation. • Develop the pattern using MF-319 followed by DI H₂O rinse. 	<p>Pattern for measuring etch thickness</p>
LT-GaAs layer etch	<ul style="list-style-type: none"> • Selective LT-GaAs layer etch using an etchant solution of C₆H₈O₇:H₂O₂ mixed at 3:1. • 2 μm thick LT-GaAs layer etch at an etching rate of ~300 nm/minute followed by DI H₂O rinse. 	<p>Exposed AlAs surface</p>
AlAs (etch stop) layer etch and resist strip	<ul style="list-style-type: none"> • Selective AlAs (etch stop) layer etch using an etchant solution of HF:H₂O mixed at 1:10. • 100 nm thick AlAs layer etch at an approximate etching rate of ~5 μm/minute followed by DI H₂O rinse. • Resist strip by sample soak in acetone and IPA. 	<p>Exposed GaAs cap surface</p>

Appendix 3: Selective etch for second generation integrated structure

Selective etch process		
Resist spin	<ul style="list-style-type: none"> Sample cleaning using acetone and IPA. Blow dry using nitrogen. Shipley 1813 photoresist coating at 5000 rpm for 30 seconds. 	<p>S1813 resist</p> <p>2DES AlAs LT-GaAs</p>
Photolithography	<ul style="list-style-type: none"> Soft bake S-1813 at 115 °C for 60 seconds. Expose the sample using UV radiation. Develop the pattern using MF-319 followed by DI H₂O rinse. 	<p>Pattern for measuring etch thickness</p> <p>GaAs cap</p>
GaAs/AlGaAs heterostructure etch	<ul style="list-style-type: none"> Selective GaAs/AlGaAs heterostructure containing the 2DES etch using an etchant solution of C₆H₈O₇:H₂O₂ mixed at 3:1. 570 nm thick GaAs/AlGaAs heterostructure etch at an etching rate of ~300 nm/minute for GaAs layers and a rate of ~10 nm/minute for AlGaAs layers. DI H₂O rinse. 	<p>Exposed AlAs surface</p>
AlAs (etch stop) layer etch and resist strip	<ul style="list-style-type: none"> Selective AlAs (etch stop) layer etch using an etchant solution of HF:H₂O mixed at 1:10. 100 nm thick AlAs layer etch at an approximate etching rate of ~5 μm/minute followed by DI H₂O rinse. Resist strip by sample soak in acetone and IPA. 	<p>Exposed LT-GaAs surface</p>

References

- [1] K. v. Klitzing, G. Dorda, and M. Pepper, "New Method for High-Accuracy Determination of the Fine-Structure Constant Based on Quantized Hall Resistance," *Physical Review Letters*, vol. 45, pp. 494-497, 1980.
- [2] B. J. van Wees, H. van Houten, C. W. J. Beenakker, J. G. Williamson, L. P. Kouwenhoven, D. van der Marel, et al., "Quantized conductance of point contacts in a two-dimensional electron gas," *Physical Review Letters*, vol. 60, p. 848, 1988.
- [3] A. D. Burnett, W. Fan, P. C. Upadhyya, J. E. Cunningham, M. D. Hargreaves, T. Munshi, et al., "Broadband terahertz time-domain spectroscopy of drugs-of-abuse and the use of principal component analysis."
- [4] J. Cunningham, C. Wood, A. G. Davies, I. Hunter, E. H. Linfield, and H. E. Beere, "Terahertz frequency range band-stop filters," *Applied Physics Letters*, vol. 86, pp. 213503-3, 2005.
- [5] A. G. Davies, A. D. Burnett, W. Fan, E. H. Linfield, and J. E. Cunningham, "Terahertz spectroscopy of explosives and drugs," *Materials Today*, vol. 11, pp. 18-26, 2008.
- [6] C. K. Tiang, J. Cunningham, C. Wood, I. C. Hunter, and A. G. Davies, "Electromagnetic simulation of terahertz frequency range filters for genetic sensing," *Journal of Applied Physics*, vol. 100, pp. 066105-3, 2006.
- [7] P. C. C. Upadhyya, J.E. Tiang, C.K. Lachab, M. Khanna, S.P. Linfield, E.H. Davies, A.G., "Cyclotron absorption in two-dimensional electron systems monitored by terahertz time-domain spectroscopy," presented at the Infrared and Millimeter Waves, 2007 and the 2007 15th International Conference on Terahertz Electronics. IRMMW-THz. Joint 32nd International Conference, 2-9 Sept. 2007
- [8] R. Ulbricht, E. Hendry, J. Shan, T. F. Heinz, and M. Bonn, "Carrier dynamics in semiconductors studied with time-resolved terahertz spectroscopy," *Reviews of Modern Physics*, vol. 83, pp. 543-586.

- [9] Y. Ikebe, T. Morimoto, R. Masutomi, T. Okamoto, H. Aoki, and R. Shimano, "Optical Hall Effect in the Integer Quantum Hall Regime," *Physical Review Letters*, vol. 104, p. 256802, 2010.
- [10] E. A. Shaner and S. A. Lyon, "Time-resolved impulse response of the magnetoplasmon resonance in a two-dimensional electron gas," *Physical Review B*, vol. 66, p. 041402, 2002.
- [11] R. C. Ashoori, H. L. Stormer, L. N. Pfeiffer, K. W. Baldwin, and K. West, "Edge magnetoplasmons in the time domain," *Physical Review B*, vol. 45, pp. 3894-3897, 1992.
- [12] C. D. Wood, "On-chip THz Systems," School of Electronic and Electrical Engineering, The University of Leeds, 2006.
- [13] M. B. Byrne., "Pulsed imaging and spectroscopy using on-chip THz waveguides," School of Electronic and Electrical Engineering, The University of Leeds, 2008.
- [14] N. W. Ashcroft and N. D. Mermin, *Solid state physics*: Saunders College, 1976.
- [15] C. Beenakker and H. van Houten, "Quantum transport in semiconductor nanostructures," *Solid state physics*, vol. 44, pp. 1-228, 1991.
- [16] H. Ehrenreich and D. Turnbull, *Advances in Research and Applications: Semiconductor Heterostructures and Nanostructures*: Elsevier Science, 1991.
- [17] C. T. Foxon and et al., "Optimisation of (Al,Ga)As/GaAs two-dimensional electron gas structures for low carrier densities and ultrahigh mobilities at low temperatures," *Semiconductor Science and Technology*, vol. 4, p. 582, 1989.
- [18] A. Szafer and A. D. Stone, "Theory of Quantum Conduction through a Constriction," *Physical Review Letters*, vol. 62, p. 300, 1989.
- [19] R. P. Taylor, "The role of surface-gate technology for AlGaAs/GaAs nanostructures," *Nanotechnology*, vol. 5, pp. 183-198, 1994.
- [20] C. G. Smith, "Low-dimensional quantum devices," *Reports on Progress in Physics*, vol. 59, pp. 235-282, 1996.
- [21] H. van Houten, C. W. J. Beenakker, P. H. M. van Loosdrecht, T. J. Thornton, H. Ahmed, M. Pepper, et al., "Four-terminal magnetoresistance of a two-dimensional electron-gas constriction in the ballistic regime," *Physical Review B*, vol. 37, p. 8534, 1988.

- [22] A. R. Hamilton, J. E. F. Frost, C. G. Smith, M. J. Kelly, E. H. Linfield, C. J. B. Ford, et al., "Back-gated split-gate transistor: A one-dimensional ballistic channel with variable Fermi energy," *Applied Physics Letters*, vol. 60, pp. 2782-2784, 1992.
- [23] D. A. Wharam, T. J. Thornton, R. Newbury, M. Pepper, H. Ahmed, J. E. F. Frost, et al., "One-dimensional transport and the quantisation of the ballistic resistance," *Journal of Physics C: Solid State Physics*, vol. 21, pp. L209-L214, 1988.
- [24] T. Ando, A. B. Fowler, and F. Stern, "Electronic properties of two-dimensional systems," *Reviews of Modern Physics*, vol. 54, pp. 437-672, 1982.
- [25] S. Koch, R. J. Haug, K. v. Klitzing, and K. Ploog, "Size-dependent analysis of the metal-insulator transition in the integral quantum Hall effect," *Physical Review Letters*, vol. 67, p. 883, 1991.
- [26] A. M. M. Pruisken, "Universal Singularities in the Integral Quantum Hall Effect," *Physical Review Letters*, vol. 61, p. 1297, 1988.
- [27] Calvo and Miguel, "Magnetoelectric spectrum and transport properties of a shallow asymmetric quantum channel," *Physical Review B*, vol. 51, p. 2268, 1995.
- [28] V. Borisov, V. Lapin, A. Temiryazev, A. Toropov, and A. Chmil', "Features of the conductance quantization for etched 1D channels," *Journal of Communications Technology and Electronics*, vol. 54, pp. 468-472, 2009.
- [29] T. J. Thornton, M. Pepper, H. Ahmed, D. Andrews, and G. J. Davies, "One-Dimensional Conduction in the 2D Electron Gas of a GaAs-AlGaAs Heterojunction," *Physical Review Letters*, vol. 56, p. 1198, 1986.
- [30] N. K. Patel, L. Martin-Moreno, M. Pepper, R. Newbury, J. E. F. Frost, D. A. Ritchie, et al., "Ballistic transport in one dimension: additional quantisation produced by an electric field," *Journal of Physics: Condensed Matter*, vol. 2, pp. 7247-7254, 1990.
- [31] K. F. Berggren and D. J. Newson, "Magnetic depopulation of electronic subbands in low-dimensional semiconductor systems and their influence on the electrical resistivity and Hall effect," *Semiconductor Science and Technology*, vol. 1, pp. 327-337, 1986.
- [32] R. J. Brown, M. J. Kelly, R. Newbury, M. Pepper, B. Miller, H. Ahmed, et al., "The one dimensional quantised ballistic resistance in GaAs/AlGaAs

- heterojunctions with varying experimental conditions," *Solid-State Electronics*, vol. 32, pp. 1179-1183, 1989.
- [33] H. Drexler, W. Hansen, S. Manus, J. P. Kotthaus, M. Holland, and S. P. Beaumont, "One-dimensional electron channels in the quantum limit," *Physical Review B*, vol. 49, p. 14074, 1994.
- [34] J. E. F. Frost, K. F. Berggren, M. Pepper, M. Grimshaw, D. A. Ritchie, A. C. Churchill, et al., "Analytical model of a one-dimensional constriction with many occupied subbands: Calculation and experiment," *Physical Review B*, vol. 49, p. 11500, 1994.
- [35] M. L. Roukes, A. Scherer, S. J. Allen, H. G. Craighead, R. M. Ruthen, E. D. Beebe, et al., "Quenching of the Hall Effect in a One-Dimensional Wire," *Physical Review Letters*, vol. 59, p. 3011, 1987.
- [36] C. C. Eugster, J. A. del Alamo, M. J. Rooks, and M. R. Melloch, "One-dimensional to one-dimensional tunnelling between electron waveguides," *Applied Physics Letters*, vol. 64, pp. 3157-3159, 1994.
- [37] N. K. Patel, J. T. Nicholls, L. Martn-Moreno, M. Pepper, J. E. F. Frost, D. A. Ritchie, et al., "Properties of a ballistic quasi-one-dimensional constriction in a parallel high magnetic field," *Physical Review B*, vol. 44, p. 10973, 1991.
- [38] K. Nakamura, F. Nihey, H. Toyoshima, T. Itoh, and D. C. Tsui, "Electron focusing with multi-parallel 1D channels," *Superlattices and Microstructures*, vol. 9, pp. 235-239, 1991.
- [39] W. Shockley and G. L. Pearson, "Modulation of Conductance of Thin Films of Semi-Conductors by Surface Charges," *Physical Review*, vol. 74, pp. 232-233, 1948.
- [40] F. Stern and W. E. Howard, "Properties of Semiconductor Surface Inversion Layers in the Electric Quantum Limit," *Physical Review*, vol. 163, pp. 816-835, 1967.
- [41] F. F. Fang, A. B. Fowler, and A. Hartstein, "Effective mass and collision time of (100) Si surface electrons," *Physical Review B*, vol. 16, pp. 4446-4454, 1977.
- [42] J. H. English, A. C. Gossard, H. L. Stormer, and K. W. Baldwin, "GaAs structures with electron mobility of 5×10^6 cm²/V s," *Applied Physics Letters*, vol. 50, pp. 1826-1828, 1987.

- [43] Greally and et al., "Low-temperature mobility of two-dimensional electrons in (Ga,In)As-(Al,In)As heterojunctions," *Journal of Applied Physics*, vol. 79, p. 8465, 1996.
- [44] J. J. Harris, C. T. Foxon, K. W. J. Barnham, D. E. Lacklison, J. Hewett, and C. White, "Two-dimensional electron gas structures with mobilities in excess of $3 \times 10^6 \text{ cm}^2 \text{ V}^{-1} \text{ s}^{-1}$," *Journal of Applied Physics*, vol. 61, pp. 1219-1221, 1987.
- [45] G. Hill and et al., "Low-temperature mobility of two-dimensional electrons in (Ga,In)As-(Al,In)As heterojunctions," *Journal of Applied Physics*, vol. 79, p. 8465, 1996.
- [46] K. Hirakawa and H. Sakaki, "Mobility of the two-dimensional electron gas at selectively doped n -type $\text{Al}_x\text{Ga}_{1-x}\text{As}/\text{GaAs}$ heterojunctions with controlled electron concentrations," *Physical Review B*, vol. 33, p. 8291, 1986.
- [47] M. Shayegan, V. J. Goldman, C. Jiang, T. Sajoto, and M. Santos, "Growth of low-density two-dimensional electron system with very high mobility by molecular beam epitaxy," *Applied Physics Letters*, vol. 52, pp. 1086-1088, 1988.
- [48] E. E. Mendez, P. J. Price, and M. Heiblum, "Temperature dependence of the electron mobility in GaAs-GaAlAs heterostructures," *Applied Physics Letters*, vol. 45, pp. 294-296, 1984.
- [49] D. Yoshioka, *The Quantum Hall Effect*: Springer, 2002.
- [50] R. Dingle, H. L. Stormer, A. C. Gossard, and W. Wiegmann, "Electron mobilities in modulation-doped semiconductor heterojunction superlattices," *Applied Physics Letters*, vol. 33, pp. 665-667, 1978.
- [51] H. L. Stormer, A. Pinczuk, A. C. Gossard, and W. Wiegmann, "Influence of an undoped (AlGa)As spacer on mobility enhancement in GaAs-(AlGa)As superlattices," *Applied Physics Letters*, vol. 38, pp. 691-693, 1981.
- [52] V. Umansky, M. Heiblum, Y. Levinson, J. Smet, J. Nájbler, and M. Dolev, "MBE growth of ultra-low disorder 2DEG with mobility exceeding $35 \times 10^6 \text{ cm}^2/\text{V}\cdot\text{s}$," *Journal of Crystal Growth*, vol. 311, pp. 1658-1661, 2009.
- [53] P. L. N. Schlom D. G., "Oxide electronics: Upward mobility rocks!," *Nature Materials*, vol. 9, p. 3, 2010.

- [54] C. H. W. Barnes, *Quantum Transport Phenomena in Low-Dimensional Electron Systems*: Cambridge University Press, 2004.
- [55] W. Fan, A. Burnett, P. Upadhy, J. Cunningham, E. Linfield, and A. Davies, "Far-infrared spectroscopic characterization of explosives for security applications using broadband terahertz time-domain spectroscopy," *Applied spectroscopy*, vol. 61, pp. 638-643, 2007.
- [56] D. C. Tsui, H. L. Stormer, and A. C. Gossard, "Two-Dimensional Magnetotransport in the Extreme Quantum Limit," *Physical Review Letters*, vol. 48, pp. 1559-1562, 05/31/ 1982.
- [57] L. Perfetti, T. Kampfrath, F. Schapper, A. Hagen, T. Hertel, C. M. Aguirre, et al., "Ultrafast Dynamics of Delocalized and Localized Electrons in Carbon Nanotubes," *Physical Review Letters*, vol. 96, p. 027401, 2006.
- [58] M. C. Beard, J. L. Blackburn, and M. J. Heben, "Photogenerated Free Carrier Dynamics in Metal and Semiconductor Single-Walled Carbon Nanotube Films," *Nano Letters*, vol. 8, pp. 4238-4242, 2013/06/15 2008.
- [59] C. TÅ'ke, P. E. Lammert, V. H. Crespi, and J. K. Jain, "Fractional quantum Hall effect in graphene," *Physical Review B*, vol. 74, p. 235417, 2006.
- [60] D. Krokkel, D. Grischkowsky, and M. B. Ketchen, "Subpicosecond electrical pulse generation using photoconductive switches with long carrier lifetimes," *Applied Physics Letters*, vol. 54, pp. 1046-1047, 1989.
- [61] N. Katzenellenbogen and D. Grischkowsky, "Efficient generation of 380 fs pulses of THz radiation by ultrafast laser pulse excitation of a biased metal-semiconductor interface," *Applied Physics Letters*, vol. 58, pp. 222-224, 1991.
- [62] Y. C. Shen, P. C. Upadhy, E. H. Linfield, H. E. Beere, and A. G. Davies, "Ultrabroadband terahertz radiation from low-temperature-grown GaAs photoconductive emitters," *Applied Physics Letters*, vol. 83, pp. 3117-3119, 2003.
- [63] D. H. Auston, "Picosecond optoelectronic switching and gating in silicon," *Applied Physics Letters*, vol. 26, pp. 101-103, 1975.
- [64] Y. C. Shen, P. C. Upadhy, H. E. Beere, E. H. Linfield, A. G. Davies, I. S. Gregory, et al., "Generation and detection of ultrabroadband terahertz radiation using photoconductive emitters and receivers," *Applied Physics Letters*, vol. 85, pp. 164-166, 2004.

- [65] S. Gupta, J. F. Whitaker, and G. A. Mourou, "Ultrafast carrier dynamics in III-V semiconductors grown by molecular-beam epitaxy at very low substrate temperatures," *Quantum Electronics, IEEE Journal of*, vol. 28, pp. 2464-2472, 1992.
- [66] S. Gupta, M. Y. Frankel, J. A. Valdmanis, J. F. Whitaker, G. A. Mourou, F. W. Smith, et al., "Subpicosecond carrier lifetime in GaAs grown by molecular beam epitaxy at low temperatures," *Applied Physics Letters*, vol. 59, pp. 3276-3278, 1991.
- [67] K. A. McIntosh, K. B. Nichols, S. Verghese, and E. R. Brown, "Investigation of ultrashort photocarrier relaxation times in low-temperature-grown GaAs," *Applied Physics Letters*, vol. 70, pp. 354-356, 1997.
- [68] Y. Cai, I. Brener, J. Lopata, J. Wynn, L. Pfeiffer, J. B. Stark, et al., "Coherent terahertz radiation detection: Direct comparison between free-space electro-optic sampling and antenna detection," *Applied Physics Letters*, vol. 73, pp. 444-446, 1998.
- [69] Q. Wu and X. C. Zhang, "Free-space electro-optic sampling of terahertz beams," *Applied Physics Letters*, vol. 67, pp. 3523-3525, 1995.
- [70] A. Sell, A. Leitenstorfer, and R. Huber, "Phase-locked generation and field-resolved detection of widely tunable terahertz pulses with amplitudes exceeding 100 MV/cm," *Opt. Lett.*, vol. 33, pp. 2767-2769, 2008.
- [71] M. B. Byrne, "Pulses imaging and spectroscopy using on-chip THz waveguides," University of Leeds, 2008.
- [72] E. Castro-Camus, L. Fu, J. Lloyd-Hughes, H. H. Tan, C. Jagadish, and M. B. Johnston, "Photoconductive response correction for detectors of terahertz radiation," *Journal of Applied Physics*, vol. 104, pp. 053113-7, 2008.
- [73] K. Liu, J. Xu, and X. C. Zhang, "GaSe crystals for broadband terahertz wave detection," *Applied Physics Letters*, vol. 85, pp. 863-865, 2004.
- [74] S. L. Dexheimer, *Terahertz Spectroscopy: Principles and Applications*: Taylor & Francis, 2007.
- [75] M. King and J. C. Wiltse, "Surface-wave propagation on coated or uncoated metal wires at millimeter wavelengths," *Antennas and Propagation, IRE Transactions on*, vol. 10, pp. 246-254, 1962.
- [76] K. Wang and D. M. Mittleman, "Metal wires for terahertz wave guiding," *Nature*, vol. 432, pp. 376-379, 2004.

- [77] J. A. Deibel, K. Wang, M. Escarra, N. Berndsen, and D. M. Mittleman, "The excitation and emission of terahertz surface plasmon polaritons on metal wire waveguides," *Comptes Rendus Physique*, vol. 9, pp. 215-231, 2008.
- [78] J. A. Deibel, K. Wang, M. D. Escarra, and D. Mittleman, "Enhanced coupling of terahertz radiation to cylindrical wire waveguides," *Opt. Express*, vol. 14, pp. 279-290, 2006.
- [79] M. Walther, M. R. Freeman, and F. A. Hegmann, "Metal-wire terahertz time-domain spectroscopy," *Applied Physics Letters*, vol. 87, pp. 261107-3, 2005.
- [80] J. Cunningham, M. Byrne, P. Upadhy, M. Lachab, E. H. Linfield, and A. G. Davies, "Terahertz evanescent field microscopy of dielectric materials using on-chip waveguides," *Applied Physics Letters*, vol. 92, pp. 032903-3, 2008.
- [81] C. Wood, J. Cunningham, I. C. Hunter, P. Tosch, E. H. Linfield, and A. G. Davies, "On-chip pulsed terahertz systems and their applications," *International Journal of Infrared and Millimeter Waves*, vol. 27, pp. 557-569, 2006.
- [82] M. B. Byrne, J. Cunningham, K. Tych, A. D. Burnett, M. R. Stringer, C. D. Wood, et al., "Terahertz vibrational absorption spectroscopy using microstrip-line waveguides," *Applied Physics Letters*, vol. 93, pp. 182904-3, 2008.
- [83] C. D. Wood, D. Mistry, L. H. Li, J. E. Cunningham, E. H. Linfield, and A. G. Davies, "On-chip THz generation and detection at milli-Kelvin temperatures for the study of ultrafast phenomena in confined semiconductor systems," in *Infrared, Millimeter, and Terahertz Waves (IRMMW-THz)*, 2012 37th International Conference on, pp. 1-3.
- [84] E. Yablonovitch, T. Sands, D. M. Hwang, I. Schnitzer, T. J. Gmitter, S. K. Shastry, et al., "Van der Waals bonding of GaAs on Pd leads to a permanent, solid-phase-topotaxial, metallurgical bond," *Applied Physics Letters*, vol. 59, pp. 3159-3161, 1991.
- [85] H. M. Heiliger, M. Nagel, H. G. Roskos, H. Kurz, F. Schnieder, W. Heinrich, et al., "Low-dispersion thin-film microstrip lines with cyclotene (benzocyclobutene) as dielectric medium," *Applied Physics Letters*, vol. 70, pp. 2233-2235, 1997.
- [86] J. F. Bulzacchelli, L. Hae-Seung, K. G. Stawiasz, S. Alexandrou, and M. B. Ketchen, "Picosecond optoelectronic study of superconducting microstrip transmission lines," *Applied Superconductivity, IEEE Transactions on*, vol. 5, pp. 2839-2843, 1995.

- [87] S. B. Cohn, "Slot Line on a Dielectric Substrate," *Microwave Theory and Techniques*, IEEE Transactions on, vol. 17, pp. 768-778, 1969.
- [88] S. Gupta, J. F. Whitaker, and G. A. Mourou, "Subpicosecond pulse propagation on coplanar waveguides: experiment and simulation," *Microwave and Guided Wave Letters*, IEEE, vol. 1, pp. 161-163, 1991.
- [89] T. Akalin, A. Treizebre, and B. Bocquet, "Single-wire transmission lines at terahertz frequencies," *Microwave Theory and Techniques*, IEEE Transactions on, vol. 54, pp. 2762-2767, 2006.
- [90] K. F. Sander and G. A. L. Reed, *Transmission and Propagation of Electromagnetic Waves*: Cambridge, Ma University Press, 1986.
- [91] L. Dazhang, J. Cunningham, M. B. Byrne, S. Khanna, C. D. Wood, A. D. Burnett, et al., "On-chip terahertz Goubau-line waveguides with integrated photoconductive emitters and mode-discriminating detectors," *Applied Physics Letters*, vol. 95, pp. 092903-3, 2009.
- [92] C. Russell, C. D. Wood, L. Dazhang, A. D. Burnett, L. H. Li, E. H. Linfield, et al., "Increasing the bandwidth of planar on-chip THz devices for spectroscopic applications," in *Infrared, Millimeter and Terahertz Waves (IRMMW-THz)*, 2011 36th International Conference on, pp. 1-3.
- [93] M. Griebel, J. H. Smet, J. Kuhl, K. von Klitzing, D. C. Driscoll, C. Kadow, et al., "Picosecond sampling with fiber-illuminated ErAs:GaAs photoconductive switches in a strong magnetic field and a cryogenic environment," *Applied Physics Letters*, vol. 82, pp. 3179-3181, 2003.
- [94] M. Y. Frankel, S. Gupta, J. Valdmanis, and G. A. Mourou, "Terahertz attenuation and dispersion characteristics of coplanar transmission lines," *Microwave Theory and Techniques*, IEEE Transactions on, vol. 39, pp. 910-916, 1991.
- [95] D. M. Pozar, *Microwave Engineering*: Wiley.
- [96] S. Ramo, J. R. Whinnery, and T. Van Duzer, *Fields and Waves in Communication Electronics*: Wiley, 1994.
- [97] J. Richter, H. Sigg, K. v. Klitzing, and K. Ploog, "Cyclotron resonance in donor and acceptor $\hat{\Gamma}$ -doped $\text{Al}_x\text{Ga}_{1-x}\text{As}/\text{GaAs}$ heterostructures," *Physical Review B*, vol. 39, pp. 6268-6271, 1989.
- [98] E. A. Shaner and S. A. Lyon, "Picosecond Time-Resolved Two-Dimensional Ballistic Electron Transport," *Physical Review Letters*, vol. 93, p. 037402, 2004.

- [99] J. K. Luo, H. Thomas, D. V. Morgan, and D. Westwood, "Transport properties of GaAs layers grown by molecular beam epitaxy at low temperature and the effects of annealing," *Journal of Applied Physics*, vol. 79, pp. 3622-3629, 04/01/1996.
- [100] S. E. Ralph and D. Grischkowsky, "Trap-enhanced electric fields in semi-insulators: The role of electrical and optical carrier injection," *Applied Physics Letters*, vol. 59, pp. 1972-1974, 1991.
- [101] E. Shaner, *Picosecond Waveguide Spectroscopy and Time-resolved Ballistic Electron Transport*: Princeton University, 2004.
- [102] R. N. Simons, *Coplanar Waveguide Circuits, Components, and Systems*: Wiley, 2004.
- [103] D. Maryenko, "Picosecond time-resolved transport studies in a two-dimensional electron system."
- [104] P. G. Young, R. R. Romanofsky, S. A. Alterovitz, R. A. Mena, and E. D. Smith, "A 10-GHz amplifier using an epitaxial lift-off pseudomorphic HEMT device," *Microwave and Guided Wave Letters, IEEE*, vol. 3, pp. 107-109, 1993.
- [105] P. G. Young, S. A. Alterovitz, R. A. Mena, and E. D. Smith, "RF properties of epitaxial lift-off HEMT devices," *Electron Devices, IEEE Transactions on*, vol. 40, pp. 1905-1909, 1993.
- [106] M. Alexe and U. Gösele, *Wafer Bonding: Applications and Technology*: Springer, 2004.
- [107] K. Zhang and D. Miller, "Electrical properties of low-temperature GaAs grown by molecular beam epitaxy and migration enhanced epitaxy," *Journal of Electronic Materials*, vol. 22, pp. 1433-1436, 1993.
- [108] H. S. Loka, S. D. Benjamin, and P. W. E. Smith, "Influence of material growth and annealing conditions on recombination processes in low-temperature-grown GaAs," *Optics Communications*, vol. 161, pp. 232-235, // 1999.
- [109] J. Cunningham and et al., "Monolithic integration of low-temperature-grown GaAs with a two-dimensional electron gas," *Semiconductor Science and Technology*, vol. 22, p. 811, 2007.
- [110] M. A. Reed, W. P. Kirk, and P. S. Kobiela, "Investigation of parallel conduction in GaAs/ Al_xGa_{1-x}As modulation-doped structures in the quantum limit," *Quantum Electronics, IEEE Journal of*, vol. 22, pp. 1753-1759, 1986.

- [111] Z. Liliental-Weber, W. Swider, K. M. Yu, J. Kortright, F. W. Smith, and A. R. Calawa, "Breakdown of crystallinity in low-temperature-grown GaAs layers," *Applied Physics Letters*, vol. 58, pp. 2153-2155, 1991.
- [112] D. Eaglesham, "Limited thickness epitaxy in GaAs molecular beam epitaxy near 200°C," *Appl. Phys. Lett.*, vol. 58, p. 65, 1991.
- [113] L. David C, "Molecular beam epitaxial GaAs grown at low temperatures," *Thin Solid Films*, vol. 231, pp. 61-73, 1993.
- [114] N. Zamdmer, Q. Hu, S. Verghese, and A. Forster, "Mode-discriminating photoconductor and coplanar waveguide circuit for picosecond sampling," *Applied Physics Letters*, vol. 74, pp. 1039-1041, 1999.
- [115] G. K. White, *Experimental techniques in low-temperature physics*, 1987.
- [116] S. Verghese, N. Zamdmer, Q. Hu, and A. Forster, "Cryogenic picosecond sampling using fiber-coupled photoconductive switches," *Applied Physics Letters*, vol. 70, pp. 2644-2646, 1997.
- [117] H. Zhang, B.-J. Yang, Y.-M. Liu, Q.-G. Wang, L. Yu, and X.-G. Zhang, "Zero dispersion wavelength and dispersion slope control of hollow-core photonic bandgap fibres," *Chinese Physics B*, vol. 18, p. 1116, 2009.
- [118] C. Wood, J. Cunningham, P. C. Upadhy, E. H. Linfield, I. C. Hunter, A. G. Davies, et al., "On-chip photoconductive excitation and detection of pulsed terahertz radiation at cryogenic temperatures," *Applied Physics Letters*, vol. 88, pp. 142103-3, 2006.
- [119] B. Tissafi, A. S. Grimault, and F. Aniel, "Effect of InGaAs surface states and interfaces on the photo-generated THz pulse shape," in *Infrared, Millimeter and Terahertz Waves, 2008. IRMMW-THz 2008. 33rd International Conference on, 2008*, pp. 1-2.
- [120] N. Zamdmer, Q. Hu, K. A. McIntosh, and S. Verghese, "Increase in response time of low-temperature-grown GaAs photoconductive switches at high voltage bias," *Applied Physics Letters*, vol. 75, pp. 2313-2315, 1999.
- [121] E. R. Brown, K. A. McIntosh, F. W. Smith, K. B. Nichols, M. J. Manfra, C. L. Dennis, et al., "Milliwatt output levels and superquadratic bias dependence in a low-temperature-grown GaAs photomixer," *Applied Physics Letters*, vol. 64, pp. 3311-3313, 06/13/ 1994.

- [122] J. P. Ibbetson and U. K. Mishra, "Space-charge-limited currents in nonstoichiometric GaAs," *Applied Physics Letters*, vol. 68, pp. 3781-3783, 06/24/ 1996.
- [123] G. C. DeSalvo, W. F. Tseng, and J. Comas, "Etch Rates and Selectivities of Citric Acid/Hydrogen Peroxide on GaAs , Al_{0.3}Ga_{0.7}As , In_{0.2}Ga_{0.8}As , In_{0.53}Ga_{0.47}As , In_{0.52}Al_{0.48}As , and InP," *Journal of The Electrochemical Society*, vol. 139, pp. 831-835, January 1, 1992 1992.
- [124] M. Konno, "Conductor loss in thin-film transmission lines," *Electronics and Communications in Japan (Part II: Electronics)*, vol. 82, pp. 83-91, 1999.
- [125] K. Saeed, N. A. Dodoo-Amoo, L. H. Li, S. P. Khanna, E. H. Linfield, A. G. Davies, et al., "Impact of disorder on frequency scaling in the integer quantum Hall effect," *Physical Review B*, vol. 84, p. 155324.
- [126] P. Cheung, M. S. Islam, D. P. Neikirk, and T. Itoh. Circuit model of coplanar waveguide phase shifter on GaAs substrates [Online].
- [127] W. K. H. Panofsky and M. N. Phillips, *Classical Electricity and Magnetism*: Addison-Wesley Pub. Co., 1955.
- [128] R. W. McGowan, D. Grischkowsky, and J. A. Misewich, "Demonstrated low radiative loss of a quadrupole ultrashort electrical pulse propagated on a three strip coplanar transmission line," *Applied Physics Letters*, vol. 71, pp. 2842-2844, 1997.
- [129] U. D. Keil, D. R. Dykaar, A. F. J. Levi, R. F. Kopf, L. N. Pfeiffer, S. B. Darack, et al., "High-speed coplanar transmission lines," *Quantum Electronics, IEEE Journal of*, vol. 28, pp. 2333-2342, 1992.
- [130] S. Joo-Hiuk, W. Hsi-Huai, J. F. Whitaker, and G. A. Mourou, "Picosecond pulse propagation on coplanar striplines fabricated on lossy semiconductor substrates: modeling and experiments," *Microwave Theory and Techniques, IEEE Transactions on*, vol. 41, pp. 1574-1580, 1993.
- [131] J. F. Whitaker, R. Sobolewski, D. R. Dykaar, T. Y. Hsiang, and G. A. Mourou, "Propagation model for ultrafast signals on superconducting dispersive striplines," *Microwave Theory and Techniques, IEEE Transactions on*, vol. 36, pp. 277-285, 1988.
- [132] N. Zhitenev, R. Haug, K. v. Klitzing, and K. Eberl, "Experimental determination of the dispersion of edge magnetoplasmons confined in edge channels," *Physical Review B*, vol. 49, pp. 7809-7812, 1994.

- [133] D. Some and A. V. Nurmikko, "Real-time electron cyclotron oscillations observed by terahertz techniques in semiconductor heterostructures," *Applied Physics Letters*, vol. 65, pp. 3377-3379, 1994.
- [134] D. B. Mast, A. J. Dahm, and A. L. Fetter, "Observation of Bulk and Edge Magnetoplasmons in a Two-Dimensional Electron Fluid," *Physical Review Letters*, vol. 54, pp. 1706-1709, 1985.
- [135] F. Stern, "Polarizability of a Two-Dimensional Electron Gas," *Physical Review Letters*, vol. 18, pp. 546-548, 1967.
- [136] K. W. Chiu and J. J. Quinn, "Plasma oscillations of a two-dimensional electron gas in a strong magnetic field," *Physical Review B*, vol. 9, pp. 4724-4732, 1974.
- [137] Y. Ma, R. Fletcher, E. Zaremba, M. DiIorio, C. T. Foxon, and J. J. Harris, "Energy-loss rates of two-dimensional electrons at a GaAs/Al_xGa_{1-x}As interface," *Physical Review B*, vol. 43, pp. 9033-9044, 1991.
- [138] C. D. Wood, D. Mistry, L. H. Li, J. E. Cunningham, E. H. Linfield, and A. G. Davies, "On-chip terahertz spectroscopic techniques for measuring mesoscopic quantum systems," *Review of Scientific Instruments*, vol. 84, pp. 085101-6, 08/00/ 2013.
- [139] G. Hasnain, K. W. Goossen, and W. H. Knox, "Effect of optical phonons on femtosecond pulse propagation in coplanar striplines," *Applied Physics Letters*, vol. 56, pp. 515-517, 1990.
- [140] M. J. Kelly, R. J. Brown, C. G. Smith, D. A. Wharam, M. Pepper, H. Ahmed, et al., "One-dimensional ballistic resistor in hot-electron regime: nonlinear and negative differential resistance to 10 THz," *Electronics Letters*, vol. 25, pp. 992-993, 1989.